Science

The Tsetse Fly Genome

CONTENTS

page 355

page 361

ON THE WEB THIS WEEK

>> *Science* Podcast
On this week's show: the genome sequence of the tsetse fly and a roundup of stories from our daily news site.

>> Find More Online
Check out *Science* Express, the weekly podcast, videos, daily news, our research journals, and *Science* Careers at **www.sciencemag.org**.

COVER

A pregnant female tsetse fly (*Glossina morsitans*), roughly equivalent in size to a housefly. Tsetse flies are the sole carriers of human African trypanosomiasis (sleeping sickness). See pages 349 and 380 for a description of the sequencing and annotation of the tsetse fly genome.

Photo: Geoffrey M. Attardo, Yale School of Public Health

pages 365 & 400

pages 370 & 376

Double Helix, Doubled

Chromatin consists of genomic DNA packaged onto nucleosomes—double donut-shaped complexes of histone proteins. Roughly 150 base pairs of DNA are wrapped around each nucleosome with variable lengths of linker DNA in-between. Using cryogenic electron microscopy, **Song et al.** (p. 376; see the Perspective by **Travers**) determined the 11 angstrom–resolution structure of a 12-nucleosome string of DNA. The segment forms a 30-nanometer fiber structure, which is itself double-helical, like the DNA it packages.

Africa's Bane

Tsetse are blood-feeding, fast-flying flies that transmit a range of *Trypanosoma* spp. protozoan pathogens, which cause sleeping sickness in humans and their nagana in their livestock. The **International *Glossina* Genome Initiative** (p. 380) sequenced the genome of *Glossina morsitans* and identified the genes for many attributes of the tsetse's remarkable biology, including viviparity and the expression of analogs of mammalian milk proteins. Tsetse are host to several specific symbionts that appear to synthesize essential nutrients for the fly and also to hitherto undiscovered parasitoid-derived viruses. Deeper exploration of this genome will reveal what makes these fly species so host- and trypanosome specific.

Understanding N Loss

Biologically available nitrogen (N) is essential for marine plants, and shortage of N limits photosynthesis. Marine N can be removed by denitrification and anaerobic ammonia oxidation (anammox) processes, but what controls the balance between these two pathways? **Babbin et al.** (p. 406, published online 10 April) tested the effects of stoichiometry on N removal in the lab and found that the balance of N loss processes depends on the stoichiometry of the source organic material.
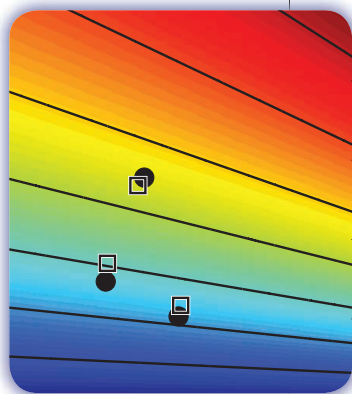
Optogenetic Insights>>

Mapping functional neural circuits for many behaviors has been almost impossible, so **Vogelstein et al.** (p. 386, published online 27 March; see the Perspective by **O'Leary and Marder**) developed a broadly applicable optogenetic method for neuron-behavior mapping and used it to phenotype larval *Drosophila* and thus developed a reference atlas. As optogenetic experiments become routine in certain fields of neuroscience research, creating even more specialized tools is imperative (see the Perspective by **Hayashi**). By engineering channelrhodopsin, **Wietek et al.** (p. 409, published online 27 March) and **Berndt et al.** (p. 420) created two different light-gated anion channels to block action potential generation during synaptic stimulation or depolarizing current injections. These new tools not only improve understanding of channelrhodopsins but also provide a way to silence cells.
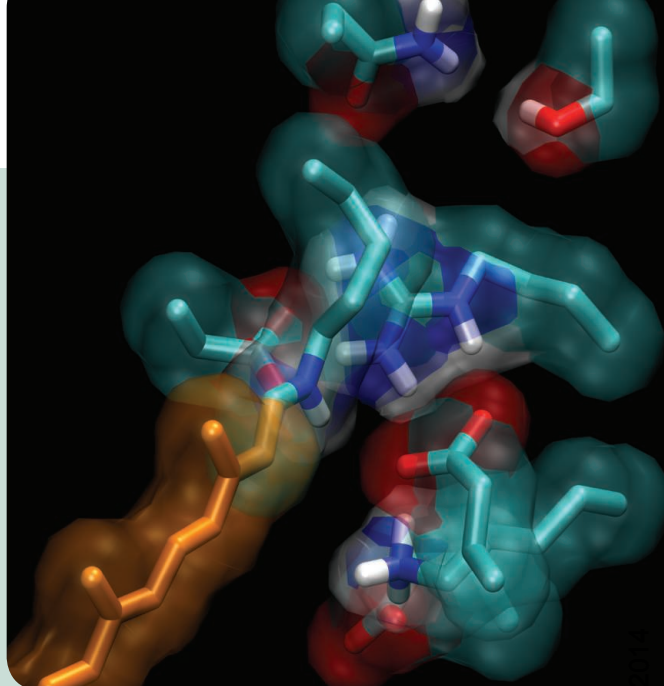
A Dual Approach to 2 + 2

Asymmetric catalysis generally accelerates the pathway to one specific product geometry that can be manipulated by reducing the temperature to slow down competing reactions. It is more difficult to be selective in photochemical reactions, but in the [2 + 2] coupling of olefins to make four-membered rings, **Du et al.** (p. 392; see the Perspective by **Neier**) used a ruthenium catalyst that absorbs visible light to activate the substrates below the frequency threshold where they absorb intrinsically. Then a second—a chiral Lewis acid—catalyst directs the product stereochemistry. A major advantage of the dual reactions is that each catalyst can be tuned independently.

Wetted Apatite

The long-running story of the dry Moon was rewritten a few years ago when hydrogen-bearing glass spherules were discovered. The highest water contents are found in lunar apatite, at levels suspiciously comparable to the water content of Earth apatites. **Boyce et al.** (p. 400, published online 20 March; see the Perspective by **Anand**) now show that the water content of lunar apatite is not a reliable indicator of the abundance of water in mare basalts. The existence of apatite with high water content is an almost inevitable consequence of the loss of tiny amounts of fluorine-rich apatite from a melt and replacement by hydrogen and is thus no indication of a "wet" Moon.

House or Face?

The neural mechanisms of spatial attention are well known, unlike nonspatial attention. **Baldauf and Desimone** (p. 424, published online 10 April) combined several technologies to identify a fronto-temporal network in humans that mediates nonspatial object-based attention. There is a clear top-down directionality of these oscillatory interactions, establishing the inferior-frontal cortex as a key source of nonspatial attentional inputs to the inferior-temporal cortex. Surprisingly, the mechanisms for nonspatial attention are strikingly parallel to the mechanisms of spatial attention.

No Light Control

Light is the main source of energy for plants and is also used as a signal for growth and development: Indeed, it can modulate up to a fifth of the entire transcriptome in both *Arabidopsis thaliana* and rice. **Petrillo et al.** (p. 427, published online 10 April) show that light can affect gene expression through alternative splicing of the serine-arginine rich protein *At-RS31*, required for proper plant growth. But photoreceptors are not involved; rather, a mobile retrograde signal from the chloroplast controls the alternative splicing of *At-RS31*.

Additional summaries

Magnified Flare-Up

The rise and fall of the luminosity of a supernova detected in 2010 was typical for its class, but its apparent brightness was 30 times greater than similar events. **Quimby** *et al.* (p. 396) compared spectra from the time of peak brightness and after the supernova faded, from which they concluded that something was interfering with our line of sight to the supernova. A previously unknown foreground galaxy turned out to be acting as a lens, bending and magnifying the light from the supernova. Potentially, spacetime warping like this could allow direct testing of cosmic expansion.

Deep Freeze

Geologists usually consider glaciers and ice sheets to be gigantic abrasives, scouring the ground beneath them and carving out relief on the underlying landscapes. **Bierman** *et al.* (p. 402, published online 17 April) show that this is not always the case. They found that the silt at the very bottom of the Greenland Ice Sheet Project 2 core contained significant amounts of beryllium-10, an isotope produced in the atmosphere by cosmic rays and which adheres to soils when it is deposited on them. Hence, the dust at the bottom of the ice sheet indicates the persistence of a landscape under 3000 meters of glacial ice that is millions of years old.

RNA Heteroplasmy

Like nuclear DNA, the mitochondrial genome has to be posttranscriptionally modified to function properly; however, among individuals, mitochondrial RNA (mtRNA) transcripts vary in ways that are poorly understood. **Hodgkinson** *et al.* (p. 413) looked at mtRNA editing events and post-transcriptional methylation in more than 700 individuals. Interestingly, variation at the ninth position within transfer RNAs showed a high frequency of variation that, in some cases, is genetically attributable.
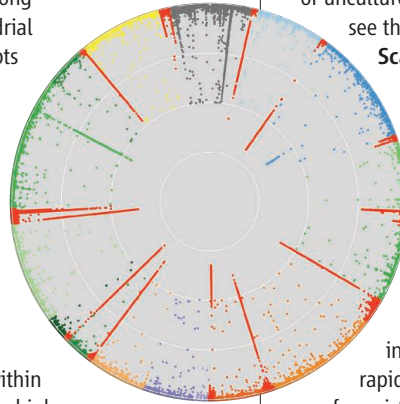
Oceans of Cyanobacterial Diversity

What does it mean to be a global species? The marine cyanobacterium *Prochlorococcus* is ubiquitous and, arguably, the most abundant and productive of all living organisms. Although to our eyes the seas look uniform, to a bacterium the ocean's bulk is a plethora of microhabitats, and by large-scale single-cell genomic analysis of uncultured cells, **Kashtan** *et al.* (p. 416; see the Perspective by **Bowler and Scanlan**) reveal that *Prochlorococcus* has diversified to match. This "species" constitutes a mass of subpopulations—each with million-year ancestry—that vary seasonally in abundance. The subpopulations in turn have clades nested within that show covariation between sets of core alleles and variable gene content, indicating flexibility of responses to rapid environmental changes. Large sets of coexisting populations could be a general feature of other free-living bacterial species living in highly mixed habitats.

Addressing Vaccine Hesitancy

Barry R. Bloom is a professor at the Harvard School of Public Health, Boston, MA 02115. E-mail: bbloom@hsph.harvard.edu

Edgar Marcuse is a professor emeritus at University of Washington School of Medicine, Seattle, WA 98195.

Seth Mnookin is an assistant professor at the Massachusetts Institute of Technology, Cambridge, MA 02139.

LAST MONTH, THE WORLD HEALTH ORGANIZATION CERTIFIED INDIA AND SOUTHEAST ASIA AS BEING polio-free, an extraordinary achievement given that the polio vaccine was declared safe and effective only 59 years ago. Vaccines are one of the safest and most cost-effective medical interventions in history. By immunizing infants, children, and teenagers, vaccines protect the entire community. Nevertheless, there is a surge of outbreaks in vaccine-preventable diseases in the United States. What research is needed to reverse this trend?

The crux of the problem is our inability to demonstrate to skeptical parents that vaccinations save lives. On the one hand, the United States has sustained impressive uptake rates for vaccinations overall. During the 2012–2013 school year, the median coverage was about 92% for vaccines against measles-mumps-rubella, diphtheria-tetanus-acellular pertussis, and varicella. Yet over the past 5 years, outbreaks of everything from measles to mumps to pertussis show that there is a growing number of communities with vaccine coverage below the levels needed to maintain herd immunity—when vaccination of a substantial portion of a population protects those who have not developed immunity. Many factors probably contribute to this decline: exposure to a report (that was later retracted) linking the measles vaccine to autism, warnings from ill-informed peers, scare tactics of antivaccine groups, and misinformation by celebrity personalities. Regardless of the source, the results are the same: debilitating infections, hospitalizations, and in tragic cases, death.

This frustrating reality illustrates that the facts do not always speak for themselves. We need only look at Western Europe to see how a few dozen cases of a vaccine-preventable disease can explode into a countrywide epidemic: In 2007, France reported 40 measles cases; in 2011, there were 15,000 cases with 6 deaths. In 2011, the United States experienced its largest number of individual measles cases (222) and outbreaks (17) since 1996. The source of nearly every outbreak was someone who was intentionally unvaccinated—often a U.S. resident traveling abroad or someone of unknown vaccine status. 2013 saw the largest single measles outbreak (58 patients) in the United States in nearly 20 years.

A recent report concluded that current public health communication about vaccines may actually increase misperceptions or reduce vaccination intention, and that attempts to increase concerns about communicable diseases or correct false claims about vaccines may be counterproductive.* Research is needed to develop evidence-based strategies that guide health care providers on how best to communicate the importance of immunization to parents who are uncertain about what to believe. Last fall, an interdisciplinary group of scientists, clinicians, and social scientists convened at the American Academy of Arts and Sciences to discuss priorities in communication research that would provide specific solutions on how to move forward. The group's conclusion (the report, for which we were co-chairs, has just been released†) was that we need research that addresses how and when attitudes and beliefs about vaccines are formed, how people make decisions about immunization, how best to present information about vaccines to hesitant parents, and how to identify communities at risk of vaccine-preventable disease outbreaks. A study of the 2008 San Diego measles outbreak‡ found that the cost to the public health system of each measles infection was $10,376, whereas the total cost to contain the outbreak was $124,517. If the type of research proposed by the American Academy report helps to prevent even a handful of outbreaks, it will have more than paid for itself.

Strategies to combat antivaccine messages cannot be developed by educated guesswork. Evidence-based approaches that facilitate vaccination are needed if we are to prevent diseases that can easily be avoided and fulfill the potential of modern vaccine research.

– Barry R. Bloom, Edgar Marcuse, Seth Mnookin

---

*http://pediatrics.aappublications.org/content/early/2014/02/25/peds.2013-2365. †www.amacad.org/vaccines. ‡D. E. Sugerman *et al.*, *Pediatrics* **125**, 747 (2010).
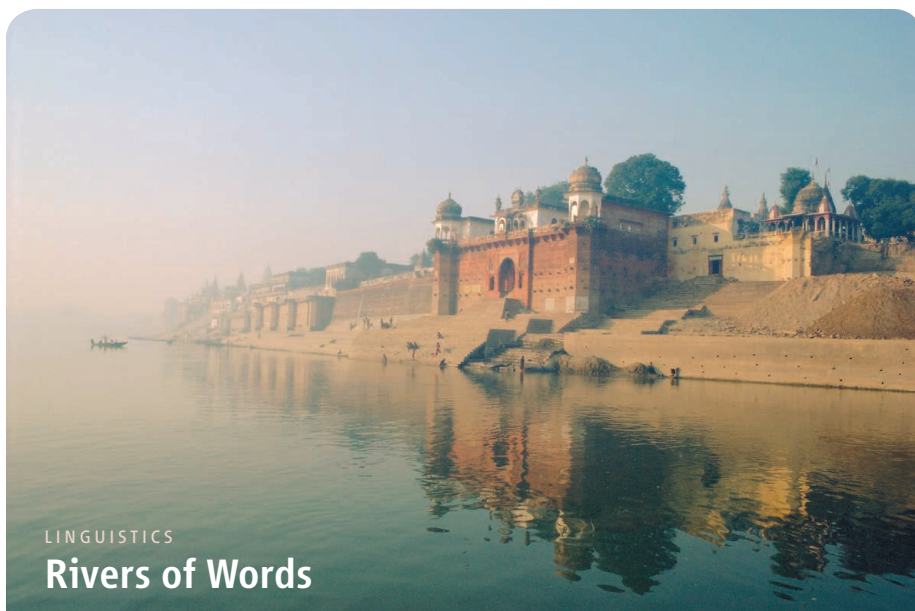
LINGUISTICS
Rivers of Words

The distribution of the ~7000 remaining linguistic groups around the globe is highly heterogeneous, with high linguistic diversity in Africa (2562 living languages) and Asia and the Pacific (2762), and less diversity in Europe (396) and the Americas (1132). As with species distribution, evidence—for example, latitudinal gradients in the density of some human languages and a correlation between landscape elevation and language density—suggests that the environment plays an important role in language distributions.

Using a variety of publicly available data sets, Axelsen and Manrubia compare 14 environmental variables, including human population density, against linguistic diversity both globally and for several continental regions (the Americas, Europe, Africa, and the Asia Pacific region). Statistical analysis of partial correlations between the 14 different factors reveals specific local dependencies in individual regions. For example, low linguistic diversity in the Americas is most correlated with population density and linked to the effects of European colonization. Globally, rivers and landscape roughness (altitude) are the most important factors underlying high linguistic diversity. Landscape roughness may promote linguistic isolation and diversification, whereas the transportation function that rivers provide may have brought disparate language groups together, seeding the formation of new ones. — GR

Proc. R. Soc. London Ser. B 10.1098/rspb.2013.3029 (2014).

GEOCHEMISTRY
Expelled Xe

Based on the distribution of other noble gases, Earth's atmosphere is apparently depleted in Xe. Although some may have been lost to space, Earth's interior—the original source of atmospheric gases—could also act as a reservoir by preferentially holding onto Xe as the planet formed and differentiated. Because of the size of the mantle, it would be an ideal candidate; however, it is unclear whether Xe reacts with the major Si-rich phases of the mantle at the corresponding pressures and temperatures. Zhu et al. performed total energy calculations at the extreme temperature and pressure conditions of Earth's inner core to determine that Xe reacts with Fe and Ni, the two dominant constituents of the solid inner core. Crystal structure predictions found several stable phases of Xe-Fe/Ni alloys, including the stable phases of $XeFe_3$ and $XeNi_3$, suggesting that the inner core may be Earth's missing reservoir of Xe. — NW
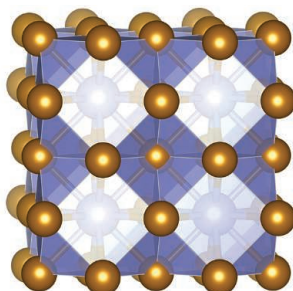
Nat. Chem. 10.1038/NCHEM.1925 (2014).

MATERIALS SCIENCE
Safe Sopping

Cleaning up oil or an industrial solvent after a spill is complicated by the danger that the combustible liquid might catch fire. Ruan et al. sought to minimize this risk by taking advantage of the flame-retardant properties of melamine. By sequentially immersing a commercial melamine-formaldehyde sponge in solutions of dopamine and then fluoroalkyl thiols, they rendered the porous material superhydrophobic. A series of tests showcased the sorption properties of the modified sponge: efficient uptake (on the order of 100 times its weight) of common solvents as well as crude oil, followed by recovery through mechanical squeezing. The material proved resilient to cycling 100 times, as well as an hour's worth of heating to 200°C or cooling by liquid nitrogen. In a comparison with a polypropylene-based sorbent, it also showed substantially greater resistance to combustion. The authors suggest that the simplicity of the synthetic protocol bodes well for possible scale-up manufacturing. — JSY

Angew. Chem. Int. Ed. **53**, 10.1002/anie.201400775 (2014).

BIOMATERIALS
Slime Fibers

When attacked, hagfish will release protein threads and mucin vesicles, which interact with seawater to form copious quantities of slime. Before release, the threads exist as coiled skeins that occupy almost the entire volume of specialized gland thread cells. The threads unravel in a fraction of a second from a 150-µm-long ellipsoid bundle to a thread that is 100 times longer, which clearly requires sophisticated ordering within the cell. As the threads also have comparable mechanical properties to those of spider silk, there is interest in understanding the organization and morphology of the coiled thread in both mature and immature gland thread cells, in order to design synthetic reactors. Using electron microscopy, Winegard et al. were able to identify changes in thread length, diameter, and morphology as the cells matured. Beyond this, they were able to see changes in the cell shape as it shifted from being rounded after differentiation to becoming spindle-shaped, with a more conical profile and flared base. This suggests that the cell nucleus acts as a template over which the staggered thread loops form. Using a focused ion beam within a scanning electron microscope, the three-dimensional structure of the loops was determined, including the ways that adjacent

layers overlay and the cabled appearance of the skein where the threads run circumferentially along the outer surface. — MSL

Nat. Comm. 10.1038/ncomms4534 (2014).

GENETICS

Blood and Brains

Epigenetic changes, such as gene methylation, can be detected directly by examining the status of DNA within specific tissues. However, it is desirable to identify epigenetic changes from afar, especially in tissues that may be hard to survey, such as the brain. Working with a mouse model of Cushing's disease, characterized by changes in methylation as a response to exposure to glucocorticoids, Ewald *et al.* found that methylation and expression of the *Fkpb5* gene within the hippocampus correlated with its degree of methylation in the blood. Although limited by the examination of only a single gene, the observed correlation highlights that for some diseases, it may be possible to use blood monitoring to infer epigenetic changes in the brain. — LMZ

Psychoneuroendocrinology **44**, 112 (2014).

CELL BIOLOGY

Sleep Circuit

The neurotransmitter molecule γ-aminobutyric acid (GABA) promotes sleep in mammals and flies, but the molecular details of this regulation have not been clear. Chen *et al.* provide new

insight into this complex pathway, finding that GABA transaminase (GABAT), a mitochondrial enzyme that breaks down GABA, controls GABA amounts to affect sleep in *Drosophila*. Sleep is controlled by the protein sleepless (SSS), which is expressed in neurons of the fly brain. Its absence in mutant flies increases neural activity and decreases sleep. Mutant flies lacking SSS expressed more GABAT in the brain. Consequently, GABA amounts decreased by 30% in the brain, and compared to control flies, mutant flies slept less. Disrupting GABAT expression increased

GABA amounts and boosted total daily sleep. Furthermore, reducing GABAT in mutant flies lacking SSS restored sleep. Flies expressing mutant GABAT showed an increase in overall daily sleep, and the time it took flies to fall asleep was reduced. Moreover, treatment of adult flies lacking SSS with ethanolamine O-sulfate, an inhibitor of GABAT, rescued sleep. These results suggest that SSS promotes sleep and that its absence increases neuron excitability, which may demand more energy. This could alter cell metabolism in neighboring glia, including changes in GABAT activity in the mitochondria. Changes in GABAT activity have been implicated in epilepsy (characterized by increased neural activity) and other neuropsychiatric disorders. The connection of GABAT and cell metabolism to sleep control may explain sleep problems associated with these conditions. — LC

Mol. Psychiatry 10.1038/mp.2014.11 (2014).

BIOPHYSICS

AFM Uncompromised

Atomic force microscopy (AFM) is a powerful tool used both for subnanometer imaging and for mechanical probing of molecules. The key measurement in AFM is the deflection of a cantilever, which depends on the force it experiences. AFM is used in single-molecule force spectroscopy to monitor the folding and unfolding of biomolecules. This application requires sensitivity to very small changes in force on short time scales, but also requires long-term force stability. Current AFMs are optimized either for short-term force precision (achieved by using shorter, stiffer cantilevers to reduce hydrodynamic drag) or for long-term force stability (better performance comes from longer, softer cantilevers). Bull *et al.* modified a short cantilever with a focused ion beam to achieve excellent short-term precision and long-term stability. AFM cantilevers are typically gold-coated to improve signal intensity, but the gold reduces stability. Removal of the gold except for a protected patch at the end of the cantilever maintained high signal without compromising stability. A protein unfolding assay highlighted the short-term precision, whereas stretching a surface-anchored protein showed sub-pN performance over a force bandwidth of 0.01 to 1000 Hz. Monitoring abrupt unfolding of a protein showed that the cantilever had a temporal response time of about 70 μs. These responsive yet stable cantilevers should benefit diverse AFM studies. — VV

ACS Nano. 10.1021/nn5010588 (2014).

CREDIT: DIGITALSKILLET/ISTOCKPHOTO

AROUND THE WORLD
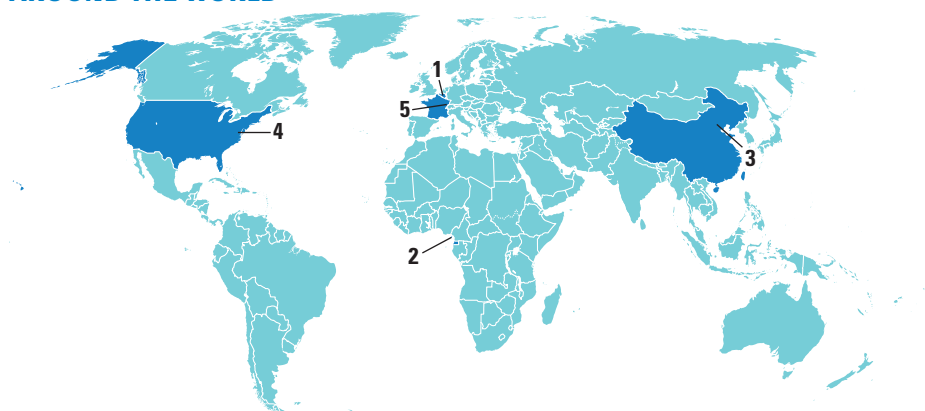
Brussels 1

Sentinel-1A Sends First Pics

The European Space Agency's (ESA's) Sentinel-1A satellite, launched on 3 April, has sent home its first radar images of Earth, including this image of Brussels taken on 12 April. It shows the dense city center in white, vegetation in green, and waterways in black. Sentinel-1A uses advanced radar
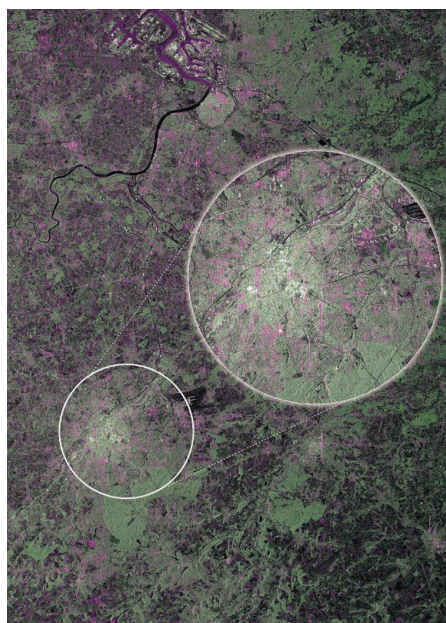
technology to "see" in the dark or through obstacles such as clouds and rain. It can capture images that can be used for urban planning and to monitor glaciers, manage water resources, or devise emergency response.

The mission is the first in a new family of satellite missions that will form part of the Copernicus environmental monitoring program, an €8.4 billion joint initiative of the European Commission and ESA. Coperni-cus will pull together data from the environmental satellites as well as ground-based and airborne stations to study the overall health of the planet.

Malabo 2

Polio Spreads Farther Into Central Africa

The polio outbreak in Cameroon detected last October is spreading. As of last week, three cases were reported in neighboring Equatorial Guinea, which was polio-free for 15 years. The situation is "very alarming," says Bruce Aylward, who heads the global initiative to eradicate polio. The Cameroon virus is closely related to one last seen in Chad in 2011, which suggests it has been circulating undetected in the region for several years due to poor surveillance and low immunization rates. In Equatorial Guinea, the routine immunization rate is about 40%.

Experts are on high alert to detect further spread to nearby countries—particularly Nigeria, which has been making impressive gains in quashing the virus, and the war-torn Central African Republic, where mounting an emergency response would be extremely challenging.

Beijing 3

China's Soil Woes In Sharper Focus

The Chinese government has lifted the veil a bit on a nationwide soil survey that it had classified as a state secret (*Science*, 28 March, p. 1415). The environment ministry posted a bulletin to its website on 17 April divulging that 16% of sites tested during the 5-year survey are polluted. The report concludes that China's overall soil environment is "not optimistic."

Especially worrying to researchers is that pollution is most widespread on agricultural lands, where 19% of sites are tainted. Major contaminants, the bulletin noted, are heavy metals such as cadmium, mercury, arsenic, and lead. The report blames mining and industrial waste for fouling croplands. However, much of the data from the survey—which ran from 2005 to 2010—remains under lock and key. "The transparency is not enough," says Chen Ruishan, a geologist at Hohai University in Nanjing.

China's State Council has ordered the environment ministry to formulate a plan for curtailing future soil pollution and for remediating contaminated land, the bulletin states. But "we need to know about the spatial distribution" of the soil pollution to devise a remediation strategy, Chen says—and that kind of map has not been released to the public.

Richmond 4

Climate Scientist Prevails In Virginia High Court

The Virginia Supreme Court has ruled in favor of climatologist Michael Mann in a fight over whether the former University of Virginia (UVA) climatologist must turn over e-mails requested by means of a 2011 state Freedom of Information Act (FOIA) request. The court upheld a lower court ruling that UVA did not have to hand over the e-mails to the Energy & Environment Legal Institute (formerly the American Tradition Institute). It ruled that the e-mails, which touched on scientific data and publications, essentially belonged to Mann and were not public property.

"It is the end of this episode, and a win in this battle," says Mann, now at Pennsylvania State University, University Park. He says the decision sets an important precedent for "many similar FOIA-based bad faith attacks on climate scientists in the months and years ahead in other states." The Reporters Committee for Freedom of the Press, however, says the ruling provides overly broad protections for universities seeking to withhold e-mails from reporters and the public.

Strasbourg, France 5

E.U. Parliament Clears Beefed-Up Industry Partnerships

The European Parliament has endorsed a €9 billion spending package for big research partnerships with industry. In several votes held last week in Strasbourg,

Saturn's New Friend

As viewed by NASA's Cassini spacecraft, "Peggy" is just an unassuming bright dot right at the edge of Saturn's outermost ring (the A ring). But in fact, Cassini may have observed the birth of a brand-new moon around the ringed planet, scientists reported online in the journal *Icarus* last week. Cassini snapped the picture on 15 April 2013, documenting a bright arc and an unusual distension of the ring that scientists think are caused by the gravitational effects of the object. Although the moon itself may not hold together long, witnessing its birth could help better explain the formation of Saturn's other icy moons within long-vanished, even more massive rings. NASA scientists plan to move Cassini's orbit closer to the outer edge of the A ring in 2016 to get a better look at Peggy.

France, the Parliament approved the creation or continuation of six Joint Technology Initiatives (JTIs), part of the so-called Innovation Investment Package announced last year (http://scim.ag/JTIEU). JTIs are large programs that support industry research in areas considered complex, slow, or risky—such as the development of clean aircraft or novel medicines. Businesses say they will match public funds in kind, to reach about €17 billion for all six JTIs over the next 7 years.

The European Union's contribution will come from the budget for Horizon 2020, the bloc's research funding program for 2014 to 2020. At the request of member states, industry partnerships were protected from cuts that affected the rest of Horizon 2020's budget during planning negotiations. That protection prompted criticism from universities, who argue that academic grants lost out to industry research.

Member states are expected to formally approve the decisions before the programs are launched in July.

NEWSMAKERS

Science Wins Awards for Archaeology, Polio Stories

Science's immersive multimedia story "The Thousand-Year Graveyard" by **Ann Gibbons** has won the annual Gene S. Stuart Award for archaeology writing from the Society for American Archaeology. The story's slideshows, videos, and text (http://scim.ag/thouyear) take readers to a graveyard in Tuscany as archaeologists uncover a tortured history of death and disease. The online treatment of the 13 December 2013 story was created by a six-person team.

And for her 4 October 2013 story on polio eradication in northern Nigeria

Gibbons

Roberts

(http://scim.ag/polioerad), *Science* Deputy News Editor **Leslie Roberts** received a 2013 Award for Excellence in Health Care Journalism from the Association of Health Care Journalists. To learn about the "art" of eradicating polio, Roberts traveled through the African nation with a former Nigerian health minister, exploring the roles of money, tradition, education, and violence in efforts to stamp out the disease.

FINDINGS

New Stem Cells a Genetic Match for Adults

Scientists are a step closer to developing replacement tissue that won't be rejected by a patient's immune system. Researchers have created human embryonic stem cells carrying the DNA of specific adults. Theoretically, such stem cells can form any of the body's cell types and could be used in new treatments for Parkinson's disease, diabetes, and many other diseases.

Researchers, led by Young Gie Chung of the Research Institute for Stem Cell Research in Los Angeles, California, reported creating the stem cells using skin cells from one 35-year-old male and one 75-year-old male online on 17 April in *Cell Stem Cell*. The scientists built on the work of a team led by Shoukhrat Mitalipov of the Oregon Health & Science University in Portland. Mitalipov's group removed the DNA-containing nucleus from human eggs and replaced it with skin cells from infants and fetuses, a technique called somatic cell nuclear transfer (SCNT). SCNT was used to clone Dolly the sheep in 1996—but rather than clone humans, researchers take the early-stage embryos that result from SCNT and derive stem cells. The new study's team showed that with minor tweaks, this technique also works for adults.

THEY SAID IT

"[B]anishing this research from Boston, the world's densest concentration of medical brainpower, would impede scientists' ability to learn from one another."

—Editorial in *The Boston Globe* on 13 April reacting to a proposed city ordinance to ban biosafety level 4 research at Boston University's National Emerging Infectious Diseases Laboratories.

Incognita. The fastest warming part of the globe, the Arctic, lacks temperature stations in many areas.
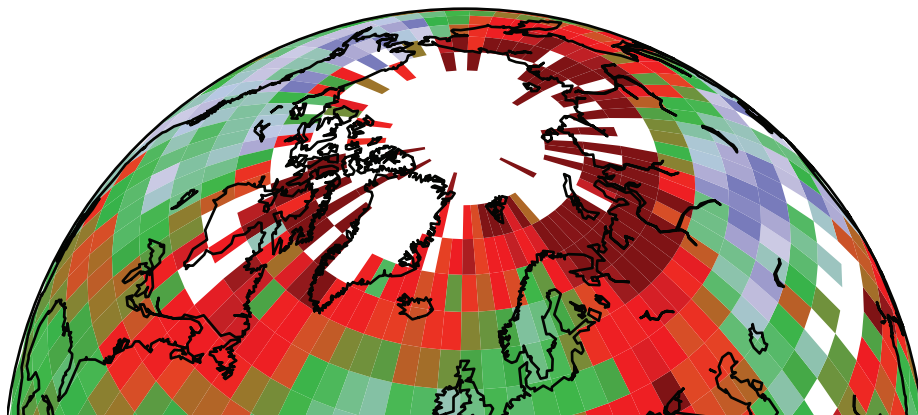
CLIMATE SCIENCE

Climate Outsider Finds Missing Global Warming

POTSDAM, GERMANY—Kevin Cowtan had a clear message to deliver earlier this month when he spoke to researchers here at the Potsdam Institute for Climate Impact Research (PIK): Standard data sets of worldwide surface temperatures underestimate recent global warming, and the much-publicized slowdown in warming isn't as slow as it seems. Crystal clear, one might say: Unlike the 25 scientists and students listening to his talk, Cowtan is not a climate scientist—he's a protein crystallographer at the University of York in the United Kingdom.

Cowtan described how he and a graduate student had recently reanalyzed data underpinning key global temperature data sets. Among their findings: The two most prominent data sets, one maintained by a British collaboration and the other by NASA, have underestimated the pace of warming between 1997 and 2012 by an estimated 158% and 49%, respectively.

That's not a big difference in absolute temperature rise, says PIK climatologist Stefan Rahmstorf, given the relatively short period covered (see table). But it shows that the slowdown, or "hiatus," has been less pronounced than previously described, he says. Correcting the data sets "should have been done ages ago," Rahmstorf adds. In an e-mailed statement to *Science*, climatologists at the National Oceanic and Atmospheric Administration (NOAA) call the recent work "important contributions" to the climate field.

Cowtan and his partner Robert Way, of the University of Ottawa, got drawn into the problem by participating in the climate-science advocacy website SkepticalScience.com. They learned that researchers had been trying for years to explain why global temperature data sets show different rates of warming—and are below what many climate models have predicted. The British and NASA data sets, along with others maintained by NOAA and academic scientists in Berkeley, California, rely on data from thousands of weather stations around the globe along with satellite measurements of ocean temperatures.

Yet gaps in the network of stations exist over Antarctica, Africa, and, crucially, the Arctic—the region that satellites, weather models, and shrinking sea ice point to as the fastest warming on the planet. The various data sets deal with the gaps in different ways. The British one, known as HadCRUT, omits missing regions from its calculations of global mean temperature trends; NASA extrapolates temperatures for those areas using data from their edges. Both groups have previously warned that that sparse coverage may lead to underestimates of global warming.

Cowtan and Way set out to quantify those underestimates. They applied a new method that fills in missing temperatures over sea ice by combining satellite data for missing areas with a method known as kriging, which calculates missing data by checking nearby temperature station readings. Then they compared their method's skill in interpolation with that of the NASA and Hadley approaches in the Arctic by systematically removing known data and using each of the three techniques to reconstruct the data set. Cowtan says his and Way's approach proved the most reliable, and data from Arctic buoys and three weather models support it.

The takeaway? A slowdown in warming that's half as big as previously thought. "When you fill in the gaps, temperatures in recent years go up, and temperatures around 1998 go down," Cowtan told the climate scientists in Potsdam. The planet has warmed most where scientists are watching least, enhancing the perceived size of the slowdown in warming.

Cowtan and Way first drew attention to their methods in November 2013, when their paper focusing on HadCRUT was first published online in the *Quarterly Journal of the Royal Meteorological Society*. In Potsdam, Cowtan shared an unpublished result that suggests a data-smoothing algorithm may be tuning down temperature measurements that NOAA's Arctic climate stations supply to NASA. NOAA says it is adding new stations to its network to address the Arctic data gap. Philip Jones of the University of East Anglia in Norwich, U.K., which runs HadCRUT jointly with the U.K. Met Office, says HadCRUT is also seeking to add stations.

TEMPERATURE TRENDS
1997–2012

Source	Warming (°C/decade)
Climate models	0.102–0.412
NASA data set	0.080
HadCRUT data set	0.046
Cowtan/Way	0.119

Getting warmer. New method brings measured temperatures closer to projections.

Cowtan's talk at PIK and remarks the previous day to a Potsdam meeting on the temperature record were his first ever talks before climate researchers. He attributes his odd interest in climate to "an obsession with solving computational problems." He and Way have done the work on nights and weekends, raising $3000 from readers at Skeptical Science to pay for open-access fees for their November paper.
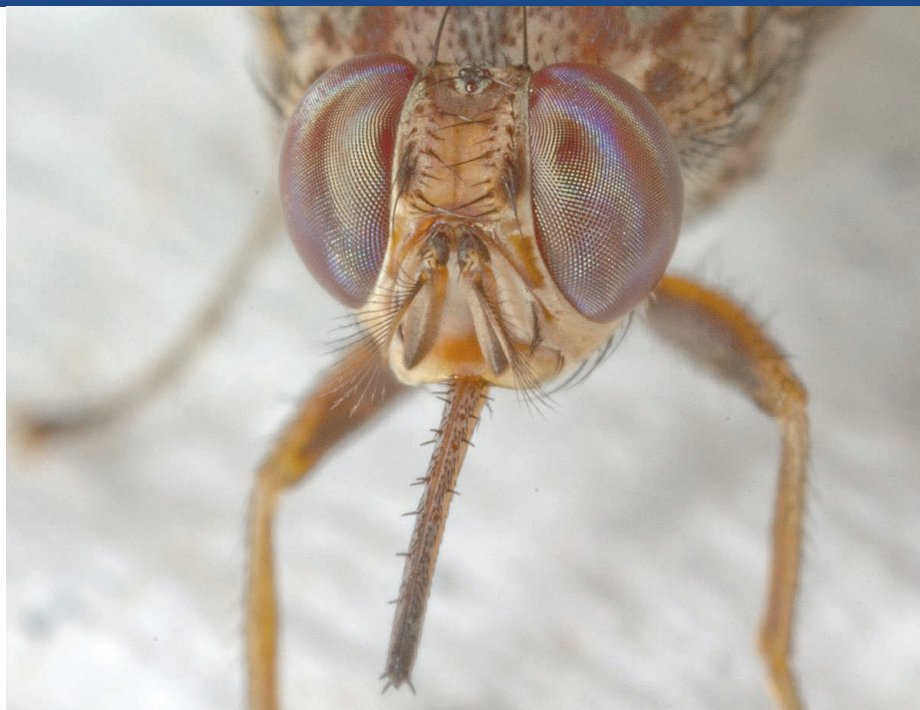
"It's impressive when someone outside the field makes a useful contribution," says Dim Coumou, an atmospheric scientist at PIK. Cowtan says he appreciates the recognition but that improving the data sets is what really matters: "The reason I started this is that I wanted the problem fixed."

–ELI KINTISCH

Ouch! With each brutal bite, a tsetse fly can take in almost its weight in blood.

GENOMICS

Genome Yields Clues to Tsetse Fly's Strange and Deadly Ways

A tsetse fly bite feels like a hammer blow. Smaller than horse flies but more aggressive, these African insects also carry trypanosome parasites responsible for sleeping sickness and the cattle disease nagana, two scourges of sub-Saharan Africa. Chemical traps and aerial spray programs targeting tsetse flies have replaced cruder control methods—inspectors at car checkpoints used to swat any flies they saw on dashboards. But 70 million Africans are still at risk for sleeping sickness, which causes extreme lethargy and can be fatal, and an estimated 3 million farm animals die each year from nagana.

Now, the first sequenced genome of a tsetse fly species, *Glossina morsitans*, may prime the pump for better control efforts. On page 380, and in 11 satellite papers in Public Library of Science (PLOS) journals, a collaboration called the International Glossina Genome Initiative (IGGI) reveals hints of what makes tsetse flies so successful and how the disease-causing trypanosomes interact with the flies that carry them. "Understanding the biology of the tsetse fly is an essential step to fight the disease and limit its diffusion," says Philippe Bastin, a parasitologist at the Institut Pasteur in Paris.

Most people think of mosquitoes as bloodsuckers, but they pale in comparison with tsetse flies, arguably the vampires of the insect world. Whereas mosquitoes also sip nectar and only the females suck blood, one tsetse fly can drink almost its weight in blood each meal, and both sexes consume nothing else. The fly needs a special repertoire of proteins for procuring, filtering, and packaging blood, as well as resident bacteria to provide nutrients not found in blood. Researchers are also eager to understand the genes and proteins underlying another tsetse fly oddity: They bear live young—one at a time—and nourish the developing larva with "milk" secreted from special glands.

The new genome is still in many pieces, but Serap Aksoy and Geoffrey Attardo of Yale University and their colleagues have already discerned 12,300 protein-coding genes. The research team also surveyed gene activity in various tissues, such as the salivary glands, which trypanosomes use as a launching point for infecting their next hosts, and milk glands, to see what proteins were important.

With its narrow blood diet, the tsetse fly doesn't need the full range of taste and odor receptors found, for example, in fruit flies, says Daniel Masiga, a molecular biologist at the International Centre of Insect Physiology and Ecology in Nairobi. He and his colleagues uncovered what appear to be 46 tsetse proteins sensitive to odors (the fruit fly has 58) and just 14 proteins for taste (the fruit fly has 73), with none sensitive to sugar. The fly also has fewer genes for proteins that recognize pathogens—possibly because its restricted diet exposes it to fewer infectious threats. The tsetse fly has more proteins for detecting carbon dioxide, however, likely useful for finding mammalian quarry through their exhalations.

Once a tsetse fly bites a victim, 250 proteins in its saliva work to keep blood from coagulating and to protect against the bitten host's immune system, among other things. But the team found that a trypanosome interferes with this efficient feeding machine—likely to its own benefit. With the parasite in its salivary glands, the fly produces fewer of these proteins, making feeding less efficient and forcing it to bite more often. That "will favor transmission" of the parasite, Bastin says.

To cope with its diet, the fly has an unusually large number of genes for proteins called aquaporins, which move water between cells. When those genes are knocked out, the tsetse fly has trouble excreting the bolus of water in ingested blood, has lower heat tolerance, and spends a longer time pregnant, the initiative reports in *PLOS Neglected Tropical Diseases*. Some aquaporin genes are particularly active in the milk gland and may be important in formulating milk, the researchers note. The genome also contains eight newly discovered milk protein genes, and a paper in *PLOS Genetics* reports that when a female is lactating, those genes and other associated milk gland genes rev up their activity 40-fold and account for half of the fly's total gene activity.

■ Tsetse fly region

Risky territory. People and livestock across Central Africa are at risk for diseases carried by the tsetse fly.

As part of the tsetse fly genome project, Aksoy's collaborator, Matthew Berriman of the Wellcome Trust Sanger Institute in Hinxton, U.K., also sequenced the DNA of some of the insect's resident microbes. One that had been previously sequenced, *Wigglesworthia glossinidia*, is a bacterium that lives in a specialized organ in the insect's gut and helps keep it well nourished. The microbe, for example, has genes for the synthesis of vitamin B, whereas the tsetse has only proteins for transporting this vitamin. "Without these obligate microbes, the fly cannot maintain fecundity," Aksoy says.

IGGI hopes the tsetse fly sequence will help revive the long-stalled fight against the insect and the misery it spreads. Even though epidemics of sleeping sickness erupted in the 1980s and 1990s, the number of researchers studying the host tsetse fly sharply declined during that period, with many switching to the better funded fields of malaria and AIDS. Beginning in 2004, Aksoy and the few remaining researchers in the field established the initiative on a shoestring—about $50,000 per year from the World Health Organization. Then in 2006, the Wellcome Trust committed about $4 million in in-kind sequencing toward decoding one tsetse fly species. All told, 146 researchers helped decipher the new genome.

No vaccines against trypanosome diseases now exist, and the available drugs cause severe side effects including convulsions. One control strategy that seeks to get rid of tsetse flies by flooding the population with sterile males is showing some success (*Science*, 20 July 2007, p. 310). But better control strategies are needed. The new genome suggests one: Chemical inhibitors targeting the single transcription factor that controls milk protein production could inhibit tsetse fly fecundity and lower parasite transmission rates. And now that researchers know the tsetse fly's repertoire of taste and odor receptors, they should be able to improve traps by including more attractive chemical baits. "This is really going to drive research in how to control tsetse flies in the next 2 decades," says Stephen Richards, an arthropod genomicist at Baylor College of Medicine in Houston, Texas.

However, researchers studying malaria and other insect-transmitted diseases caution that translating genome data into control strategies is difficult. Najib El-Sayed, a parasitologist at the University of Maryland, College Park, has sequenced several parasite genomes, and each time he expected that cures for their associated diseases or ways to prevent their spread would be forthcoming in 5 years. "Now I know better," he says. "The genome is just the beginning." **–ELIZABETH PENNISI**

BIOMEDICAL FUNDING

At NIH, Two Strikes Policy Is Out

The National Institutes of Health (NIH) is relaxing a 5-year-old policy that gave researchers just two chances to submit essentially the same grant application before having to start over with a new idea—a rule that many worried was especially hard on young investigators. Instead, the agency announced on 17 April, applicants can now resubmit a proposal as many times as they like.

Scientists seem "uniformly pleased," by the change, says Howard Garrison, deputy executive director for policy at the Federation of American Societies for Experimental Biology (FASEB) in Bethesda, Maryland. "They see it as a sign that NIH has taken into account the pain and the difficulties that people are experiencing."

The shift is the result of years of complaints from FASEB and others about the agency's "two strikes" rule, in place since 2009. It gave investigators two chances to pitch a research proposal: an initial "A0" version that received reviewer comments and, if rejected, a subsequent A1 version that the applicant could retool based on the first round of comments. If the A1 also missed funding, however, the scientist had to start over with a new A0 application that was substantially different.

That requirement created problems for early-career investigators, who often lack the staff and resources needed to generate the preliminary data used to support totally fresh ideas, says Sally Rockey, NIH's deputy director for extramural research. It was forcing even established labs to abandon productive long-term studies that probably would have been funded in a better budget climate, she adds.

Under the new policy, scientists will still have just one chance to submit an A1 proposal. If it fails, however, they will be free to resubmit the same application in the next funding round as an A0, and the same NIH reviewers will be told to view it as a fresh proposal. "I'm very optimistic that this change will give the research community greater versatility in allowing them to present their phenomenal ideas to NIH," Rockey said in a call with reporters.

NIH's resubmission policy has varied over the years. Before 2009, investigators could submit essentially the same proposal three times—the A0, A1, and A2 versions. The problem was that reviewers tended to give lower scores to first-time proposals, knowing the applicant had two more chances, and then often recommended funding them on the second or third try. This had the effect of putting researchers in a holding pattern, many times for an extra year, until their grant was finally funded. To make the process less agonizing and more efficient, NIH adopted the reduced two strikes policy, and it worked, Rockey says: More A0s were funded.

Many scientists, however, clamored to bring back the A2, arguing for more than one chance to revise their pitches. And some scientific leaders have urged the agency to adopt a 2008 recommendation from an advisory panel: that every proposal be considered a new A0, even if it was already reviewed. The panel also recommended NIH allow unlimited resubmissions. The new plan is a hybrid of these two scenarios, and "the simplest way to approach this issue," Rockey said.

Some research advocates don't go that far, but are pleased. The new policy "is a little bit … convoluted, but I think it's the right direction," says Stefano Bertuzzi, executive director of the American Society for Cell Biology in Bethesda. It won't solve NIH's overall money problems, he and others note, and it does not necessarily mean more applications will be funded, Rockey said.

Some NIH watchers lamenting the agency's growing budget woes have taken to blogs to describe the shift as rearranging the deck chairs on the *Titanic*. Others worry researchers will now submit the same proposals over and over, driving up application numbers, lowering success rates, and increasing the burden on reviewers.

Rockey says NIH does expect an initial rise in the number of applications because more investigators may have more than one proposal under review simultaneously. But she thinks that, in the long term, the numbers will stabilize as researchers "revert" to a one-at-a-time approach. All the same, Rockey says NIH will closely monitor the results of future funding rounds.

–JOCELYN KAISER

> *"This change will give the research community greater versatility in allowing them to present their phenomenal ideas."*
>
> **—SALLY ROCKEY, NIH**

NEURODEGENERATION

Potential Alzheimer's Drug Spurs Protein Recycling

In 2004, veteran structural biologists Gregory Petsko and Dagmar Ringe were looking for a way to make an impact on Alzheimer's disease. Frustration ensued. "We couldn't see a fresh approach," Petsko says.

Then, at a meeting in Colorado, they heard Scott Small, a young Columbia University neurologist, describe his research probing the brains of people who had died of the neurodegenerative disorder. "Along comes Scott with a totally new pathway," involving an obscure molecular complex called a retromer, Petsko says. "This really got our attention."

Their lunch that day with Small set the agenda for a decadelong collaboration that this week unveils, in *Nature Chemical Biology*, a potential new drug lead for Alzheimer's. By stabilizing the components of retromers, which act like recycling bins in cells, the compound could slow or stop the implacable spread of a protein fragment called β amyloid, a likely culprit in neuron death in Alzheimer's. Although preliminary—so far the published work has been done only in cells—the new results have nonetheless impressed some veterans of the Alzheimer's field.

What Small found a decade ago was that in the hippocampus, a key brain region for memory processing, one area typically ravaged by Alzheimer's disease contained less of a key retromer component than a resistant area. The retromer is a linked set of proteins that encloses cargoes of cell surface proteins, including β amyloid's precursor, helping to recycle them from the cell interior to the outer membrane (see diagram).

Small's discovery that retromers are lacking in the precise area of the brain first affected by Alzheimer's disease offered a possible solution to one of the condition's biggest puzzles. In the roughly 99% of Alzheimer's cases that lack a known genetic cause, no one knows why β amyloid builds up in the brain.

For the fragment to exist, certain enzymes must cleave its parent, amyloid precursor protein (APP). This is thought to happen in an organelle called the endosome. Based on his brain studies, Small hypothesized that a lack of retromer activity causes more APP (and other proteins) to linger in endosomes,

giving enzymes greater opportunity to generate β amyloid. (Enlarged endosomes are often seen in Alzheimer's disease.) "You have APP residing for too long in the endosome," Small says. "And so—bam—that's where the enzymes start cleaving."

In 2004, however, it wasn't clear if the retromer defect was a cause or consequence of the brain disorder. Evidence for causality has accumulated over the last decade. Knocking out one copy of a retromer gene in mice leads to higher β amyloid and to memory deficits, and variants in several retromer-related genes are associated with Alzheimer's risk. "Some of the story remains speculative," says neurologist Samuel Gandy of the Mount Sinai School of Medicine in New York City. "Importantly, nothing has come along that disproves the model."

While Small was building the case for ret-

Recycle, don't trash. Retromers help return APP to the neuron surface, preventing its breakup into toxic β amyloid in the endosome.

romer dysfunction in Alzheimer's, Petsko, Ringe, and graduate student Vincent Mecozzi, all at Brandeis University in Waltham, Massachusetts, set out to design a "chaperone" compound that would stabilize the complex retromer structure and thereby boost overall retromer numbers. Using structural biology tools, they identified a weak point in the linked retromer proteins where a single compound might bind them more tightly together, thus stabilizing the complex and slowing typical degradation in a cell. After several years of work, and somewhat to their own surprise, they found such a compound.

In cultured hippocampal neurons, the

small molecule boosts the amount of retromer proteins by 50% or more, and reduces levels of human β amyloid by 39% in neurons from mice expressing a mutant APP seen in Alzheimer's disease. "The new pro-retromer drug is brilliant. … If you had asked me whether I thought the retromer could be tweaked specifically, I would have guessed no," Gandy says. "Time (and trials) will tell whether it has true promise as a therapeutic."

Indeed, indiscriminate recycling of molecules in cells could cause side effects—APP isn't the only cargo retromers carry. The goal of treatment, Small says, is to tweak the system to bring retromer activity back to normal levels, but he admits that such a drug could end up increasing cargo "flow" in normal cells, which could be harmful—no one knows. "These are all incredibly important questions that we're actively involved with," Small says.

The compound's success also depends on endosomes being the site of most APP processing. Most studies confirm this, but a few locate β amyloid production in the Golgi apparatus, an organelle that packages proteins for delivery elsewhere (see diagram). If β amyloid is mainly produced there, a pro-retromer drug could exacerbate Alzheimer's disease by delivering more APP.

A retromer-boosting drug may also work in Parkinson's disease. In 2011, two papers revealed that rare mutations in a retromer gene cause that neurodegenerative disorder in families. "That was a big surprise to all of us," says Petsko, who's moving to Weill Cornell Medical College in New York City, where he'll try to identify the critical retromer cargo in Parkinson's neurons.

The group is now raising money for further drug discovery and development—they've started to give their compound to mice. The retromer team knows the long odds of developing a safe and effective drug for Alzheimer's disease, let alone for two brain conditions. "Most attempts at therapy fail," Petsko says. "I can live with that. I couldn't live with not trying."

–KEN GARBER

Ken Garber is a writer based in Ann Arbor, Michigan.

Tanks for the Batteries

The need to store energy from wind, solar, and other renewable energy sources could spark a revival of a dormant battery technology

EVERY LARGE-SCALE ENERGY SOURCE comes with a downside. For fossil fuels, it's carbon emissions; for nuclear power, it's radioactive waste; for renewables, it's intermittency, the inability to produce power when the sun isn't shining and the wind is still. Given society's pressing need to switch from fossil to renewable fuels to prevent catastrophic climate change, intermittency is a headache fast becoming a migraine. Many experts worry that the steadily climbing share of electricity supplied by renewables will eventually make portions of the electric grid unstable. "The clock is ticking," says Graham Fisher, chief scientist of SunEdison in St. Peters, Missouri, one of the largest providers of solar power in the United States.

Researchers working on the cutting edge of battery technology are increasingly confident that they have the means to steady the grid and smooth the path to renewables. They're updating a 130-year-old technology called flow batteries, aiming to create versions that can bank massive amounts of electricity from renewables when it's not needed and then feed it back into the grid during times of heavy demand.

Unlike traditional batteries, which pack their chemical power supply and the electrodes needed to tap it into one package, flow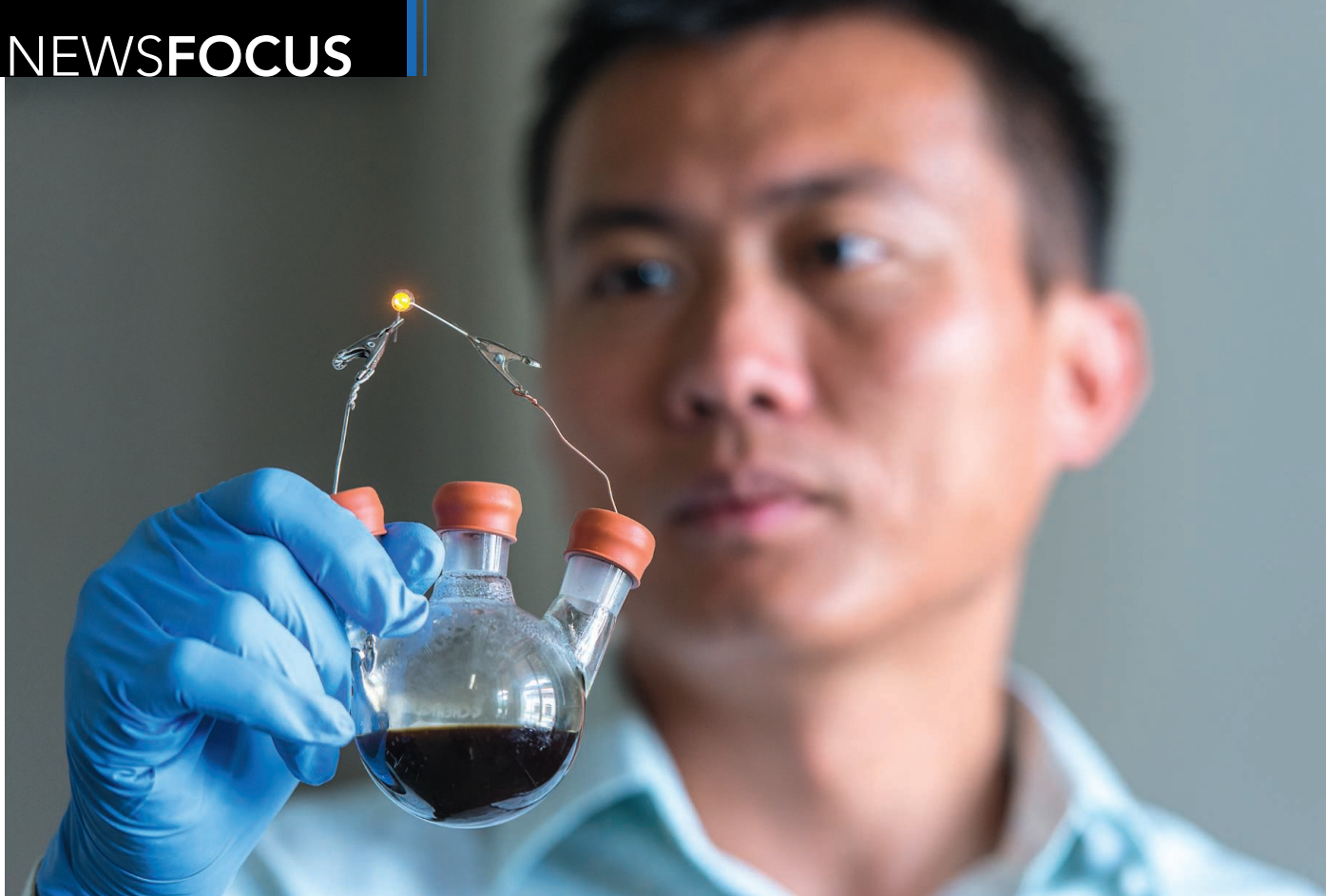 batteries separate those two jobs, storing energy in tanks of liquid electrolyte that can be scaled up to industrial dimensions. That strategy could help them avoid an unwelcome trade-off: Normal batteries are good at producing either large amounts of power for short periods or small amounts of power for days. "The key challenge is to find a battery system that can span these two," says John Lemmon, a program director at the Department of Energy's (DOE's) Advanced Research Projects Agency–Energy in Washington, D.C. Because the power delivered and the amount of energy stored can be optimized separately, flow batteries are "very promising," he says.

Now, many battery researchers are taking a second look. "There are new ideas out there that have the potential to be game changing," says Michael Aziz, a flow battery expert at Harvard University. Researchers are exploring dozens of different battery chemistries, hoping to find one that produces large amounts of power for sustained periods while being dirt-cheap, safe, and robust enough to last for decades. "It's still too early to say one system will get past all the hurdles," adds Yet-Ming Chiang, a materials scientist and battery expert at the Massachusetts Institute of Technology in Cambridge. "Right now it's about getting multiple shots on goal."

A huge niche

Developed in the 1970s, modern flow batteries did not catch on at the time because they were expensive and the market was nonexistent. But the push to renewables could change the calculus. Thirty-one U.S. states, for example, now have so-called renewable portfolio standards that require their energy mix to include as much as 40% renewables in the near future. The vagaries of sun and wind will create peaks and valleys of renewable

Bright idea. Yi Cui demonstrates a prototype of a flow battery in his lab at Stanford University.

generation, which will have to be smoothed out to provide sustained, reliable power. "Most people believe that when renewables make up 15% to 20% of [electricity generating] capacity, the intermittency issue will become a problem," Fisher says.

Not everybody agrees with Fisher's numbers, and there are alternatives to energy storage for coping with the fluctuating power from renewables—for example by shuttling power between different regions of the grid. But many energy researchers see storage as key. Last fall, for example, California lawmakers passed a mandate to add 200 megawatts (MW) of storage capacity by the end of this year and 1325 MW by 2020. "California's program will serve as a big kickstart and experimentation enabler," wrote Devi Glick, an energy policy expert at the Rocky Mountain Institute (RMI) in Snowmass, Colorado, in a recent RMI blog post. According to recent analyses by a pair of market research firms, the global demand for installing grid storage could reach more than $100 billion annually by 2020.

Today, many communities store electricity by using it to pump water to hilltop reservoirs, and then letting the water run back down through turbines when the power is needed. Such pumped hydro setups typically store power for about $100 per kilowatt-hour of capacity, now the cheapest option. Other companies and communities use conventional lead-acid, lithiumion, and sodium-sulfur batteries for smaller scale energy storage (see figure, p. 354). But not all communities have the topography and water needed for pumped hydro, and conventional batteries are prone to fires and typically have trouble producing large power loads for many hours or days at a time.

That's where flow batteries could find their niche. They look nothing like sleek lithium-ion batteries or even cumbersome lead-acid car batteries. Instead, an electrode assembly, known as a stack, sits in the middle of the device, and charged liquid electrolytes are pumped from external tanks through the stack. In most designs, the positively charged electrode strips electrons from the electrolyte and sends them through an external circuit. This process produces positively charged ions, which flow through a specialized membrane to a second electrolyte on the other side, where they meet up with the electrons and complete the circuit (see figure, below). To charge the battery, the fluids are simply pumped in reverse while electricity fed into the stack replenishes the energetic charges to the initial solution.

Because the jobs of energy storage and extraction are separated, it's easy to scale up storage by simply building bigger tanks of electrolytes. Likewise, the power produced by the battery can be scaled up by adding more electrode assemblies to the stack. This division of labor also makes flow batteries generally safer and less prone to overheating, because the electrodes can take up electrons (a reaction that produces heat) only when the electrolytes are pumped through the stack.

But flow batteries tend to have low energy
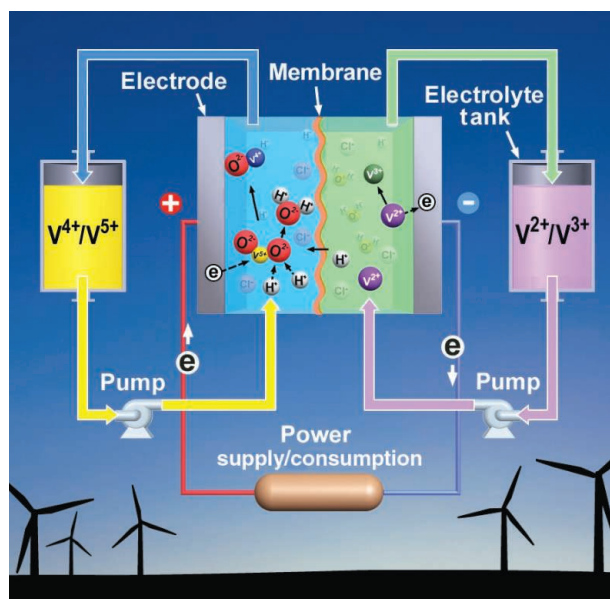
Electrifying. Vanadium flow batteries generate current from tanks of liquid electrolytes; recharging them runs the same reactions in reverse.

density, so they have to be large. Whereas state-of-the-art lithium-ion batteries have an energy density (known as specific energy) of 128 watt-hours per kilogram (Wh/kg), in the most common flow batteries that number ranges from 20 to 50 Wh/kg. Most modular units now under development range in size from refrigerators to railcars. A flow battery in Osaka, Japan, that's capable of storing a megawatt of power generated by 28 concentrated solar panels is larger than a dozen rail cars and was backed by tens of millions of dollars by the national and regional governments. That's too expensive for most applications today. So flow battery researchers are hunting for electrolytes, membranes, and designs that could lower costs and increase energy density.

Value-added vanadium

For decades, the leading class of flow batteries has been a group known as aqueous redox flow batteries, which rely on water-based electrolytes to ferry charges. The most advanced type, vanadium flow batteries, came on the scene in the mid-1980s. Vanadium's strong suit is that its ions are stable with several different amounts of charge. In one common setup, during discharge V^{2+} ions give up electrons at one electrode to become V^{3+}. Those electrons then move through an external circuit and are returned to a counter electrode where they convert V^{5+} ions to V^{4+}. The vanadium ions swim in a water-based electrolyte spiked with dilute sulfuric acid. Protons in this electrolyte pass through a proton-conducting polymer membrane to balance the charges (see figure).

Several vanadium redox flow batteries (VRBs) are already on the market, and more are on the way. Sumitomo Electric Industries Ltd., for example, announced last year that it's planning to build one of the biggest, a 60-megawatt-hour VRB for Hokkaido Electric Power Co. in Japan. According to Japanese news reports, the single battery will help the utility company smooth out its power delivery enough to increase its use of solar power by 10%.

But vanadium is expensive. Building a battery capable of generating 1 kilowatt-hour of electricity—about enough to power one 100-watt light bulb for a night—costs $80 for the vanadium alone. Adding the tanks, pumps, and electrode assemblies brings the typical price of a VRB to about $700 to $800 for each kilowatt-hour of capacity, far above the typical cost for pumped water storage, about $100 per kilowatt-hour. Another challenge is that V^{5+} ions are highly caustic, so manufacturers must use a durable but expensive polymer film called Nafion as the proton-conducting membrane.

Recent advances appear likely to cut VRB prices. In March 2011, for example, researchers at Pacific Northwest National Laboratory (PNNL) in Richland, Washington, developed a new sulfate-and-chloride-based electrolyte that can hold 70% more vanadium ions, enabling a smaller —and cheaper—battery to deliver the same amount of energy. The setup also can run at higher temperatures, reducing the need for cooling. That technology has already been licensed to three companies, which are get-

ting close to installing units in the field, according to Imre Gyuk, program manager for energy storage research at the DOE's Office of Electricity Delivery and Energy Reliability in Washington, D.C.

In a separate advance, the PNNL team removed the V^{4+} and V^{5+} ions from one side of the reaction and replaced them with iron ions that cycle between Fe^{2+} and Fe^{3+}. Because the iron ions are far less corrosive than vanadium ions, the PNNL team could also replace the expensive membrane with a cheap plastic used in wastewater treatment plants. The lower cost could make V-Fe flow batteries ideal for applications that require multiple electrodes and membrane assemblies to store large amounts of power and deliver it quickly, as is often needed to match electricity supply with demand, says Wei Wang, a materials scientist who leads the PNNL group.

Michael Perry, a chemical engineer with United Technologies Research Center in East Hartford, Connecticut, and colleagues focused on the electrodes instead. At a meeting of the Materials Research Society meeting in Boston in December 2013, they reported reengineering the stack to have an interdigitated electrode: a setup that looks like alternating fingers on two hands clasped together. The design is common in fuel cells, which generate electricity from hydrogen or other fuels. The group has also improved the conductivity of the polymer membranes. Perry estimates that the changes have slashed the cost of the electrode stack by 83%. "We think we're now in the $300 to $350 kWh range" for the entire setup, Perry says.

Savings galore

Other researchers are reconfiguring the entire battery to reduce costs. Last year, for example, Yi Cui and colleagues at Stanford University in California came up with a "semisolid" flow battery that removes the need for a membrane altogether, usually the most expensive part of the electrode stack. To do so, they made a hybrid battery that's part flow and part conventional battery. The setup has just a single tank of electrolyte liquid, which contains lithium-sulfur compounds such as Li_2S_8. These interact with an electrode made of lithium metal that's covered with a thin coating to prevent it from undergoing unwanted side reactions. When discharging, the lithium metal gives up electrons and sheds lithium ions through the coating into the electrolyte. Those ions, along with electrons that have passed through an external circuit, convert the Li_2S_8 into Li_2S_4. Li_2S_8 reforms upon charging, and the extra lithium ions are redeposited on the metal electrode. In the May 2013 issue of *Energy & Environmental Science*, Cui and his colleagues reported that their lab-scale prototype generated as much as 170 watt-hours per kilogram and 190 watt-hours per liter, more than three times the output of conventional redox flow batteries. The hybrid battery also proved stable for thousands of charge and discharge cycles. And by removing vanadium from the mix, Cui estimates his setup could slash the cost of the raw materials for the battery to half that of VRBs.

Aziz's team at Harvard recently offered a potentially even cheaper option. They replaced the metal ions with far cheaper organic compounds called quinones, abundant in both plants and petroleum, which consist of at least one ring of carbon atoms, plus a tail of carbons, hydrogens, and oxygens. They have an electronic advantage as well as a cost one, Aziz says. In most flow battery setups, metal ions typically shuttle single electrons at a time. Each quinone molecule, by contrast, can ferry pairs of electrons—potentially giving quinone flow batteries a higher energy density than most metal-based flow batteries. Going organic carries another bonus: getting rid of water. Redox flow batteries have to keep their output voltage low or they run the risk of destroying their electrolyte by splitting water into hydrogen and oxygen gas. Organics without water can run at higher voltages and thus produce more power with fewer electrodes in the stack, Gyuk says.

Quinones readily snag and give up electrons. So several years ago, Aziz began experimenting with batteries using hydrogen-containing quinones, known as hydroquinones, as the charge carriers. After some mediocre results, he and his students teamed up with theoretical chemists at Harvard led by Alán Aspuru-Guzik. Guzik and his colleagues calculated properties of more than 10,000 quinones and hit on a likely top performer, abbreviated $AQDSH_2$—a compound nearly identical to one naturally found in rhubarb.

Aziz and his students filled one tank of a flow battery with $AQDSH_2$ dissolved in an organic electrolyte. In the other tank they placed bromine liquid, or Br_2. During discharge, each hydroquinone gives up two electrons and two protons. The protons crossed through a membrane, where they met up with two bromine atoms and electrons that had passed through an external circuit to make two molecules of HBr. As the team reported in the 9 January issue of *Nature*, they could recharge the hydroquinones by running the reaction in reverse and feeding in electricity.

"It's a great new material set," Perry says. And unlike metal-based flow batteries, the organic batteries have the potential to be easily tailored using the standard tools of organic chemistry. But—as with every candidate for flow battery material—they have drawbacks. For starters, the organic electrolytes tend to be viscous, slowing the exchange of electrons at the electrode. And the bromine in Aziz's design is highly caustic.

Gyuk says overcoming such challenges will spur innovation. Indeed, the field is feverish with ideas and prototypes. "Flow batteries are starting to see a renaissance," Perry says. If so, a renewable-energy Enlightenment could well be close behind. **–ROBERT F. SERVICE**
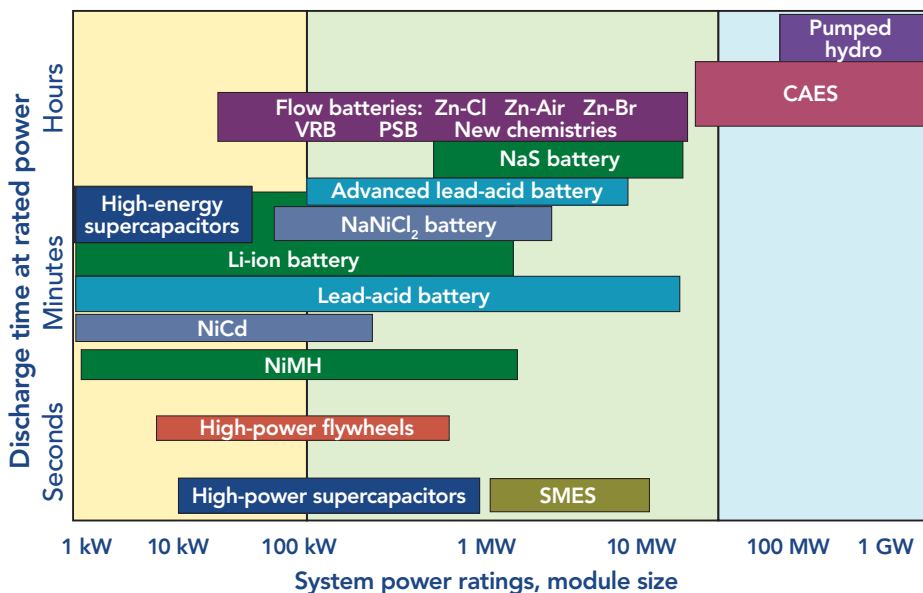
Workhorses. Flow batteries deliver more power for longer periods than most other storage technologies can.

A shattered community. Haiyan is believed to have been the strongest typhoon ever to make landfall.

After the Deluge

Hard data and survivor interviews are helping researchers unravel the science of Supertyphoon Haiyan and its storm surge

TACLOBAN AND DULAG, PHILIPPINES—It was a night Jayde de Veyra will never forget. High winds swirling around his two-story house woke him at about 2 in the morning last 8 November. By 5 a.m. the storm was raging so fiercely, he says, "I couldn't go outside." The wind's whistling hurt the ears; the rain was torrential. After about 2 hours, the winds suddenly died and the rain stopped. De Veyra stepped outside into a dark, eerily calm morning. Neighbors were milling about, checking their houses, asking after others. But then, just as suddenly, the winds started picking up. "People outside started screaming, 'It's coming again, it's coming again.'" De Veyra went back inside, while the storm got even worse than it had been before.

The description of a lull—the storm's eye—was just what Josh Morgerman hoped for when he struck up a conversation with De Veyra here in Dulag, a town 37 kilometers south of Tacloban. A dedicated storm chaser, Morgerman and two colleagues rode out

Supertyphoon Haiyan at the Hotel Alejandro in Tacloban, where they captured dramatic footage of winds whipping away windows, rain pouring through punctured roofs and cascading down stairways, and a storm surge that transformed streets into canals. Clips of their videos were featured on CNN and helped alert the world to the unfolding disaster triggered by what is believed to have been the strongest typhoon to ever make landfall.

Four months later, on a sunny, early spring day, Morgerman was taking a giant stride beyond chasing Haiyan, known in the Philippines as Yolanda. He was traveling along the storm-scarred coast of Leyte province south of Tacloban, gathering eyewitness accounts and snapping hundreds of GPS-tagged photos of uprooted trees and damaged buildings, all to confirm Haiyan's exact landfall, the eye's dimensions, wind strength, and the depth of surging waters that accounted for most of the deaths. He is one of dozens of scientists, disaster experts,

and adventurers working to document the storm and its impact. The goal of this detailed postmortem: to understand what made this typhoon so powerful and its surge so devastating, and to gather clues to how to keep future storms from matching Haiyan's toll, which now runs to more than 6000 dead, 28,000 injured, and 1000 still missing, and over $2 billion in damage.

Already, the researchers are documenting how a coastline stripped of natural barriers, poorly built homes placed too close to shore, insufficient disaster planning, and a lack of public awareness combined with an unusually ferocious storm to produce a costly tragedy. "We have a long way to go to have a culture of safety and preparedness," says Alfredo Mahar Lagmay, a geologist at the University of the Philippines, Diliman (UPD).

Out in front

The Philippines is possibly the most storm-battered country on Earth. At the western

edge of the North Pacific, the archipelago "is right along the alleyway of typhoons and right up front," says Cesar Villanoy, a physical oceanographer at UPD. Eight or nine damaging typhoons wallop the country each year, on average.

But Haiyan was in a class of its own (*Science*, 29 November 2013, p. 1027). Typhoons draw their energy from the heat in surface waters, and those waters were plenty warm last year along Haiyan's track. Typically typhoon winds stir up deeper, cooler water, curtailing a storm's energy buildup. But over the past 2 decades, unusual0ly steady easterly trade winds have piled warm water into the western Pacific, warming and thickening subsurface waters, forming a larger reservoir of storm-fueling heat. The tropical cyclone heat potential, a measure of this subsurface heat, has increased 10% since the early 1990s in the western Pacific, according to I-I Lin, a specialist in typhoon-ocean interactions at National Taiwan University in Taipei. Haiyan also originated more than 3000 kilometers east of the Philippines, giving it plenty of open ocean to muster strength for its assault on land.

Haiyan is already recognized as the most intense tropical storm ever at the time of landfall, but some scientists think it has a claim to being the most intense—period. Meteorologists rank tropical storms by their sustained wind speed, wind radius—how far from the storm's center that winds of a given speed are found—and barometric pressure, with a lower pressure usually correlating with faster winds.

By all three criteria, the reigning champ is 1979's Supertyphoon Tip, which achieved a peak sustained wind speed of 165 knots, a whopping 30-knot wind radius of 1100 kilometers, and a sea-level pressure of 870 millibars. Tip set all these records while meandering around the western North Pacific; it weakened significantly and was no longer a supertyphoon when it swept through Japan, causing widespread flooding and killing 42.

"It may be time to recognize a new modern-era world record" for storm intensity, argues Mark Lander, a meteorologist at the University of Guam in Mangilao. In a paper presented at an American Meteorological Society conference earlier this month, he noted that the Joint Typhoon Warning Center, operated by the U.S. Navy and Air Force in Pearl Harbor, Hawaii, estimated Haiyan's peak sustained wind speed at 170 knots, based on satellite imagery.

Pacific cyclones are poorly monitored; winds and pressures are mostly estimated from satellite observations. Other recent storms may have rivaled Haiyan, and it might even have been matched by an 1897 typhoon that also devastated Tacloban. In the aftermath of that storm, José María Algué, a Jesuit priest in charge of meteorological observations at the Manila Observatory, led a mission to survey damage and interview survivors. He then wrote a 50-plus page monograph documenting the devastation left by the winds and storm surge, which claimed 1299 lives.

The surge heights he recorded suggest the 1897 storm "was potentially just as strong" as Haiyan, says Fernando Siringan, a UPD geologist working with Villanoy.

The Cyclone Addict

Some of the most revealing data about last year's Supertyphoon Haiyan—the strongest ever known to hit land—came not from a team of Ph.D.s but from an advertising executive named Josh Morgerman, who eagerly puts himself in the path of storms. For Morgerman, who is based in the Los Angeles area, storm chasing is "like an addiction," he says. "Some people need that adrenaline rush."

Morgerman first pursued a storm when Hurricane Bob slammed New England in 1991. "I followed it by riding the train to Providence, Rhode Island, and carrying paper maps," he says. Now he's equipped with altimeters, barometers, and GPS-equipped iPads, uploading data and images to his iCyclone website (www.icyclone.com) and the tropical storms mail list. He chases storms with two kindred spirits: Mark Thomas, an entrepreneur in Taipei, and James Reynolds, a videographer working out of Hong Kong.

Morgerman, 44, ventured to Asia last fall, driven by "the dearth of storm activity in North America." After covering three western Pacific typhoons, he hit the jackpot by landing right in Haiyan's path.

On 7 November, the team checked into Hotel Alejandro in the heart of Tacloban, a commercial and political hub in the central Philippines. The next day, from the hotel's balconies, they documented winds blowing out windows and ripping off roofs while shards of glass, bits of tin roofing, tree limbs, and other debris flew by. They captured the chaos within the hotel's hallways, where guests and neighbors cowered in the dark. At one

Up-close and personal. Josh Morgerman (*inset*) getting Haiyan's ferocity on tape.

point, Morgerman and Thomas helped guests trapped in first-floor rooms escape the fast-rising waters through smashed windows. Afterward, they documented downed power lines, overturned trucks, shacks reduced to splinters, and people poking in the rubble for survivors.

The team's harrowing videos, shown on CNN, even impress storm survivors. "Every time somebody asks about the storm, I just show them the videos and they have no more questions," says Christian Rey, an emergency medical technician with the Tacloban fire department. And for those not on the scene, the videos provide "immediate and dramatic evidence of the scale of the disaster, and probably increased the speed and amount of aid," says Mark Lander, a meteorologist at University of Guam in Mangilao.

Morgerman's videos and ground-truthing are making the scientific rounds as well. In a poster at the American Meteorological Society's 31st Conference on Hurricanes and Tropical Meteorology earlier this month in San Diego, California, Morgerman presented information distilled from dozens of interviews, hundreds of photos, storm surge estimates, and pressure measurements. His observations will be "invaluable if we are to better understand the satellite data," says Bryan Norcross, a meteorologist and hurricane specialist at The Weather Channel.

"I'm excited that scientists can take what I've provided—a body of detailed evidence collected on the ground—and take it from there," Morgerman says. His one regret is that he didn't get into Haiyan's eye, which passed south of Tacloban. "It breaks my heart thinking that I could have gotten the only pressure reading ever from the center of a Category 5 storm," he says.

–D. N.

"It's sad," adds Gemma Narisma, a climate scientist at the Manila Observatory. "Every time something strikes, there is the notion that we don't get hit this way, and we go back to the archives and show, yep, it has hit before."

Whatever Haiyan's ranking, it unleashed a devastating storm surge on the coast around Tacloban. Researchers have documented a wall of water that, depending on local topography, was 4 to 7 meters high and ran as far as 2 kilometers inland. "There was almost complete destruction for the first couple hundreds of meters off the coast," says Adam Switzer, a coastal geomorphologist at Nanyang Technological University in Singapore. Even hundreds of meters inland, people were forced onto the roofs of two-story homes. "There was nowhere else to go," says Switzer, who participated in a post-storm survey. A couple who lives in a modern apartment building in downtown Tacloban told Morgerman of pulling a boy from the surge waters to safety on their second-floor balcony.

To understand what generated the tsunamilike surge, Villanoy, Switzer, and a reconnaissance team gathered evidence of the timing, height, direction, and extent of inundation. "We think we have the story almost straight," Villanoy says. The stage was set by the unusual trade winds that intensified the storm. They have literally piled up water in the western Pacific, raising sea levels by more than 20 centimeters over the past 20 years.

The swelling sea combined with quirks of Leyte's geography to devastating effect. Tacloban sits at the top of San Pedro and San Pablo Bay, a small thumb of water jutting northward from Leyte Gulf. Just above Tacloban, the narrow and twisting San Juanico Strait separates Leyte and Samar islands. People living along the bay's north rim told Villanoy's team of a curious phenomenon: As Haiyan approached, the sea retreated far from land. The storm's counterclockwise winds had driven water from the shallow northern end of the bay south, away from Tacloban. When the storm passed, the southerly winds behind the eye pushed the water back north—with a vengeance. The shift in the winds happened quickly enough for the slosh of water returning from the south to amplify the northward surge, much like a boxer winding up for a knock-out punch by

drawing his fist back. Full data on casualties are not yet available, but Villanoy says the surge appears to have caused most of the deaths.

Storm clouds on the horizon

Few scientists predict that cyclone-prone areas should expect more storms with Haiyan's ferocity as Earth warms. In a report last September, the Intergovernmental Panel on Climate Change found that no increase in typhoon activity in the western Pacific has been documented and that it has "low confidence" of any increase in storm frequency or intensity in the coming decades. But one trend is crystal clear: Natural disaster casualties and damage are rising.

Over decades, coconut plantations have supplanted storm-resistant natural mangroves across much of the Philippines. And nationwide, hundreds of thousands of "informal settlers"—the politically correct term for squatters—have built shanty towns along shorelines, often with houses on stilts above tidal flats and on the wrong side of seawalls. There were an estimated 35,000 informal settlers in Tacloban alone.

The Philippine government warned those in harm's way. As Haiyan was barreling across the Pacific in the first week of November, meteorologists forecast days in advance

where and how hard it was likely to hit. A new government program called Project NOAH, for Nationwide Operational Assessment of Hazards, also predicted storm surge heights throughout the region.

But the warnings did not work as well as hoped, as researchers have learned in post-storm surveys. Many shoreline residents took refuge in one-story schools and churches that collapsed in the winds or were flooded by the surge. Others ignored the warnings because they were used to typhoons. The storm surge also came on so quickly—in a matter of minutes—that it caught many by surprise. And many residents in the disaster zone reported simply not knowing what a storm surge is. "The impact of disasters is not so dependent on the characteristics of typhoons, it depends on exposures and vulnerabilities," says Narisma, who is also a professor at Ateneo de Manila University.
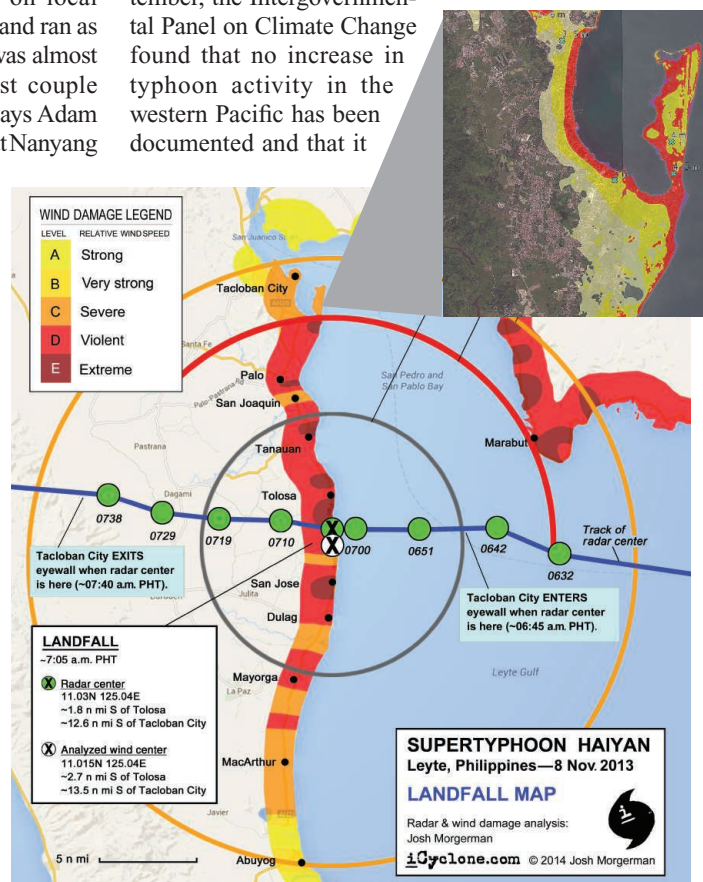
In Haiyan's aftermath, the national government declared there could be no rebuilding within 40 meters of the high tide line; local officials hope to convince families to move inland once new housing is built. But these efforts will meet resistance. Worried that they would lose their old spots and unwilling to wait months for the promised housing, many squatters have already rebuilt their homes using storm debris and tarps provided by relief agencies.

Project NOAH is also helping prepare new maps that will enable local governments to identify evacuation areas. And Lagmay hopes to bring social scientists into Project NOAH to devise ways to encourage citizens to take action on their own during an emergency. "Raising awareness is the first step toward disaster preparedness," he says.

Morgerman wants to help, too. Since returning from what he calls "the ultimate chase," he has been obsessed with Haiyan. "It was such an intense storm and had such an impact," he says, noting that this is the first time in 4 decades that such a populous city has been hit by such a powerful storm. By trying "to document as carefully as possible what happened," he hopes to ease the impact of the next supertyphoon.

–DENNIS NORMILE

Postmortem for a monster. On-the-ground observations underpin this map of Haiyan's track and wind damage, as well as its surge inundation (inset).

LETTERS

edited by Jennifer Sills

Protecting Lemurs: Madagascar's Forests

IN THEIR POLICY FORUM "AVERTING LEMUR EXTINCTIONS AMID Madagascar's political crisis" (21 February, p. 842), C. Schwitzer and colleagues make an impassioned plea for emergency action to save Madagascar's lemurs. The need for such action is unquestionable, but the authors repeat a tenacious misconception concerning human impact on the island by saying that "only 10 to 20% of Madagascar's original forest cover" remains (p. 842).

The evidence for the oft-repeated claim that people have eradicated 80 to 90% of Madagascar's forests [also cited in (*1–3*)] is dubious at best. It is not supported by the reference provided by Schwitzer *et al.* (*4*); for that study to be a source for the claim, its estimate of recent forest cover must be used in conjunction with an assumption of near-complete forest cover when humans first arrived. This assumption has long been in doubt, and a decade of palaeoecological investigation has revealed that a variety of nonforest vegetation covers predate humans (*5*). We should temper our claims about cumulative historical human impacts on the island accordingly.

WILLIAM J. MCCONNELL[1]* AND CHRISTIAN A. KULL[2]

[1]Center for Systems Integration and Sustainability, Michigan State University, East Lansing, MI 48823, USA. [2]School of Geography and Environmental Science, Monash University, VIC 3800, Australia.

*Corresponding author. E-mail: mcconn64@msu.edu

References
1. M. A. Barrett, J. L. Brown, M. K. Morikawa, J.-N. Labat, A. D. Yoder, *Science* **328**, 1109 (2010).
2. J. Bohannon, *Science* **323**, 1654 (2009).
3. J. Bohannon, *Science* **328**, 23 (2010).
4. Office National pour l'Environnement (ONE), "Evolution de la couverture de forêts naturelles à Madagascar (2005–2010) (ONE, Antananarivo, Madagascar, 2013); www.pnae.mg/index.php/Autres/evolution-de-la-couverture-de-forets-naturelles-a-madagascar-2005-2010.html [in French].
5. W. J. McConnell, C. A. Kull, in *Conservation and Environmental Management in Madagascar*, I. R. Scales, Ed. (Routledge, London, 2014), pp. 67–104.

Protecting Lemurs: Ecotourism

IN THEIR POLICY FORUM "AVERTING LEMUR extinctions amid Madagascar's political crisis" (21 February, p. 842), C. Schwitzer *et al.* call for ecotourism, community reserves, and research stations as tools for lemur conservation. In fact, ecotourism already generates net conservation gains for at least 13 lemur species (*1*).

Ecotourism provides half the funds for research and captive breeding at Parc Ivoloina (*1*) for the critically endangered greater bamboo, blue-eyed black, and black-and-white ruffed lemur (species cited in the Policy Forum's supplementary table S1). Funds from ecotourism also pay local guides who protect the endangered Hubbard's sportive lemur near the mining town of Ilakaka, where unguarded woodland is cleared for firewood. In addition, these funds support entrance and guide fees at the community-owned Reniala Reserve on the dry southwest coast (*1*).

Tourism does cause some problems (*1*). Wildlife smugglers capture aye-ayes, release them briefly for tourists, and then recapture them. Ring-tailed lemurs at Isalo National Park are fed for the benefit of tourists. Caged captured fossas are put on show for tourists near Mantadia National Park. Lemurs on display at a rehabilitation center near Analamazaotra Nature Reserve may be captured for tourism. These concerns are not specific to Madagascar's primates. Similar exploitation concerns have been raised about orangutan rehabilitation centers in Borneo and chained captured jaguars on show to tourists in the Amazon.

On balance, however, ecotourism helps protect lemurs against logging (*2–4*), poaching, and bushmeat hunting (*5*, *6*). Many endangered and critically endangered species worldwide rely on ecotourism revenue for conservation (*7*). Ecotourism works when it switches local communities from cash or subsistence consumption to tourism earnings based on conservation (*1*, *8*, *9*).

RALF BUCKLEY

Department of Environment, Griffith University, Gold Coast, QLD 4222, Australia. E-mail: r.buckley@griffith.edu.au

References
1. R. C. Buckley, *Conservation Tourism* (CABI, Oxford, 2010).
2. M. A. Barrett, J. L. Brown, M. K. Morikawa, J.-N. Labat, A. D. Yoder, *Science* **328**, 1109 (2010).
3. M. A. Barrett, J. L. Brown, A. D. Yoder, *Nature* **499**, 29 (2013).
4. P. H. Raven *et al.*, *Conservation Biology: Voices from the Tropics* (Wiley, New York, 2013), pp. 33–39.
5. M. A. Barrett, J. Ratsimbazafy, *Nature* **461**, 470 (2009).
6. J. H. Razafimanahakaa *et al.*, *Oryx* **46**, 584 (2012).
7. R. C. Buckley *et al.*, *PLOS ONE* **7**, e44134 (2012).
8. R. C. Buckley, H. S. Pabla, *Nature* **489**, 33 (2012).
9. E. F. Pienaar *et al.*, *Ecol. Econ.* **98**, 39 (2014).

Response

MCCONNELL AND KULL QUESTION WHETHER the current forest habitat represents "only 10 to 20% of Madagascar's original forest cover." We agree that it would have been more pru-

dent to replace "original forest cover" with "surface." We also concur that there is palaeoecological evidence for nonforest vegetation, particularly in the highlands, predating human colonization. However, Madagascar's original forest cover is a controversial issue for which no final consensus has been reached.

For instance, there is clear evidence in the subfossil record that Madagascar's central plateau, today almost completely denuded, once harbored forest-dependent lemur communities (1). The currently disjunct distribution of extant species indicates that forests in the plateau must have been continuous enough to serve as conduits for migration for species such as ayes-ayes, brown lemurs, and others (2). Evidence from palaeo-pollen sequences indicates that the central plateau, as well as other Malagasy ecosystems, has been highly dynamic over the past millennia, with significant biotic and abiotic changes predating human settlements (3). Whatever the precise percentage of forest lost in this and other regions, however, deforestation is now—and has been in the recent past—extensive in Madagascar. Even conservative estimates are substantial, such as the ~40% forest loss from 1950 to 2000 that McConnell

and Kull cautiously conclude in their recent review (4). Another estimate would be more than 52%, the forest loss from 1950 to 2010 as calculated from (5) and (6).

Accepting a lower estimate of forest loss need not affect our thinking about the current crisis. For example, we must not conflate the potentially mosaic nature of past landscapes with an interpretation that lemurs and other forest-dwelling species are adapted to such habitats. To the contrary: Although some extinct lemurs may have used open country, extant lemurs are forest-dependent. Moreover, there is little doubt that most of the 17 extinct lemurs were lost between 500 and 1500 CE, a period when human settlements expanded (7).

We fully agree with Buckley that case studies show that ecotourism can be very effective in lemur conservation, but also detrimental to some species or local populations if not properly managed. Indeed, we strongly believe that lemurs are Madagascar's most important global brand, that ecotourism represents the best long-sustainable economic option for the many communities living in close proximity to lemur habitats, and that it could become Madagascar's most important foreign exchange earner

in the near future if the biodiversity upon which it is based is conserved. We all agree that we need to focus on finding solutions for the problems at hand. Our action plan (8) is largely devoted to spreading conservation to previously unhelped corners of Madagascar harboring threatened lemur communities and to identifying and promoting successful conservation initiatives.

CHRISTOPH SCHWITZER,[1]* LOUNES CHIKHI,[2,3] GIUSEPPE DONATI,[4] MITCHELL IRWIN,[5] STEIG E. JOHNSON,[6] RUSSELL A. MITTERMEIER,[7] HEATHER PEACOCK,[8] JONAH RATSIMBAZAFY,[9,10] JOSIA RAZAFINDRAMANANA,[10] EDWARD E. LOUIS JR.,[11] IAN C. COLQUHOUN,[12] JEN TINSMAN,[13] RAINER DOLCH,[14] MARNI LAFLEUR,[15] STEPHEN NASH,[7,16] ERIK PATEL,[17] BLANCHARD RANDRIANAMBININA,[18] TOVONANAHARY RASOLOFOHARIVELO,[10] PATRICIA C. WRIGHT[16]

[1]Bristol Zoological Society, c/o Bristol Zoo Gardens, Clifton, Bristol BS8 3HA, UK. [2]Instituto Gulbenkian de Ciência, 2781-901, Oeiras, Portugal. [3]EDB, CNRS, UMR 5174 Université Paul Sabatier, 31062, Toulouse, France. [4]Department of Social Sciences, Oxford Brookes University, Oxford, OX3 0BP, UK. [5]Northern Illinois University, DeKalb, IL 60115, USA. [6]University of Calgary, Calgary, AB T2N 1N4, Canada. [7]Conservation International, Arlington, VA 22202, USA. [8]Golder Associates, Calgary, AB, T2A 7W5, Canada. [9]Durrell Wildlife Conservation Trust, Antananarivo 101, Madagascar. [10]Groupe d'Etude et de Recherche sur les Primates de Madagascar, Antananarivo 101,

Madagascar. [11]Omaha's Henry Doorly Zoo, Omaha, NE 68107, USA. [12]Western University, London, ON, N6A 5C2, Canada. [13]American Museum of Natural History, New York, NY 10024, USA. [14]Association Mitsinjo, Andasibe 514, Madagascar. [15]University of Veterinary Medicine Vienna, 1210, Vienna, Austria. [16]SUNY at Stony Brook, NY 11794, USA. [17]Duke Lemur Center, Durham, NC 27705, USA. [18]Université de Mahajanga, Mahajanga 401, Madagascar.

*Corresponding author. E-mail: cschwitzer@bcsf.org.uk

References

1. R. D. E. MacPhee *et al*., *Int. J. Primatol.* **6**, 463 (1985).
2. International Union for Conservation of Nature (IUCN), *The IUCN Red List of Threatened Species: Version 2013.2* (IUCN, 2014); www.iucnredlist.org.
3. M. Virah-Sawmy, K. J. Willis, L. Gillson, *Glob. Ecol. Biogeogr.* **18**, 98 (2009).
4. W. J. McConnell, C. A. Kull, in *Conservation and Environmental Management in Madagascar*, I. R. Scales, Ed. (Routledge, London, 2014), pp. 67–104.
5. H. Humbert, G. Cours-Darne, "Carte international du tapis végétal et de conditions écologiques à 1:1,000,000: Notice de la carte Madagascar" (Travaux de la Section Scientifique et Technique de l'Institut Français de Pondichéry, hors série, 1965).
6. Office National pour l'Environnement (ONE), "Evolution de la couverture de forêts naturelles à Madagascar (2005-2010)" *(ONE, Antananarivo, 2013)*; www.pnae.mg/index.php/Autres/evolution-de-la-couverture-de-forets-naturelles-a-madagascar-2005-2010.html [in French].
7. R. E. Dewar, in *Conservation and Environmental Management in Madagascar*, I. R. Scales, Ed. (Routledge, London, 2014), pp. 44–64.
8. C. Schwitzer *et al.*, *Lemurs of Madagascar: A Strategy for Their Conservation 2013–2016* (IUCN SSC Primate Specialist Group, Bristol Conservation and Science Foundation, and Conservation International, Bristol, 2013); www.primate-sg.org/storage/pdf/Lemurs_of_Madagascar_Strategy_for_Their_Conservation_20132016_low_res.pdf.

TECHNICAL COMMENT ABSTRACTS

Comment on "A Complete Skull from Dmanisi, Georgia, and the Evolutionary Biology of Early *Homo*"

Jeffrey H. Schwartz, Ian Tattersall, Zhang Chi

Lordkipanidze *et al*. (Research Article, 18 October 2013, p. 326) conclude, from gross morphological comparisons and geometric-morphometric analysis of general shape, that the five hominid crania from Dmanisi in Georgia represent a single regional variant of *Homo erectus*. However, dental, mandibular, and cranial morphologies all suggest taxic diversity and, in particular, validate the previously named *H. georgicus*.

Full text at http://dx.doi.org/10.1126/science.1250056

Response to Comment on "A Complete Skull from Dmanisi, Georgia, and the Evolutionary Biology of Early *Homo*"

Christoph P. E. Zollikofer, Marcia S. Ponce de León, Ann Margvelashvili, G. Philip Rightmire, David Lordkipanidze

Schwartz *et al*. hold that variation among the Dmanisi skulls reflects taxic diversity. The morphological observations to support their hypothesis, however, are partly incorrect and not calibrated against intraspecific variation in living taxa. After proper adjustment, Schwartz *et al*.'s data are fully compatible with the hypothesis of a single paleodeme of early *Homo* at Dmanisi.

Full text at http://dx.doi.org/10.1126/science.1250081

CORRECTIONS AND CLARIFICATIONS

Perspectives: "Enzyme kinetics, past and present" by X. S. Xie (20 December 2013, p. 1457). A production error resulted in a misspelled word in the first sentence of the paragraph in which Equation 4 appears; the sentence should read "In single-molecule turnover experiments, each enzyme experiences constant substrate and product [not produce] concentrations in the volume of interest (dashed circle)." In addition, bars should have appeared over the constants k_{cat} and K_M in Equation 3. The HTML and PDF versions online have been corrected.

Letters to the Editor

Letters (~300 words) discuss material published in *Science* in the past 3 months or matters of general interest. Letters are not acknowledged upon receipt. Whether published in full or in part, Letters are subject to editing for clarity and space. Letters submitted, published, or posted elsewhere, in print or online, will be disqualified. To submit a Letter, go to www.submit2science.org.

SCIENCE AND SOCIETY

Reproductions Through Technology

Charis Thompson

Biology is increasingly social. Bioscientists are investigating nature-nurture through epigenetics, the role of social interaction in how brains function, the relation between food cultures and microbiomes, and the impacts of wealth and status inequality on mental and physical health. The list goes on. Social scientists, for their part, are finding that the life sciences and biomedicine are increasingly central to describing, measuring, analyzing, and theorizing society's fundamental organizational dynamics. Assisted reproductive technologies are changing what counts as a family. Biometric and genomic information are now part of how we separate legal from illegal residents of a country and assign blame for or exonerate criminal behavior. Healthcare is a major part of national economies, and its finance and organization are markers of modern political alternatives. Synthetic biology and regenerative medicine promise to make made-to-order life an economic powerhouse while also extending life spans for some in the process. Being well informed about these areas of contemporary biology requires familiarity with both natural and social sciences. Sarah Franklin's *Biological Relatives: IVF, Stem Cells, and the Future of Kinship* provides a much-needed account of one such area.

The book's title is a pun on our ability to use new reproductive biology techniques to make new kinds of relatives and families and on the ways in which reproduction has changed relative to those techniques. Since its first success in 1978, in vitro fertilization (IVF) has become a relatively routine way to have children, with an estimated 5 million babies born to date. IVF changed human fertilization from something natural that occurred inside women's bodies and required one man and one woman to something technologically assisted that can occur outside the body and allows more people to be involved in reproduction. The normalization of IVF has led to new ways to combine and screen embryos and new possibilities for who can bear children. The techniques that were developed to make IVF possible simultaneously made human reproduction visible and amenable to manipulation. IVF and its associated techniques in turn became part of what Franklin (a sociologist at the University of Cambridge) calls "a global technological platform" that includes preimplantation genetic diagnosis; research on stem cells, cloning, and mitochondria; and regenerative medicine. Thus she argues that biology is increasingly technological. So understanding recent advances in human reproductive biology requires a continual crossing of two great distinctions: those between nature and society and between science and technology.

Focusing on Britain, the book covers a wide range of phenomena, including the interface between IVF and stem cell research, bioart, feminist reproductive politics, bioethics debates around "cybrid" animal-human embryos and mitochondrial DNA, the history

> **Biological Relatives**
> IVF, Stem Cells, and the Future of Kinship
>
> *by Sarah Franklin*
> Duke University Press, Durham, NC, 2013. 374 pp. $94.95, £62. ISBN 9780822354857. Paper, $26.95, £17.99. ISBN 9780822354994. Experimental Futures: Technological Lives, Scientific Arts, Anthropological Voices.

of embryology's tools evident in today's handmade micropipettes, and the role of gender in bioeconomies. In each of these seemingly disparate arenas, Franklin combines her unparalleled knowledge of social theory, feminist scholarship, and activism on reproductive technologies with an attention to the histories and technical details of the labs and clinics where the patients, practitioners, and technologies make new life. Her range is wide, but her examples are precise and disciplined.

Reading the book illuminates ways to see across divides, and there are some striking images along the way. Illustrations of embryological tools accompany Franklin's discussions of their forging and use. One of the author's photos shows "clean" shoes demarcating the border between the quality-controlled room in which stem cell lines are derived and cultured and the dirtier clinical world of IVF egg-retrieval surgery. Artist Gina Glover's male karyotype constructed of pairs of stripy socks (most donated by life scientists) bears an uncanny resemblance to a textbook human karyotype—down to the G-banding stripes, the smaller size of pairs 16 to 22, the centromeres suggested by the socks' heels, and the eaten-by-the-washing-machine, unmatched 23rd pair. The embryology tools tie the present to the past. The shoes take us from the world of clinical IVF to the stem cell research laboratory and back, illustrating the way in which "normal" clinical IVF is now a stem technology for a growing biotech sector. The socks take us from everyday domesticity to cutting-edge biomedicine and back.

Biological Relatives does another kind of genealogical work. It produces an archive for a new kind of social science of reproductive technologies. Franklin draws on theorists and scholars of kinship, gender, economy, reproductive and productive labor, and reproductive and regenerative technologies. It would be easy to miss how generative these parts of the book are, given that it is standard social science practice to cite the secondary literature in one's field. The scholars Franklin taps are not

Gina Glover, *Chromosome Socks* (detail, 2002–2003). Installation in the Guy's Hospital Genetics Clinic.

The reviewer, the author of *Good Science: The Ethical Choreography of Stem Cell Research*, is at the Department of Sociology, London School of Economics and Political Science, Houghton Street, London WC2A 2AE, UK. E-mail: c.m.thompson@lse.ac.uk

usually read together, and without her own body of work over the years, there would not be a field for the book to serve as an archive. It would also be easy to miss how generous this aspect of the book is. Franklin need not have, and yet does, distribute credit widely. She also rereads too-easily forgotten or dismissed feminist debates about reproductive technologies. Using the idiom of ambivalence, Franklin argues that feminist activists and scholars have taken seriously the excitement of frontier science, the experience of infertility, and the societal aspects of IVF and its progeny. Ambivalence is not antiscience or weak-minded. It is instead a productive, affective lens through which to think about the biologization of technology and society.

INTERNET AND SOCIETY
To Best Rule the Net

Daniel J. Weitzner

O n the 25th anniversary of the World Wide Web, Laura DeNardis' *The Global War for Internet Governance* brings us a sweep through the history of technical and political wrangling that led to the creation of the global Internet. Internet governance is an imprecise term, sometimes meant narrowly, to refer to the process by which Internet technical standards and the Domain Name System (.com, .edu, etc.) are managed, and sometimes taken very broadly to include the wide range of legal policy issues regarding the way people use the Internet, from security and copyright to privacy and government surveillance. DeNardis (American University) employs the broader definition.

In the face of rapid Internet growth—from less than 1% of the world's population online in 1994 to over 35% in 2014—we rightly marvel at the engineers and computer scientists who gave shape to the technical architecture of Internet and the Web. While honoring those government policy-makers who had the wisdom to allow the Internet to explode around the world with minimal government regulation, we should also commend those officials charged with protecting personal privacy, security, and intellectual property for insisting that the rule of law has its place even amid light-speed innovation. And perhaps most of all, we should recognize that the social and

The reviewer is at the Computer Science and Artificial Intelligence Laboratory, Massachusetts Institute of Technology, Cambridge, MA 02139, USA. E-mail: djweitzner@csail.mit.edu

intellectual progress that the Internet has enabled is largely due to the creativity of individuals and local institutions around the world who have found in the Internet an open platform for building and sharing knowledge.

DeNardis' detailed account of the technical and administrative arrangements essential to the Internet helps us appreciate the magnitude of the human effort involved in "governing" this infrastructure. She also points to the challenges going forward, addressing privacy, security, equitable access, and the demands of nation-states to control information flow. Largely descriptive, her treatment of these issues presents a number of factual challenges and then leaves us, at the end of each chapter, with some questions to answer.

In the end, she instructs us that

> *The Internet is governed. Internet governance control points are not legal control points, nor are they confined within nation-state boundaries. They are often manifested through the design of technical architecture, the decisions of global institutions of Internet governance, or the policies of private companies, all globally transcending forces in constant flux and in constant tension with national legal systems, intergovernmental treaties, and regional cultural norms.*

We face a frustrating lack of intellectual guidance about both how to understand the forces that have led to the Internet we know today and, more important, to help policy-makers navigate the myriad decisions posed as the Internet expands around the globe. Consider the challenges we face.

Privacy is very much on the public's mind and of concern to scientists who want to take advantage of new troves of personal data to advance social and life sciences research. Yet, as an empirical matter, we still have a very hard time actually measuring the impacts various research or commercial uses of personal data have on privacy. When does worthwhile research infringe privacy rights? Does the profiling and tracking used to figure out which ads to deliver to billions of Internet users constitute a reasonable business practice or an assault on human dignity? Although in part policy questions, these would be easier to answer if we had more clear ways to measure privacy impact. Recent efforts at more rigorous mathematical and systematic characterizations of privacy risk may help [e.g.,

The Global War for Internet Governance

by Laura DeNardis

Yale University Press, New Haven, CT, 2014. 296 pp. $38, £25. ISBN 9780300181357.

(*1*)], but we are still a long way from being able to measure privacy impact with the precision that we can measure other important public resources, such as characteristics of the economy or our climate.

Cybersecurity is a key priority as the entire world becomes more dependent on the Internet. Yet we understand very little about what factors affect the resilience and reliability of large networks. DeNardis cites the debate over a proposed intellectual property enforcement law known as the Stop Online Piracy Act (SOPA). That bill was ultimately defeated, in part because of allegations that it would "break the Internet." There were good anecdotal arguments that SOPA might cause security risks, but these were more gut feelings on the part of experienced network engineers than any kind of well-substantiated theory.

Much of the global tension about the Internet stems from an urgent need for developing economies to come online as soon as possible. What are the best regulatory models for achieving this goal? Market forces have encouraged enormous investment in Internet infrastructure, but those resources have not been evenly distributed, leaving citizens in rural areas of developed economies and many in the developing world still waiting for affordable access. Better economic research into the Internet transport market, as well as more advanced network engineering to develop wireless architecture, could help inform policy-makers about how best to achieve their goals.

The Global War for Internet Governance describes a conflict being fought with the tools of raw political power, long on ideological rhetoric and well-meaning interpretation of what seemed to have worked in the past. For as much as we depend on the Internet, we have a very hard time measuring—much less explaining—the behavior of the technical and sociotechnical mechanisms on which its operation depends. That we know so much but understand so little about how the Internet actually works is a huge opportunity for researchers in a wide variety of fields. Few doubt the intrinsic social and economic value of the open, global Internet. But we still have a lot to learn across a range of computer, social, and behavioral sciences to understand how to keep the Internet going and growing.

References
1. http://web.mit.edu/bigdata-priv/agenda.html.

LAND USE

Cracking Brazil's Forest Code

Brazil's controversial new Forest Code grants amnesty to illegal deforesters, but creates new mechanisms for forest conservation.
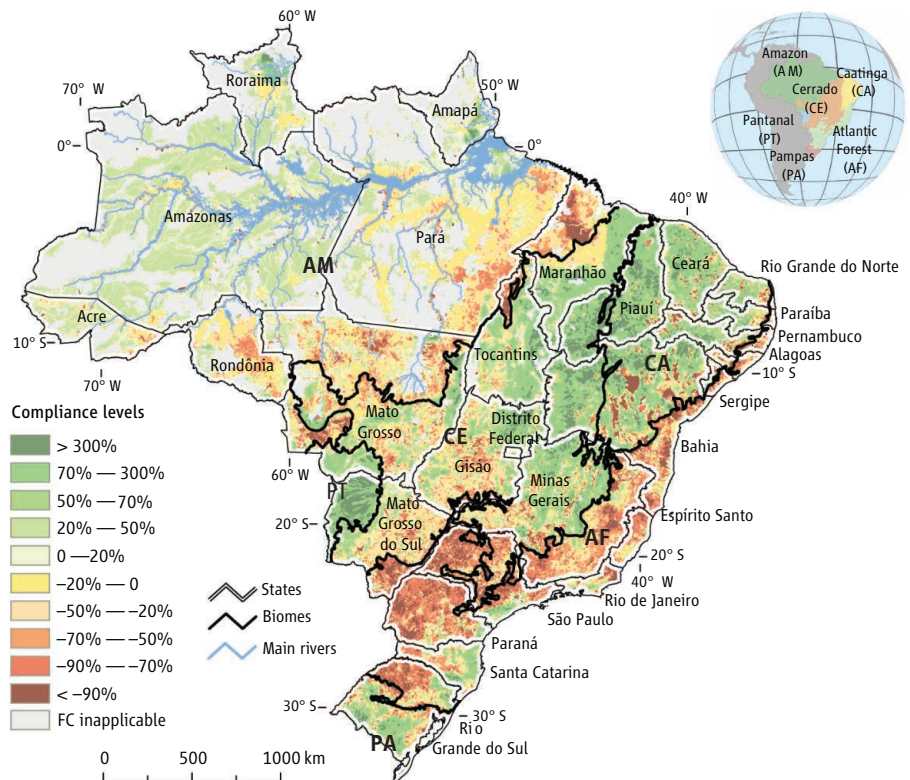
Britaldo Soares-Filho,[1]* Raoni Rajão,[1] Marcia Macedo,[1,2] Arnaldo Carneiro,[3] William Costa,[1] Michael Coe,[2] Hermann Rodrigues,[1] Ane Alencar[4]

Roughly 53% of Brazil's native vegetation occurs on private properties. Native forests and savannahs on these lands store 105 ± 21 $GtCO_2e$ (billion tons of CO_2 equivalents) and play a vital role in maintaining a broad range of ecosystem services (1). Sound management of these private landscapes is critical if global efforts to mitigate climate change are to succeed. Recent approval of controversial revisions to Brazil's Forest Code (FC)—the central piece of legislation regulating land use and management on private properties—may therefore have global consequences. Here, we quantify changes resulting from the FC revisions in terms of environmental obligations and rights granted to land-owners. We then discuss conservation opportunities arising from new policy mechanisms in the FC and challenges for its implementation.

Created in 1965, the FC was transformed during the 1990s into a de facto environmental law via a series of presidential decrees. As of 2001, the FC required landowners to conserve native vegetation on their rural properties, setting aside a Legal Reserve (LR) that occupies 80% of the property area in the Amazon and 20% in other biomes [supplementary material (SM), fig. S1, and table S1]. The law also designated environmentally sensitive areas as Areas of Permanent Preservation (APPs), aiming to conserve water resources and prevent soil erosion. APPs include both Riparian Preservation Areas (RPAs) that protect riverside forest buffers, and Hilltop Preservation Areas (HPAs) at hilltops, high elevations, and steep slopes.

The FC severely restricted deforestation on private properties but proved challenging to enforce, particularly in the Amazon. As deforestation rates rose in the early 2000s, efforts to strengthen enforcement increased pressure on the farming sector, which triggered a backlash against the FC. The agribusiness lobby took advantage of a favorable political moment, related to a substantial drop

[1]Universidade Federal de Minas Gerais, Belo Horizonte, MG 31270-901, Brazil. [2]Woods Hole Research Center, Falmouth, MA 02540, USA. [3]Secretaria de Assuntos Estratégicos da Presidência da República, Brasília, DF 70052-900, Brazil. [4]Instituto de Pesquisa Ambiental da Amazônia, Brasília, DF 71.503-505, Brazil. *Corresponding author: britaldo@csr.ufmg.br

Compliance levels under Brazil's 2012 FC. Percent difference between the remaining area of native vegetation and the area required to comply with the 2012 FC. Positive values indicate forest surpluses or land that may be legally deforested. Negative values indicate forest debts or land that requires restoration. See SM for details.

in deforestation rates in the Brazilian Amazon, to propose creation of a new FC, which was approved in late 2012 (2). Some criticize the legislation for being too lenient on landowners; others maintain that it is a barrier to agricultural development. Regulations detailing key implementation mechanisms of the revised FC are still under negotiation.

Amnesty for Illegal Deforestation

The 2012 FC maintains conservation requirements for LRs and RPAs—i.e., land that may not be deforested (table S1). These two requirements protect 193 ± 5 Mha of native vegetation containing 87 ± 17 $GtCO_2e$ (see the map). Changes in the definition of HPAs reduced their total area by 87% (table S8).

Because the new law differentiates between conservation and restoration requirements, the 2012 FC reduced by 58% Brazil's "environmental debt"—i.e., areas of LR and RPA deforested illegally before 2008 that,

under the previous FC, would have required restoration at the landowner's expense (fig. S2). This was accomplished by forgiving the LR debt of "small" properties, ranging in size from 20 ha in southern Brazil to 440 ha in the Amazon. Under these new rules, 90% of Brazilian rural properties qualify for amnesty. Further reductions resulted from including RPAs in the calculation of the LR area, reducing the LR restoration requirement to 50% in Amazonian municipalities occupied predominantly by protected areas, and relaxing RPA restoration requirements on small properties (table S1).

Together, these measures decreased the total area to be restored from 50 ± 6 to 21 ± 1 Mha, of which 78% encompasses LRs and 22% RPAs (tables S2 and S3). Reductions in the environmental debt were uneven across states and biomes, affecting mainly the Amazon, Atlantic Forest, and Cerrado (fig. S2). These losses may have a large impact on

biodiversity conservation (*3*) and forest restoration programs (*4*), especially in the Atlantic Forest, where only 12 to 16% of the original forest cover remains (*5*).

Furthermore, both old and new FCs allow an additional 88 ± 6 Mha of legal deforestation on private properties (table S4 and the figure). This area of native vegetation, exceeding LR and RPA conservation requirements, constitutes an "environmental surplus" with the potential to emit 18 ± 4 GtCO$_2$e (SM, §2.1).

New Mechanisms for New Markets
Although the 2012 FC reduces restoration requirements, it introduces new mechanisms to address fire management, forest carbon, and payments for ecosystem services, which could reduce deforestation and bring environmental benefits. Perhaps the most important mechanism is the Environmental Reserve Quota (Portuguese acronym, CRA), a tradable legal title to areas with intact or regenerating native vegetation exceeding the FC requirements. The CRA (surplus) on one property may be used to offset a LR debt on another property within the same biome and, preferably, the same state. Implementating the CRA could create a trading market for forested lands, adding monetary value to native vegetation. This CRA market could potentially abate 56% of the LR debt (fig. S3). Given the high costs of forest restoration (*6*), exchange of CRAs could become a cost-effective way to facilitate compliance, meanwhile protecting forest surpluses that might otherwise be legally deforested. A balanced use of CRAs should focus on improving functional and ecological attributes of forested landscapes, e.g., habitat integrity (and thus biodiversity), carbon stocks, and water balance regulation, crucial for maintaining hydroelectric power generation in Brazil (*7*).

One of the strongest arguments of the agribusiness lobby is that forest restoration conflicts with agricultural production. Our results suggest that, with respect to land availability, this concern is unfounded. Of the 4.5 ± 1 Mha of RPAs slated for restoration, only 0.6 ± 0.35 Mha are currently occupied by crops, representing less than 1% of all croplands nationwide. Moreover, if restoration of the remaining LR debt (after compensation via CRAs) occurred exclusively in pasturelands unsuitable for agriculture, as few as ≈ 550,000 ha of required restoration would remain in arable lands (SM §§2.2 and 2.3 and figs. S3 to S5). Such a large-scale transition from cattle ranching to agriculture would require substantial increases in stocking densities to sustain current levels of meat production and allow for forest restoration. To this end, Bra-

zil has created a national Low-Carbon Agriculture (ABC) program that provides ~U.S. $ 1.5 billion in annual subsidized loans aimed at increasing agricultural productivity while reducing associated carbon emissions and supporting forest restoration (table S5).

Key to success of the FC is the Rural Environmental Registry System (SICAR), a georeferenced Web system that will enable documentation of over 5 million rural properties, improving transparency and providing a pathway to environmental compliance. SICAR could facilitate the market for CRAs and payments for ecosystem services [for example, (*8*)], which will be critical to offset the often-prohibitive costs of forest restoration, especially for small landowners. We estimate that elimination of the FC debt via forest restoration would sequester up to 9 ± 2 GtCO$_2$e (SM, §2.1).

Enforcement and Private Initiatives
Effective implementation of Brazil's 2012 FC will be enormously challenging. The first crucial challenge is to convince the agribusiness sector of the potential gains from the new FC. Even though law enforcement activities have intensified in recent years, the agribusiness constituency has historically taken advantage of the government's relatively weak enforcement of environmental laws. Amnesty afforded by the new FC could lead to the perception that illegal deforesters are unlikely to be prosecuted and may even be exonerated in future law reforms. To meet this challenge, Brazil must continue to invest in its monitoring and enforcement capabilities. Satellite-based deforestation monitoring systems maintained by the National Institute for Space Research (INPE) need to be expanded to other Brazilian biomes and adapted to detect subtler land-use changes, including forest degradation and deforestation in savannahs, riparian forests, and small remnants of the Atlantic Forest.

More important, there is a need to strengthen and integrate efforts across the myriad state and federal agencies responsible for implementing the FC, establishing clear land tenure, granting environmental licenses, and supporting agricultural production. This integrated system must be transparent and harnessed to economic incentives for conservation; otherwise, it might only exhort landowners to exercise rights to deforest (*9*).

Fortunately, private initiatives are aligning to assist landowners in attaining compliance. These include international certification standards, commodity roundtables, and boycotts of agricultural products grown in recently deforested or high-biodiversity areas.

Increasingly, farmers and ranchers are adhering to voluntary registries that require commitments to improving social and environmental performance [for example, (*10*, *11*)]. Both certification schemes and voluntary registries may eventually enable access to special markets that provide financial incentives to participating producers. These mechanisms are particularly important in the Cerrado, the most coveted biome for agribusiness expansion, given its 40 ± 3 Mha of environmental surplus that could be legally deforested (table S4). Moreover, conservation efforts must aim at expanding protected areas outside the Amazon. Whereas these areas cover 46% of the Brazilian Amazon, the level of protection in other major biomes (7% of the Cerrado and 2.6% of the Atlantic Forest) is well below the 17% recommended by the 10th Convention on Biological Diversity. Conservation initiatives will be vital to protect large expanses of native vegetation, particularly in the Cerrado and Caatinga, where additional protection by land-use zoning is low.

Brazil has achieved an unprecedented success in reducing deforestation in the Amazon. However, this gain is not yet secured. Recently, deforestation rates ceased to decline in the Amazon and Atlantic Forest, and surged in the Cerrado (fig. S6). Our analysis suggests that the FC will allow additional deforestation, especially in the Cerrado and Caatinga. Economic incentives for conserving forests, including the Warsaw Framework for Reducing Emissions from Deforestation and Forest Degradation as (REDD+), will be essential to help implement the FC and to enable Brazil to better reconcile environmental conservation with agricultural development.

References and Notes
1. Millennium Ecosystem Assessment, *Ecosystem and Human Well-Being: Synthesis* (Island Press, Washington, DC, 2005); www.millenniumassessment.org/en/index.aspx.
2. Federal Law 12.727, 17 October 2012; www.planalto.gov.br/ccivil_03/_Ato2011-2014/2012/Lei/L12727.htm.
3. A. C. Lees, C. A. Peres, *Conserv. Biol.* **22**, 439 (2008).
4. R. Rodrigues *et al.*, *For. Ecol. Manage.* **261**, 1605 (2011).
5. M. Ribeiro *et al.*, *Biol. Conserv.* **142**, 1141 (2009).
6. R. Cury, O. Carvalho, "Manual para restauro florestal: Florestas de transição" (IPAM, Canarana, 2011).
7. C. M. Stickler *et al.*, *Proc. Natl. Acad. Sci. U.S.A.* **110**, 9601 (2013).
8. Project Oasis, Fundação Grupo Boticário; www.fundacaogrupoboticario.org.br/en/what%20we%20do/oasis/pages/default.aspx.
9. R. Rajão *et al.*, *Public Adm. Dev.* **32**, 229 (2012).
10. Aliança da Terra, aliancadaterra.org.br.
11. Round Table on Responsible Soy Association, responsible-soy.org.

PLANETARY SCIENCE

Analyzing Moon Rocks

A better inventory of lunar volatiles will help improve our understanding of the origin and evolution of the Earth-Moon system.

Mahesh Anand

The paradigm of a "dry Moon" was recently challenged on the basis of reexamination of lunar samples collected during the Apollo missions, raising the possibility of a volatile-rich lunar interior (*1–6*). Several of these studies measured appreciable quantities of water (reported as equivalent H, OH, or H_2O) and other volatiles (e.g., Cl, F) in the mineral apatite (*4–6*), which is ubiquitous in lunar basalts (mare basalts) (see the figure). However, an accurate estimation of the water content of the magmatic liquid from which apatite formed, and ultimately of the mantle source regions of mare basalts, depends on a number of parameters. In cases where apatite in a mare basalt formed through the process of fractional crystallization (when newly formed crystals in a cooling magma are physically separated, preventing any further interaction with the remaining melt), it may not be possible to obtain any reliable estimates of the water contents of the parental magma (and its source region). On page 400 of this issue, Boyce *et al.* (*7*) present an elegant numerical model, applicable to mare basalt apatite formed through fractional crystallization, to demonstrate that some of the highest water contents reported for lunar apatite can be reconciled with an original melt containing not much water at all. These new results cast doubt on the utility of apatite volatile abundances in reliably estimating the water content of mare basalt source regions.

The difficulties in determining volatile abundances primarily arise because of the unconventional partitioning behavior of OH between melt and apatite in the presence of F and Cl. The partitioning behaviors of these three species are all interdependent—a fact not recognized previously. In case of lunar basalts, the fluorine concentration in the melt has a major influence on the partitioning behavior of water into apatite. Thus, the fluorine concentration in the melt from which apatite crystals grew needs to be known in order to estimate the concentration of water in the melt, which is nontrivial. Such complexities hamper efforts to reliably estimate the water contents of the basalt source regions from the volatile contents of apatite.

Planetary and Space Sciences, Open University, Milton Keynes MK7 6AA, UK. E-mail: mahesh.anand@open.ac.uk

Dry and wet? The lunar apatite paradox derives from the observation that there are "wet" apatite samples in an otherwise "dry" Moon.

Does this mean that we have come full circle in terms of our understanding of the volatile inventory of the Moon, and that the bulk Moon is an anhydrous body, as proposed soon after initial investigations of the first returned lunar samples from the Apollo 11 mission? In all likelihood, the answer is no for a number of reasons. Unlike apatite (which usually forms late during the crystallization of a basaltic magma), water-rich melts trapped in olivine crystals, which were some of the earliest-formed crystals in lunar volcanic glasses, point to a wet lunar interior (*2, 3*). Similarly, a recent spectroscopic analysis of plagioclase crystals (a nominally anhydrous mineral that forms much earlier in a cooling magma than apatite) from rocks thought to represent direct crystallization products of the lunar magma ocean reveal quantities of water that suggest that this magma ocean is wet (*8*).

It is also worth noting that not all apatite samples that have been analyzed correspond to the fractional crystallization scenario as proposed by Boyce *et al.* Water contents of apatite have been measured in mare samples that seem to approximate equilibrium crystallization conditions. In such cases, it may be feasible to estimate the water contents of the basalt source region (*9*), especially if the F contents of the melt and apatite were also known. The key to using apatite volatile abundances to estimate the volatile abundances of a mantle source region is a thorough understanding of the textural context in which apatite occurs in a given rock sample, thereby establishing the main mode of crystallization (fractional or equilibrium). Indeed, calculations using apatite analysis from such texturally well-constrained lunar samples seem to indicate a relatively wet lunar interior, consistent with results emerging from studies of lunar volcanic glasses and nominally anhydrous minerals.

Another important development is that of new high-precision measurements for volatile elements such as C and N in lunar

CREDIT: NASA

samples. In addition to measuring elemental abundances, some studies have also measured isotopic compositions of H, C, and N; taken together, the combined data set is more in agreement with a relatively wet lunar interior as well as a common origin for water and other associated volatiles in the Earth-Moon system (*2*, *10–12*). Such links are further strengthened by results of dynamical modeling of the Moon formation event, which suggest that the material forming the magma disc around the proto-Earth after the putative giant impact could have retained volatiles sufficiently well relative to what was believed to be the case previously (*13*). Thus, a giant-impact origin of the Moon does not necessarily require the formation of an anhydrous Moon, and the presence or absence of water cannot be used as evidence for or against various models involving some variations of the giant-impact origin of the Moon.

Over the past decade, considerable improvements in analytical instrumentation and advances in numerical modeling have led to a dramatic change in our understanding of lunar volatiles. An approach that combines multi-element and multi-isotopic measurements on the same samples provides better constraints on the volatile history of lunar samples and of their source regions. A series of new measurements and experiments need to be performed to confirm some of the predictions based on numerical modeling and in turn would provide data for refining such models. A better understanding of the volatile inventory of the lunar interior will not only improve our understanding of the origin and evolution of the Earth-Moon system but will also provide key insights into the origin and sources of volatiles necessary for life.

References

1. A. E. Saal *et al.*, *Nature* **454**, 192 (2008).
2. A. E. Saal *et al.*, *Science* **340**, 1317 (2013).
3. E. H. Hauri *et al.*, *Science* **333**, 213 (2011).
4. J. W. Boyce *et al.*, *Nature* **466**, 466 (2010).
5. F. M. McCubbin *et al.*, *Proc. Natl. Acad. Sci. U.S.A.* **107**, 11223 (2010).
6. R. Tartèse *et al.*, *Geochim. Cosmochim. Acta* **122**, 58 (2013).
7. J. W. Boyce *et al.*, *Science* **344**, 400 (2014); 10.1126/science.1250398.
8. H. Hui *et al.*, *Nat. Geosci.* **6**, 177 (2013).
9. R. Tartèse *et al.*, *Geology* **42**, 363 (2014).
10. J. J. Barnes *et al.*, *Earth Planet. Sci. Lett.* **390**, 244 (2014).
11. J. I. Mortimer *et al.*, *Lunar Planet. Sci.* **45**, abstract 2529 (2014).
12. D. T. Wetzel *et al.*, *Lunar Planet. Sci.* **45**, abstract 2238 (2014).
13. M. Nakajima, D. Stevenson, *Lunar Planet. Sci.* **45**, abstract 2770 (2014).

GENETICS

Being Selective in the *Prochlorococcus* Collective

Single-cell sequencing reveals the micro-diversity of the most abundant photosynthetic organism on Earth.

Chris Bowler[1] and David J. Scanlan[2]

Marine phytoplankton are a key component in global biogeochemical cycles and marine food webs. The structure and function of phytoplankton communities varies throughout the oceans, organized by ocean circulation and resource delivery, and is intertwined with the acclimation (physiological plasticity) and adaptation of the organisms to the prevailing conditions. Cyanobacteria of the genus *Prochlorococcus* are a dominant component of such communities in oligotrophic (nutrient-poor) regions of the oceans between 45°N and 40°S (*1*). On page 416 of this issue, Kashtan *et al.* (*2*) use single-cell genomics to describe the genotypes of individual *Prochlorococcus* cells co-occurring at the Bermuda-Atlantic Time-series Study site in the Sargasso Sea. The work provides a detailed view of the population genetics of this organism, revealing an array of diverse genotypes that hint at the evolutionary and environmental forces that generate and maintain *Prochlorococcus* diversity. More generally, the study brings a new dimension to what can be done today in environmental microbiology by combining single-cell isolation from the field with DNA sequencing technologies.

The *Prochlorococcus* genus contains distinct ecotypes or clades that are adapted to the different seasonal and geographical light and nutrient gradients in the sunlit upper layers of the ocean (*3*, *4*) (see the figure). These population adjustments occur within *Prochlorococcus* communities even though overall population density is relatively constant, at 100,000 cells/ml in surface waters (*5*). Kashtan *et al.* analyzed single-cell genome sequences from cells collected at three different times of the year. They found subpopulations at the whole-genome level that correlate with the relationships defined previously by ribosomal RNA sequences—an important confirmation of the value of the more traditional methods used to identify clades and assess community diversity and dynamics. Moreover, they found that although the overall genetic diversity was maintained in each sample collected during different seasons, there were changes in the abundance of specific genotypes that led to their dominance in certain conditions. The environment thus appears to select winning genotypes from the *Prochlorococcus* collective, likely according to differential fitness in changing environmental conditions, refuge from phages and grazers, and other extrinsic and intrinsic factors (*6*, *7*).

Kashtan *et al*. conclude that the previously defined ecotypes are in fact a collection of many coexisting subpopulations. Each has a distinct "genomic backbone" consisting of highly conserved alleles of a majority of "core" genes and a smaller distinct set of flexible genes that is associated with a particular set of core gene alleles. Although conserved within clades, these combinations are different between clades. Furthermore, variation within clades appears to be targeted to specific regions of the genome, implying a mechanism for generating genetic diversity that links the core and flexible genomes. This fine-scale co-variation between the core alleles and flexible gene content represents previously unknown microdiversity within wild *Prochlorococcus* populations of co-occurring cells. In reality, the extent of diversity is remarkably high, with as much as 3% of the genome being affected at the sub-clade level; the authors propose that this is because these backbone subpopulations diverged at least a few million years ago. If this is the case, it would suggest an ancient niche partitioning that is stable over long time scales. Genes that appear to be particularly prone to nucleotide variations in both the core and flexible gene

[1]Institut de Biologie de l'Ecole Normale Supérieure, CNRS UMR8197, 75005 Paris, France. [2]School of Life Sciences, University of Warwick, Coventry CV8 1FN, UK. E-mail: cbowler@biologie.ens.fr; d.j.scanlan@warwick.ac.uk
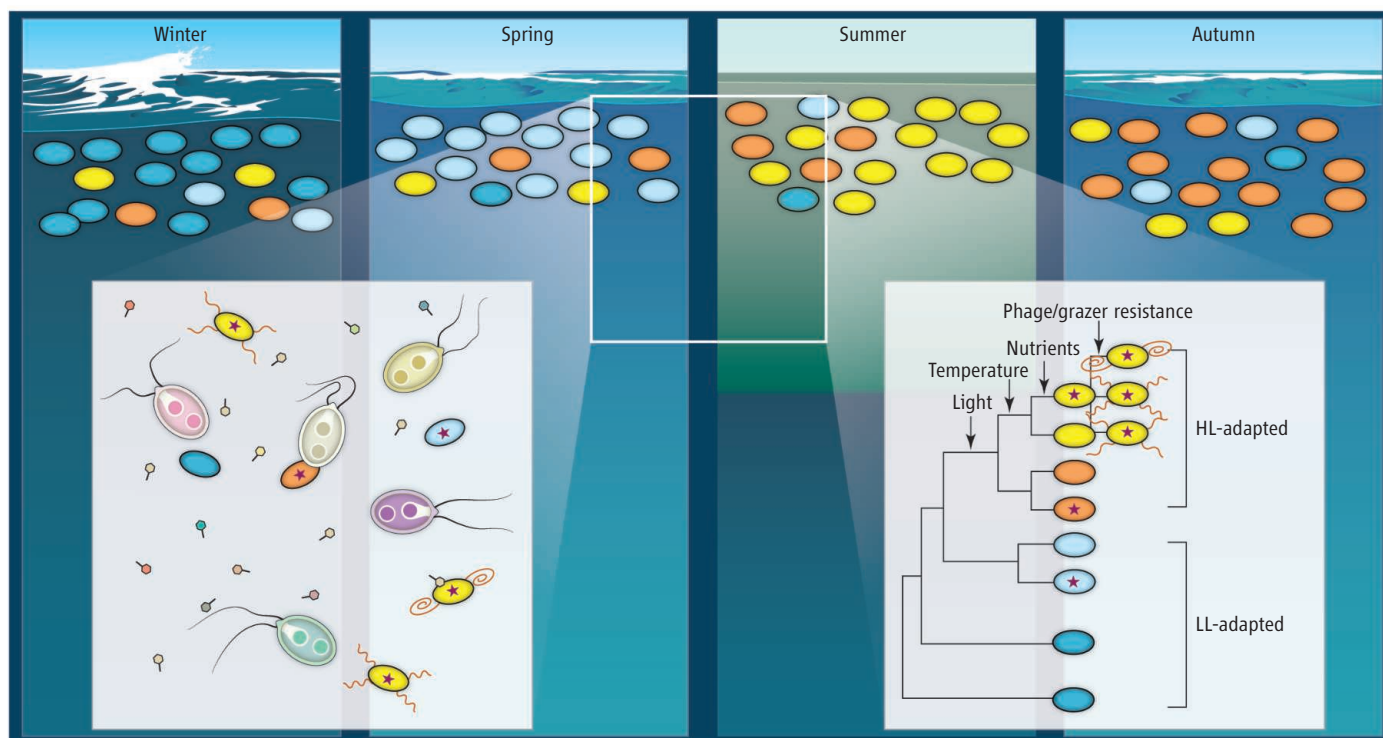
Prochlorococcus diversity in the ocean. Seasonal selection of genotypes (different-colored cells) from similar-sized populations of the *Prochlorococcus* collective throughout a schematic annual cycle. **(Inset)** Bottom left: An idealized population of plankton in which different genotypes of *Prochlorococcus* coexist with different protist grazers (flagellated cells) and different phages (not to scale). **(Inset)** Bottom right [adapted from (9)]: Diversification based on physical parameters (temperature, light, and nutrients) may be operative at higher taxonomic levels, whereas the fine-scale "leaves" of the tree are likely maintained by biological phenomena such as nutrient acquisition and phage/grazer resistance. Stars and squiggles indicate the importance of the cell surface in fine-scale genotype selection (HL, high light–adapted ecotypes; LL, low light–adapted ecotypes).

sets encode proteins that are involved in the interface that the cell presents to the external environment (e.g., by modifying the cell surface). In future studies, it will be of interest to ascertain the rates of diversification of these proteins and how they have varied over time. It will also be important to go beyond genome sequencing and examine the expression of these alleles in the different populations throughout the year.

What must also be addressed is how the diversity is maintained and on which scale it is acting (8). With the cell surface implicated as a major driver of microdiversity, the biotic environment seems likely to be playing a large role (9). This might be a result of the arms race between predator and prey and/or between virus and host. Depending on physical transport of cells (e.g., by ocean currents and wind-driven mixing), this might further mean that an individual genotype is never eaten by the same grazer twice (or infected by the same phage twice)—which would slow the pace of biotic selection—or that locally there is some sort of biological network where more rapid coevolution occurs (10, 11).

The work by Kashtan *et al.* is necessarily descriptive; the oceanographic context is simplified, the study is based on only three sampling dates, and the mechanisms that drive genome structure changes over the proposed time scales are not addressed. The authors also focused only on high light–adapted (HL) ecotypes; it is likely that low light–adapted (LL) ecotypes will display even greater diversity. Although the results essentially support an "everything is everywhere but the environment selects" regime (12), further work is required to show whether the same genotypes come back year after year, and if not why not. Furthermore, it will be interesting to extend the observations beyond the Sargasso Sea to assess whether ocean circulation can ensure a global distribution of the same seed populations. Given the huge effective population size of *Prochlorococcus* and the modeling of physical mixing that the authors present, this appears likely to be the case, but it will be important to show that the different genotypes are indeed everywhere, at least at population levels that can be detected by ultradeep sequencing.

By providing a new window into natural microbial communities, DNA sequencing–based technologies seem likely to continue to provide dramatic increases in our understanding of the evolution and ecology of phytoplankton populations. Key questions in microbial oceanography that can now be addressed include how adaptation to the environment organizes populations into biomes (networks of interacting organisms) having specific biogeochemical functions, the relative role of acclimation and genetic adaptation in shaping these networks, and the importance of physical transport and intermingling of populations by ocean circulation with respect to local adaptation. No doubt *Prochlorococcus* will continue to lead the way in revealing the ocean's secrets.

References
1. P. Flombaum *et al.*, *Proc. Natl. Acad. Sci. U.S.A.* **110**, 9824 (2013).
2. N. Kashtan *et al.*, *Science* **344**, 416 (2014).
3. L. R. Moore, G. Rocap, S. W. Chisholm, *Nature* **393**, 464 (1998).
4. Z. I. Johnson *et al.*, *Science* **311**, 1737 (2006).
5. R. R. Malmstrom *et al.*, *ISME J.* **4**, 1252 (2010).
6. A. D. Barton, S. Dutkiewicz, G. Flierl, J. Bragg, M. J. Follows, *Science* **327**, 1509 (2010).
7. F. Rodriguez-Valera *et al.*, *Nat. Rev. Microbiol.* **7**, 828 (2009).
8. F. Azam, F. Malfatti, *Nat. Rev. Microbiol.* **5**, 782 (2007).
9. M. L. Coleman, S. W. Chisholm, *Trends Microbiol.* **15**, 398 (2007).
10. C.-E. T. Chow *et al.*, *ISME J.* **8**, 816 (2014).
11. K. Zwirglmaier *et al.*, *Environ. Microbiol.* **11**, 1767 (2009).
12. L. Tirichine, C. Bowler, *Plant J.* **66**, 45 (2011).

CHEMISTRY

A Two-Catalyst Photochemistry Route to Homochiral Rings

A synthetic route photoactivates one reactant and then controls stereochemistry of subsequent steps to form a single isomer of a four-membered ring.

Reinhard Neier

Many biologically active compounds used in medicine and agriculture are still produced as a racemic mixture, even though only one isomer is actually active. The presence of the inactive isomer can lead to unwanted side effects. The efficient synthesis of only one stereoisomer—homochiral molecules—is a key goal in organic synthesis (*1*). Synthesizing homochiral molecules with light and a photocatalyst has been an unmet challenge for many years (*2*), yet the combination of light and catalysis to create chiral products is a hallmark of photosynthesis. On page 392 of this issue, Du *et al.* (*3*) report an efficient chiral selection by combining a transition-metal photocatalyst with a stereocontrolling cocatalyst. They obtained four-membered rings in good yields and with excellent enantioselectivity. This approach avoids the problems associated with the noncatalyzed background reaction, which hampers most photocatalytic processes.

Enantioselective photochemical reactions have attracted the interest of chemists since the pioneering work of Kuhn in the 1930s (*4*). Visible light is environmentally benign and can be used to overcome the energetic barrier of reaction pathways not accessible by thermal processes. The [2 + 2] cycloaddition is an archetypical photochemical reaction (*5*) that in one step

Chemistry Department, University of Neuchatel, Rue Emile-Argand 11, Neuchatel, Switzerland. E-mail: reinhard.neier@unine.ch

converts simple achiral starting materials into strained four-membered rings that can contain up to four different asymmetric centers. Part of the activation energy provided by the photon is not dissipated but is stored as ring strain. The products of these reactions are versatile synthetic intermediates.

Since the ground-breaking work from the groups of Knowles (*6*), Sharpless (*7*), and Noyori (*8*), organic chemists have focused on the development of efficient catalytic enantioselective transformations that can replace the synthesis of mixtures of isomers requiring wasteful separation procedures. Instead, chiral catalysts bind reactants to favor the formation of one isomer during reaction. Many enantioselective transformations that can be used with a wide range of substrates have been reported, and the scope of this approach has expanded to include radical reactions (*9*) and transition-metal–free organocatalytic reactions (*10–12*). With this approach, the synthesis on the ton scale of valuable, biologically active compounds in pure form can be performed with just grams of an optically active catalyst (*1*).

In view of these developments, it was surprising and disappointing that photochemistry did not follow the trend until recently. The reasons for this belated arrival of success in the development of enantioselective photocatalytic processes can be traced back to a lack of knowledge on the energy surface of the activated state and the short lifetime of excited molecules. To obtain high enantiose-

lectivities, non-enantioselective background reactions must be suppressed. In thermal reactions, this problem can sometimes be addressed simply by lowering the reaction temperature and sacrificing a lower rate for greater selectivity. Bach and co-worker have pioneered a photocatalytic approach in which the complex between the catalyst and the substrate has a distinct absorption maximum from the uncomplexed starting material (*13*). Carefully choosing the wavelength of irradiation allows selective excitation of the complexed substrate, which is then transformed with high enantioselectivity.

The approach chosen by Du *et al.* totally decouples the photoactivation from the process responsible for the enantioselectivity (see the figure). Irradiating the ruthenium complex with visible light creates a redox-active excited species that reduces the α,β-unsaturated phenylketone only, when activated by an adequately chosen Lewis acid. The complexed radical anion formed by this process then undergoes a stepwise reaction

Coupling light energy to achieve a selective transformation. In the reaction developed by Du *et al.*, light activates a ruthenium complex (**A**), which selectively reduces an α,β-unsaturated phenylketone complex. (**B**) In a radical process, a formal [2 + 2] cycloaddition is achieved with high enantioselectivity (**B**). Abbreviations: SET, single-electron transfer; MLCT, metal-to-ligand charge transfer; bpy, bipyridyl; *i*-Pr, isopropyl; OTf, triflate; Me, methyl; Et, ethyl; Ph, phenyl; Eu, europium; and L, the multidentate chiral ligand.
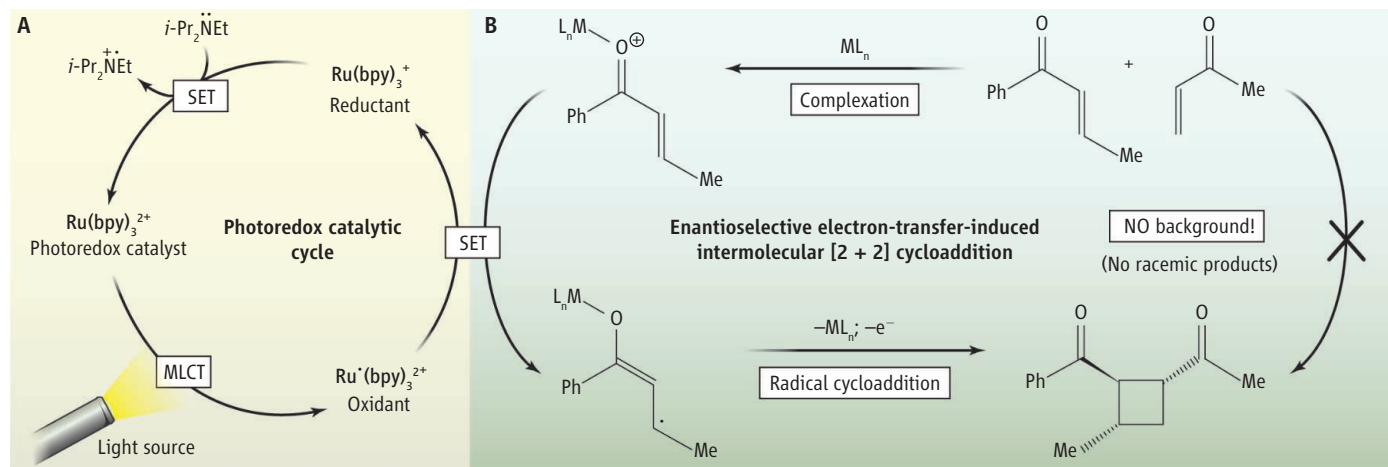
CREDIT: P. HUEY/SCIENCE

sequence leading to the enantioselective formation of the four-membered ring under the influence of the chiral ligand. Optimizing all the parameters of this photoredox-catalyzed reaction allowed products to be obtained typically in 50 to 80% synthetic yields and with consistently high enantiomeric excess of 85 to >95%. The utility of photoredox-catalyzed reactions has been demonstrated already for C–C bond–forming processes by MacMillan and co-worker (14). The attractiveness of the Du et al. procedure is that the process achieved via a redox sequence is a genuinely photochemical transformation, the [2 + 2] photocycloaddition.

The process reported mimics in its strategy the process of photosynthesis, which decouples the primary photochemical event from the utilization of the harnessed energy for synthetic transformations. The initial photochemical event creates a redox potential. The synthetic part harnesses the photochemical energy in creating energy-rich chemical structures. The results reported are notable because of the synthetic importance of the synthesized structures, but also because they allow studying the coupling of the energy collected from photons to the energy stored in interesting chemical structures.

References
1. H.-U. Blaser, *Chem. Commun. (Camb.)* **2003**, 293 (2003).
2. P. Wessig, *Angew. Chem. Int. Ed.* **45**, 2168 (2006).
3. J. Du, K. L. Skubi, D. M. Schultz, T. P. Yoon, *Science* **344**, 392 (2014).
4. W. Kuhn, E. Knopf, *Z. Phys. Chem.* **7**, 292 (1930).
5. G. Ciamician, P. Silber, *Ber. Deutschen Chem. Gesellschaft* **41**, 1928 (1908).
6. W. S. Knowles, M. J. Sabacky, B. D. Vineyard, *Chem. Commun.* **1972**, 10 (1972).
7. T. Katsuki, K. B. Sharpless, *J. Am. Chem. Soc.* **102**, 5974 (1980).
8. A. Miyashita et al., *J. Am. Chem. Soc.* **102**, 7932 (1980).
9. M. P. Sibi, N. A. Porter, *Acc. Chem. Res.* **32**, 163 (1999).
10. K. A. Ahrendt, C. J. Borths, D. W. C. MacMillan, *J. Am. Chem. Soc.* **122**, 4243 (2000).
11. U. Eder, G. Sauer, R. Wiechert, *Angew. Chem. Int. Ed. Engl.* **10**, 496 (1971).
12. Z. G. Hajos, D. R. Parrish, *J. Org. Chem.* **39**, 1615 (1974).
13. R. Brimioulle, T. Bach, *Science* **342**, 840 (2013).
14. D. A. Nicewicz, D. W. C. MacMillan, *Science* **322**, 77 (2008).

BIOPHYSICS

Silencing Neurons with Light

Engineered channelrhodopsins conduct anions rather than cations, changing the action potential of neurons.

Shigehiko Hayashi

Neural networks control the activity of living individuals as central processing units control the functions of modern computers. In a neuronal circuit, information is transmitted through neurons in the form of an action potential, which is the electric potential difference between the inside and the outside of a neuron. Ion channel proteins in the neuronal membrane act as molecular devices that create and regulate action potentials. A technology called optogenetics (1) allows neuronal circuits to be manipulated by a combination of optics and genetically targeted incorporation of microbial retinal binding proteins, called opsins (2), into neurons. On pages 409 and 420 of this issue, Wietek et al. and Berndt et al. (3, 4) use structure-based molecular engineering to invert the charge selectivity of different opsins, channelrhodopsins from algae, resulting in much improved neuron silencers for use in optogenetics.

Through heterologous expression of light-sensitive opsins, researchers can control the electric signals of neurons underlying the activities of living animals with light. Optogenetics thus provides precise neuronal control that can resolve highly complex neuronal activity in the brain, contributing, for example, to understanding of psychiatric disease states. However, microbial opsins have limited functionality for optogenetics; for example, their ion conductance and ion selectivity are sufficient for microbial activity but are too low for the efficient control of animal neuronal activity. The recent determination of the three-dimensional atomic structure of a chimeric protein formed from parts of two different channelrhodopsins (5) from algae (6, 7) has opened the way to rational molecular engineering of opsins with novel functionalities.

Ion selectivity, a key functional component of ion channels, enables the regulation of action potentials (see the figure). In the resting state of a neuron, the membrane is polarized, with a membrane potential of about –70 mV, through differences in ion concentrations maintained by energy-driven ion transporters. Upon light illumination, channelrhodopsins conduct cations but not anions (see the figure, panel A), thereby depolarizing the membrane and inducing
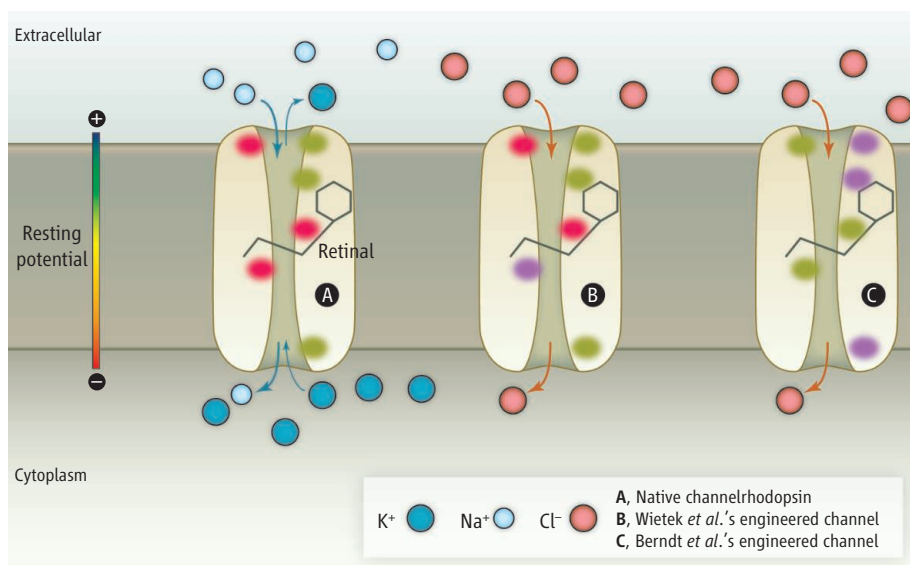
Better neuron silencers for optogenetics. Native channelrhodopsins conduct cations (**A**). In contrast, the channelrhodopsins engineered by Wietek et al. (**B**) and by Berndt et al. (**C**) conduct chlorine anions. Different residues were mutated to create the two Cl⁻ channels, with mutated residues shown in red (acidic), blue (basic), and green (neutral). Mutated residues that do not change their polarity are omitted.

Department of Chemistry, Graduate School of Science, Kyoto University, Japan. E-mail: hayashig@kuchem.kyoto-u.ac.jp

an action potential. However, light-sensitive ion channels for silencing neurons must be selective for chloride (Cl⁻) or potassium (K⁺) to further decrease the membrane potential (hyperpolarization) and thereby turn off the action potential. Such ion channels have not yet been found in natural species. In optogenetics, light-driven chloride and proton pumps from archaeal halobacteria have been used instead; however, pumps conduct only a single ion per photon and are therefore less efficient than channels.

Wietek et al. and Berndt et al. now provide drastic solutions to this problem. They use molecular engineering to convert cation-conducting channelrhodopsins into light-gated ion channels that selectively conduct Cl⁻. Further, they show that these engineered opsins can be used to efficiently hyperpolarize the membrane.

The conversions of ion selectivity obtained by the two groups occur in completely different ways (see the figure). Wietek et al. convert the ion selectivity of their channel through a single mutation, replacing an acidic residue with a positively charged arginine at a gating site located in the middle of the putative pore (see the figure, panel B). This observation suggests that the gating site may act as a selectivity filter. In contrast, Berndt et al. achieve Cl⁻ selectivity through multiple mutations that alter the electrostatic environment along an extended region of the pore, while replacing the acidic residue at the gating site by a neutral one (see the figure, panel C). The mechanisms underlying the Cl⁻ selectivity of the two engineered channels are thus remarkably different.

Ion channels are thought to achieve high ion selectivity through precisely defined pore architectures that efficiently conduct particular ions, as seen in tetrameric K⁺ selective channels (8). However, the different ion selectivity mechanisms of the two engineered channelrhodopsins show that charge selectivity of ion channels can be controlled in more variable ways. A clue to the permissive feature of channelrhodopsins may come from experimental evidence that channelrhodopsin is a light-driven proton pump as well as an ion channel (9) and that a single mutation in the middle of the proton channel can convert another light-driven opsin proton pump into a Cl⁻ pump (10). In both systems, the proton pump function is fulfilled by concerted motion of protons between acidic residues, positively charged basic side chains, and water molecules in the pore (11); the flexibility of these residues may contribute to making channelrhodopsins amenable to molecular engineering.

The highly controllable charge selectivity of engineered channelrhodopsins demonstrated by Wietek et al. and Berndt et al. should encourage researchers to further augment and improve functionalities of channelrhodopsins for optogenetics applications. Understanding of the physicochemical mechanism by which channelrhodopsins operate will also help to guide the design of novel ion channels with controllable selectivity through de novo protein design (12), synthetic engineering (13), and biomimetic synthesis of artificial macromolecules.

References

1. K. Deisseroth, Sci. Am. 303, 48 (2010).
2. F. Zhang et al., Cell 147, 1446 (2011).
3. J. Wietek et al., Science 344, 409 (2014); 10.1126/science.1249375.
4. A. Berndt, S. Y. Lee, C. Ramakrishnan, K. Deisseroth, Science 344, 420 (2014).
5. H. E. Kato et al., Nature 482, 369 (2012).
6. G. Nagel et al., Science 296, 2395 (2002).
7. G. Nagel et al., Proc. Natl. Acad. Sci. U.S.A. 100, 13940 (2003).
8. D. A. Doyle et al., Science 280, 69 (1998).
9. K. Feldbauer et al., Proc. Natl. Acad. Sci. U.S.A. 106, 12317 (2009).
10. J. Sasaki et al., Science 269, 73 (1995).
11. O. P. Ernst et al., Chem. Rev. 114, 126 (2014).
12. N. R. Zaccai et al., Nat. Chem. Biol. 7, 935 (2011).
13. W. Grosse, L.-O. Essen, U. Koert, ChemBioChem 12, 830 (2011).

STRUCTURAL BIOLOGY

The 30-nm Fiber Redux

Do alternating stacking modes of nucleosomes underlie the compaction of chromatin?

Andrew Travers[1,2]

The DNA of eukaryotic cells is packaged onto nucleosomes—complexes composed of histone proteins—that together form chromatin, enabling tight packing of the genome within the cell nucleus. In the first folded structure of chromatin to be characterized, nucleosomes were coiled into a ~30-nm-diameter helix, with the "linker" histone located in the interior of the fiber (1). The precise molecular organization of this 30-nm fiber has long been extensively debated. Initially, structural studies on fibers assembled on natural DNA sequences were hampered by variation in the length of the linker DNA between nucleosomes. However, more recently, the construction of regularly spaced tandem DNA repeats for precise nucleosome positioning (2) has revolutionized analysis. On page 376 of this issue, Song et al. (3) determine by cryo–electron microscopy the 11 Å–resolution structure of 30-nm fibers assembled from arrays of 12 nucleosomes.

Song et al. unequivocally identify the path of linker DNA. They show that in the fiber, a linear array of nucleosomes is packed in two interwound left-handed helical stacks with a straight linker DNA between successive nucleosomes in the array crossing the interior of the fiber. In agreement with an emerging consensus, this finding resolves the fundamental issue as to whether the fiber is built from one nucleosome stack—a solenoid—or from two. However, importantly, the new structure differs in one largely unanticipated aspect from most previous models. Instead of the monotonous helix previously imposed by the limitations of the available information, the 30-nm fiber is formed by the tight helical packing of a tetranucleosome unit. Within this unit, first observed by the crystallization of a tetranucleosome lacking linker histone (4), the two opposing nucleosome dimers are fully stacked on each other with only a small angular separation. Between the units, the angular separation is larger and each unit is staggered relative to its neighbor. The structure agrees well with all other direct measurements but does not exclude the possibility that a nucleosome array may still have the potential to fold into other helical forms.

The first hint of a lack of structural uniformity of nucleosomes in the folded fiber came from the observation of alternating pattern of deoxyribonuclease I (DNase I) digestion in successive nucleosomes (5). Subsequent modeling of the fiber showed that retention of the tetranucleosome unit necessitated the

[1]MRC Laboratory of Molecular Biology, Francis Crick Avenue, Cambridge CB2 0QH, UK. [2]Department of Biochemistry, University of Cambridge, 80 Tennis Court Road, Cambridge CB2 1GA, UK. E-mail: aat@mrc-lmb.cam.ac.uk
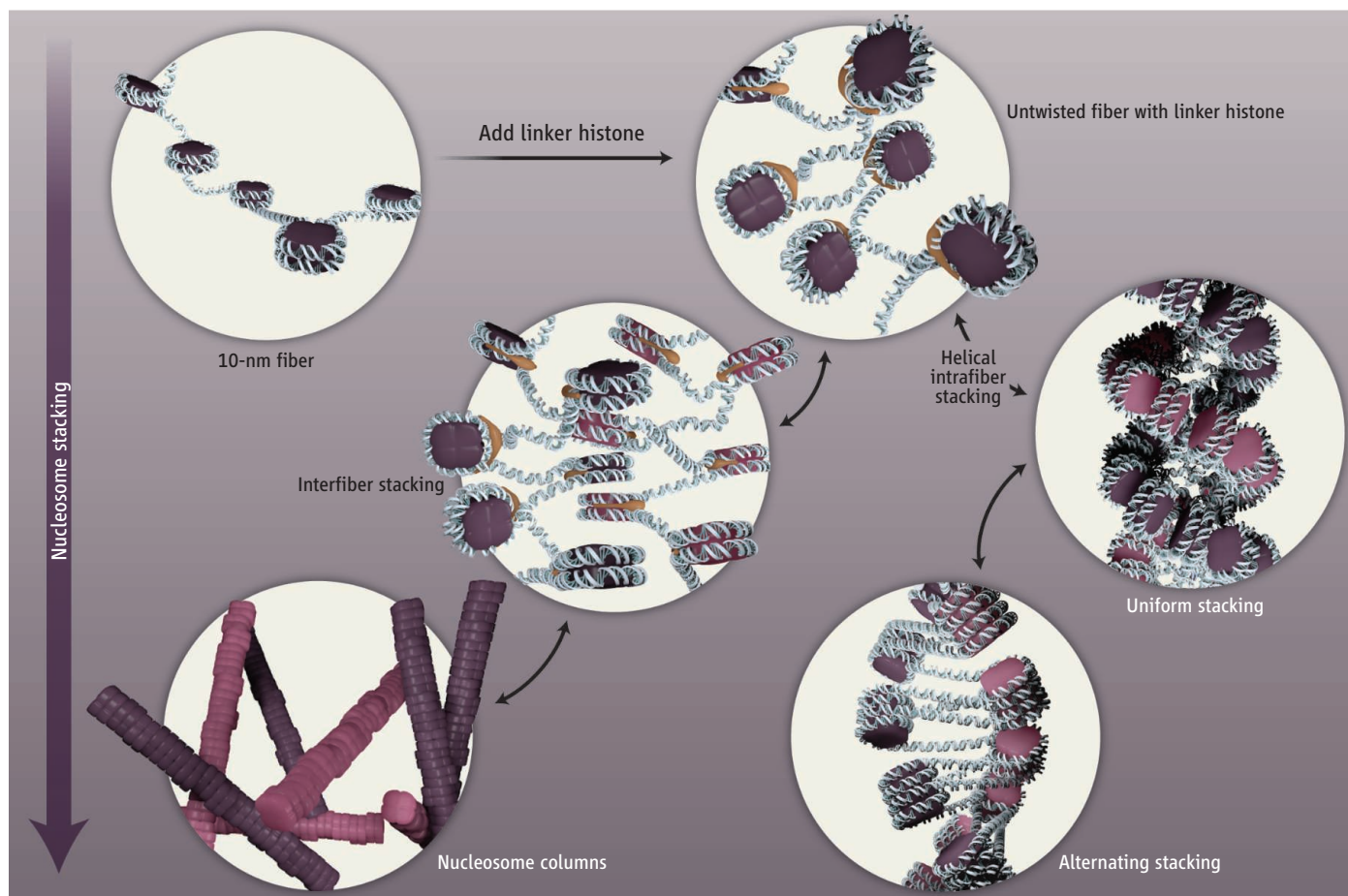
Stacking for packing. Possible modes of how a chromatin fiber folds into helical or columnar forms are shown. The structure described by Song *et al*. is a tightly packed helical form. The DNA linking nucleosomes is not shown in the columns.

alternating angular separation of nucleosomes (*4*) observed by Song *et al*. However, in a second "idealized" model, some stacking interactions were broken to allow the formation of a more regular structure.

The presence of alternating stacking modes between spatially adjacent nucleosomes implies alternating internucleosomal contacts. In the tetranucleosomal dimer stacks, a major contact is between the exposed surfaces of two H2A–H2B core histone dimers. This interaction is absent in the inter-tetranucleosome contacts, where instead there are contacts between the amino-terminal tail of H4, primarily involving residue arginine-23 and the acidic patches on the faces of the opposed nucleosomes. The packing density of the visualized fibers is about six or seven nucleosomes per 11-nm rise, in good agreement with many other determinations but lower than the 10 to 12 nucleosomes per 11 nm of more compact fibers assembled under conditions favoring more charge neu-

tralization (*6*). In principle, a higher packing density could be accommodated by a concertina motion reducing the vertical separation between successive turns of the fiber.

The 30-nm fiber structure determined by Song *et al*. addresses another contentious issue—that of the location of the linker histone. In the assembled fibers, the bulk of the globular domain of the linker histone is placed asymmetrically with respect to the inward-facing nucleosome dyad so that the principal contacts are at the dyad itself and with each of the entering linker DNA duplexes. This arrangement agrees best with previous suggestions based on DNase I footprinting (*7*, *8*) and computation (*9*). The linker histone thus confers polarity on the symmetric core nucleosome (*10*) in such a way that in the fiber, successive nucleosomes in a stack have opposite polarities, thereby stabilizing coherent stacking in the tetranucleosome unit and helical curvature between these units.

The structure determined by Song *et al*. emphasizes the importance of nucleosome stacking in chromatin compaction. Although the formation of continuous stacks by nucleosome core particles is well established, their biological relevance has been unclear (*11*). In natural folded 30-nm fibers with fewer

nucleosomes per turn, the discontinuous nature of the stacks accommodates the curvature of the helix, but as the fiber unfolds with decreasing ionic strength, stacking can become more continuous (*12*). However, in the most unfolded state, stacking within an individual fiber is no longer apparent, potentially facilitating interfiber stacking. The polarity of the internucleosomal contacts in more extensive stacks would not necessarily be identical to that in the helical fiber.

The 30-nm fiber has long been assumed to constitute the first level of a hierarchical folding pathway, ultimately generating the most compact chromatin, but recently the relevance, and even the existence in vivo, of the 30-nm fiber have been seriously challenged (*13*). Although a major nuclear component of both certain amitotic terminally differentiated cells and echinoderm sperm, no structural signatures for the more highly folded forms of the fiber have been detected in either mitotic chromosomes or interphase mammalian nuclei. Structurally, the helical form of the 30-nm fiber is well adapted to respond to the torsional (*14*) and tensional (*15*) forces generated by a transcribing RNA polymerase but not necessarily to the assumed predominantly tensional

forces operating during mitosis. In this context, the pervasively depicted mechanism of chromatin compaction assuming an ordered hierarchical folding should perhaps be discarded. Instead, the unwound state of the 30-nm chromatin fiber containing the linker histone could adopt alternative modes of nucleosome stacking—either a helix corresponding to the canonical 30-nm fiber or a network of more continuous stacks containing nucleosomes from one, or even several, individual fibers (see the figure).

The details of the structure elucidated by Song *et al*. raise several important questions. Does it correspond to the "native" 30-nm fiber with fewer nucleosomes per turn or to an alternative structure? And does unwinding of the fiber involve change to

internucleosomal interactions? The alternating stacking suggests the potential for fine-tuning epigenetic marks and array organization. A prime candidate for this would be the interface of the globular domains of the linker histone within the tetranucleosomal unit. Similarly, the details of the epigenetics and the transition to mitotic chromatin are poorly understood. These, and related, questions should ensure that, despite its purported demise, the 30-nm fiber, in whatever form, will continue to be a structure of intense interest for biologists.

References
1. J. T. Finch, A. Klug, *Proc. Natl. Acad. Sci. U.S.A.* **73**, 1897 (1976).
2. P. T. Lowary, J. Widom, *J. Mol. Biol.* **276**, 19 (1998).
3. F. Song *et al.*, *Science* **344**, 376 (2014).
4. T. Schalch, S. Duda, D. F. Sargent, T. J. Richmond, *Nature* **436**, 138 (2005).
5. D. Z. Staynov, *Nucleic Acids Res.* **28**, 3092 (2000).
6. P. J. J. Robinson, L. Fairall, V. A. Huynh, D. Rhodes, *Proc. Natl. Acad. Sci. U.S.A.* **103**, 6506 (2006).
7. D. Z. Staynov, C. Crane-Robinson, *EMBO J.* **7**, 3685 (1988).
8. S. H. Syed et al., *Proc. Natl. Acad. Sci. U.S.A.* **107**, 9620 (2010).
9. L. Fan, V. A. Roberts, *Proc. Natl. Acad. Sci. U.S.A.* **103**, 8384 (2006).
10. A. C. Lennard, J. O. Thomas, *EMBO J.* **4**, 3455 (1985).
11. F. Livolant *et al.*, *Philos. Trans. A Math. Phys. Eng. Sci.* **364**, 2615 (2006).
12. M. P. Scheffer, M. Eltsov, J. Bednar, A. S. Frangakis, *J. Struct. Biol.* **178**, 207 (2012).
13. E. Fussner *et al.*, *Trends Biochem. Sci.* **36**, 1 (2011).
14. P. Recouvreux *et al.*, *Biophys. J.* **100**, 2726 (2011).
15. Y. Cui, C. Bustamante, *Proc. Natl. Acad. Sci. U.S.A.* **97**, 127 (2000).

NEUROSCIENCE

Mapping Neural Activation onto Behavior in an Entire Animal

A combination of technologies reveals which neurons constitute circuits for specific behaviors in *Drosophila* larvae.

Timothy O'Leary and Eve Marder

For almost a century, neuroscientists have tried to understand how patterns of neuronal activity generate behavior. Many of the early studies turned to the "simple" systems of invertebrates in the hope of discovering the components of circuits and their connections. A striking finding was the existence of "command neurons" in arthropods and molluscs that produce complex and coordinated movements when stimulated (*1*, *2*). The challenge was then to identify the connections between these neurons and other neurons important for those behaviors. This approach was always limited to examining only a few neurons from the tens or hundreds of thousands in the animal (*3*). On page 386 of this issue, Vogelstein *et al*. (*4*) usher in a new era of integrated methods for deciphering how an entire nervous system generates behavior.

The nervous systems of even simple organisms like the fruit fly typically comprise thousands of densely interconnected neurons with a variety of specialized signaling properties. Mapping neural activity patterns onto behavior therefore requires unambiguous identification and control of small, distinct sets of neurons. Moreover,

Volen Center and Biology Department, Brandeis University, Waltham, MA 02453, USA. E-mail: marder@brandeis.edu
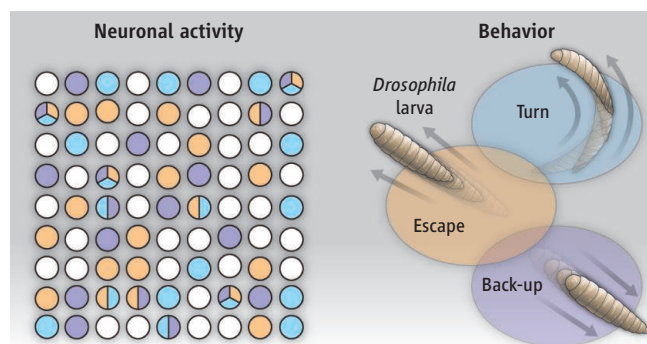
Neurons and behavior. Neural activity induced in single cells (**left**) is associated with behavioral output (**right**), shown in the color-coded schematic. In general, this relationship is probabilistic and not necessarily one-to-one: Multiple behaviors can be associated with activation of the same neurons and multiple neurons can trigger the same behavior.

the behavioral repertoire itself is complex—how many different "behaviors" does an animal have? Can they be delineated in a principled, practical way?

Three new technologies enabled Vogelstein *et al*. to attack these questions in a way that was unimaginable only a few years ago. Genetic tools (*5*) developed in *Drosophila melanogaster* enable reliable genetic tagging of the same sets of neurons in different animals. Optogenetics, in particular light-activated ion channels (*6*), allow precisely timed, noninvasive activation and deactivation of individual neurons. And advances in machine learning algorithms and computer hardware facilitate the daunting task of turning thousands of hours of video-recorded behavior into a manageable

data set. What makes the study of Vogelstein *et al*. unique and important is that it successfully combines these technologies to analyze the function of an entire nervous system.

Over 1000 different genetic lines of *Drosophila* were used to target specific neurons in the larval nervous system. Vogelstein *et al*. then systematically stimulated the identified neurons and recorded behavioral output, resulting in a large data set. A key step in handling the data was to reduce their dimension in a way that preserved features (such as forward-backward locomotion and body curvature) such that they could be sorted by an unsupervised classification algorithm into distinct classes of behaviors (see the figure).

The advantage of unsupervised learning is that one does not require training examples (usually human-curated), which can be time consuming to generate and may be subject to human bias or error. Instead, such algorithms find inherent structures or clusters in the data, which can be interpreted as meaningful (e.g., distinct behavioral states). A potential disadvantage is that although such learning algorithms do not have human bias, they necessarily contain bias in their underlying assumptions and parameters. Vogelstein *et al*. carefully validated their analysis post-hoc, finding several identifiable behaviors including turning, escaping, and backing up.

Interestingly, repeated stimulation of the same neurons on different trials did not always elicit the same behavior. For example, in single animals, the activation of a neuron produced "left-right-avoid" in some trials and "straight escape" behaviors in others. Similarly, an identified neuron-behavior relation did not always hold between animals. Specific neurons sometimes evoked turning whereas in other animals they evoked reversal of motion. In general, the relationships between neural activation and

behavior were best characterized as probabilistic rather than deterministic. Aside from noise, two generic features of nervous systems can explain this. One aspect is that the effect of an input, or activation of a neuron or circuit, is often state-dependent—in other words, what the rest of the circuit is doing can determine the effect of a repeated activity perturbation in a subset of neurons. The other feature is that all nervous systems—even those with genetically identifiable neurons—are unique to each individual due to phenotypic variability and environmental fluctuations.

One limitation of the approach taken by Vogelstein *et al*. is that strong, stereotyped stimulation of single neurons is not likely to mimic in vivo activity patterns, nor does it capture the coordinated activation of multiple neurons and the relative strengths and timings of their activation. As a consequence, the data in this study provide a fabulous starting point for understanding which neurons are likely to participate in the circuits for one or many behaviors. But truly understanding how these circuits work will require the marriage of these new approaches with a wiring diagram, or so-called "connectome" (*7*), as

well as characterizing relevant physiological properties of the neurons themselves. This will then allow the manipulation of multiple circuit elements to test specific ideas about how these circuits work.

Vogelstein *et al*. have thus achieved a technical, multidisciplinary tour de force that will provide a rich source of research questions. The next big challenge is developing coherent theory to make sense of the data. Machine learning and computational models are likely to be important in this endeavor, pointing to a growing and intriguing symbiosis between computational and experimental neuroscience, both for data analysis and theory development.

References
1. C. A. Wiersma, K. Ikeda, *Comp. Biochem. Physiol.* **12**, 509 (1964).
2. I. Kupfermann, K. R. Weiss, *Behav. Brain Sci.* **1**, 3 (1978).
3. E. Marder, R. L. Calabrese, *Physiol. Rev.* **76**, 687 (1996).
4. J. T. Vogelstein *et al*., *Science* **344**, 386 (2014); 10.1126/science.1250298
5. B. D. Pfeiffer *et al*., *Proc. Natl. Acad. Sci. U.S.A.* **105**, 9715 (2008).
6. A. Fiala, A. Suska, O. M. Schlüter, *Curr. Biol.* **20**, R897 (2010).
7. C. I. Bargmann, E. Marder, *Nat. Methods* **10**, 483 (2013).

GEOCHEMISTRY

Carbon Storage in Basalt

Field projects are beginning to demonstrate the potential for carbon storage in basaltic rocks.

Sigurdur R. Gislason[1] and Eric H. Oelkers[2,3]

All the carbon in the atmosphere, living creatures, and dissolved in the oceans is derived from rocks and will eventually end up in rocks, the largest carbon reservoir on Earth. The carbon moves from one reservoir to another in what is called the carbon cycle (*1*). Humans have accelerated this cycle by mining and burning fossil fuel since the beginning of the industrial revolution, causing rising atmospheric carbon dioxide (CO_2) concentrations that are the main cause of global warming. One option for mitigating high levels of global warming is to capture CO_2 and safely store it for thousands of years or longer in subsurface rocks. By accelerating carbonate mineral formation in these rocks, it is possible to

rebalance the global carbon cycle, providing a long-term carbon storage solution. However, this approach is both technically challenging and economically expensive.

Most subsurface carbon storage projects to date have injected CO_2 into large sedimentary basins. Perhaps the best known of these projects is that at Sleipner, west of Norway, where about 1 million metric tons of CO_2 have been injected annually since 1996 and stored more than 700 m below the ocean floor in the Utsira sandstone. However, the transformation of CO_2 to carbonate minerals in such systems, referred to as mineral trapping, takes tens of thousands of years, if it occurs at all (see the figure, panel A) (*2*). This limitation results from both the low reactivity of silicate minerals in sedimentary rocks and a lack of the calcium, magnesium, and iron required to make carbonate minerals.

An alternative, designed to overcome these limitations, is the injection of CO_2 into

reactive basaltic rocks. This approach has several advantages. Basalt contains about 25% by weight of calcium, magnesium, and iron oxides (*3*). Basaltic rocks are also far more reactive in water than are sedimentary silicate rocks, and the metals contained in basalts are therefore readily available to combine with injected CO_2 to form carbonate minerals (*3–5*). And basaltic rocks are abundant on Earth's surface; ~10% of the continents and much of the ocean floor is composed of basalt (*4, 6*). Basalt carbonation could therefore become an important carbon storage solution. However, one challenge to storing carbon in both sedimentary and basaltic rocks is the buoyancy of CO_2, which could cause it to rise toward Earth's surface through pores and fractures, eventually escaping back to the atmosphere.

Two ongoing field injection projects are assessing the feasibility of carbon storage in basalts: the CarbFix project in southwest Iceland (*4, 7*), where carbon injection started

[1]Institute of Earth Sciences, University of Iceland, Sturlugata 7 Reykjavík, 101 Iceland. [2]GET-UMR 5563 CNRS, Université Paul-Sabatier IRD, 14, Avenue Edouard Belin, Toulouse, 31400 France. [3]Earth Sciences, University College London, WC1E 6BT London, UK. E-mail: sigrg@hi.is; eric.oelkers@get.obs-mip.fr
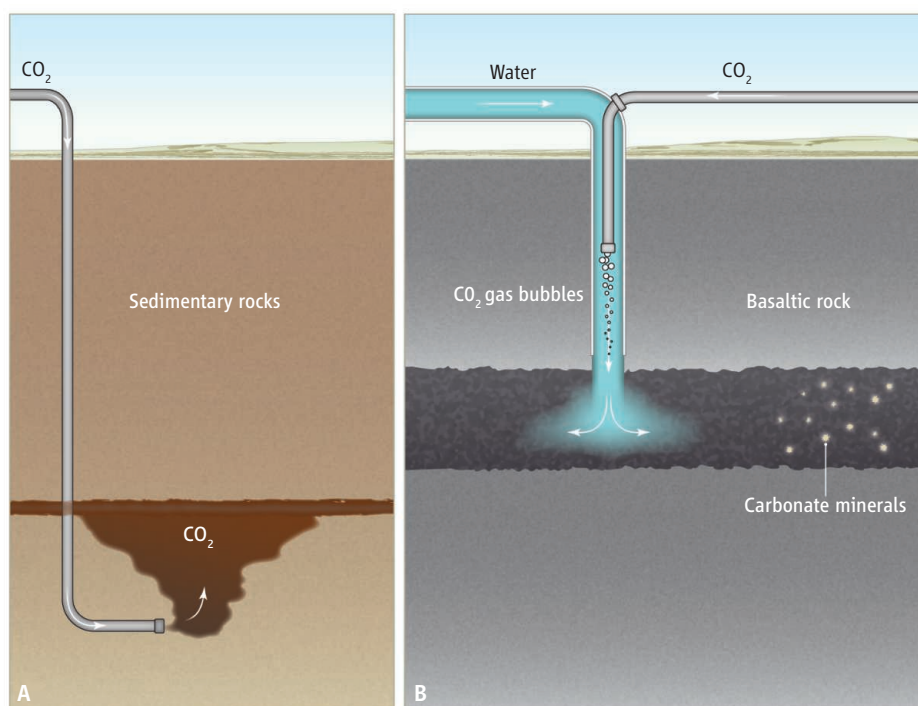
Carbon storage in sedimentary basins and basaltic rocks. (**A**) Carbon storage in sedimentary basins proceeds via the injection of pure CO_2 into porous sedimentary rocks. Ideally this CO_2 is trapped below an impermeable cap rock. Eventually some of this CO_2 becomes stuck in small pores, limiting its mobility (structural and residual trapping) (*15*). Over time, CO_2 dissolves in the formation water (solubility trapping). Some of this dissolved CO_2 reacts to form stable carbonate minerals (mineral trapping). As one progresses from structural to mineral trapping, the CO_2 becomes more immobile and thus the storage more secure, though this process can take thousands of years or more (*15*). (**B**) In the CarbFix method, CO_2 is dissolved into water during its injection into porous basaltic rocks. No cap rock is required because the dissolved CO_2 is not buoyant and does not migrate back to the surface. Solubility trapping occurs immediately, and the bulk of the carbon is trapped in minerals within 1 year (*10*, *11*).

in January 2012, and the Big Sky Carbon Sequestration Partnership (BSCP) in the northwest United States near Wallula, Washington, where injection started in July 2013 (*8*, *9*). A major difference between these two projects is the method through which the CO_2 is injected. In the BSCP project, pure CO_2 is injected as a separate buoyant phase into a porous basaltic layer at more than 800-m depth; it is anticipated that the presence of an impermeable layer will keep the CO_2 from escaping back to the surface. In the CarbFix project, CO_2 is released as small bubbles at 350-m depth into down-flowing water within the injection well. The CO_2 bubbles dissolve in the water before it enters the rock. Once dissolved in water, CO_2 is no longer buoyant, and the CO_2-charged water accelerates metal release from basalt and formation of solid carbonate minerals. Once stored as a mineral, the CO_2 is immobilized for geological time scales. More than 80% of CO_2 injected into the CarbFix injection site was carbonated within a year at 20° to 50°C and 500- to 800-m depth [(*10*, *11*); see the figure, panel B]. This result suggests that the

CarbFix method can change the time scale of mineral carbon trapping considerably.

The CarbFix method requires substantial water; only 5% of the injected mass is CO_2. Porous basalts near the continental margins have huge storage capacities adjacent to nearly unlimited supplies of seawater. On the continents, the water present in the target storage formation can be pumped up and used to dissolve CO_2 during the injection. Although the pumping of water from the subsurface may increase costs, water pumping is also necessary during the later stages of pure CO_2 injection into sedimentary basins, when a large portion of the pore space has been filled with CO_2.

A major challenge to all carbon capture and storage projects is the cost. The estimated cost of storing and transporting a ton of CO_2 at maximum reservoir exploitation at the CarbFix site via dissolved water injection is about $17 (*12*); this cost is about twice that of geologic storage via direct CO_2 injection at the BSCP site and in typical sedimentary basins (*9*, *12*, *13*), but offers enhanced security because CO_2 dissolved in

water is not buoyant. However, the cost of carbon capture and storage is dominated by capture and gas separation, which costs $55 to $112/ton CO_2 (*13*). In contrast, the current price for a ton of CO_2 emission at the European Union Emission Trading Scheme, the world's largest carbon market, is about $7/ton CO_2. Until either market forces or taxes result in a higher price on carbon emission, there is no financial incentive for carbon capture and storage using any of these technologies.

Carbon storage via basaltic rock carbonation is still in its infancy, but if it can be scaled up, it may provide a more secure alternative to the injection of pure CO_2 into sedimentary basins. Natural analogs have shown that up to 70 kg of CO_2 can be stored in a cubic meter of basaltic rock (*14*). This means that the storage potential of all the ocean ridges is an order of magnitude larger than the estimated CO_2 emissions stemming from burning all fossil fuel resources on Earth. How much of this storage potential will be of practical use in the future may depend more on political will and economic realities than on scientific efforts.

References and Notes
1. D. Archer, *J. Geophys. Res.* **110**, C09S05 (2005).
2. S. M. V. Gilfillan *et al.*, *Nature* **458**, 614 (2009).
3. T. Schaef, B. P. McGrail, A. T. Owen, *Int. J. Greenh. Gas Control* **4**, 249 (2010).
4. S. R. Gislason *et al.*, *Int. J. Greenh. Gas Control* **4**, 537 (2010).
5. R. J. Rosenbauer, B. Thomas, J. L. Bischoff, J. Palandri, *Geochim. Cosmochim. Acta* **89**, 116 (2012).
6. D. S. Goldberg, T. Takahashi, A. L. Slagle, *Proc. Natl. Acad. Sci. U.S.A.* **105**, 9920 (2008).
7. E. S. Aradóttir, E. Sonnenthal, G. Bjornsson, H. Jonsson, *Int. J. Greenh. Gas Control* **9**, 24 (2012).
8. B. P. McGrail, F. A. Spane, E. C. Sullivan, D. H. Bacon, G. Hund, *Energy Procedia* **4**, 5653 (2011).
9. B. P. McGrail *et al.*, *Int. J. Greenh. Gas Control* **9**, 91 (2012).
10. S. R. Gislason *et al.*, *Min. Mag. (Lond.)* **77**, 1178 (2013).
11. J. M. Matter *et al.*, American Geophysical Union Fall Meeting, abstract V41A-2753 (2013).
12. E. Ragnheidardottir, H. Sigurdardottir, H. Kristjansdottir, W. Harvey, *Int. J. Greenh. Gas Control* **5**, 1065 (2011).
13. Global CCS Institute, Economic Assessment of Carbon Capture and Storage Technologies: 2011 Update; see www.globalccsinstitute.com/publications/economic-assessment-carbon-capture-and-storage-technologies-2011-update (2011).
14. F. Wiese, Th. Fridriksson, H. Ármannsson, *Tech. Rep., ÍSOR-2008/003*, Iceland Geosurvey, www.os.is/gogn/Skyrslur/ISOR-2008/ISOR-2008-003.pdf (2008).
15. S. Benson *et al.*, in *IPCC Special Report on Carbon Dioxide Capture and Storage,* B. Metz, O. Davidson, H. Coninck, M. Loos, L. Meyer, Eds. (Cambridge Univ. Press, New York, 2005), pp. 195–276.

Partners in science. At the Cuban Academy of Sciences headquarters, Alan I. Leshner, Gerald Fink, Ismael Clark Arxer, president of the CAS, and Sergio Jorge Pastrana stand before a sculpture of the famous Cuban scientist Carlos Finlay. (Above) A street scene outside Havana.

SCIENCE DIPLOMACY

AAAS Signs Historic Agreement with Cuban Academy of Sciences

HAVANA, CUBA—In an elegant meeting room of the 84-year-old Hotel Nacional, where mobsters and movie stars once rubbed shoulders with intellectuals and heads of state, the leaders of AAAS and the Cuban Academy of Sciences this month signed a landmark agreement to advance scientific cooperation by Cuban and U.S. scientists in key areas of mutual interest to both countries.

The signing of the memorandum of understanding followed 2 days of meetings between a AAAS-organized group and a broad assortment of scientists and physicians across Havana. The group also met with the Chief of Mission of the U.S. Interests Section there, who expressed his support for the visit.

"This trip was a wonderful opportunity to reinvigorate the long-standing friendship between U.S. and Cuban scientists and to form a specific plan of action," said AAAS President Gerald Fink, who is also a professor of biology at the Whitehead Institute at MIT.

The memorandum identifies four areas in the life sciences where AAAS and the Cuban Academy of Sciences will seek opportunities for sustained cooperation: emerging infectious diseases, brain disorders, cancer, and antimicrobial drug resistance.

Merely 45 minutes from Miami by plane, Cuba is a natural choice for scientific partnerships with the United States. The country has committed a large amount of its resources to its scientific, medical, and public health systems, including a hardy biotechnology industry that exports a number of vaccines, antibody-based drugs, and other biomedical technologies.

While greater longevity is typically associated with wealthier populations, life expectancy in Cuba rivals that in the United States. "Cuban people live as poor people but die as rich people," said Luís Herrera Martínez, director general of the Center for Genetic Engineering and Biotechnology in Havana. Cuba could thus be fertile ground for research on aging populations and the diseases that affect them, such as cancer or age-related neurodegenerative diseases.

The Cubans are also well positioned to detect emerging infectious diseases of concern to the United States, such as dengue and chikungunya, serious mosquito-borne viral diseases for which no vaccines exist. Officials at the Hermanos Ameijeiras hospital in Havana told the U.S. group that Cuba has already implemented surveillance measures for chikungunya, which has just turned up in the Caribbean in recent months. The virus is spreading rapidly in the region, raising fears among U.S. public health experts that it may soon make an appearance in the U.S.

The obstacles to scientific collaboration are formidable, however. The Cuban economy, which crashed after the dissolution of the Soviet Union, is still faltering despite modest economic reforms in recent years. And, in addition to blocking U.S. federal research funding from reaching Cuban scientists, the U.S. embargo has imposed other constraints on the scientific enterprise. Throughout the visit, several researchers voiced frustration that U.S. researchers could not attend most of the scientific meetings that take place in Cuba.

While the effects of the diplomatic impasse between Cuba and the United States largely will require political solutions, the agreement between AAAS and the Cuban Academy of Sciences signals a joint desire for scientific cooperation to move forward.

"In spite of existing political differences, scientists can always get together and talk. With this signing, we are providing support for communities dealing with very similar problems," said Sergio Jorge Pastrana, foreign secretary and executive director of the Cuban Academy of Sciences.

The AAAS group included Alan I. Leshner, chief executive officer of AAAS and executive publisher of *Science*; Peter Agre, Nobel laureate and past president of AAAS; Vaughan Turekian, AAAS' chief international officer; and several other scientists and policy experts.

–KATHY WREN

CREDIT: K. WREN/AAAS

Cryo-EM Study of the Chromatin Fiber Reveals a Double Helix Twisted by Tetranucleosomal Units

Feng Song,[1,2]* Ping Chen,[1]* Dapeng Sun,[1,2] Mingzhu Wang,[1] Liping Dong,[1,2] Dan Liang,[1,2] Rui-Ming Xu,[1] Ping Zhu,[1]† Guohong Li[1]†

The hierarchical packaging of eukaryotic chromatin plays a central role in transcriptional regulation and other DNA-related biological processes. Here, we report the 11-angstrom–resolution cryogenic electron microscopy (cryo-EM) structures of 30-nanometer chromatin fibers reconstituted in the presence of linker histone H1 and with different nucleosome repeat lengths. The structures show a histone H1-dependent left-handed twist of the repeating tetranucleosomal structural units, within which the four nucleosomes zigzag back and forth with a straight linker DNA. The asymmetric binding and the location of histone H1 in chromatin play a role in the formation of the 30-nanometer fiber. Our results provide mechanistic insights into how nucleosomes compact into higher-order chromatin fibers.

Understanding the structure of chromatin is key to illuminating the functions of chromatin dynamics in epigenetic regulation of gene expression. The structure of the native 30-nm chromatin fiber in nuclei or isolated from nuclei is a regular helix of nucleosomes with a diameter of about 30 nm and a packing density of about 6 to 7 nucleosomes per 11 nm (1–7). Nucleosomes can be arranged either linearly in a one-start solenoid-type helix with bent linker DNA or zigzag back and forth in a two-start stack of nucleosomes connected by a relatively straight DNA linker (7–9). The latter class can be further divided into the helical ribbon model and the twisted crossed-linker model by the different orientation angles between the linker DNA and fiber axes (8–10). The manner by which nucleosome core particles (NCPs) interact with each other in a beads-on-a-string nucleosomal array to form a condensed 30-nm chromatin fiber remains unresolved (11). The irregular native chromatin fiber cannot readily form a homogeneous structure suitable for high-resolution structural analyses. The problem has been partially addressed by reconstituting chromatin fibers in vitro on regular tandem repeats of unique nucleosome-positioning DNA sequences with purified histone proteins (12, 13). Fibers reconstituted in the presence of histone H5 with different nucleosome repeat lengths (NRLs) showed similar structures and could fit the one-start interdigitated solenoid structure (14). Chromatin fiber with two-start zigzag conformation was also observed on long reconstituted nucleosome arrays (15). The x-ray crystal structure of a tetranucleosome with a 20–base pair (bp) linker DNA and without linker histones reveals two stacks of nucleosomes connected by straight linker DNA (16); however, a tetranucleosomal array is too short to form a solenoid structure. Linker histones, which are present at close to one molecule per nucleosome in the majority of eukaryotic organisms, have been considered to be essential for 30-nm chromatin fiber formation (17–20), but their precise location and exact roles in the organization of the higher-order structure still remain to be determined.

Cryo-EM Reconstruction of 30-nm Chromatin Fibers

We have determined, at about 11 Å resolution, a three-dimensional (3D) cryogenic electron microscopy (cryo-EM) structure of 30-nm chromatin fibers reconstituted in vitro on the 12 tandem repeats of 187-bp and 177-bp (12 × 187 bp and 12 × 177 bp) 601 DNA sequence with recombinant *Xenopus laevis* canonical histones lacking post-translational modifications (Fig. 1). The reconstituted 30-nm fibers are in a compact form in the presence of histone H1 with stoichiometry about one H1 per nucleosome under low-salt conditions (fig. S1). The reconstituted chromatin fibers were fixed by 0.2% glutaraldehyde before cryo-EM analysis and displayed as homogeneously compacted particles in the representative field views of the cryo-EM images (Fig. 1A). About 31,000 particles of 12 × 187 bp and 25,000 particles of 12 × 177 bp 30-nm fibers were visually screened and subjected to 2D classification and 3D reconstruction, beginning with an initial model of a featureless Gaussian blob (fig. S2A). The Euler angle distribution indicates that the particles used in our 3D reconstruction have no preferred orientation (fig. S2B). Some selected unsupervised 2D classification averages (Fig. 1A, right) agree well with the raw particles, as indicated by the white box in the micrograph (Fig. 1A, left). The 3D cryo-EM map defines the spatial location of all individual nucleosomes and the path of linker DNA in the 30-nm fiber (Fig. 1, B and C, and movie S1). The overall structure of the dodecanucleosomal 30-nm fiber comprises three tetranucleosomal structural units, which are twisted against each other with linker DNA extended straight to form a two-start helix (Fig. 1, B and D). This disposition can also be deduced from the particularly oriented reference-free average, in which obvious densities connect two adjacent nucleosomes (Fig. 1A, right, white dashed brackets indicated). The four nucleosomes within the structural unit zigzag back and forth to form two stacks of two nucleosome cores (Fig. 1D), which is consistent with the previous observations that deoxyribonuclease I digestion of nuclei produces dinucleosomal periodicity patterns (21). According to the previously proposed zigzag two-start helix model, the diameter of the chromatin fiber could be increased accordingly with the length of DNA crossing back and forth between the two-start helix (8–10). To analyze how the variations in NRLs affect the overall structure of the resulting fibers, we compared the 3D cryo-EM structures of 30-nm fibers reconstituted with two different NRLs, that is, 12 × 187 bp and 12 × 177 bp 601 DNA sequences (Fig. 1C and fig. S2). The two 30-nm fibers with 177-bp NRL and 187-bp NRL display a very similar overall stacking mode of nucleosomes with the connected linker DNAs extended and straight. An increase of 10 bp of NRL does not affect the overall structure and organization of the reconstituted chromatin fiber, but the increase does change the fiber dimension (diameter × height) from about 27.2 × 28.7 nm for 177-bp repeats to about 29.9 × 27.0 nm for 187-bp repeats (Fig. 1C), which is consistent with a basic zigzag two-start helix model. Overall, our cryo-EM structure shows that the 30-nm chromatin fiber follows a path that is basically compatible with a zigzag two-start helix (Fig. 1D), although the fine details of the structure are distinct from the originally proposed model.

Tetranucleosomal Unit with a Two-Start Zigzag Conformation

Within the tetranucleosomal structural unit of the 30-nm fiber, two stacks of two nucleosome cores are connected by straight linker DNA (Fig. 2A and fig. S3C). The two nucleosomes in each stack directly contact head to head through their octamer surfaces. For the structural unit with a 187-bp NRL, the two stacked nucleosome cores are separated center to center by 53.6 Å with each superhelical axis and dyad axis angled at 11.8° and 16.5°, respectively (Fig. 2A, left). In the interface between the cores, a bulk density is present at the junction of the adjacent H2A-H2B dimer, indicating a strong interaction between the H2B-helix α1/αC and the adjacent H2A-helix α2 (Fig. 2B). As described in the x-ray structure of the tetranucleosome, this strong interacting interface does not allow the internucleosomal interaction between the positive N terminus of histone H4

[1]National Laboratory of Biomacromolecules, Institute of Biophysics, Chinese Academy of Sciences, Beijing 100101, China. [2]University of Chinese Academy of Sciences, Beijing 100049, China.

*These authors contributed equally to this work.
†Corresponding author. E-mail: liguohong@ibp.ac.cn (G.L.); zhup@ibp.ac.cn (P.Z.)

(amino acids 16 to 26) and the acidic patch of the H2A-H2B dimer observed in the nucleosome core-particle structure (16). The H2B-α3/αC internucleosomal four-helix bundle might be involved in the compaction and stabilization of chromatin fiber (22), which was not observed in our cryo-EM map of reconstituted chromatin fiber, presumably because of the interaction of DNA involved in chromatin reconstitutions.

The two dinucleosomal stacks are separated by 196 Å center to center and are rotated 54.5° left-handed with respect to their stack axes (the axis passing through the centers of the two nucleosomes in each stack) for the 187-bp NRL (Fig. 2A, right). We docked the x-ray atomic structure of the 167-bp NRL in the absence of linker histone (16) into the EM density map of our tetranucleosomal structural units with 187- and 177-bp NRLs, respectively (Fig. 2B and fig. S3C). The structures for each stack of two nucleosomes fit very well with our cryo-EM map in both cases. However, the distance and rotation between the two stacks are quite different, which may be caused by the presence of histone H1 or the different NRLs used. The two stacks are separated by 146.1 Å for the tetranucleosome with the 167-bp NRL used for x-ray investigation, compared with 167 Å for the 177-bp NRL (fig. S3C) and 196 Å for the 187-bp NRL (Fig. 2A) in this study, confirming that the fiber diameters change accordingly to the lengths of the NRLs. In addition, the rotation between the two stacks in the x-ray structure is left-handed by 71.3°, compared with 63.7° for the 177-bp NRL and 54.5°

for the 187-bp NRL in our cryo-EM structure (Fig. 2 and fig. S3). If we only consider the intrinsic property of the difference in NRLs, each 10-bp increment in linker DNA should increase the length of DNA by 3.4 nm and change the twist between adjacent nucleosomes by −17 based on the DNA twist of 10.5 bp per turn, suggesting that the presence of H1 may impose additional effects on the specific distance and the rotation of the two stacks in our cryo-EM structure (Fig. 3A). The defined location of H1 in each nucleosome, as indicated in Fig. 3B, reveals that the direct interaction of H1 with both the dyad and the entering and exiting DNA in the NCPs may alter the angle of the entry-exit DNA and constrain the linker length and rotation angle between the stacks.

Twist and Interactions Between Tetranucleosomal Units

For the dodecanucleosomal 30-nm chromatin fiber, we define three structural units as unit 1 for nucleosomes N1 to N4, unit 2 for N5 to N8, and unit 3 for N9 to N12. The rotation angles and the separation distances between units 1 and 2 and between units 2 and 3 are slightly different, which may be a result of the end effect of the dodecanucleosomal chromatin fiber. In the cryo-EM structure of the 30-nm fiber with the 187-bp NRL, units 1 and 2 are related by a 48.9° rotation around the fiber axis and a 72.2 Å translation along the axis, whereas a 52.9° rotation and a 68.8 Å translation were observed for units 2 and 3. Here, the fiber axis is defined as the axis bisecting the angle

between the two stack axes and orthogonally intersecting the axis connecting the centers of the two stacks in each structural unit. The internucleosomal interactions between the structural units are different from that observed within the tetranucleosomal units. The internucleosomal interface between the structural units displays relatively strong density where the N terminus of H4 meets the adjacent H2A-H2B dimer (Fig. 3C), which indicates that the internucleosomal interactions between the positively charged residues of the H4 N-terminal tail (residues 16 to 23) and the acidic patch of the H2A-H2B dimer may account for the twist between the tetranucleosomal units. The interactions within this region were not observed in the previous x-ray tetranucleosome structure (16), but these interactions have been reported to be crucial for the formation of the 30-nm chromatin fibers (15, 23). We generated a series of single mutants in the H4 N-terminal tail, including H4 Lys^{16}→Ala^{16} (K16A), H4R17A (R, Arg), H4R19A, H4K20A, and H4R23A, to examine the functions of these residues in chromatin folding in the presence of histone H1 (fig. S4). Sedimentation velocity in conjunction with van Holde–Weischet analysis was used to identify the structural changes in the chromatin fibers. The 30-nm chromatin fibers containing H4K16A, H4R17A, H4R19A, or H4K20A showed very similar distributions of sedimentation coefficients in comparison with those of the wild-type fibers with a S_{ave} of $46.6S \pm 1.7S$ (where S_{ave} is defined as the sedimentation coefficient at the boundary fraction equal to 50%). However, the chromatin
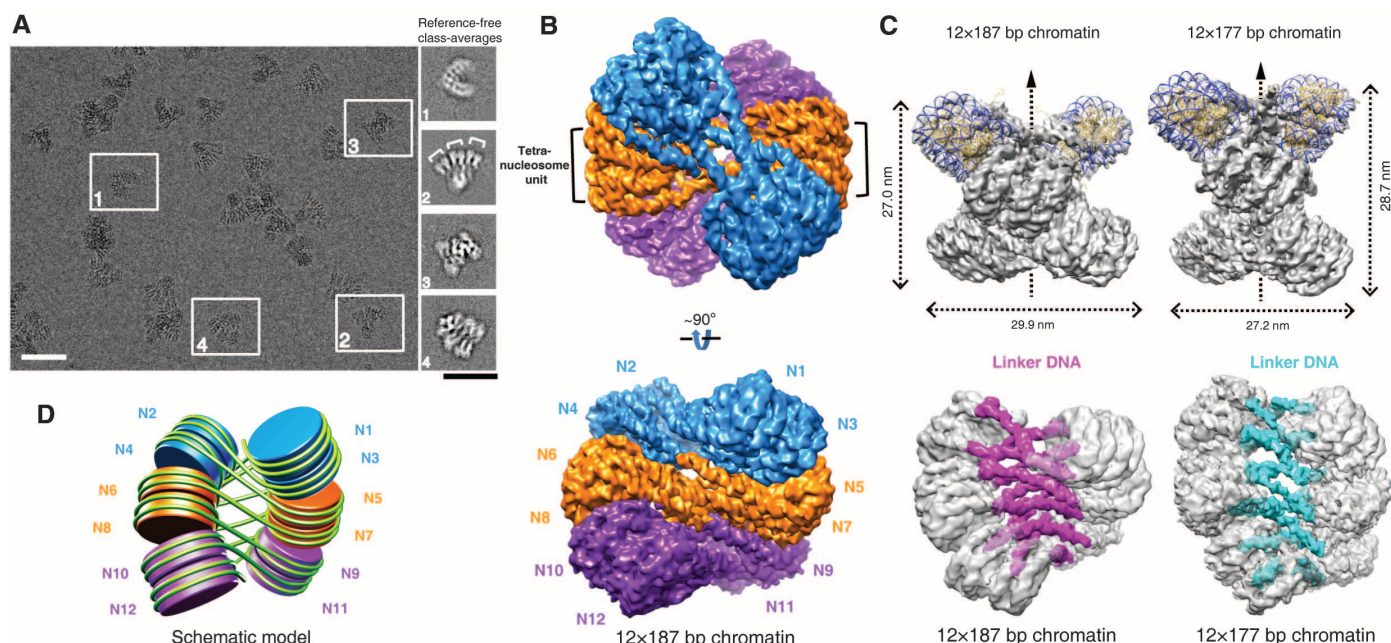
Fig. 1. Cryo-EM reconstruction of 30-nm chromatin fibers. (**A**) A representative cryo-EM micrograph of 30-nm chromatin fibers reconstituted on 12 × 187 bp DNA. Scale bars indicate 50 nm. Four selected unsupervised classification generated averages are shown in the right images, which are in good agreement with the raw particles indicated by white boxes in the micrograph. (**B**) The overall 3D cryo-EM map of the 30-nm chromatin fibers reconstituted on 12 × 187 bp DNA with the three tetranucleosomal structural units highlighted by different colors and viewed from two angles. (**C**) A comparison of the overall structure of 30-nm chromatin fibers reconstituted on 12 × 187 bp and 12 × 177 bp DNA, viewed from two angles with the fiber dimensions directly labeled and their straight linker DNA highlighted. (**D**) A schematic representation of the cryo-EM structure of 30-nm chromatin fibers as shown in (B).

fibers containing H4R23A shifted the sedimentation coefficient distribution to a S_{ave} of 50.8S (fig. S4, B and C), which indicated that the chromatin containing H4R23A could still fold into a compact structure but that the mutant H4R23A might alter the chromatin folding mode. Cryo-EM images and the corresponding reference-free class averages of the H4R23A 30-nm fibers showed that the particles appeared much more frequently as two parallel stacks of nucleosomes than the wild-type fibers and with more blurred averages (Fig. 3, D and E). The results suggest that the mutant H4R23A changes the internucleosomal interactions between the structural units and makes it difficult for the tetranucleosomal units to twist stably against each other to form a helical structure.

The Asymmetric Location and Self-Association of Histone H1 in Chromatin Fiber

The incorporation of histone H1 plays a fundamental role in determining the higher-order structure of the 30-nm chromatin fiber. As shown in Fig. 3A and figs. S1 and S5A, histone H1 in the 30-nm fibers exhibit a proper 1:1 stoichiometric association with the nucleosome cores. The well-defined locations of the 12 histone H1 molecules in the dodecanucleosomal 30-nm fiber can be visualized in our cryo-EM structure (Fig. 3A, fig. S5A, and movie S2). In each nucleosome core, histone H1 directly interacts with both the dyad and the entering and exiting linker DNA (Fig. 3B), which determines the trajectory of the entry or exit linker DNA segments in nucleosomes and stabilizes the fiber. This interaction mode of histone H1 with the nucleosome core has been proposed previously (20, 24–26). In addition, an
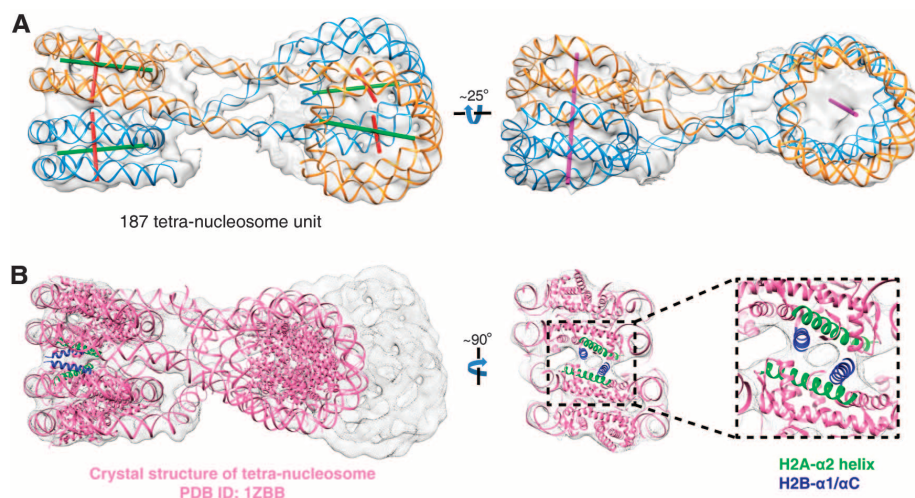
Fig. 2. The structure of a tetranucleosomal unit with the 187-bp NRL. (**A**) The segmented density map for the tetranucleosomal unit in the 30-nm chromatin fibers reconstituted on 12 × 187 bp DNA, shown with the atomic structure of DNA from a docked mononucleosome crystal structure (PDB 1AOI) and modeled presumptive linker DNA and viewed from two angles. Different axes are highlighted by colors, including nucleosome core dyad (green), nucleosome superhelix axes (red), and stack axes (pink). (**B**) A comparison of the 3D cryo-EM map (gray) with the x-ray structure (PDB 1ZBB, pink) of the tetranucleosome (16). The strong density where the adjacent H2A-H2B dimer meets is magnified and highlighted in the interface between the nucleosome cores within each stack.
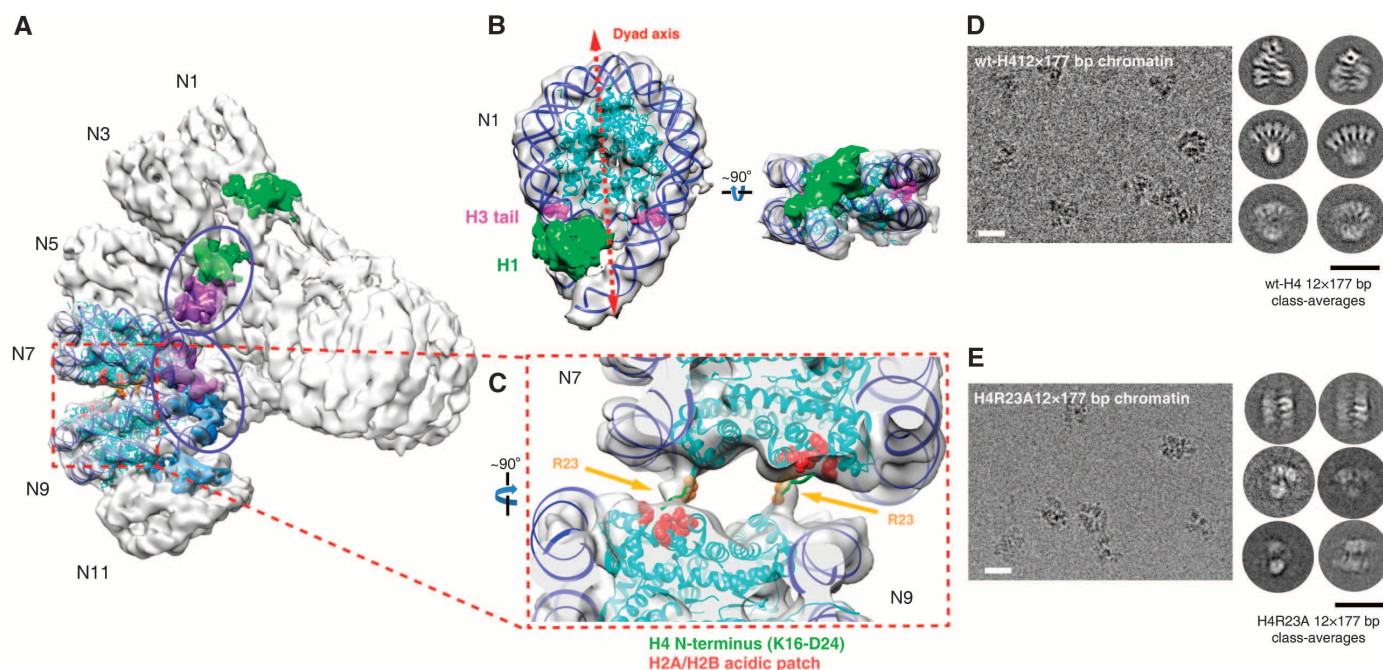
Fig. 3. The interactions between the tetranucleosomal units within the 30-nm fibers. (**A**) The tetranucleosomal units are twisted against each other to form 30-nm fibers. The locations of H1 are highlighted by colors. (**B**) The asymmetric location of H1 in the nucleosome core as viewed from two angles. The mononucleosome N1 segmented from the 12 × 187 bp map (A) with linker DNA density at both entry and exit regions is fitted with an atomic structure of the mononucleosome with an arbitrary length of linker DNA extracted from the tetranucleosome structure (PDB 1ZBB). The presumptive histone H1 is highlighted in green. The H3 tails in the x-ray structure are colored in magenta to locate their relative positions to H1. (**C**) Detail of the strong density where the N terminus of H4 meets the adjacent H2A-H2B dimer. (**D** and **E**) A comparison of the cryo-EM images of the particles and their related unsupervised classification generated averages for 30-nm chromatin fibers reconstituted with wild-type (wt)—H4 (D) and H4R23A (E), respectively. A subset of the wt-H4 12 × 177 bp data with the same particle number, 2664, as that of the H4R23A 12 × 177 data set were randomly picked from the entire data set and subjected to an independent unsupervised 2D classification for comparison. Scale bars, 30 nm.

apparent off-axis location of the globular domain of histone H1 not only in a mononucleosome (Fig. 3B) but also in a tetranucleosomal unit (Fig. 3A, fig. S5A, and movie S2) can be observed in our cryo-EM structure, and this domain localization plays a critical role in the formation of a twist between tetranucleosomal units. The asymmetric location of H1 in mononucleosomes results in the discrimination between different sides of a nucleosome, similar to a coin; we define the "head" as the side of nucleosome with the small portion of H1 and the "tail" as the side with the large portion of H1. The head-to-head nucleosomal interaction in each stack within each tetranucleosomal unit only permits the tail-to-tail nucleosomal interactions between tetranucleosomal units for further stacking and twisting of the chromatin fiber (Fig. 3A). The self-association of H1 had been reported to play an important role in the organization and stabilization of the 30-nm chromatin fiber (27). Our cryo-EM structure also revealed a previously unknown arrangement of histone H1 molecules in the reconstituted 30-nm chromatin fiber, in which only the large portions of H1 (most likely its global domain) on the tail side of nucleosomes can interact directly with each other and impart an additional twist between each structural unit (Fig. 3A and fig. S5A). The specific asymmetric binding and location of histone H1 in both mononucleosome and tetranucleosomal units determine the formation of the double-helical 30-nm fiber with a spiral twist of tetranucleosomal units. To further explore the interactions between histone H1 and nucleosomal DNAs, we extracted the densities of individual mononucleosomes with the presumptive H1 from the reconstructed map of the dodecanucleosomal chromatin fiber and averaged them on a 3D level (for details, see materials and methods). Guided by a rigid-body fitting, we found that the crystal structure of *Gallus gallus* histone H5 globular domain (gH5) [Protein Data Bank (PDB) code 1HST] can be docked well into a region, which is a part of the presumptive H1 density, in the averaged H1-containing mononucleosomal EM density map (fig. S5B). This region, most likely the globular domain of human histone H1.4 used in this study, interacts with the nucleosomal entry, exit, and dyad DNAs in a three-contact mode (fig. S5B, red dots), in agreement with the computational analysis of gH5 (28) and the mapping of histone H1.5-nucleosome interactions (24). Extra densities that cannot be assigned to the globular domain of H1 are presumably contributed by the N- and C-termini of H1 (fig. S5B, blue lines and black stars indicated) and/or partially contributed by the N-termini of histone H3 (Fig. 3B and fig. S5B, magenta tail), which was previously shown to contribute to chromatin folding (29).

Structural Model for Chromatin Fibers

Our 3D cryo-EM structure of the 30-nm chromatin fiber allows construction of a fine structural model for 30-nm fibers in the presence of histone H1 (Fig. 4). To evaluate the possible end effects of the relatively short 12 tandem repeats of nucleosomes, we reconstituted the 30-nm fibers with 24 repeats of 177-bp (24×177 bp) 601 DNA template and acquired the 3D cryo-EM structure at ~25 Å resolution (Fig. 4A, fig. S6, and movie S3). Two copies of 12×177 bp chromatin density map can be docked into the map of 24×177 bp chromatin without further modification (Fig. 4B). In addition, the interactions between the intra- and interunits in the 24×177 bp chromatin are well maintained compared with the 12×177 bp

chromatin model (fig. S6E). We then built the model of 30-nm chromatin by directly stacking the cryo-EM structure of dodecanucleosomal 30-nm fibers on top of each other to form a continuous fiber. The resulting direct model reveals that the chromatin fiber is exhibited as a left-handed double helical structure twisted by tetranucleosomal units (Fig. 4C). The 30-nm fiber with the 187-bp NRL contains 7.07 tetranucleosomal units (28.3 nucleosomes) per turn in a period of 49.9 nm, yielding a nucleosome packing density of about 6.2 nucleosomes per 11 nm; this density is very similar to the measured values for mass per unit length of the chromatin fiber (4, 30). To examine the effects of the previously indicated slight difference in rotation and separation between different units in the 30-nm fiber of dodecanucleosomes in the model construction, we also built two other models with a repeat stacking of units 1 and 2 or units 2 and 3, respectively (fig. S7, A and B). These two alternative models show a high resilience to the double-helical twist model formed from the direct stacking of dodecanucleosomes, except for slight changes in the packing density of nucleosomes that were identified as 6.1 nucleosomes per 11 nm for the model built by units 1 and 2 and 6.4 nucleosomes per 11 nm for the model built by units 2 and 3 (Fig. 4C and fig. S7).

Conclusions

The existence of 30-nm fibers in nuclei still remains to be elucidated, whereas the structure of chromatin fiber must be variable in vivo because of its highly dynamic and heterogeneous property with intrinsic compositions, such as different NRLs, linker histones, histone and DNA modifications, and histone variants. Although our 3D cryo-EM structures for the reconstituted 30-nm chromatin fiber show basically a two-start zigzag configuration for nucleosome arrangement, other forms of chromatin structures may exist in different conditions, for example, the one-start solenoid structure in the presence of H5 and magnesium with longer NRLs as suggested previously (14, 31). Nevertheless, the formation of the double-helical structure of the reconstituted canonical 30-nm fibers using the 177-bp and 187-bp NRLs in the presence of H1 under a low-salt condition is basically driven by their intrinsic biophysical and biochemical properties; thus, the fundamental principles may also be applicable in vivo. Histone modifications and histone variants may also play important roles in the regulation of higher-order chromatin structure via modulating the internucleosomal surface interactions between tetranucleosomal units.

References and Notes

1. R. Ghirlando, G. Felsenfeld, *J. Mol. Biol.* **376**, 1417–1425 (2008).
2. E. C. Pearson, P. J. Butler, J. O. Thomas, *EMBO J.* **2**, 1367–1372 (1983).
3. V. Graziano, S. E. Gerchman, D. K. Schneider, V. Ramakrishnan, *Nature* **368**, 351–354 (1994).
4. S. E. Gerchman, V. Ramakrishnan, *Proc. Natl. Acad. Sci. U.S.A.* **84**, 7802–7806 (1987).

Fig. 4. The 30-nm chromatin fiber model. (A) The overall 3D cryo-EM map of the 30-nm chromatin fiber reconstituted on 24 × 177 bp 601 DNA, with the length and diameter of the fiber indicated. **(B)** The structure of 24 × 177 bp 30-nm fibers is docked by two copies of the cryo-EM structure of 12 × 177 bp 30-nm fibers. The fitting was optimized by the reported correlation value in UCSF Chimera. **(C)** A pseudo-atomic model (left, structure of H1 is not included) and its corresponding density map low-pass filtered to 11 Å (right), built by directly stacking the cryo-EM structure of the dodecanucleosomal 30-nm fiber with 187-bp NRLs on top of each other to form a continuous fiber. Scale bar, 11 nm.

A
Cryo-EM map of 24×177 bp chromatin fiber
27.2 nm
55.8 nm

B

C
Pseudo-atomic model of 48×187 bp chromatin fiber

Low-pass filtered model of 48×187 bp chromatin fiber
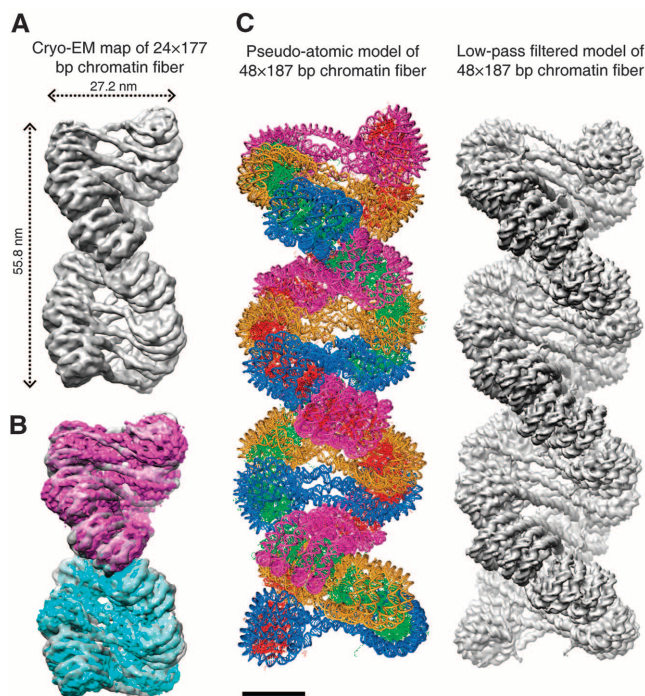
5. J. Widom, A. Klug, *Cell* **43**, 207–213 (1985).
6. J. P. Langmore, J. R. Paulson, *J. Cell Biol.* **96**, 1120–1131 (1983).
7. J. T. Finch, A. Klug, *Proc. Natl. Acad. Sci. U.S.A.* **73**, 1897–1901 (1976).
8. C. L. Woodcock, L. L. Frado, J. B. Rattner, *J. Cell Biol.* **99**, 42–52 (1984).
9. S. P. Williams *et al.*, *Biophys. J.* **49**, 233–248 (1986).
10. M. F. Smith, B. D. Athey, S. P. Williams, J. P. Langmore, *J. Cell Biol.* **110**, 245–254 (1990).
11. H. G. Davies, J. V. Small, *Nature* **217**, 1122–1125 (1968).
12. L. M. Carruthers, C. Tse, K. P. Walker 3rd, J. C. Hansen, *Methods Enzymol.* **304**, 19–35 (1999).
13. P. T. Lowary, J. Widom, *J. Mol. Biol.* **276**, 19–42 (1998).
14. P. J. Robinson, L. Fairall, V. A. Huynh, D. Rhodes, *Proc. Natl. Acad. Sci. U.S.A.* **103**, 6506–6511 (2006).
15. B. Dorigo *et al.*, *Science* **306**, 1571–1573 (2004).
16. T. Schalch, S. Duda, D. F. Sargent, T. J. Richmond, *Nature* **436**, 138–141 (2005).
17. F. Thoma, T. Koller, A. Klug, *J. Cell Biol.* **83**, 403–427 (1979).
18. J. O. Thomas, *Curr. Opin. Cell Biol.* **11**, 312–317 (1999).
19. D. L. Bates, J. O. Thomas, *Nucleic Acids Res.* **9**, 5883–5894 (1981).
20. J. Allan, P. G. Hartman, C. Crane-Robinson, F. X. Aviles, *Nature* **288**, 675–679 (1980).
21. D. Z. Staynov, *Bioessays* **30**, 1003–1009 (2008).
22. T. D. Frouws, H. G. Patterton, B. T. Sewell, *Biophys. J.* **96**, 3363–3371 (2009).
23. K. Luger, A. W. Mäder, R. K. Richmond, D. F. Sargent, T. J. Richmond, *Nature* **389**, 251–260 (1997).
24. S. H. Syed *et al.*, *Proc. Natl. Acad. Sci. U.S.A.* **107**, 9620–9625 (2010).
25. D. Z. Staynov, C. Crane-Robinson, *EMBO J.* **7**, 3685–3691 (1988).
26. B. R. Zhou *et al.*, *Proc. Natl. Acad. Sci. U.S.A.* **110**, 19390–19395 (2013).
27. G. J. Carter, K. van Holde, *Biochemistry* **37**, 12477–12488 (1998).
28. L. Fan, V. A. Roberts, *Proc. Natl. Acad. Sci. U.S.A.* **103**, 8384–8389 (2006).
29. S. H. Leuba, C. Bustamante, K. van Holde, J. Zlatanova, *Biophys. J.* **74**, 2830–2839 (1998).
30. J. Bednar *et al.*, *Proc. Natl. Acad. Sci. U.S.A.* **95**, 14173–14178 (1998).
31. A. Routh, S. Sandin, D. Rhodes, *Proc. Natl. Acad. Sci. U.S.A.* **105**, 8872–8877 (2008).

Genome Sequence of the Tsetse Fly (*Glossina morsitans*): Vector of African Trypanosomiasis

International *Glossina* Genome Initiative*†

Tsetse flies are the sole vectors of human African trypanosomiasis throughout sub-Saharan Africa. Both sexes of adult tsetse feed exclusively on blood and contribute to disease transmission. Notable differences between tsetse and other disease vectors include obligate microbial symbioses, viviparous reproduction, and lactation. Here, we describe the sequence and annotation of the 366-megabase *Glossina morsitans morsitans* genome. Analysis of the genome and the 12,308 predicted protein–encoding genes led to multiple discoveries, including chromosomal integrations of bacterial (*Wolbachia*) genome sequences, a family of lactation-specific proteins, reduced complement of host pathogen recognition proteins, and reduced olfaction/chemosensory associated genes. These genome data provide a foundation for research into trypanosomiasis prevention and yield important insights with broad implications for multiple aspects of tsetse biology.

African trypanosomiasis is transmitted by the tsetse fly to humans (sleeping sickness) and livestock (nagana) throughout sub-Saharan Africa, with an estimated 70 million people at risk of infection. Rearing livestock in endemic areas is difficult to impossible and results in an economic loss in agricultural output of several billion U.S. dollars per year. Human infections are fatal if untreated, but tools for disease control are limited because it has not been possible to develop vaccines and current trypanocidal drug treatments result in undesirable side effects with growing reports of drug resistance. The reduction or elimination of tsetse populations is an effective method for disease control that could be improved with greater knowledge of their biology and genetics (*1*).

Tsetse flies are key representatives of the dipteran clade Calyptratae, which represents 12% of the known diversity within the dipteran order. Many of the calyptrate species are blood feeders of biomedical importance (*2*). In addition, members of the calyptrate family of Glossinidae and superfamily Hippoboscoidea, to which tsetse belong (fig. S1) (*3*), are defined by the ability to nourish intrauterine offspring from glandular secretions and give birth to fully developed larvae (obligate adenotrophic viviparity). Tsetse flies live considerably longer than other vector insects, which somewhat compensates for their slow rate of reproduction. Trypanosome infections in tsetse are acquired by blood feeding from an infected vertebrate host, and trypanosomes have to overcome multiple immune barriers to establish an infection within the fly. As a result, trypanosome infection prevalence is low in field populations and in experi-mentally infected tsetse (*4*). Tsetse have symbionts that compensate for their nutritionally restricted diet by the production of specific metabolites and influence multiple other aspects of the fly's immune and reproductive physiology (*5*).

In 2004, the International *Glossina* Genome Initiative (IGGI) was formed (*6*) to expand research capacity for *Glossina*, particularly in sub-Saharan Africa, through the generation and distribution of molecular resources, including bioinformatics training. An outcome of the effort undertaken by IGGI is the annotated *Glossina morsitans* genome presented here and further developed in satellite papers on genomic and functional biology findings that reflect the unique physiology of this disease vector (*7–14*).

Characteristics of the *Glossina* Genome

A combination of sequencing methods were used to obtain the *Glossina morsitans morsitans* (*Gmm*) genome, including Sanger sequencing of bacterial artificial chromosomes (BACs), small-insert plasmid and large-insert fosmid libraries, and 454 and Illumina sequencing (tables S1 and S2). The sequences were assembled into 13,807 scaffolds of up to 25.4 Mb, with a mean size of 27 kb and half the genome present in scaffolds of at least 120 kb. The 366-Mb genome is more than twice the size of the *Drosophila melanogaster* genome (fig. S2A and table S3). Clear conservation of synteny was detected between *Glossina* and *Drosophila*, but with the blocks of synteny tending to be twice as large in *Glossina* due to larger introns and an increase in the size of intergenic sequences, possibly as a result of transposon activity and/or repetitive sequence expansions. Sequences from most of the major groups of retrotransposons and DNA transposons are found in the *Glossina* genome (table S4). These sequences comprise ~14% of the assembled genome, in contrast to 3.8% of the *Drosophila*

*Members of the International *Glossina* Genome Initiative, affiliations, and individual contributions appear at the end of this paper.
†Corresponding author. E-mail: serap.aksoy@yale.edu (Serap Aksoy); geoffrey.attardo@yale.edu (G.M.A.); mb4@sanger.ac.uk (M.B.)

euchromatic genome (*15*). The *Glossina* genome is estimated to contain 12,308 protein-encoding genes based on automated and manual annotations. Although this number is fewer than *Drosophila*, the average gene size in *Glossina* is almost double that of *Drosophila* (fig. S2B). The number of exons and their average size is roughly equivalent in both fly species (fig. S2C), but the average intron size in *Glossina* appears to be roughly twice that of *Drosophila* (fig. S2D).

Orthologous clusters of proteins were generated by comparing the predicted *Glossina* protein sequences to five other complete Dipteran genomes (*Drosophila melanogaster*, *Aedes aegypti*, *Anopheles gambiae*, *Culex quinquefasciatus*, and *Phlebotomus papatasi*). Each cluster contained members from at least two taxa; groups from a single taxon were considered species-specific paralogs.

In total, 9172 (74%) of *Glossina* genes (from 8374 orthologous clusters) had a Dipteran ortholog,

2803 genes (23%) had no ortholog/paralog, and 482 (4%) had a unique duplication/paralog in *Glossina*. The ortholog analysis across the Diptera (fig. S3A) shows that 94% (7867 of 8374) of clusters that contain a *Glossina* gene also contain an ortholog with *Drosophila* (fig. S3B).

Blood Feeding and Nutrition

Blood feeding has originated at least 12 times in Diptera, and this genome facilitates a perspective for the comparative evolutionary biology of hematophagy (*2*). Unlike its distantly related blood-feeding relatives in the suborder Nematocera (such as mosquitoes and sandflies), which supplement their diet with plant nectar, both male and female *Glossina* use blood as their sole source of nutrients and energy.

Adult tsetse have several salivary molecules that are essential for efficient blood feeding and digestion because they counteract the complex

physiological responses of the host that impede blood feeding, including coagulation, blood platelet aggregation, and vasoconstriction (table S5 and Fig. 1) (*16*). One gene family, *tsal*, is the most abundant in the *Glossina* sialome (*16*) and encodes high-affinity nucleic acid–binding proteins that lack strong endonuclease activity (*17*). Orthologs to *tsal* are not found in *Drosophila*, but they are present in sandflies (Phlebotomus genus) and mosquitoes (*Culex* species only). In mosquitoes and sandflies, a single gene is responsible for the production of salivary endonucleases with hydrolysis activity (*18*). *Glossina* carries three distinct *tsal* genes (GMOY012071, GMOY012361, and GMOY012360) that colocalize to a 10-kb locus.

Another family of abundant salivary proteins, related to adenosine deaminases and insect growth factors (ADGFs) are thought to reduce the inflammation and irritation resulting from adenosine and inosine-induced mast cell activation. In
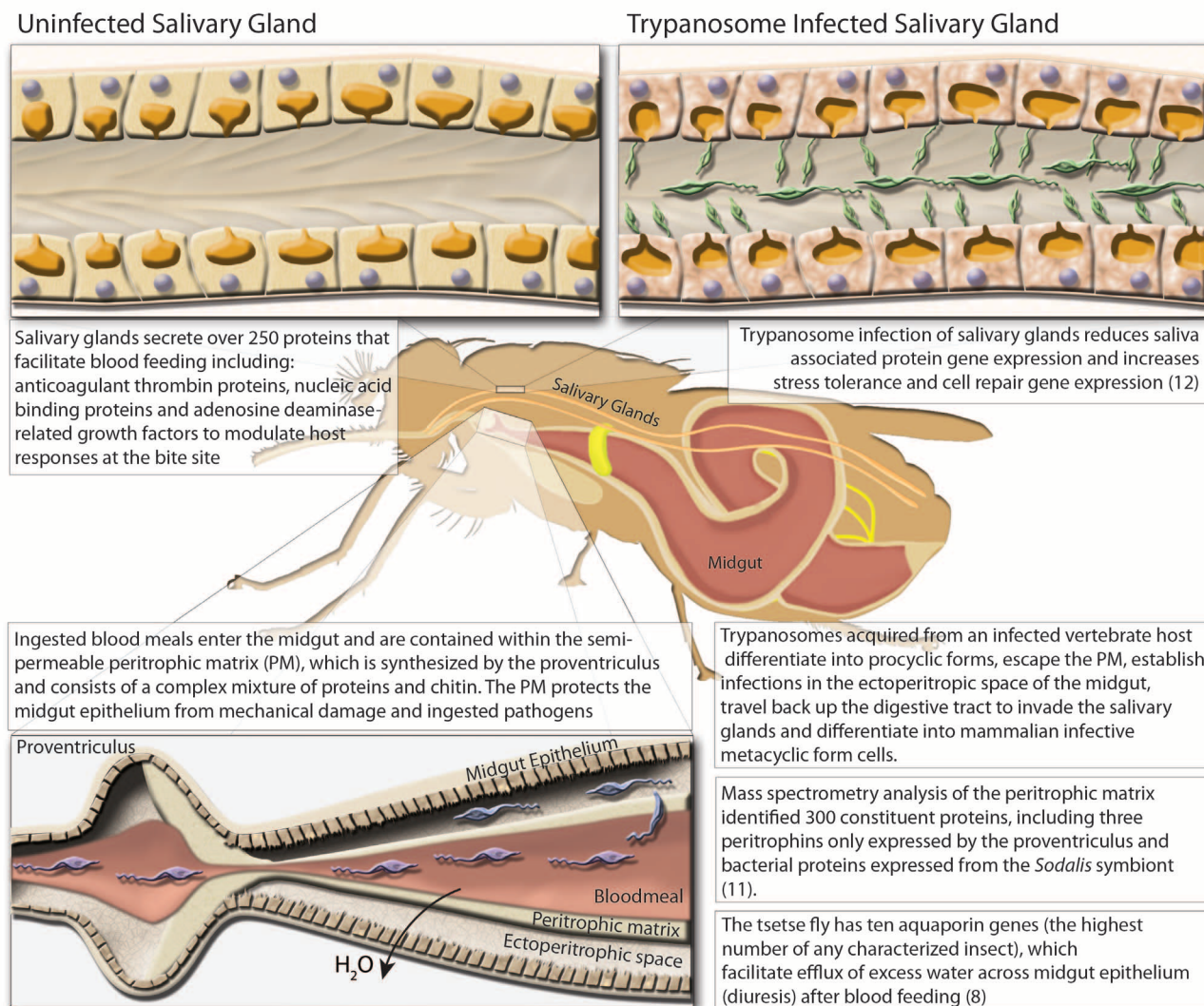
Fig. 1. Diagrammatic presentation of major findings regarding the effects of trypanosome infection of the salivary glands and midgut, proteomic analysis of the peritrophic matrix, and the role of aquaporin proteins in blood meal digestion and diuresis. (Top) comparison of trypanosome-uninfected and -infected states of *Glossina* salivary glands. **(Left)** Representative protein components of *Glossina* salivary secretions. **(Right)** Pathogenic effects of trypanosome infection on salivary gland function. **(Bottom)** *Glossina* digestive physiology and the infection process by trypanosomes. Associated satellite references for these findings are listed within the figure as numbers in parentheses and correspond to the reference list (*8, 11, 12*).

tsetse, the *ADGF* genes are uniquely organized as a cluster of four genes in a 20-kb genomic locus (*GMOY002973, GMOY012372, GMOY012373,* and *GMOY012374*). An *adenosine deaminase* (*ada*) gene (*GMOY008741*) without the putative growth factor domain is encoded elsewhere in the genome. In *Drosophila*, five *ADGF* genes can be found in various loci and are associated with developmental regulation (*19*). Nematoceran Diptera, including sandflies and mosquitoes, have a maximum of three *ADGF* genes. Other arthropods, such as *Ixodes scapularis*, *Rhodnius prolixus*, and *Pediculus humanus*, have only bona fide adenosine deaminases.

Recent studies show that specific genes and proteins are down-regulated in salivary glands during parasite infection, which promotes trypanosome transmission because feeding efficiency is reduced and feeding time is extended (*20*). RNA-seq analysis of salivary gland gene expression during parasite infection confirmed the reduction of transcript abundance for previously identified genes, such as *ada*, *tsal1*, *tsal2*, and *5' nucleotidase*, as well as of many other putative secreted salivary protein genes (*12*). Additionally, genes involved in stress tolerance and cell repair showed increased expression, indicating that considerable salivary gland tissue damage is caused by trypanosome infections.

Upon blood-meal ingestion, the peritrophic matrix (PM), which separates the midgut epithelium from the blood bolus, protects gut cells from damaging or toxic dietary elements, allows for compartmentalized digestion and metabolism of the blood meal, and is a barrier against infection (*5*). *Glossina* produces a type-II PM, which is secreted continuously as concentric sleeves by the proventriculus and separates the lumen of the midgut (endoperitrophic space) from the mono-layer of epithelial cells (*21*). Type-II PMs are generally composed of chitin, peritrophin proteins, glycosaminoglycans (GAGs), and mucin-like molecules. Analysis of isolated PMs of male flies by mass spectrometry identified ~300 proteins, including multiple uncharacterized peritrophins and peritrophin-like glycoproteins. This proteomic data identified the corresponding genes in the *Glossina* genome. Three of these genes are exclusively expressed by the proventriculus (table S6) (*11*).

Glossina takes a blood meal that is almost equivalent to its own weight, and excess water is rapidly excreted by means of the Aquaporin family of transport proteins (*22*). Ten *aquaporin* genes (*aqps*) were identified in *Glossina*, compared with six and eight in mosquitoes and *Drosophila*, respectively (table S7). In *Glossina*, two *aqp* genes are duplicates: the orthologs

Fig. 2. Diagrammatic presentation of the *Glossina* microbiome, tissue localization of bacterial symbionts, physiological importance, and summary of genomic interactions. (Top) *Glossina* reproductive physiology and associated symbiont localizations. **(Bottom)** *Glossina* digestive physiology and the associated symbiont localizations. Associated text describes significant findings regarding the *Glossina* microbiome and the associated impacts in terms of *Glossina* immunity, nutrition, vectorial capacity, and vector control. Associated satellite references are listed within the figure as numbers in parentheses and correspond to the reference list (*11, 13*).

Wolbachia
- Multiple natural *Glossina* populations (including *Gmm*) harbor *Wolbachia* infections.
- Infections are localized to the ovarian germ cells and testes.
- Multiple horizontal transfer events have resulted in transfer of >1 MB of the *Wolbachia* genome into the tsetse genome with unknown functional implications (13).
- The genome of cytoplasmic *Wolbachia* has reduced numbers of ankyrin and phage genes relative to strains in *Drosophila*.
- Infection causes cytoplasmic incompatibility phenomena in tsetse which gives infected females a reproductive advantage over uninfected flies.
- *Wolbachia* is a potential driver for paratransgenic agents (such as *Sodalis*).

Wigglesworthia
- Localized to bacteriome, milk gland tubules and larval gut.
- Provide nutritional supplementation required for female fecundity and larval development, including B-vitamins which may be critical to supplement tsetse's diet.
- Provide immune stimulation required for larval immune system development.

Sodalis
- Found intra- and extra-cellularly throughout the fly.
- May contribute towards tsetse's susceptibility to trypanosomes as they secrete a chitinase which may weaken the structural integrity of the peritrophic matrix (11).
- Can be genetically modified to express trypanocidal molecules
- Shows promise as a potential paratransgenesis agent

Salivary Gland Hypertrophy Virus (SGHV) and Bracoviral Insertions
- Multiple *Glossina* species (including *morsitans*) harbor a large DNA hytrosavirus (SGHV)
- Sequences homologous to Bracoviral genes have also been identified in the tsetse genome, suggesting wasp parasitization.

of the *aqp2* and the *Drosophila integral protein* (*drip*) genes. Knockdown of aquaporins inhibited post–blood meal diuresis, increased dehydration tolerance, reduced heat tolerance, and extended the duration of lactation and pregnancy in females. The *drip* orthologs are particularly abundant in the female accessory gland (milk glands), suggesting a role in hydration of glandular secretions (*8*).

In comparison with mosquitoes and sandflies, *Glossina* has a marked reduction in genes associated with carbohydrate metabolism, instead using a proline-alanine shuttle system for energy distribution and triglycerides and diglycerides for storage in the fat body and milk secretions. Little to no sugar nor glycogen is detectable in these

flies (*23*). Genes involved in lipid metabolism are generally conserved, with gene expansions associated with fatty acid synthase, fatty acyl-CoA reductase, and 3-keto acyl-CoA synthase functions (table S8). In addition, three multivitamin transporters from the solute:sodium symporter (SSS) family are found in *Glossina* and mosquitoes, but not in *Drosophila*, suggesting an association with blood-meal metabolism (table S9).

Microbiome

Glossina harbor multiple maternally transmitted mutualistic and parasitic microorganisms, including the obligate *Wigglesworthia glossinidia*, which reside intracellularly in cells that com-

promise the midgut-associated bacteriome organ as well as extracellularly in the milk gland lumen (Fig. 2). In the absence of *Wigglesworthia*, female flies tend to prematurely abort their larval offspring unless they receive dietary supplements (*18*). However, the larvae that have undergone intrauterine development in the absence of *Wigglesworthia* metamorphose into immune-compromised adults (*24*).

The predicted proteome of *Wigglesworthia* indicates a capacity for B vitamin biosynthesis (*25*) and synthesis of thiamine monophosphate (TMP). *Glossina* lacks this capacity; however, it carries genes for thiamine transporters, a member of the reduced folate carrier family (*GMOY009200*), and a folate transporter (*GMOY005445*).

Milk gland secretory cell (Lactating)

Hemolymph

Lipids

Milk gland specific DRIP-type aquaporin required for milk hydration. [8]

Amino acids

Milk gland specific Ladybird late homeodomain transcription factor activates milk protein gene expression. [9]

Milk Storage Vacuole

Milk Gland Lumen

Milk gland secretory cell (Post-parturition)

Hemolymph

Tsetse milk [10]
- Consists of proteins and lipids emulsified in an aqueous solution.
- Milk proteins include: Transferrin, Acid sphingomyelinase, MGP 1 (lipocalin), MGPs 2-10 (novel) and PGRP-LB.
- ~50% of all transcripts in lactating flies are milk proteins
- Proteins are analogous in function to mammalian milk proteins

Antioxidant Response [7]
- Milk protein synthesis generates oxidative stress.
- Antioxidant enzymes alleviate stress pre- and post-parturition.
- Inhibition of these enzymes results in cumulative oxidative damage and loss of fecundity.
- Critical to maintaining long term reproductive capacity of female tsetse.

Milk Gland Lumen

Lipid Droplet | DRIP-type Aquaporin | Amino acids | Wigglesworthia/ Sodalis
Nucleus | Amino acid Transporter | Milk proteins | Antioxidant enzymes

Fig. 3. Diagrammatic presentation of milk gland secretory cell physiology and milk production during lactation and after parturition. (Left) Lactation. Nutrients including lipids, amino acids, and water are taken up by the cell through various transporters. Lipids are aggregated into droplets while amino acids are incorporated into the synthesis of a battery of milk proteins. During pregnancy, milk protein genes are up-regulated by the Ladybird Late homeodomain protein. Lipids, proteins, and water are combined to form the milk constituents, which are stored in a large extracellular secretory reservoir. Stored milk is secreted into the lumen, which also houses the extracellular obligate bacterial symbiont *Wigglesworthia*. The milk and symbionts are transported through the gland to the uterus, where the developing larvae feeds upon these secretions. **(Right)** Involution and recovery. After parturition, milk gland cells shrink, undergo autophagy, and express antioxidant enzymes to inhibit oxidative damage. The recovered cells prepare for the next round of lactation by regeneration of protein synthesis and structural components. Associated satellite references for these findings are listed within the figure as numbers in parentheses and correspond to the reference list (*7*–*10*).

Wolbachia is another symbiont present in some wild *Glossina* populations (and in the strain sequenced here), which resides in gonadal tissues. Laboratory studies have shown that this associated *Wolbachia* strain induces cytoplasmic incompatibility (CI) in *Glossina morsitans* (*26*). Furthermore, at least three horizontal transfer events (HTEs) from *Wolbachia* were detected in *Glossina* chromosomes. The two largest insertions carry a total of 159 and 197 putative functional protein-coding genes, whereas the third lacks any protein coding genes. In situ staining of *Glossina* mitotic chromosomes with *Wolbachia*-specific DNA probes identified multiple insertions on the X, Y, and B chromosomes (table S10) (*13*). Although no *Wolbachia*-specific transcripts were detected arising from chromosomal insertions, the functional and evolutionary implications of these insertions require study.

Many *Glossina* species, including the strain sequenced here, harbor a large DNA hytrosavirus, the *Glossina pallidipes* salivary gland hypertrophy virus (GpSGHV) (*27*). The virus can reduce fecundity and life span in *Glossina* and cause salivary gland pathology and swelling at high densities. Also, the analysis of a group of genes lacking dipteran orthologs revealed many putative bracoviral genes [Basic Local Alignment Search Tool (BLAST) *E* values of $<1 \times 10^{-50}$] spread over 151 genomic scaffolds (tables S11 and S12). The putative bracoviral sequences bear highest homology to those identified from the parasitic braconid wasps *Glyptapanteles flavicoxis* and *Cotesia congregata*. This suggests that *Glossina* was or is parasitized by an as-yet-unidentified braconid wasp.

Immunity

Multiple factors, including age, sex, nutritional status, and symbionts, influence tsetse's competence as a vector for trypanosomes. Peptidoglycan (PGN) recognition proteins (PGRPs), antimicrobial effector peptides (AMPs) produced by immune deficiency (IMD) pathway, midgut lectins, antioxidants, EP protein (defined by its glutamic acid and proline repeats), and the gut-associated peritrophic matrix structure are all components that regulate the nature of the interactions between the fly and its symbionts (*28*).

Microbial detection is a multistep process that requires direct contact between host pattern recognition receptors (PRRs) and pathogen-associated molecular patterns (PAMPs). *Drosophila* has 13 PGRPs that play a role in the recognition of PGN, an essential component of the cell wall of virtually all bacteria. In *Glossina*, only six *pgrp* genes were identified, four in the long subfamily (*pgrp-la*, *-lb*, *-lc*, and *-ld*) and two in the short subfamily (*pgrp-sa* and *-sb*), whereas *Drosophila* has a gene duplication resulting in two related forms of *pgrp-sb*. Based on both genome annotation and transcriptome data, *Glossina* lacks orthologs of the PGN receptors, *-le*, *-lf*, *-sc*, and *-sd*, found in *Drosophila*. The reduced *pgrp* repertoire of *Glossina* may reflect its blood-specific diet, which likely exposes its gut to fewer microbes than *Drosophila*. In the *Drosophila* gut, PGRP-LE functions as the master bacterial sensor, which induces both responses to infectious bacteria and tolerance to microbiota by up-regulating suppressors of the IMD pathway, including PGRP-LB (*29*). In the case of *Glossina*, loss of amidase -SC1 along with PGRP-LE may indicate a host immune response that has evolved to protect the symbiosis with *Wigglesworthia*. Reduced immune capacity is also observed in aphids that also harbor obligate symbionts (*30*). A complete listing of orthologs to *Drosophila* immune genes is presented in table S13.

Reproduction and Developmental Biology

The reproductive biology of tsetse is unique to the Hippoboscoidea superfamily. The evolution of adenotrophic viviparity (intrauterine larval development and nourishment by glandular secretions) has required ovarian follicle reduction (two follicles per ovary compared with 30 to 40 in *Drosophila*), expansion and adaptation of the uterus to accommodate developing larvae, and adaptation of the female accessory gland to function as a nutrient synthesis and delivery system.

Glossina, *Drosophila*, and other Brachyceran flies use lipase-derived yolk proteins for vitellogenesis, unlike non-Brachyceran flies that use the vitellogenin family of yolk proteins (*31*). *Drosophila* and Brachyceran flies outside of the Hippoboscidae superfamily produce multiple oocytes per gonotrophic cycle. However, *Glossina* only develops a single oocyte each cycle. Unlike *Drosophila*, which has three yolk protein genes (*yp1*, *yp2*, and *yp3*) localized on the X chromosome, *Glossina* has a single yolk protein gene, which is orthologous to Drosophila *yp2* (GMOY002338), expressed only in the ovaries, and lacks fat body–associated expression. Multiple yolk proteins have been identified in other Brachyceran flies, indicating that *Glossina* may have lost these genes in association with its reduction in reproductive capacity (*31*).

Glossina larvae are dependent on their mother's milk gland secretions for nutrition, as well as for transfer of symbiotic fauna (Fig. 3). This gland is highly specialized and secretes a complex mixture of stored lipids and milk proteins. Analysis of differential gene expression in lactating versus nonlactating females confirmed the presence of previously characterized milk protein genes—including a *lipocalin* (*mgp1*), a *transferrin* (*trf*), an *acid sphingomyelinase* (*asmase*), *milk proteins 2 + 3* (*mgp2* and *-3*), and *pgn recognition protein lb* (*pgrp-lb*) (*28*)—but also revealed a previously undiscovered suite of eight paralogs to the *mgp2* and *-3* genes. Annotation of the 40-kb genomic loci encompassing *mgp2* and *mgp3* revealed that these genes have arisen via gene duplication events. These genes have similar exon/intron structures and are expressed in the same stage- and tissue-specific manner as *mgp2* and *mgp3* (*10*). The newly identified milk proteins may function as lipid emul-

sification agents, sources of amino acids, and phosphate carriers. The 12 genes associated with milk synthesis make up almost half of all maternal transcriptional activity during lactation (table S14) (*10*). The combined suite of *Glossina* milk proteins bear remarkable functional similarities to those of placental mammals and marsupials (Fig. 3).

The massive level of protein synthesis during lactation generates substantial oxidative stress in tsetse females, but females can undergo this process 8 to 10 times during their life spans without evidence of reproductive senescence. Transcriptional analysis of antioxidant enzyme (AOE) gene expression revealed an increase in abundance of these genes during lactation and after birth (*7*) (table S15), such that knockdown of these enzymes decreases fecundity in subsequent reproductive cycles. The mediation of oxidative stress by AOEs at key points in tsetse reproduction appears critical to preservation of fecundity late into *Glossina*'s life span (*7*) (Fig. 3).

The milk proteins produced by tsetse are under tight transcriptional regulation and are only expressed in the female accessory gland. The expression level of these genes is coordinated with the stage of pregnancy and increases with larval development. The system regulating these genes appears conserved as transgenic *Drosophila* carrying the *mgp1* gene promoter sequence drive the expression of a green fluorescent protein reporter gene exclusively in the female accessory glands in coordination with oogenesis/ovulation. Comparative analysis of the promoter sequences from multiple milk protein genes revealed the presence of conserved binding sites for homeodomain transcription factors. Analysis of the homeodomain transcription factors in *Glossina* (table S16) identified a gene, *ladybird late* (*lbl*), which is expressed exclusively in the milk gland of adult female flies and the female accessory glands of *Drosophila*. Knockdown of *lbl* results in a global reduction of milk gland protein expression in tsetse and causes loss of fecundity (*9*) (Fig. 3).

Sensory Genes as Targets for *Glossina* Control Strategies

Glossina species differ in host preferences and vary in their response to chemical and visual cues from different mammalian hosts or for mate finding. Sensory proteins range from odorant binding proteins (OBP), chemosensory proteins (CSP), odorant receptors (OR), gustatory receptors (GR), and ligand-gated ionotropic receptors (IR) to sensory neuron membrane proteins (SNMP) (*32*).

Detailed annotation of *Glossina* sensory receptors reveals that they have fewer olfactory proteins relative to *Drosophila, An. gambiae*, and *Apis mellifera* (table S17) (*14*). Of note, six ORs are homologous to a single *Drosophila* OR, which is associated with female mating deterrence. In addition, GR genes associated with sweet tastes, present in all other Diptera, are missing in tsetse. These genetic differences are consistent with the

combination of a restricted diet of vertebrate blood and their narrow host range.

The visual system of *Glossina* is very similar to that of other calyptrate Diptera, which are generally fast flying, such as the house fly *Musca domestica* and the blow fly *Calliphora vicina* (*33*). In tsetse, both sexes employ vision for rapid host identification and pursuit (*34*); males, however, also depend on vision for long-distance spotting and tracking of female mating partners (*35*). Morphology and function of the compound eye retina is highly conserved throughout the Brachycera, allowing for direct comparisons with *Drosophila* (*36*). The search for vision-associated genes revealed that all of the core components of the highly efficient *Drosophila* phototransduction cascade are conserved in *Glossina* (table S18). This is also the case for four of the five opsin transmembrane receptor genes that are differentially expressed in the photoreceptors of the *Drosophila* compound eye: *Rh1*, *Rh3*, *Rh5*, and *Rh6*. Most important, the recovery of opsin *Rh5* indicates the likely presence of blue-sensitive R8p photoreceptors in *Glossina* that have been missed in experimental studies (*33*). This finding is consistent with tsetse's attraction to blue/black, which has been widely exploited for the development of traps to reduce vector populations (*37*). It is further notable that the study of opsin conservation and expression in the blow fly retina recovered the same four opsin paralogs (*38*), suggesting that the deployment of a single ultraviolet (UV)–sensitive opsin (*Rh3*) represents the ground state for calyptrate Diptera, in contrast to the expression of two UV-sensitive opsins (*Rh3* and *Rh4*) in the eyes of *Drosophila*. The *Glossina* genome also contains the ortholog of the *Drosophila Rh7* opsin gene, which is still of unknown function in *Drosophila*.

Future Directions

The assembly and annotation of the *Glossina* genome highlights its unique biology and facilitates the application of powerful high-throughput technologies in a way that was previously impossible. In addition, genomic and transcriptomic data on five *Glossina* species (*G. fuscipes fuscipes*, *G. palpalis gambiensis*, *G. brevipalpis*, *G. austeni*, and *G. pallidipes*) are being generated to produce additional genome assemblies for evolutionary and developmental analyses to study genomic differences associated with host specificity, vectorial capacity, and evolutionary relationships.

References and Notes

1. S. C. Welburn, I. Maudlin, P. P. Simarro, *Parasitology* **136**, 1943–1949 (2009).
2. B. M. Wiegmann *et al.*, *Proc. Natl. Acad. Sci. U.S.A.* **108**, 5690–5695 (2011).
3. F. T. Petersen, R. Meier, S. N. Kutty, B. M. Wiegmann, *Mol. Phylogenet. Evol.* **45**, 111–122 (2007).
4. M. J. Lehane, S. Aksoy, E. Levashina, *Trends Parasitol.* **20**, 433–439 (2004).
5. B. L. Weiss, J. Wang, M. A. Maltz, Y. Wu, S. Aksoy, *PLOS Pathog.* **9**, e1003318 (2013).
6. S. Aksoy *et al.*, *Trends Parasitol.* **21**, 107–111 (2005).
7. V. Michalkova, J. B. Benoit, G. M. Attardo, J. Medlock, S. Aksoy, *PLOS ONE* **9**, e87554 (2014).
8. J. B. Benoit *et al.*, *PLOS Negl. Trop. Dis.* **8**, e2517 (2014).
9. G. M. Attardo *et al.*, *PLOS Negl. Trop. Dis.* **10**, e2645 (2014).
10. J. B. Benoit *et al.*, *PLOS Genet.* **10**, e1003874 (2014).
11. C. Rose *et al.*, *PLOS Negl. Trop. Dis.* **8**, e2691 (2014).
12. E. L. Telleria *et al.*, *PLOS Negl. Trop. Dis.* **8**, e2649 (2014).
13. C. Brelsford *et al.*, *PLOS Negl. Trop. Dis.* **8**, e2728 (2014).
14. G. F. O. Obiero *et al.*, *PLOS Negl. Trop. Dis.* **8**, e2663 (2014).
15. J. S. Kaminker *et al.*, *Genome Biol.* **3**, RESEARCH0084 (2002).
16. J. Alves-Silva *et al.*, *BMC Genomics* **11**, 213 (2010).
17. G. Caljon *et al.*, *PLOS ONE* **7**, e47233 (2012).
18. J. M. Ribeiro, B. J. Mans, B. Arcà, *Insect Biochem. Mol. Biol.* **40**, 767–784 (2010).
19. T. Dolezal, E. Dolezelova, M. Zurovec, P. J. Bryant, *PLOS Biol.* **3**, e201 (2005).
20. J. Van Den Abbeele, G. Caljon, K. De Ridder, P. De Baetselier, M. Coosemans, *PLOS Pathog.* **6**, e1000926 (2010).
21. M. J. Lehane, *Annu. Rev. Entomol.* **42**, 525–550 (1997).
22. E. M. Campbell, A. Ball, S. Hoppler, A. S. Bowman, *J. Comp. Physiol. B* **178**, 935–955 (2008).
23. D. A. Norden, D. J. Paterson, *Comp. Biochem. Physiol.* **31**, 819–827 (1969).
24. B. L. Weiss, M. Maltz, S. Aksoy, *J. Immunol.* **188**, 3395–3403 (2012).
25. R. V. Rio *et al.*, *MBio* **3**, e00240-11 (2012).
26. U. Alam *et al.*, *PLOS Pathog.* **7**, e1002415 (2011).
27. A. M. Abd-Alla *et al.*, *J. Virol.* **82**, 4595–4611 (2008).
28. N. A. Dyer, C. Rose, N. O. Ejeh, A. Acosta-Serrano, *Trends Parasitol.* **29**, 188–196 (2013).
29. V. Bosco-Drayon *et al.*, *Cell Host Microbe* **12**, 153–165 (2012).
30. C. G. Elsik, *Genome Biol.* **11**, 106 (2010).
31. K. Hens, P. Lemey, N. Macours, C. Francis, R. Huybrechts, *Insect Mol. Biol.* **13**, 615–623 (2004).
32. R. Liu *et al.*, *Insect Mol. Biol.* **21**, 41–48 (2012).
33. R. Hardie, K. Vogt, A. Rudolph, *J. Insect Physiol.* **35**, 423–431 (1989).
34. G. Gibson, S. J. Torr, *Med. Vet. Entomol.* **13**, 2–23 (1999).
35. J. Brady, *Physiol. Entomol.* **16**, 153–161 (1991).
36. M. Friedrich, *Encyclopedia of Life Sciences* (Wiley, Chichester, 2010); doi: 10.1002/9780470015902.a0022898.
37. J. M. Lindh *et al.*, *PLOS Negl. Trop. Dis.* **6**, e1661 (2012).
38. A. Schmitt, A. Vogt, K. Friedmann, R. Paulsen, A. Huber, *J. Exp. Biol.* **208**, 1247–1256 (2005).

Members of the International *Glossina* Genome Initiative (IGGI)
Project leadership and conception: Junichi Watanabe,[76] Masahira Hattori,[6] Matthew Berriman,[64] Michael J. Lehane,[43] Neil Hall,[53,79] Philippe Solano,[49] Serap Aksoy,[36] Winston Hide,[67,80] Yeya Touré.[68] **Manual annotation coordinator, editor, and illustrator:** Geoffrey M. Attardo.[36] **Sequence production, assembly and global analysis:** Alistair C. Darby,[53] Atsushi Toyoda,[7] Christiane Hertz-Fowler,[64] Denis M. Larkin,[51] James A. Cotton,[64] Junichi Watanabe,[76] Mandy J. Sanders,[64] Martin T. Swain,[51] Masahira Hattori,[6] Matthew Berriman,[64] Michael A. Quail,[64] Noboru Inoue,[63] Sophie Ravel,[50] Todd D. Taylor,[66] Tulika P. Srivastava,[66,74] Vineet Sharma,[78,66] Wesley Warren,[69] Richard K. Wilson,[69] Yutaka Suzuki.[6] **Annotation automatic, manual annotation capture, and public release:** Daniel Lawson,[47] Daniel S. T. Hughes,[47] Karyn Megy.[47] **Olfaction group leaders:** Daniel K. Masiga,[61] Paul O. Mireji.[10] **Reproduction and development group leader:** Geoffrey M. Attardo.[36] **Signaling group leader:** Immo A. Hansen.[21] **Salivary group leader:** Jan Van Den Abbeele.[24] **Metabolism and stress response group leader:** Joshua B. Benoit.[14,36] **Horizontal transfer group leader:** Kostas Bourtzis.[34,3,35] **Digestion group leader:** Michael J. Lehane.[43] **Immunity group leader:** Serap Aksoy.[36] **Sensory annotations:** Daniel K. Masiga,[61] George F. O. Obiero,[61,67] Hugh M. Robertson,[33] Jeffery W. Jones,[17] Jing-Jiang Zhou,[13] Linda M. Field,[13] Markus Friedrich,[17] Paul O. Mireji,[10] Steven R. G. Nyanjom.[11] **Salivary annotations:** Erich L. Telleria,[36] Guy Caljon,[24] Jan Van Den Abbeele,[24] José M. C. Ribeiro.[57] **Midgut and digestion annotations:** Alvaro Acosta-Serrano,[42,43] Joshua B. Benoit,[14,36] Cher-Pheng Ooi,[43] Clair Rose,[43] David P. Price,[21] Lee R. Haines,[43] Michael J. Lehane.[43] **Metabolism annotations:** Alan Christoffels,[67] Cheolho Sim,[19] Daphne Q. D. Pham,[16] David L. Denlinger,[31] Dawn L. Geiser,[40] Irene A. Omedo,[26] Joshua B. Benoit,[14,36] Joy J. Winzerling,[39] Justin T. Peyton,[37] Kevin K. Marucha,[10] Mario Jonas,[67] Megan E. Meuti,[31] Neil D. Rawlings,[60] Paul O. Mireji,[10] Qirui Zhang,[31] Rosaline W. Macharia,[5,67] Veronika Michalkova,[36,54] Zahra Jalali Sefid Dashti.[67] **Signaling annotations:** Aaron A. Baumann,[65] Gerd Gäde,[15] Heather G. Marco,[15] Immo A. Hansen,[21] Jelle Caers,[20] Liliane Schoofs,[20] Michael A Riehle,[32] Wanqi Hu,[12] Zhijian Tu.[12] **Reproduction and development annotations:** Aaron M Tarone,[30] Anna R. Malacrida,[18] Caleb K. Kibet,[61] Joshua B. Benoit,[14,36] Francesca Scolari,[18] Geoffrey M. Attardo,[36] Jacobus J. O. Koekemoer,[44,46] Judith Willis,[25] Ludvik M. Gomulski,[18] Marco Falchetto,[18] Maxwell J. Scott,[29] Shuhua Fu,[9] Sing-Hoi Sze,[28] Thiago Luiz.[21] **Immunity annotations:** Brian Weiss,[36] Deirdre P. Walshe,[43] Jingwen Wang,[36] Joshua B. Benoit,[14,36] Geoffrey M. Attardo,[36] Mark Wamalwa,[67,77] Sarah Mwangi,[67] Serap Aksoy,[36] Urvashi N. Ramphul.[43] **Horizontal transfer and microbiome annotations:** Anna K. Snyder,[23] Corey L. Brelsford,[38] Gavin H. Thomas,[22] George Tsiamis,[35] Kostas Bourtzis,[34,3,35] Peter Arensburger,[2] Rita V. M. Rio,[23] Sandy J Macdonald,[22] Sumir Panji.[67,8] **IGGI annotation workshop contributors:** Adele Kruger,[67] Alan Christoffels,[67] Alia Benkahla,[48] Apollo S. P. Balyeidhusa,[59] Atway Msangi,[70] Cher-Pheng Ooi,[43] Chinyere K. Okoro,[72] Daniel K. Masiga,[61] Dawn Stephens,[58] Deirdre P. Walshe,[43] Eleanor J. Stanley,[47] Feziwe Mpondo,[56] Florence Wamwiri,[56] Furaha Mramba,[70] Geoffrey M. Attardo,[36] Geoffrey Siwo,[45] George F. O. Obiero,[61,67] George Githinji,[75] Gordon Harkins,[67] Grace Murilla,[56] Heikki Lehväslaiho,[1] Imna Malele,[70] Jacobus J. O. Koekemoer,[44,46] Joanna E. Auma,[56] Johnson K. Kinyua,[11] Johnson Ouma,[56,71] Junichi Watanabe,[76] Karyn Megy,[47] Loyce Okedi,[62] Lucien Manga,[73] Mario Jonas,[67] Mark Wamalwa,[67,77] Martin Aslett,[64] Mathurin Koffi,[49] Matthew Berriman,[64] Michael J. Lehane,[43] Michael W. Gaunt,[41] Mmule Makgamathe,[58] Neil Hall,[53,79] Nicola Mulder,[8] Oliver Manangwa,[70] Patrick P. Abila,[62] Patrick Wincker,[4] Paul O. Mireji,[10] Richard Gregory,[53] Rita V. M. Rio,[23] Rosemary Bateta,[10] Ryuichi Sakate,[55] Serap Aksoy,[36] Sheila Ommeh,[52] Stella Lehane,[43] Steven R. G. Nyanjom,[11] Tadashi Imanishi,[55] Todd D. Taylor,[66] Victor C. Osamor,[27] Vineet Sharma,[66,78] Winston Hide,[67,80] Yoshihiro Kawahara,[55,81] Joshua B. Benoit[14,36]

[1]Biological and Environmental Sciences and Engineering, King Abdullah University of Science and Technology (KAUST), 4700 King Abdullah University of Science and Technology, Thuwal, 23955-6900, Kingdom of Saudi Arabia. [2]Biological Sciences Department, California State Polytechnic University Pomona, 3801 West Temple Avenue, Pomona, CA 91768, USA. [3]Biomedical Sciences Research Center, Alexander Fleming Biomedical Sciences Research Center, 34 Fleming Street, Vari, 16672, Greece. [4]CEA, Genoscope, 2 Rue Gaston Crémieux, CP5706, Evry Cedex, 91507, France. [5]Center for Biotechnology and Bioinformatics, University of Nairobi, Post Office Box 30197-00100, Nairobi, Kenya, Nairobi, Kenya. [6]Center for Omics and

Bioinformatics, Department of Computational Biology, Graduate School of Frontier Sciences, The University of Tokyo, 5-1-5 Kashiwanoha, Kashiwa, Chiba, 277-8561, Japan. [7]Comparative Genomics Laboratory, National Institute of Genetics, 411-8540 Yata 1111, Mishima, Shizuoka, 411-8540, Japan. [8]Computational Biology Group, IIDMM, University of Cape Town Faculty of Health Sciences, Cape Town, 7925, South Africa. [9]Department of Biochemistry and Biophysics, Texas A&M University, 328B TAMU, College Station, TX 77843, USA. [10]Department of Biochemistry and Molecular Biology, Egerton University, Post Office Box 536, Njoro, Kenya. [11]Department of Biochemistry, Jomo Kenyatta University of Agriculture and Technology (JKUAT), Post Office Box 62000-00200, Nairobi, Kenya. [12]Department of Biochemistry, Virginia Polytechnic Institute and State University, 309 Fralin Hall, Blacksburg, VA 24061, USA. [13]Department of Biological Chemistry and Crop Protection, Rothamsted Research, West Common, Harpenden, Herts, AL5 2JQ, UK. [14]Department of Biological Sciences, McMicken College of Arts and Sciences, University of Cincinnati, Cincinnati, OH 45221, USA. [15]Department of Biological Sciences, University of Cape Town, Private Bag, Rondebosch, ZA-7700, South Africa. [16]Department of Biological Sciences, University of Wisconsin–Parkside, 900 Wood Road, Kenosha, WI 53144, USA. [17]Department of Biological Sciences, Wayne State University, 5047 Gullen Mall, Detroit, MI 48202, USA. [18]Department of Biology and Biotechnology, University of Pavia, Via Ferrata 9, Pavia, 27100, Italy. [19]Department of Biology, Baylor University, Waco, TX 76798, USA. [20]Department of Biology, KU Leuven, Naamsestraat 59, Leuven, B-3000, Belgium. [21]Department of Biology, New Mexico State University, Foster Hall 263, Las Cruces, NM 88003, USA. [22]Department of Biology, University of York, Wentworth Way, York, YO10 5DD, UK. [23]Department of Biology, West Virginia University, 53 Campus Drive, 5106 LSB, Morgantown, WV, USA. [24]Department of Biomedical Sciences, Institute of Tropical Medicine Antwerp, Nationalestraat 155, Antwerp, B-2000, Belgium. [25]Department of Cellular Biology, University of Georgia, 302 Biological Sciences Building, Athens, GA 30602, USA. [26]Department of Clinical Research, KEMRI-Wellcome Trust Programme, CGMRC, Post Office Box 230-80108, Kilifi, Kenya. [27]Department of Computer and Information Sciences, College of Science and Technology, Covenant University, P.M.B. 1023, Ota, Ogun State, Nigeria. [28]Department of Computer Science and Engineering, Department of Biochemistry and Biophysics, Texas A&M University, HRBB 328B TAMU, College Station, TX 77843, USA. [29]Department of Entomology, North Carolina State University, Campus Box 7613, Raleigh, NC 27695–7613, USA. [30]Department of Entomology, Texas A&M University, 2475 TAMU, College Station, TX 77843, USA. [31]Department of Entomology, The Ohio State University, 400 Aronoff Laboratory, 318 West 12th Avenue, Columbus, OH 43210, USA. [32]Department of Entomology, University of Arizona, 1140 East South Campus Drive, Forbes 410, Tucson, AZ 85721, USA. [33]Department of Entomology, University of Illinois at Urbana-Champaign, 505 South Goodwin Avenue, Urbana, IL 61801, USA. [34]Insect Pest Control Laboratory, Joint FAO/IAEA Programme of Nuclear Techniques in Food and Agriculture, Vienna, 1220, Austria. [35]Department of Environmental and Natural Resources Management, University of Patras, 2 Seferi Street, Agrinio, 30100, Greece. [36]Department of Epidemiology of Microbial Diseases, Yale School of Public Health, 60 College Street, New Haven, CT 06520, USA. [37]Department of Evolution, Ecology, and Organismal Biology, The Ohio State University, 300 Aronoff Laboratory, 318 West 12th Avenue, Columbus, OH 43210, USA. [38]Department of Natural Sciences, St. Catharine College, 2735 Bardstown Road., St. Catharine, KY 40061, USA. [39]Department of Nutritional Sciences, University of Arizona, Career and Academic Services, College of Agriculture and Life Sciences, Forbes Building, Room 201, Post Office Box 210036, Tucson, AZ 85721–0036, USA. [40]Department of Nutritional Sciences, University of Arizona, Shantz 405, 1177 East 4th Street, Tucson, AZ 85721–0038, USA. [41]Department of Pathogen Molecular Biology, London School of Hygiene and Tropical Medicine, Keppel Street, London, WC1E 7HT, UK. [42]Department of Parasitology, Liverpool School of Tropical Medicine, Pembroke Place, Liverpool, L3 5QA, UK. [43]Department of Vector Biology, Liverpool School of Tropical Medicine, Pembroke Place, Liverpool, L3 5QA, UK. [44]Entomology Section, Onderstepoort Veterinary Institute, Private Bag X5, Onderstepoort, 110, South Africa. [45]Eck Institute for Global Health, Department of Bio-

logical Sciences, University of Notre Dame, Notre Dame, IN 46556, USA. [46]Department of Veterinary Tropical Diseases, University of Pretoria, Private Bag X04, Onderstepoort, 110, South Africa. [47]European Molecular Biology Laboratories, European Bioinformatics Institute (EMBL-EBI), Wellcome Trust Genome Campus, Hinxton, Cambridge, Cambridgeshire, CB10 1SA, UK. [48]Group of Bioinformatics and Modeling, Laboratory of Medical Parasitology, Biotechnology, and Biomolecules, Institut Pasteur de Tunis, 13, Place Pasteur, BP74, Belvédère, Tunis, 1002, Tunisia. [49]Institut de Recherche pour le Développement (IRD), UMR 177 IRD-CIRAD INTERTRYP, CIRDES Bobo-Dioulasso, Burkina Faso. [50]Institut de Recherche pour le Développement (IRD), UMR 177 IRD-CIRAD INTERTRYP, LRCT Campus International de Baillarguet, Montpellier, France. [51]Institute of Biological, Environmental, and Rural Sciences, University of Aberystwyth, Old College, King Street, Aberystwyth, Ceredigion, SY23 3FG, UK. [52]Institute of Biotechnology Research, Jomo Kenyatta University of Agriculture and Technology (JKUAT), Post Office Box 62000-00200, Nairobi, Kenya. [53]Institute of Integrative Biology, The University of Liverpool, Crown Street, Liverpool, L69 7ZB, UK. [54]Institute of Zoology, Slovak Academy of Sciences, Dúbravská cesta 9, Bratislava, 845 06, Slovakia. [55]Integrated Database Team, Biological Information Research Center, National Institute of Advanced Industrial Science and Technology, Aomi 2-4-7, Koto-ku, Tokyo, 135-0064, Japan. [56]Kenya Agricultural Research Institute Trypanosomiasis Research Centre, Post Office Box 362, Kikuyu, 902, Kenya. [57]Laboratory of Malaria and Vector Research, National Institute of Allergy and Infectious Diseases, 12735 Twinbrook Parkway, Room 2E-32D, Rockville, MD 20852, USA. [58]Technology Innovation Agency, National Genomics Platform, Post Office Box 30603, Mayville, Durban, 4058, South Africa. [59]Department of Biochemistry and Sports Science, Makerere University, Post Office Box 7062, Kampala, Uganda. [60]Bateman Group, Wellcome Trust Sanger Institute, EMBL European Bioinformatics Institute, Wellcome Trust Genome Campus, Hinxton, Cambridge, Cambridgeshire, CB10 1SA, UK. [61]Molecular Biology and Bioinformatics Unit, International Center of Insect Physiology and Ecology, Duduville Campus, Kasarani, Post Office Box 30772-00100, Nairobi, Kenya. [62]National Livestock Resources Research Institute (NaLIRRI), Post Office Box 96, Tororo, Uganda. [63]National Research Center for Protozoan Diseases, Obihiro University of Agriculture and Veterinary Medicine, Inada-cho, Obihiro, Hokkaido, 080-8555, Japan. [64]Parasite Genomics Group, Wellcome Trust Sanger Institute, Wellcome Trust Genome Campus, Hinxton, Cambridge,

Cambridgeshire, CB10 1SA, UK. [65]Riddiford Laboratory, Janelia Farm Research Campus, Howard Hughes Medical Institute, 19700 Helix Drive, Ashburn, VA 20147, USA. [66]RIKEN Center for Integrative Medical Sciences, 1-7-22 Suehiro-cho, Tsurumi-ku, Yokohama, Kanagawa, 230-0045, Japan. [67]South African National Bioinformatics Institute, South African MRC Bioinformatics Unit, University of the Western Cape, 5th Floor Life Sciences Building, Modderdam Road, Bellville 7530, South Africa. [68]Special Programme for Research and Training in Tropical Diseases (TDR), WHO, Avenue Appia 20, 1211 Geneva 27, Switzerland. [69]The Genome Institute, Washington University School of Medicine, St. Louis, MO 63110, USA. [70]Tsetse and Trypanosomiasis Research Institute (TTRI), Majani Mapana, Off Korogwe Road, Post Office Box 1026, Tanga, Tanzania. [71]Vector Health International, Post Office Box 15500, Arusha, Tanzania. [72]Wellcome Trust Sanger Institute, Wellcome Trust Genome Campus, Hinxton, Cambridge, Cambridgeshire, CB10 1SA, UK. [73]WHO Regional Office for Africa, WHO, Cité du Djoué, Post Office Box 06, Brazzaville, Congo. [74]School of Basic Sciences, Indian Institute of Technology, Mandi 175001, Himachal Pradesh, India. [75]Department of Parasite, Vector, and Human Biology, KEMRI-Wellcome Trust Programme, CGMRC, Post Office Box 230-80108, Kilifi, Kenya. [76]Institute of Medical Science, The University of Tokyo, 4-6-1 Shirokanedai, Minato-ku, Tokyo, 108-8639, Japan. [77]Department of Biochemistry and Biotechnology, Kenyatta University, Post Office Box 43844-00100, Nairobi, Kenya. [78]Department of Biological Sciences, Indian Institute of Science Education and Research, Indore Bypass Road, Bhauri District, Bhopal, Madhya Pradesh, 462066, India.[79]Faculty of Science, King Abdulaziz University, Jeddah, 21589, SA. [80]Department of Biostatistics, Harvard School of Public Health, 655 Huntington Ave. Boston, MA 02461. [81]Bioinformatics Research Unit, Agrogenomics Research Center, National Institute of Agrobiological Sciences, 2-1-2, Kannondai, Tsukuba, Ibaraki 305-8602, Japan.

Discovery of Brainwide Neural-Behavioral Maps via Multiscale Unsupervised Structure Learning

Joshua T. Vogelstein,[1,2]* Youngser Park,[1]* Tomoko Ohyama,[3]* Rex A. Kerr,[3] James W. Truman,[3] Carey E. Priebe,[1]†‡ Marta Zlatic[3]†‡

A single nervous system can generate many distinct motor patterns. Identifying which neurons and circuits control which behaviors has been a laborious piecemeal process, usually for one observer-defined behavior at a time. We present a fundamentally different approach to neuron-behavior mapping. We optogenetically activated 1054 identified neuron lines in *Drosophila* larvae and tracked the behavioral responses from 37,780 animals. Application of multiscale unsupervised structure learning methods to the behavioral data enabled us to identify 29 discrete, statistically distinguishable, observer-unbiased behavioral phenotypes. Mapping the neural lines to the behavior(s) they evoke provides a behavioral reference atlas for neuron subsets covering a large fraction of larval neurons. This atlas is a starting point for connectivity- and activity-mapping studies to further investigate the mechanisms by which neurons mediate diverse behaviors.

Nervous systems can generate a wide range of motor outputs, depending on their incoming sensory inputs and internal state. A comprehensive understanding of how behavioral diversity and selection is achieved requires the identification of neural circuits that mediate many distinct motor patterns in a given nervous system. Mapping a functional circuit for one be-

havior in a given organism is difficult enough, but doing so for many behaviors has been almost impossible. The first step in mapping a circuit that mediates a behavior is to identify neurons whose activity is causally related to the behavior. Such a list of neurons provides a starting point for identifying the connectivity patterns between the relevant neurons. Thus, to map circuits underlying many behaviors, one would need a comprehensive neuron-behavior atlas of the nervous system that would list all neurons causally related with each behavior.

Generating such neuron-behavior maps has been difficult for several reasons. First, the experimental tools to selectively manipulate small sets of neurons while simultaneously observing natural behavior were lacking. Fortunately, recent advances in genetic toolkits allow reasonably selective manipulation of neuron types in genetic model organisms, such as *Drosophila* (*1–3*). Advances in behavior tracking methods allow high-resolution monitoring of the effect of such manipulations (*4, 5*). Neural manipulation screens can therefore be coupled with high-resolution monitoring of motor outputs to causally link complex behaviors to correspondingly complex neural circuits.

Second, establishing the causal links between neural manipulations and the resulting time-varying behavioral responses is a daunting computational statistics challenge. Existing supervised machine-learning methods can detect only predetermined

[1]Whiting School of Engineering, Johns Hopkins University, Baltimore, MD 21218, USA. [2]Department of Statistical Science, Duke University, Durham, NC 27708, USA. [3]Janelia Farm Research Campus, Ashburn, VA 20147, USA.

*These authors contributed equally to this work.
†These authors contributed equally to this work.
‡Corresponding author. E-mail: cep@jhu.edu (C.E.P.); zlaticm@janelia.hhmi.org (M.Z.)

behaviors (*6*); moreover, they are limited by the speed with which humans can annotate training data sets. An alternative approach uses unsupervised clustering of the multidimensional time series. However, the high-content and high-throughput nature of the time-varying behavior data presents both computational and statistical challenges.

We developed a methodology for data-driven neuron-behavior mapping and applied it to larval *Drosophila*. The nervous system of larval *Drosophila* consists of a well-developed brain and nerve cord containing only about 10,000 neurons, rendering it sufficiently simple to obtain a relatively comprehensive characterization of it. Moreover, there exist more than 1000 genetic GAL4 lines in *Drosophila* larvae with recently characterized sparse neuronal expression patterns that together cover most of the 10,000 neurons in the larval nervous system (http://flweb.janelia.org/cgi-bin/flew.cgi) (*3*).

Optogenetic Neural Activation Screen

We designed an optogenetic neural activation screen (see supplementary materials) to obtain a neuron line–behavior atlas of the larval nervous system that would contain causal links between neuron lines and the motor patterns they control. We used 1049 distinct GAL4 lines to selectively target channelrhodopsin-2 (ChR2) (*7*) to sparse distinct subsets of neurons, with each line activating 2 to ~15 neurons. Because these lines essentially span the entire set of larval neurons, some lines activate sensory and motor neurons as well as many neurons involved in decisions and action selection. We included four positive control lines in the screen that drive expression in nociceptive, mechanosensory, and proprioceptive neurons, previously determined to reliably mediate distinct behaviors (*8–10*), as well as one negative control line in which no neurons were optogenetically activated (*2, 10*), for a total of

1054 lines and 37,780 animals tested. In each experiment, we exposed dishes of larvae to 470-nm light stimuli (one exposure of 30 s followed by four exposures of 5 s, with a 30-s interval after the long exposure and a 10-s interval between the short exposures) to optogenetically activate Ch2-expressing neurons; we captured video before, during, and after stimulation (Fig. 1A). The Multi-Worm Tracker (MWT) software (*4*) tracked time-varying, two-dimensional closed contours of larvae and sketched eight time-varying features that collectively characterize larval shape and motion (Fig. 1B). Streaming and sketching reduced the data complexity by a factor of more than 200,000, enabling a compressive yet expressive representation of the data. These reduced data served as the input into the multiscale unsupervised structure learning methodology to reveal data-driven behavior types (Fig. 1C). Each behavior type was then linked to the subset of lines that mediate them (Fig. 1D).

Discovery of Behavior Types via Multiscale Unsupervised Structure Learning

As a first step, we sought to discover a large, inclusive, and nonpredetermined set of statistically distinguishable behavioral responses performed by the 37,780 animals during the first (30-s) optogenetic activation period. Recently developed methods for multiscale unsupervised structure learning (*11–13*) can be thought of as generalizations of manifold learning techniques, in that they can learn structures more general than manifolds, such as unions of manifolds. We adopted iterative denoising tree (IDT) methodology (*11, 14*), which offers demonstrated utility across several domains (*15, 16*).

The input to IDT is the collection of all 37,780 larval sketches, irrespective of which line generated each sketch (Fig. 2A). IDT consists of five key
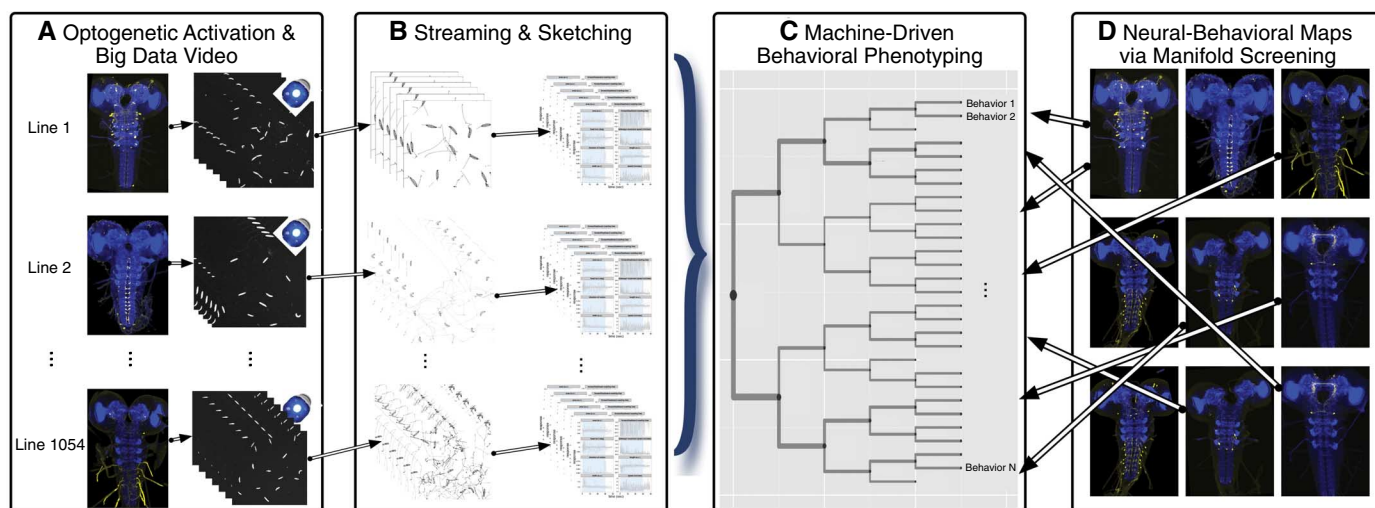
Fig. 1. Experimental design and methodology for obtaining neuron line—behavior maps. (**A**) Optogenetic activation screen of 1054 lines while digitally recording high-dimensional larval responses. (**B**) Streaming extracts the contours of each larva from each video frame; sketching extracts eight time-varying features from the contours that characterize the shape and motion of each animal. (**C**) Machine-driven behavioral phenotyping learns phenotype categories (called behaviotypes) from the sketches via multiscale unsupervised structure learning. (**D**) Manifold testing discovers which neuron lines evoke sets of behaviors that are different from negative controls, which facilitates associating each such line with some number of behaviotypes.

steps collectively resulting in a hierarchical clustering tree. In step one, IDT computes a dissimilarity between all pairs of sketches (Fig. 2B). The dissimilarity choice can have drastic computational and inferential impact; thus, choosing one that captures signal variability, and can be efficiently computed, is key to the success of IDT. This is important because the 37,780 observations yield more than 1.4 billion dissimilarities. We used a smoothed distance between the sketches of the data (17) as a dissimilarity function (see supplementary materials).

In step two, IDT transforms the interpoint dissimilarity matrix into a set of n relatively high-dimensional Euclidean vectors, via an approach such as multidimensional scaling (18). Once each data point is in Euclidean space, an extensive toolkit from classical statistical machine learning is applicable (19).

Step three consists of iterating, once per tree depth, the following substeps: (i) select a subset of the dimensions from each cluster, (ii) cluster all the nodes of the partition tree obtained thus far, and (iii) check for convergence at each resulting cluster. For each cluster at each scale, the number of dimensions to select and the number of sub-clusters to generate are decided in a data-driven adaptive fashion. The final result is a hierarchical tree characterizing families and subfamilies of behavioral responses (Fig. 2C).

To visualize the phenotype categories learned by IDT (or nodes/clusters of the tree), called behaviotypes, Fig. 2D shows, for each cluster, the time-varying means and standard errors for each of the eight sketched time-varying features. Each behaviotype is well separated from at least some other cluster for at least some of the time for at least some features. This provides an intuitive validation of the uniqueness of the behaviotypes, thereby demonstrating the efficacy of IDT.

IDT Identified Both Previously Described and Novel Behavioral Sequences

Inspection of the time-varying means of the responses of each behaviotype cluster (Fig. 2D) and of the videos of animals at the center of each cluster (movies S1 to S58) revealed that IDT clustered many of the larval behavioral responses into categories similar to those a human expert would have identified. We could label the nodes of the learned tree post hoc (Fig. 2, E and F). For example, the first division revealed by IDT differentiates between slow and fast families. The fast family is subdivided into turn-avoid and escape-crawl subfamilies. IDT further distinguished between the right turn–left turn–avoid and the symmetric left turn–right turn–avoid sequence (fig. S1) and between two types of escape crawl that are preceded by more or less hunching and wiggling (fig. S2). The slow family is subdivided into still or backup and turner; the still or backup is further subdivided into still (no movement) and backup (lots of backward crawling) (fig. S3), and the turner is subdivided into turn-turn-turn (continuous turning) and turn-slow-crawl (fig. S4).
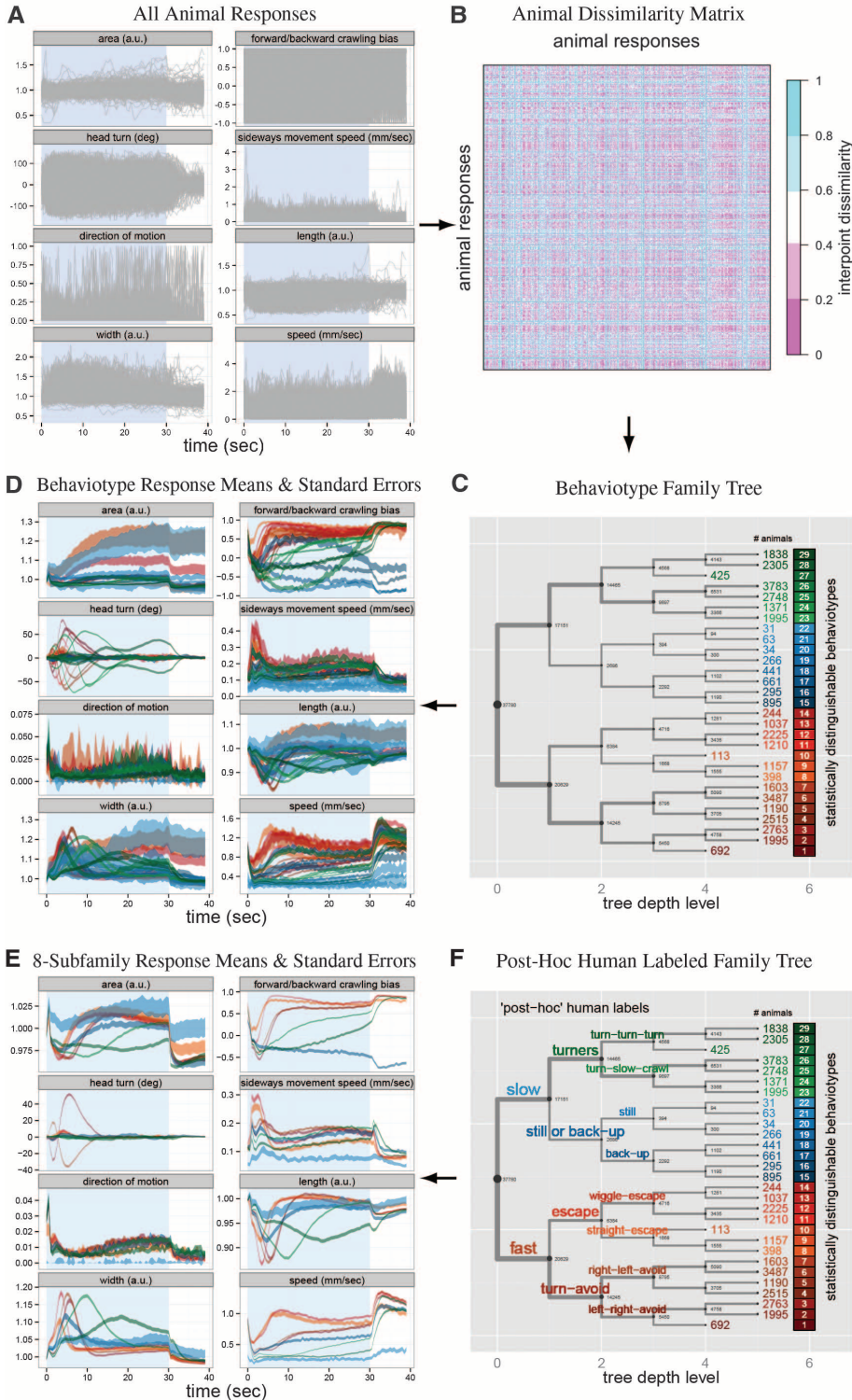
Fig. 2. IDT detected 29 distinguishable behaviotypes. (**A**) The input to IDT is the collection of all 37,780 larval sketches. Structure is not obvious. Blue shading represents the period of photostimulation in all figures. (**B**) Dissimilarity matrix between all pairs of animals. Only ~1.4 million of the ~1.4 billion pairwise dissimilarities are shown. (**C**) $\hat{K} = 29$ distinguishable behavior clusters (behaviotypes) were identified using IDT to learn a data-adaptive clustering of the high-content responses. (**D**) Mean and standard error of the responses of each of the 29 behaviotypes identified in (C), using the same color code as in (C). (**E**) Mean and standard error of the responses of the eight behaviotype subfamilies. (**F**) The same tree as in (C) but with post hoc human labels assigned to the automatically detected behaviotype families and subfamilies.

After level three of the behaviotype tree, subjective visual inspection of the videos failed to detect differences between related behaviotypes. Nonetheless, they do have distinct properties for some of the features for some of the time (Fig. 2D). Behaviotypes 17 and 18 represent animals

with tracking errors in which the MWT streaming and sketching software inverted the front and back of the animals (fig. S6 and movies S33 to S36). IDT assigned animals with this type of tracking error to the two separate behavioral clusters, conveniently isolating such errors.

Many of the optogenetically evoked, automatically detected behaviotype subfamilies are similar to previously described larval responses to various natural stimuli (10, 20, 21). IDT also detected behavioral categories not previously documented. This is unsurprising because only
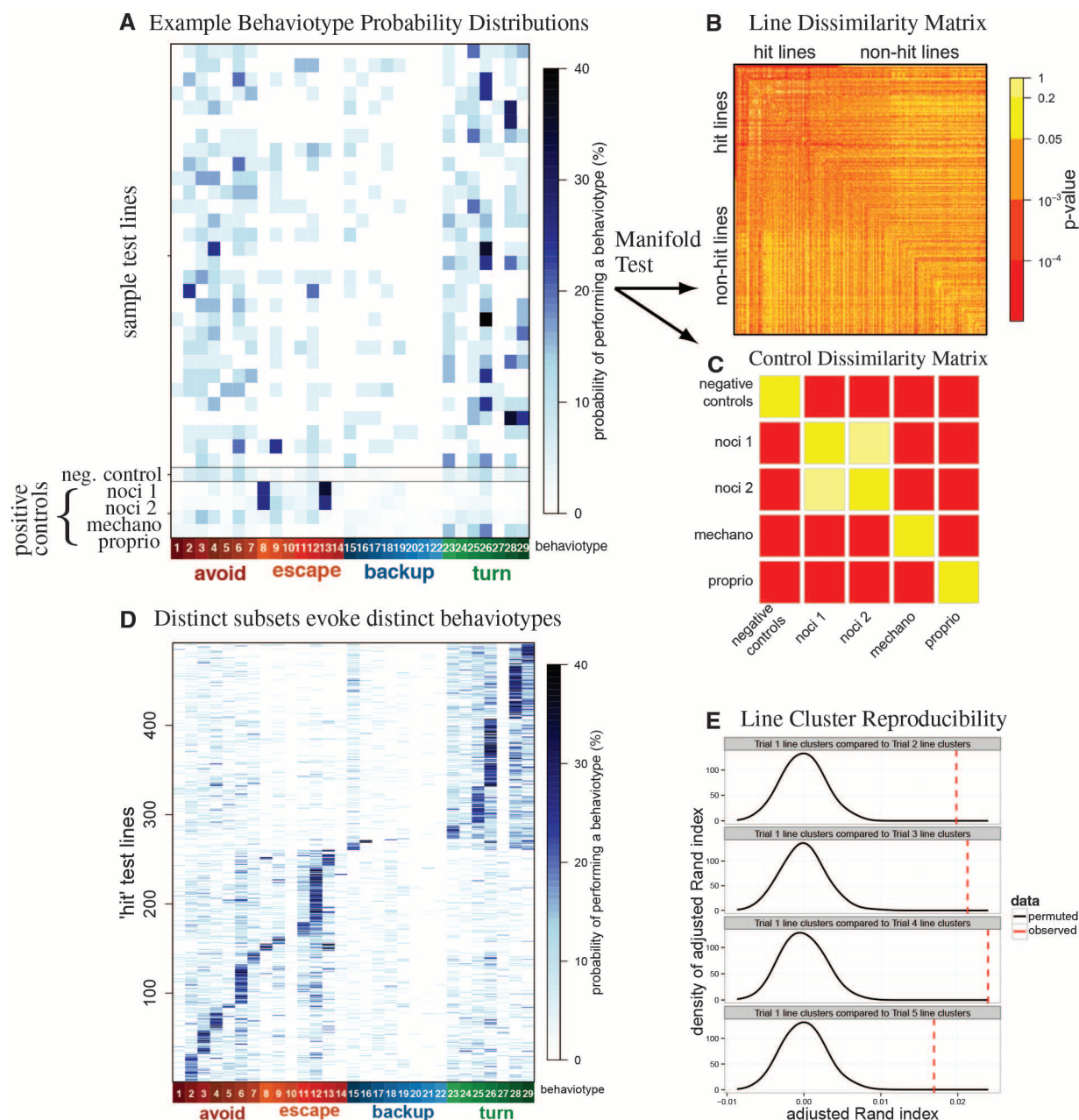
Fig. 3. Learning neuron line–behaviotype maps via manifold testing. (**A**) Behaviotype probability vectors for a number of lines. Each row shows the percentage of animals performing a behaviotype for optogenetic activation of a particular line: 30 randomly sampled test lines (top), negative controls (pBDPU-ChR2) with no optogenetically activated neurons (middle), and positive controls—nociceptive (ppk-ChR2, noci 1; R38A10-ChR2, noci 2); mechanosensory (iav-ChR2); and proprioceptive (R11F05-ChR2) neuron lines with known effects on behavior (bottom). (**B**) Line dissimilarity matrix showing pairwise P values for all 1054 lines computed via the manifold test. The first entry is the negative control. Remaining entries are sorted according to P value for the comparison with the negative control, from lowest to highest; 455 lines (4 positive controls + 451 test

lines) were significantly different from the negative control (hit lines), and 598 lines were not (nonhit lines). (**C**) The P values between all pairs of known somatosensory neuron lines and negative controls are "correct": Those that should be significantly different according to previous studies are, and those that should not be are not. This panel is a subset (top left 5 × 5 submatrix entries) of (B). (**D**) Behaviotype probability distributions for all 451 significantly distinct test neuron lines, sorted according to their maximum probability behaviotype. (**E**) The clusters of lines that bias the probability toward the same behaviotypes are reproducible, demonstrated by the fact that the mode of the empirical null distribution of the adjusted Rand index (ARI) for reliable clustering (black curve) is lower in all four repeated trials than the observed ARI (all P values < 0.01).
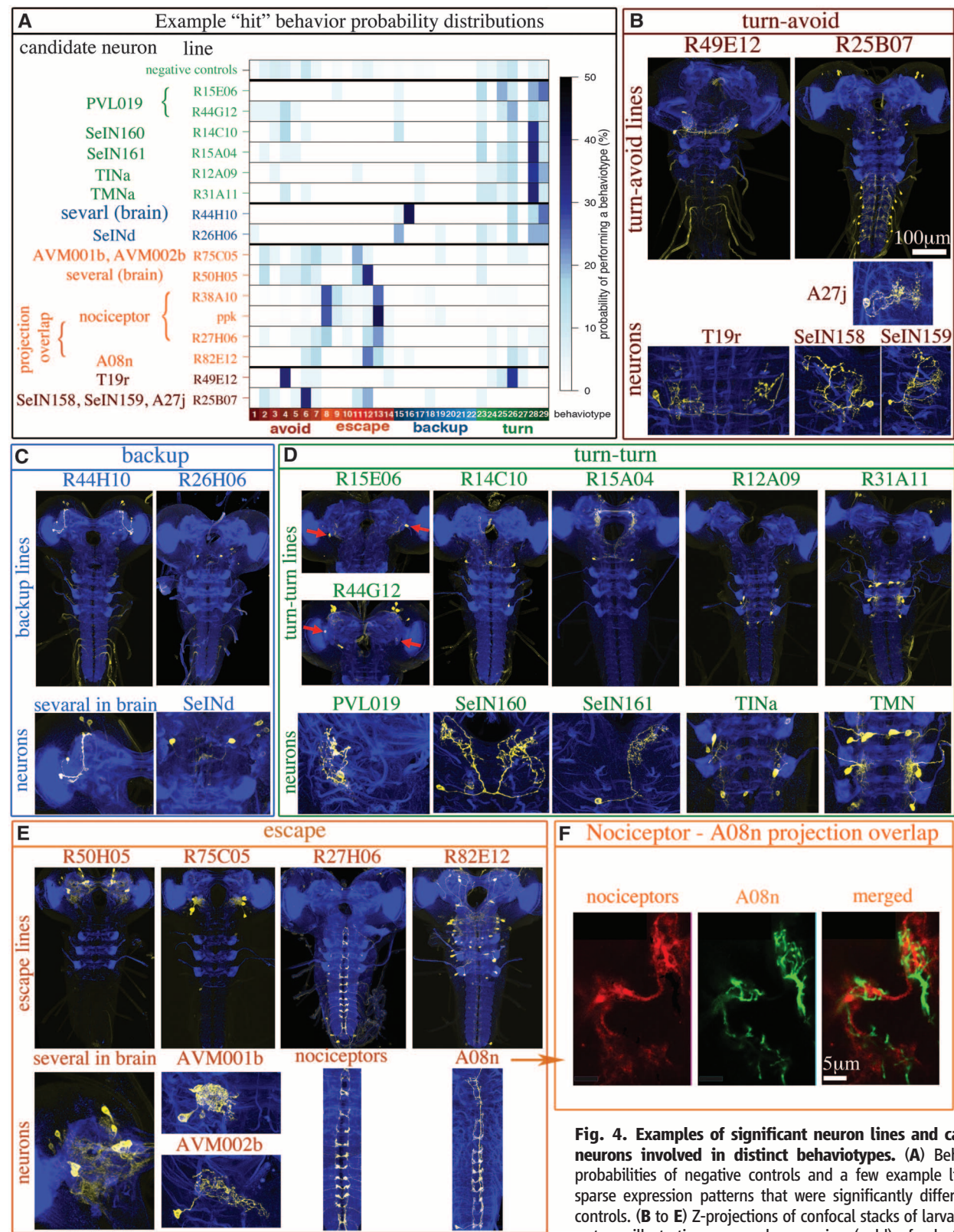
Fig. 4. Examples of significant neuron lines and candidate neurons involved in distinct behaviotypes. (**A**) Behaviotype probabilities of negative controls and a few example lines with sparse expression patterns that were significantly different from controls. (**B** to **E**) Z-projections of confocal stacks of larval nervous systems illustrating neuronal expression (gold) of selected lines. Neuropil is stained for reference with antibody to N-cadherin (blue). High-resolution images of candidate neurons from these lines are shown beneath the lower-magnification images of the entire nervous system. These lines biased the probability toward (B) turn-avoid, (C) backup, (D) turn-turn, and (E) escape behaviotype subfamilies. In some cases, two or more lines that drive in the same neuron biased the probability toward the same behaviotype. R15E06 and R44G12 both drive in PVL019 (red arrows) and biased the probability toward turn-turn behaviotypes 25, 26, 28, and 29. Ppk, R38A10, and R27H06 drive in the same nociceptor neurons and biased the probability toward escape behaviotype 13. (**F**) R82E12 projections (green) overlap tightly with nociceptive axon terminals (red) in a single 0.5-μm confocal section, likely forming synaptic contacts. These two lines both biased the probability toward the same escape behaviotype 13 and likely belong to the same anatomical and functional neural circuit.

a relatively small portion of the larval stimulus space has been explored in previous studies.

Biased Probabilistic Relationship Between Neuron Activation and Behaviotypes

We used the prior results that nociceptive, mechanosensory, and proprioceptive sensory neurons reliably mediate distinct behaviors to assess the validity of this behavior discovery approach. The optogenetic screen included lines that targeted ChR2 expression to the nociceptive [ppk and R38A10 (10, 22)], mechanosensory (iav) (9), and proprioceptive (R11F05) neurons. Activating distinct sensory neurons mostly biased the behaviotype probability toward distinct subfamilies: (i) Nociceptive stimulation tended to evoke escape behaviotypes; (ii) mechanosensory stimulation tended to evoke turn-avoid behaviotypes; and (iii) proprioceptive tended to evoke slow behaviotypes (Fig. 3A). In contrast, activating the same nociceptive neurons with two distinct GAL4 lines evoked similar behaviotype probability distributions. The response profiles of the negative controls (pBDPU-ChR2) (2, 10) that did not express ChR2 likely represented larval reactions to blue light alone and appeared different from those of animals with optogenetically activated nociceptive, mechanosensory, or proprioceptive neurons (Fig. 3A). Finally, analysis of the 1049 previously unexplored neuronal test lines (Fig. 3A; top rows show 30 examples) demonstrated that distinct lines bias the probability toward distinct behaviotypes. Optogenetic stimulation of different animals of the same line (that is, activating the "same" neurons in different animals) did not always evoke the same behavior; rather, it biased the probability toward a few possible behaviotypes.

We also applied IDT jointly to the responses from the four additional identical repeats of the 5-s optogenetic activation stimulus of the same organisms and analyzed the behaviotype distributions of the same individuals on different trials (fig. S5A). We found that even repeated activation of the same neurons in the same individual did not always evoke the same behaviotype; rather, it biased the probability toward a few possible behaviotypes (fig. S5A). However, the responses of individual animals were significantly more similar to each other than to the responses of distinct individuals (fig. S5B).

Screening Neuron Lines via Manifold Testing

Each neuron line is characterized by the empirical probability of larvae performing each behaviotype and is encoded by a $\hat{K} = 29$-dimensional vector with nonnegative entries that sum to unity. This encoding enables direct testing of each pair of lines by choosing an appropriate test statistic and applying a standard test. However, the choice of test statistic for these multivariate probability vectors is not obvious; moreover, existing tests do not sufficiently address the multiple dependent hypothesis–testing problem. We therefore devised the following manifold test (see supplementary materials).

The main idea of the manifold test is to jointly and nonlinearly embed each experiment into a lower-dimensional representation. The test first computes the Hellinger distance between all 1054^2 pairs of experiments and then uses multidimensional scaling (MDS) (18) to obtain a low-dimensional Euclidean embedding. In this space, one can easily compute the difference between any pair of trials via an "out-of-sample" extension to this embedding methodology (23). Moreover, via bootstrap, the test computes the significance of those differences (24). Then it adjusts the P values to account for multiple correlated hypotheses (25) and other batch effects (26). Using this manifold test, we identified a large fraction of lines (4 positive controls and 451 test lines) as being significantly different (hit lines) from the negative control line (Fig. 3B; see supplementary data set 1 for the list of all such lines).

The positive control lines with different neurons activated (nociceptive, mechanosensory, and proprioceptive) were all significantly distinct from the negative controls and from each other (Fig. 3C). The two positive control lines with the same nociceptive neurons activated (ppk and R38A10) were not significantly different from one another (Fig. 3C). The known somatosensory neuron controls lend additional credence to this manifold test.

A Neuron Line–Behaviotype Atlas

Given the list of lines significantly distinct from the negative controls, we desired to identify which lines bias the probability toward which behaviotypes, thereby generating a neuron line–behaviotype atlas. Many lines biased the probability of behavior primarily to one behaviotype, with the remaining probability distributed to a few related behaviotypes (Fig. 3D). We confirmed that the line clusterings are reliable by applying IDT independently to the four additional repeats of the 5-s optogenetic activation stimulus of the same organisms, and then comparing how similar the line clusters from each of these additional trials were to the first trial. The identified line clusters were indeed reproducible (P < 0.001 via an adjusted Rand index permutation test, Fig. 3E).

For most behaviotypes, activation of at least one line biased the probability toward that behaviotype significantly more than the negative controls (see supplementary data set 1 for significant line–behaviotype probability distribution numbers and P values). Collectively, these significance results constitute a reference atlas that associates each neural line with a set of behaviors it mediates (and vice versa, associating each behaviotype with a set of neural lines that mediates it). Images of neuronal expression patterns of all of these lines are available from http://flweb.janelia.org/cgi-bin/flew.cgi.

Figure 4 shows examples of behaviotype probability vectors (Fig. 4A) and neuronal expression patterns of a few significant lines that bias the probability toward turn-avoid (Fig. 4B), backup

(Fig. 4C), turn-turn (Fig. 4D), or escape subfamilies (Fig. 4E). We analyzed with higher resolution the projections of individual neurons from some of these lines using a single-cell flip-out method (27) and gave names to the identified neurons. A number of the significant lines only drove expression in single pairs of larval neurons, yet they still biased the probability toward specific behaviotypes. For example, activation of the pair of PVL019 neurons in the basal posterior region of the larval brain (with the line R15E06) or of the pair of SeIN161 neurons in the subesophageal ganglion (with the line R15A04) evoked turn-turn-turn behaviotypes in a large fraction of animals. This indicates that single pairs of cells can exert drastic control over behavior, consistent with findings in other systems (28, 29).

In some cases, we found that lines that contribute to the same behaviotypes contain neurons with anatomically overlapping projections that may constitute presynaptic and postsynaptic partners. For example, the motor neurons in R31A11 and the interneurons in R12A09 both strongly evoked turn-turn-turn behaviotype 28, and their projections occupy the same motor region of the nerve cord and likely overlap. Similarly, R27H06 and R82E12 (Fig. 4E) biased the probability toward escape behaviotype 13 and drive expression in the nociceptive neurons, and in a class of ascending projection neurons (A08n), respectively. Double labeling of the nociceptive and the A08n neurons confirmed that their arbors do indeed tightly overlap, likely forming synaptic contacts (Fig. 4F).

Discussion

An important step toward understanding the structure and function of neural circuits is to identify comprehensive lists of neurons whose activation is causally related to a comprehensive set of motor patterns. This requires statistical approaches for identifying structure in high-dimensional behavior data.

Methods for systematic, automated, and unsupervised clustering are rarely applied to high-dimensional behavioral data. A recent study used unsupervised learning to detect behavioral motifs defined as sequences of four "eigenworm" positions in mutant and wild-type freely moving *Caenorhabditis elegans* in the absence of any stimulation (30). Here, we developed methods for clustering entire behavioral response sequences during a stimulation period and made use of discovered behavioral clusters to detect significantly distinct experiments from a large-scale screen, providing statistical validation that the learned clusters are meaningful. We applied these methods to discover neurons causally related to behaviors, providing a proof of principle that it is possible to classify neurons in terms of their activation of motor outputs in a fully automated way.

The collection of neuron line–behaviotype relationships collectively constitutes an atlas. Starting with a list of lines whose activation is sufficient to evoke each behaviotype, the relevant

individual neurons from each line can readily be identified. Whereas some lines drive expression in a single pair of neurons, most drive in the range of two to five candidate neuron types. In cases where lines drive in more than one neuron, intersectional strategies can be used to target individual neurons and test the effect of their activation on behavior (2).

This reference atlas provides a valuable starting point for understanding how distinct behaviors are selected and controlled. Large-scale connectomics (31–33) and functional brain imaging methods (34, 35) will soon provide similarly comprehensive views of the structure of neural circuits and of the activity patterns within those circuits. However, a connectome by itself does not carry information about which neurons mediate which behaviors. Similarly, a brain-activity map alone shows the flow of information through the network, but does not reveal causal relationships between neurons and behavior. Together, the neuron-behavior map, the neuron-activity map, and the connectome complement one another, laying the groundwork for a brainwide understanding of the principles by which brains generate behavior.

The statistical methods presented here are generally applicable to discovery of scientifically meaningful structure from big data—a pressing problem in the information age.

References and Notes

1. B. D. Pfeiffer et al., Proc. Natl. Acad. Sci. U.S.A. 105, 9715–9720 (2008).
2. B. D. Pfeiffer et al., Genetics 186, 735–755 (2010).
3. A. Jenett et al., Cell Rep. 2, 991–1001 (2012).
4. N. A. Swierczek, A. C. Giles, C. H. Rankin, R. A. Kerr, Nat. Methods 8, 592–598 (2011).
5. K. Branson, A. A. Robie, J. Bender, P. Perona, M. H. Dickinson, Nat. Methods 6, 451–457 (2009).
6. M. Kabra, A. A. Robie, M. Rivera-Alba, S. Branson, K. Branson, Nat. Methods 10, 64–67 (2013).
7. C. Schroll et al., Curr. Biol. 16, 1741–1747 (2006).
8. R. Y. Hwang et al., Curr. Biol. 17, 2105–2116 (2007).
9. C. W.-H. Wu et al., Neuron 70, 229–243 (2011).
10. T. Ohyama et al., PLOS ONE 8, e71706 (2013).
11. C. E. Priebe, D. J. Marchette, D. M. Healy, Mod. Signal Process. 46, 223 (2003).
12. W. K. Allard, G. Chen, M. Maggioni, Appl. Comput. Harmon. Anal. 32, 435–462 (2012).
13. P. Bendich, D. Cohen-Steiner, H. Edelsbrunner, J. Harer, D. Morozov, in 48th Annual IEEE Symposium on Foundations of Computer Science (FOCS'07) (IEEE, Providence, RI, 2007), pp. 536–546.
14. K. E. Giles, M. W. Trosset, D. J. Marchette, C. E. Priebe, Comput. Stat. 23, 497–517 (2008).
15. C. E. Priebe, D. J. Marchette, D. M. Healy, IEEE Trans. Pattern Anal. Mach. Intell. 26, 699–708 (2004).
16. D. Karakos, S. Khudanpur, J. Eisner, C. E. Priebe, in Proceedings of the 2005 IEEE International Conference on Acoustics Speech and Signal Processing ICASSP (IEEE, Philadelphia, 2005), vol. 5, pp. 1081–1084.
17. C. E. Priebe, IEEE Trans. Pattern Anal. Mach. Intell. 23, 404–413 (2001).
18. I. Borg, P. J. F. Groenen, Modern Multidimensional Scaling: Theory and Applications (Springer, New York, 2010).
19. T. Hastie, R. Tibshirani, J. Friedman, The Elements of Statistical Learning: Data Mining, Inference, and Prediction (Springer, New York, 2001).
20. E. A. Kane et al., Proc. Natl. Acad. Sci. U.S.A. 110, E3868–E3877 (2013).
21. M. Kernan, D. Cowan, C. Zuker, Neuron 12, 1195–1206 (1994).
22. J. A. Ainsley et al., Curr. Biol. 13, 1557–1563 (2003).
23. M. Tang, Y. Park, C. E. Priebe, http://arxiv.org/abs/1305.4893 (2013).
24. P. I. Good, Permutation, Parametric, and Bootstrap Tests of Hypotheses (Springer, New York, 2010).
25. D. Yekutieli, Y. Benjamini, Ann. Stat. 29, 1165–1188 (2001).
26. R. A. Fisher, Statistical Methods for Research Workers (Oliver and Boyd, Edinburgh, 1925).
27. G. Struhl, K. Basler, Cell 72, 527–540 (1993).
28. I. Kupfermann, K. R. Weiss, Behav. Brain Sci. 1, 3–10 (1978).
29. B. Hedwig, J. Neurophysiol. 83, 712–722 (2000).
30. A. E. X. Brown, E. I. Yemini, L. J. Grundy, T. Jucikas, W. R. Schafer, Proc. Natl. Acad. Sci. U.S.A. 110, 791–796 (2013).
31. D. D. Bock et al., Nature 471, 177–182 (2011).
32. M. Helmstaedter, Nat. Methods 10, 501–507 (2013).
33. S.-Y. Takemura et al., Nature 500, 175–181 (2013).
34. M. B. Ahrens, M. B. Orger, D. N. Robson, J. M. Li, P. J. Keller, Nat. Methods 10, 413–420 (2013).
35. T. Schrödel, R. Prevedel, K. Aumayr, M. Zimmer, A. Vaziri, Nat. Methods 10, 1013–1020 (2013).

REPORTS

A Dual-Catalysis Approach to Enantioselective [2 + 2] Photocycloadditions Using Visible Light

Juana Du,* Kazimer L. Skubi,* Danielle M. Schultz,* Tehshik P. Yoon†

In contrast to the wealth of catalytic systems that are available to control the stereochemistry of thermally promoted cycloadditions, few similarly effective methods exist for the stereocontrol of photochemical cycloadditions. A major unsolved challenge in the design of enantioselective catalytic photocycloaddition reactions has been the difficulty of controlling racemic background reactions that occur by direct photoexcitation of substrates while unbound to catalyst. Here, we describe a strategy for eliminating the racemic background reaction in asymmetric [2 + 2] photocycloadditions of α,β-unsaturated ketones to the corresponding cyclobutanes by using a dual-catalyst system consisting of a visible light–absorbing transition-metal photocatalyst and a stereocontrolling Lewis acid cocatalyst. The independence of these two catalysts enables broader scope, greater stereochemical flexibility, and better efficiency than previously reported methods for enantioselective photochemical cycloadditions.

Modern stereoselective synthesis enables the construction of a vast array of organic molecules with precise control over their three-dimensional structure (1, 2), which is important in a variety of fields ranging from drug discovery to materials engineering. Photochemical reactions could have a substantial impact on these fields by affording direct access to certain structural motifs that are otherwise difficult to construct (3, 4). For example, the most straightforward methods for the construction of cyclobutanes and other strained four-membered rings are photochemical [2 + 2] cycloaddition reactions. The stereochemical control of photocycloadditions, however, remains much more challenging than the stereocontrol of analogous non-photochemical reactions (5, 6) despite the chemistry community's sustained interest in photochemical stereoinduction over the last century (7, 8).

Although many strategies using covalent chiral auxiliaries (9, 10) or noncovalent chiral controllers (11, 12) have been used to dictate absolute stereochemistry in photochemical cycloaddition reactions, the development of methods that utilize substoichiometric stereodifferentiating chiral catalysts has proven a more formidable challenge.

Department of Chemistry, University of Wisconsin–Madison, 1101 University Avenue, Madison, WI 53706, USA.

*These authors contributed equally to this work.
†Corresponding author. E-mail: tyoon@chem.wisc.edu

This is largely due to the difficulty of controlling uncatalyzed background photochemical processes (Fig. 1A, path i). The direct photoexcitation of an unbound achiral substrate, free from the influence of a chiral catalyst, necessarily results in racemic products; thus, regardless of how enantioselective the catalyzed reaction might be (Fig. 1A, path ii), the net enantiomeric excess (ee) of the product will be low unless the rate of the uncatalyzed
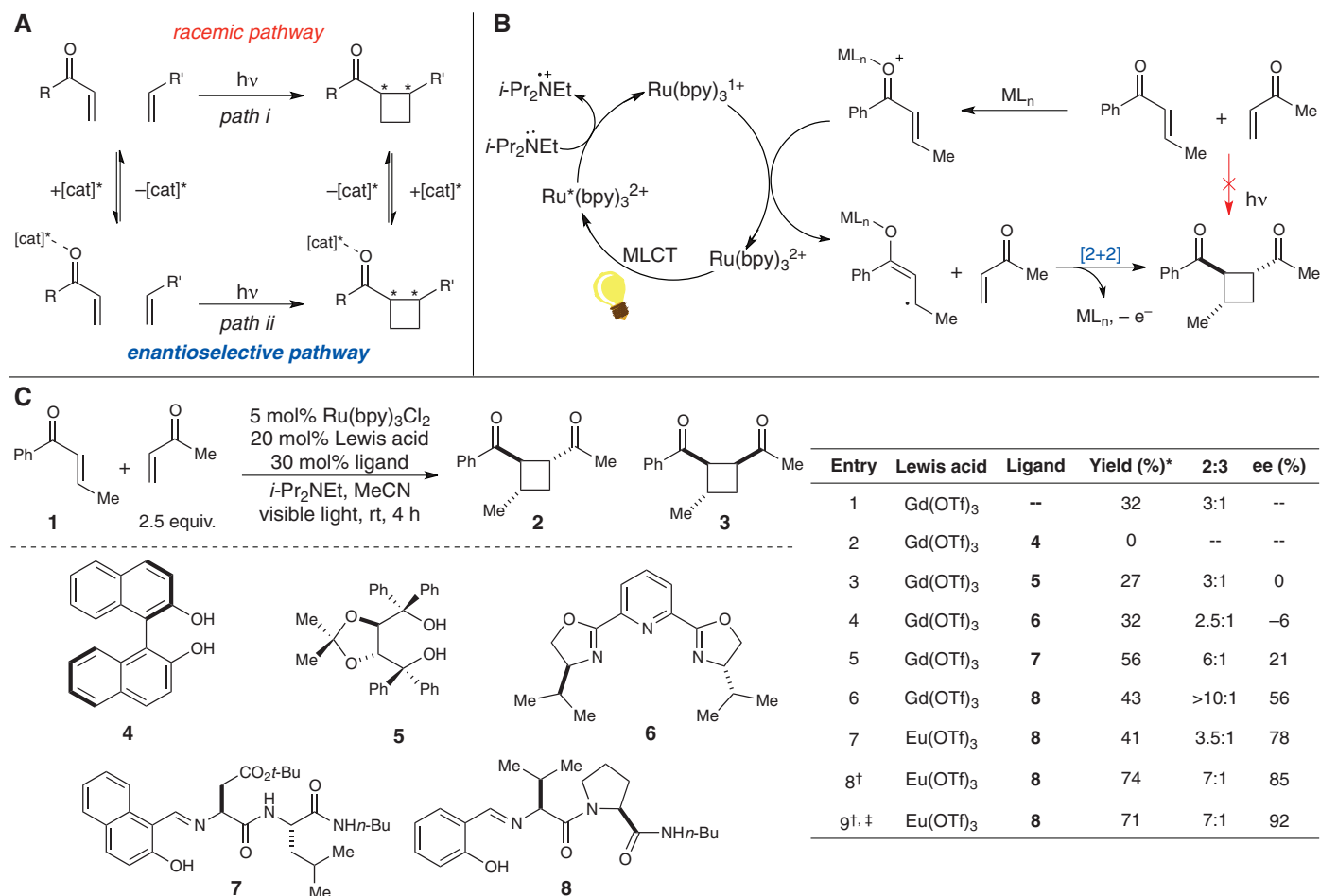
Fig. 1. Design plan for enantioselective catalytic [2 + 2] cycloaddition reactions. (**A**) Competing enantioselective and racemic pathways in asymmetric photocycloadditions. (**B**) Ru(bpy)₃²⁺-catalyzed [2 + 2] cycloaddition reaction using visible light. bpy, 2,2′-bipyridine; MLCT, metal-to-ligand charge transfer. (**C**) Survey of chiral Lewis acid cocatalysts. OTf, trifluoromethanesulfonate. rt, room temperature. *Yields determined by ¹H–nuclear magnetic resonance (NMR) analysis using an internal standard. †Optimized conditions: 5 equivalents of methyl vinyl ketone, 5 mol % Ru(bpy)₃Cl₂, 10 mol % Lewis acid, 20 mol % ligand, 0.2 M MeCN, 2 hours. ‡Reaction conducted at −20°C for 15 hours.

Entry	Lewis acid	Ligand	Yield (%)*	2:3	ee (%)
1	Gd(OTf)₃	--	32	3:1	--
2	Gd(OTf)₃	4	0	--	--
3	Gd(OTf)₃	5	27	3:1	0
4	Gd(OTf)₃	6	32	2.5:1	−6
5	Gd(OTf)₃	7	56	6:1	21
6	Gd(OTf)₃	8	43	>10:1	56
7	Eu(OTf)₃	8	41	3.5:1	78
8†	Eu(OTf)₃	8	74	7:1	85
9†,‡	Eu(OTf)₃	8	71	7:1	92
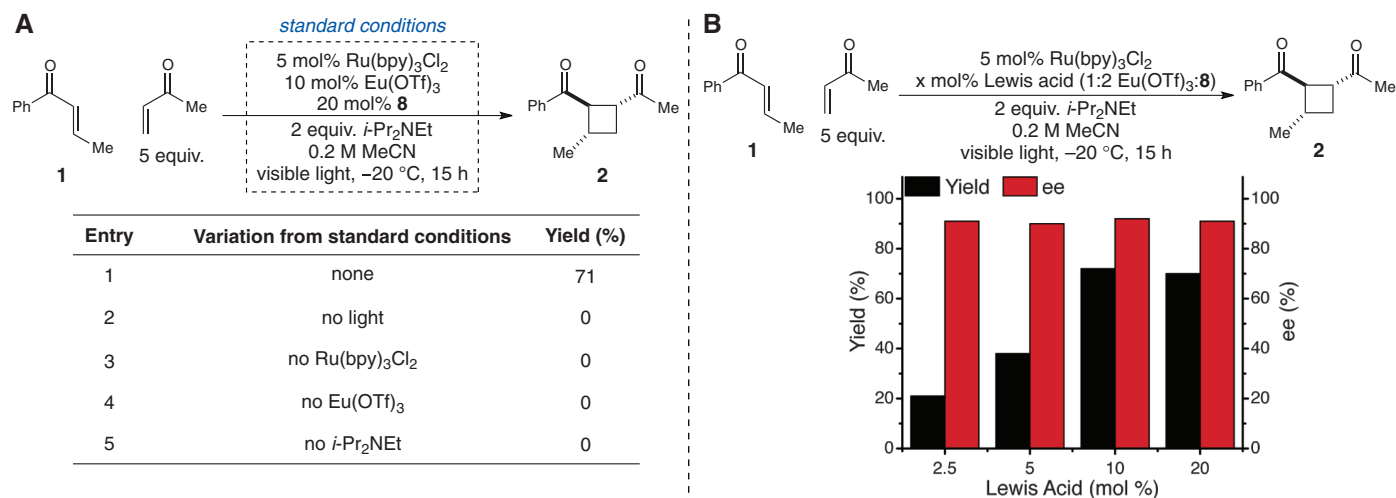
Fig. 2. Control experiments for the asymmetric visible light–photocatalyzed [2 + 2] cycloaddition. (**A**) Omission of any reaction component results in no [2 + 2] cycloaddition. (**B**) Enantioselectivity of the photocatalyzed [2 + 2] cycloaddition is not affected by the concentration of chiral Lewis acid catalyst.

Entry	Variation from standard conditions	Yield (%)
1	none	71
2	no light	0
3	no Ru(bpy)₃Cl₂	0
4	no Eu(OTf)₃	0
5	no i-Pr₂NEt	0

Fig. 3. Substrate scope of the enantioselective [2 + 2] cycloaddition reaction. Diastereomer ratios (dr) measured by ^{1}H-NMR analysis of the unpurified reaction mixtures. Reported yields represent total isolated yields of the 1,2-*cis* and 1,2-*trans* isomers. For each entry, yields represent the average of two reproducible experiments. *Reaction conducted for 24 hours.

2a: 71% yield
7:1 dr
92% ee

2b: 65% yield
7:1 dr
90% ee

2c: 69% yield
5.5:1 dr
90% ee

2d: 54% yield*
6:1 dr
86% ee

2e: 66% yield
2.5:1 dr
91% ee

2f: 70% yield
7:1 dr
93% ee

2g: 62% yield
3:1 dr
89% ee

2h: 72% yield
8:1 dr
93% ee

2i: 68% yield*
4:1 dr
91% ee

2j: 34% yield*
3:1 dr
88% ee

2k: 52% yield
4:1 dr
90% ee

2l: 62% yield*
9:1 dr
90% ee
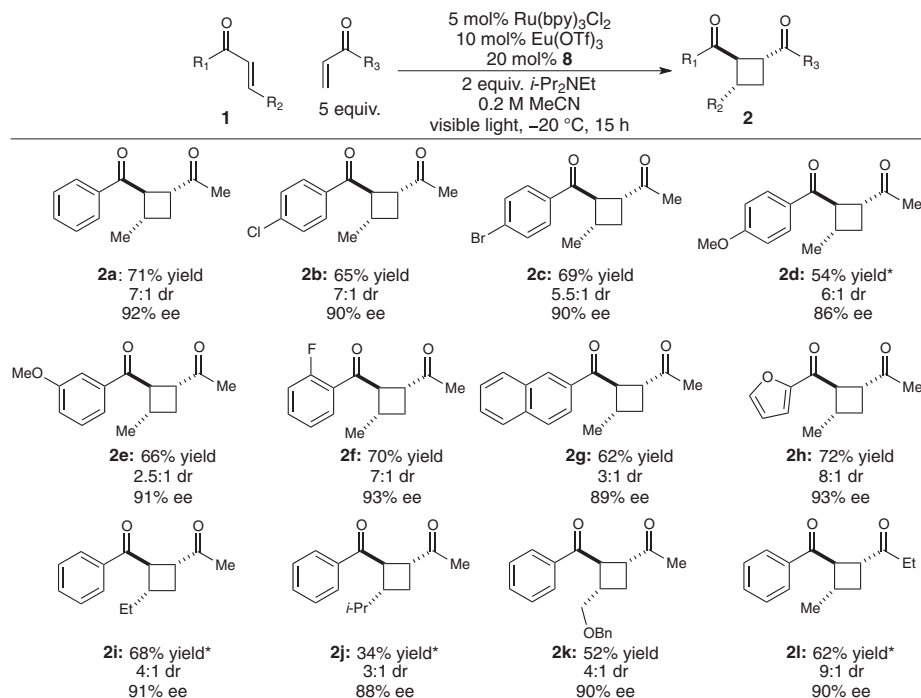
racemic background cycloaddition can be diminished. Bach, whose laboratory has reported the only highly enantioselective catalytic photocycloadditions to date, has approached this problem by designing elegant reactions in which the catalyst-substrate complex absorbs light at longer wavelengths than the free substrate. This has been accomplished either by using a chiral hydrogen-bonding xanthone-based photosensitizer (*13–15*) or by using a chiral Lewis acid catalyst capable of inducing a bathochromic shift in the bound substrate (*16, 17*). In both cases, Bach has achieved impressive enantioselectivities with substoichiometric chiral controllers. However, effective stereocontrol requires careful irradiation with a monochromatic light source that selectively excites the catalyst-substrate complex at a wavelength where absorption by the free substrate is minimized. The contribution of background reaction, though lessened in these systems, nevertheless remains appreciable and results in a dependence of the ee on catalyst concentration; optimal selectivities are obtained only at high catalyst loadings (typically ~50 mol %) at which the catalyzed process can outcompete the racemic background cycloaddition. Thus, the lack of a general strategy for completely eliminating uncatalyzed background photochemistry continues to be a fundamental impediment to the discovery of efficient enantioselective catalytic photocycloadditions.

Given these considerations, we speculated that the visible light–induced (*18*) photocatalytic [2 + 2] cycloaddition (*19, 20*) recently reported in our laboratory (Fig. 1B) might be an ideal platform for the development of a highly enantioselective catalytic photocycloaddition that is free of racemic background reaction. The crucial activation step in this cycloaddition involves the one-

electron reduction of a Lewis acid–activated aryl enone by a Ru(I) complex generated by visible-light irradiation of Ru(bpy)$_3^{2+}$ in the presence of an amine donor. There are two distinct features of this process that together prevent uncatalyzed background reactions. First, Ru(bpy)$_3^{2+}$ is activated by visible light (λ_{max} = 450 nm) at wavelengths where the enone substrates do not absorb (*21*); direct photoexcitation of the enone does not occur with the household white light sources applied in our studies. Second, a Lewis acid (LiBF$_4$) is an essential additive for cycloaddition to proceed; the Li$^+$ cation presumably activates the enone substrate toward one-electron reduction and stabilizes the resulting radical anion species (*22*). We hypothesized, therefore, that a dual-catalyst system consisting of Ru(bpy)$_3^{2+}$ and an appropriate chiral Lewis acid cocatalyst would promote highly enantioselective [2 + 2] cycloadditions without the complications arising from uncatalyzed background photoreactions.

In our initial screen of Lewis acids, we found that trivalent lanthanide salts such as Gd(OTf)$_3$ were particularly effective cocatalysts for the production of [2 + 2] cycloadducts **2** and **3** (Fig. 1C, entry 1). This observation is consistent with the high kinetic lability of lanthanides (*23*), which may aid catalyst turnover by facilitating displacement of the bidentate product by a monodentate enone substrate. Next, we evaluated a series of Gd complexes bearing chiral ligands that we hoped would influence the stereochemistry of the [2 + 2] cycloaddition. Unfortunately, several ligand classes (e.g., **4**–**6**) that have been effective in previously reported Lewis acid–catalyzed enantioselective transformations (*24*) provided negligible ee's in this reaction (entries 2 to 4). By contrast, Schiff base dipeptide ligand **7**, originally reported by

Hoveyda for Cu-catalyzed asymmetric allylic alkylation (*25*), provided [2 + 2] cycloadduct **2** with promising ee (entry 5). To our knowledge, this class of ligand has not previously been used in lanthanide-catalyzed asymmetric reactions; however, its modular structure (*26*) facilitated the rapid synthesis and evaluation of a small library of ligands composed of various salicylaldehyde and amino acid units. A Lewis acid cocatalyst composed of the optimal ligand (**8**) and Gd(OTf)$_3$ afforded cyclobutane **2** in 56% ee (entry 6). Further optimization studies revealed that by replacing the Gd salt with Eu(OTf)$_3$ and by performing the reaction at lower temperatures, the ee of **2** could be increased to 92% (entries 7 to 9).

The optimized conditions require 5 mol % Ru(bpy)$_3$Cl$_2$ as a visible-light photocatalyst and 10 mol % of a Lewis acid complex composed of a 1:2 ratio of Eu(OTf)$_3$ and chiral ligand **8**. A series of control experiments verify the necessity of each reaction component (Fig. 2A). In the absence of light, photocatalyst, or Lewis acid catalyst, either singularly or in combination, no product is formed and enone substrate **1** can be recovered in good yield. Yet, although the rate of cycloaddition is dependent on the concentration of Lewis acid catalyst, there is no noticeable impact on the ee of the product. Catalyst loadings varying from 2.5 to 20 mol % produced cycloadduct **2** with the same ee in each case (Fig. 2B). These experiments indicate that all of the [2 + 2] cycloadduct is being formed via a pathway involving the chiral Lewis acid and that there is no contribution from a competitive racemic background process, consistent with our design plan.

Previous approaches toward asymmetric catalytic photocycloaddition reactions have exhibited rather limited scope. Minor modifications

Fig. 4. Diastereocontrol through independent modification of chiral Lewis acid structure. (A) Stereoselective access to 1,2-*cis* cycloadducts **3** through reduction of chiral Schiff base ligand **8** to amine **9**. (**B**) Substrate scope of 1,2-*cis* cyclobutanes via enantioselective [2 + 2] photocycloaddition. Diastereomer ratios measured by ^{1}H-NMR analysis of the unpurified reaction mixtures. Reported yields represent total isolated yields of the 1,2-*cis* and 1,2-*trans* isomers. For each entry, yields represent the average of two reproducible experiments. *Reaction conducted for 14 hours. †Reaction conducted for 36 hours. ‡Reaction conducted at 37°C. §Isolated yield of only *cis* isomer.
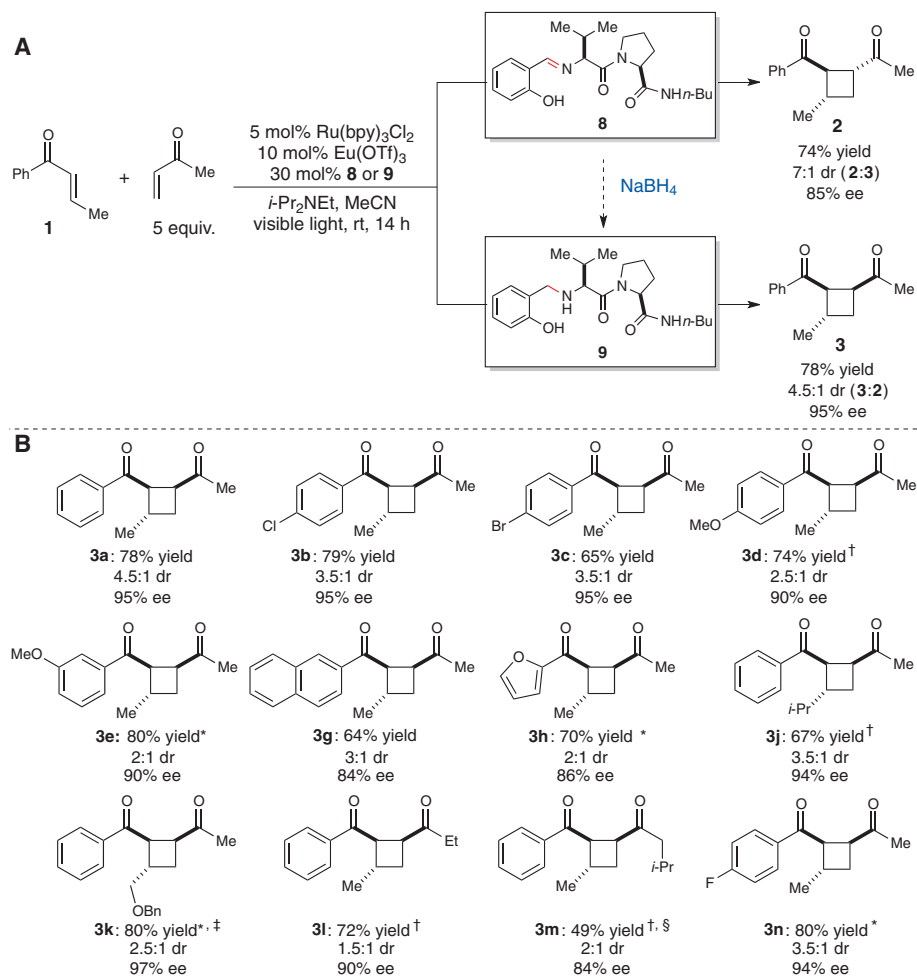
to the substrate can result in substantial spectral changes that affect the ability to selectively photoexcite the catalyst-bound substrate (*15*). In contrast, the results summarized in Fig. 3 demonstrate that our dual-catalytic system tolerates wide-ranging structural variation (*27*). Successful substrates include aryl enones bearing electron-donating and -withdrawing substituents, heteroaryl enones, and γ-substituted enones. The enantioselectivity remains high for all of these cycloadducts regardless of the ultraviolet (UV) absorptivity of the substrates (*28*). For example, the phenyl and naphthyl enones leading to cyclobutanes **2a** and **2g** both provide high ee even though the UV absorption of the latter extends to considerably longer wavelengths (fig. S1). Consistent with our studies of racemic crossed enone cycloadditions (*20*), we observe the formation of readily separable by-products arising from competitive reductive coupling and aryl enone homodimerization processes. The use of a fivefold excess of the aliphatic enone increases the overall rate of formation of [2 + 2] cycloadducts and minimizes the formation of homocoupling products. Overall, these results represent a substantial improvement in the structural variety of enantioenriched [2 + 2] cycloadducts available by catalysis. Each of the previous reports of asymmetric catalytic photo-

cycloadditions has involved intramolecular reactions of cyclic enone substrates and thus furnished bicyclic products. Our intermolecular cycloaddition of acyclic enones can produce a diverse range of simple monocyclic cyclobutane products in good ee.

One important advantage of this dual-catalytic system is the functional independence of the photocatalyst and the chiral Lewis acid catalyst (*29*). Extensive variations can be made to the structure of the chiral Lewis acid without any deleterious effect on the photochemical properties of the Ru(bpy)$_3$$^{2+}$ chromophore. This feature facilitates both the optimization of the enantioselectivity and the discovery of complementary reactivity. For example, reduction of Schiff base ligand **8** with NaBH$_4$ afforded secondary amine ligand **9**, the Eu(OTf)$_3$ complex of which was also a highly enantioselective Lewis acid cocatalyst for [2 + 2] cycloaddition. These conditions, however, favored the formation of 1,2-*cis* diastereomer **3** in good ee (Fig. 4A) (*30*). The scope of the cycloaddition using **9** exhibits the same general breadth as reactions conducted with ligand **8** (Fig. 4B), but with complementary diastereoselectivity (*31*).

These studies demonstrate that transition-metal photocatalysts are compatible with a variety of

structurally diverse chiral Lewis acid catalysts. The factors governing the success of chiral Lewis acids in asymmetric catalysis have been studied for decades and are now well-understood (*32*). The ability to combine the power and versatility of chiral Lewis acids with the unique reactivity of photocatalytically generated intermediates has the potential to be a valuable platform for the development of a wide range of broadly useful stereocontrolled reactions.

References and Notes

1. E. N. Jacobsen, A. Pfaltz, H. Yamamoto, *Comprehensive Asymmetric Catalysis* (Springer, Berlin, New York, 1999).
2. I. Ojima, *Catalytic Asymmetric Synthesis* (Wiley, Hoboken, NJ, ed. 3, 2010).
3. J. Iriondo-Alberdi, M. F. Greaney, *Eur. J. Org. Chem.* **2007**, 4801–4815 (2007).
4. N. Hoffmann, *Chem. Rev.* **108**, 1052–1103 (2008).
5. H. Rau, *Chem. Rev.* **83**, 535–547 (1983).
6. Y. Inoue, *Chem. Rev.* **92**, 741–770 (1992).
7. J. A. Le Bel, *Bull. Soc. Chim. Fr.* **22**, 337 (1874).
8. W. Kuhn, E. Knopf, *Naturwissenschaften* **18**, 183 (1930).
9. M. Demuth *et al.*, *Angew. Chem. Int. Ed. Engl.* **25**, 1117–1119 (1986).
10. L. M. Tolbert, M. B. Ali, *J. Am. Chem. Soc.* **104**, 1742–1744 (1982).
11. T. Bach, H. Bergmann, K. Harms, *Angew. Chem. Int. Ed.* **39**, 2302–2304 (2000).
12. F. Toda, H. Miyamoto, S. Kikuchi, *J. Chem. Soc. Chem. Commun.*, 621–622 (1995).

13. C. Müller, A. Bauer, T. Bach, *Angew. Chem. Int. Ed.* **48**, 6640–6642 (2009).
14. M. M. Maturi *et al.*, *Chem. Eur. J.* **19**, 7461–7472 (2013).
15. C. Müller *et al.*, *J. Am. Chem. Soc.* **133**, 16689–16697 (2011).
16. H. Guo, E. Herdtweck, T. Bach, *Angew. Chem. Int. Ed.* **49**, 7782–7785 (2010).
17. R. Brimioulle, T. Bach, *Science* **342**, 840–843 (2013).
18. C. K. Prier, D. A. Rankic, D. W. MacMillan, *Chem. Rev.* **113**, 5322–5363 (2013).
19. M. A. Ischay, M. E. Anzovino, J. Du, T. P. Yoon, *J. Am. Chem. Soc.* **130**, 12886–12887 (2008).
20. J. Du, T. P. Yoon, *J. Am. Chem. Soc.* **131**, 14604–14605 (2009).
21. K. Kalyanasundaram, *Coord. Chem. Rev.* **46**, 159–244 (1982).
22. F. Fournier, M. Fournier, *Can. J. Chem.* **64**, 881–890 (1986).
23. K. Mikami, M. Terada, H. Matsuzawa, *Angew. Chem. Int. Ed.* **41**, 3554–3572 (2002).
24. H. C. Aspinall, *Chem. Rev.* **102**, 1807–1850 (2002).
25. M. A. Kacprzynski, A. H. Hoveyda, *J. Am. Chem. Soc.* **126**, 10676–10681 (2004).
26. A. H. Hoveyda, *Chem. Biol.* **5**, R187–R191 (1998).
27. Consistent with our prior studies, crossed [2 + 2] cycloadditions can be achieved with one aryl enone that can easily be reduced to the corresponding radical anion and a second β-unsubstituted alkyl enone that possesses a more negative redox potential but is a less sterically encumbered Michael acceptor.
28. The absolute configuration of **2c** was determined by x-ray crystallographic analysis of the corresponding 2,4-dinitrophenylhydrazone (**S3**) using anomalous dispersion. See supplementary materials for details. The configurations of other 1,2-*trans* cycloadducts were assigned by analogy.
29. A. E. Allen, D. W. MacMillan, *Chem. Sci.* **2012**, 633–658 (2012).
30. Reactions conducted with ligand **9** at −20 °C proceeded at prohibitively slow rates and offered little improvement in ee.
31. The absolute configuration of **3c** was determined by x-ray crystallographic analysis using anomalous dispersion. See supplementary materials for details. The configurations of other 1,2-*cis* cycloadducts were assigned by analogy.
32. H. Yamamoto, *Lewis Acids in Organic Synthesis* (Wiley-VCH, Weinheim, New York, 2000).

Detection of the Gravitational Lens Magnifying a Type Ia Supernova

Robert M. Quimby,[1]* Masamune Oguri,[1,2] Anupreeta More,[1] Surhud More,[1] Takashi J. Moriya,[3,4] Marcus C. Werner,[1,5] Masayuki Tanaka,[6] Gaston Folatelli,[1] Melina C. Bersten,[1] Keiichi Maeda,[7] Ken'ichi Nomoto[1]

Objects of known brightness, like type Ia supernovae (SNIa), can be used to measure distances. If a massive object warps spacetime to form multiple images of a background SNIa, a direct test of cosmic expansion is also possible. However, these lensing events must first be distinguished from other rare phenomena. Recently, a supernova was found to shine much brighter than normal for its distance, which resulted in a debate: Was it a new type of superluminous supernova or a normal SNIa magnified by a hidden gravitational lens? Here, we report that a spectrum obtained after the supernova faded away shows the presence of a foreground galaxy—the first found to strongly magnify a SNIa. We discuss how more lensed SNIa can be found than previously predicted.

A peculiar supernova, PS1-10afx, was discovered by the Panoramic Survey Telescope & Rapid Response System 1 (Pan-STARRS1) on 31 August 2010 (universal time) (*1*). The unusually red color of the object spurred the Pan-STARRS1 team to conduct an array of follow-up observations, including optical and near-infrared spectroscopy, which yielded a redshift of $z = 1.39$. Combined with relatively bright photometric detections, this redshift would imply a peak luminosity of 4×10^{44} erg s^{-1}, which is 400 times brighter than the typical core-collapse supernova. A rare class of superluminous supernovae (SLSN) (*2*) have shown similarly high bolometric outputs, but PS1-10afx distinguishes itself from all other SLSN on two important counts: PS1-10afx is much redder (cooler) and evolved much faster than any SLSN. A generic feature of SLSN models (*3–9*) is that they employ high temperatures (*T*) and/or large photospheric radii (*R*) to generate high luminosities (*L*) (recalling that $L \propto T^4 R^2$). The observations of PS1-10afx do not fit with these models, suggesting that if it is a SLSN, it is in a class of its own.

An alternate hypothesis (*10*) is that PS1-10afx is actually a regular type Ia supernova (SNIa) with a normal luminosity, but its apparent brightness has been magnified by a gravitational lens. Spectra of PS1-10afx are well fit by normal SNIa templates, as are the colors and light curve shapes. However, normal SNIa exhibit a tight relation between the widths of their light curves and their peak luminosities (*11–14*), and PS1-10afx appears 30 times brighter than expected, according to this relation. Such a large magnification of brightness can only occur naturally from strong gravitational

lensing, whereby the light emanating from the supernova is bent to form an Einstein-Chwolson ring, or several discrete magnified images (typically two or four) if the alignment is not axisymmetric. Pan-STARRS1 has surveyed sufficient volume to expect such a chance alignment (*15, 16*), and it is possible that the angular extent of the lensed images was simply too small to be resolved by the observations available. However, for this hypothesis to be confirmed, we must explain why the existing observations give such conclusive photometric and spectroscopic evidence for the presence of the supernova's host galaxy, but the same observations fail to obviously indicate the presence of a foreground lens.

We used the Keck-I telescope with the Low-Resolution Imaging Spectrograph (LRIS) (*17*) with the upgraded red channel (*18*) to observe the host galaxy and any foreground objects at the sky position of PS1-10afx on 7 September 2013 (see fig. S1) (*16*). As illustrated in Fig. 1, there are two narrow emission features that persist at the location of PS1-10afx now that the supernova itself has faded away. The [O II] emission doublet ($\lambda\lambda = 3726.1$, 3728.8 Å in the rest frame) from the host galaxy previously identified (*1*) is clearly recovered (fig. S2), but we additionally detected a second emission line at ~7890 Å. Because there are no strong emission lines expected from the host at this wavelength (~3300 Å in the host frame), this detection suggests the presence of a second object coincident with PS1-10afx.

The most probable identification for the 7890 Å feature is [O II] at $z = 1.1168 \pm 0.0001$. At this redshift, other strong emission lines such as H-β or [O III] would lie outside of our wavelength coverage. However, as depicted in Fig. 1, we detected a Mg II absorption doublet ($\lambda\lambda = 2795.5$, 2802.7 Å in the rest frame) at $z = 1.1165 \pm 0.0001$. Blueshifted absorption outflows are typical of star-forming galaxies (*19*), so this estimate is compatible with that derived from the emission lines. We also identify possible Mg I ($\lambda = 2853.0$

[1]Kavli Institute for the Physics and Mathematics of the Universe (WPI), Todai Institutes for Advanced Study, The University of Tokyo, 5-1-5 Kashiwanoha, Kashiwa-shi, Chiba 277-8583, Japan. [2]Department of Physics, The University of Tokyo, Tokyo 113-0033, Japan. [3]Argelander Institute for Astronomy, University of Bonn Auf dem Hügel 71, D-53121 Bonn, Germany. [4]Research Center for the Early Universe, Graduate School of Science University of Tokyo, Hongo 7-3-1, Bunkyo, Tokyo 113-0033, Japan. [5]Department of Mathematics, Duke University, Durham, NC 27708, USA. [6]National Astronomical Observatory of Japan 2-21-1 Osawa, Mitaka, Tokyo 181-8588, Japan. [7]Department of Astronomy, Kyoto University, Kitashirakawa-Oiwake-cho Sakyo-ku, Kyoto 606-8502, Japan.

*Corresponding author. E-mail: robert.quimby@ipmu.jp

and Fe II (λ = 2344.2, 2373.7, 2382.8, 2586.7, 2600.2) lines with a matching redshift. Given these identifications and the extended nature of the emission (see fig. S3), it is clear that the second object is a galaxy lying in front of PS1-10afx and its host. The near-maximum light spectra of PS1-10afx (*1*) show what could be Ca II absorption from this foreground galaxy (Fig. 1).

With its redshift secure, we next checked whether the foreground galaxy could satisfy the lens requirements of PS1-10afx (*10*). To do this, we derived a stellar mass for the foreground galaxy and used an empirical relation between stellar mass and one-dimensional velocity dispersion, as explained below. We fitted a set of single stellar population (SSP) models to the combined spectra to measure the stellar masses of the host and foreground galaxies (see Fig. 2 and fig. S4) (*16*). The best-fit SSP combination was a ~1-billion-year-old foreground galaxy with a stellar mass of

$(9 \pm 2) \times 10^9\ M_\odot$ and a more distant host galaxy with $(7 \pm 1) \times 10^9\ M_\odot$ and a younger (~0.1-billion-year-old) population. The extinction in the foreground galaxy is consistent with zero ($A_V = 0.28^{+0.48}_{-0.28}$), but the host galaxy requires significant reddening [$A_V = 1.62 \pm 0.18$ (where A_V is the V-band absorption in magnitudes)].

Stellar mass contributes only a fraction of a galaxy's total mass, which is usually dominated by dark matter. The ratio of these masses varies from galaxy to galaxy, but they are strongly correlated. Using the stellar mass–to–velocity dispersion relation measured from the SDSS DR7 spectroscopic sample (*20, 21*) (fig. S5), we inferred a probability distribution for the foreground galaxy's velocity dispersion (*16*). We then used this as input to a Monte Carlo simulation from which we derived the posterior distributions for the lens parameters (Fig. 3). We find that the redshift and mass of the foreground galaxy make it fully consistent with a gravitational lens that is

capable of satisfying the magnification, image-separation limits, and time-delay constraints of PS1-10afx (*10*). We thus concluded that PS1-10afx is not a superluminous supernova but a normal SNIa magnified by a strong gravitational lens at $z = 1.1168$.

Our new data further explain why the lensing galaxy was not evident in prior observations. Even though the host galaxy is slightly less massive, more extinguished, and farther away than the lensing galaxy, it harbors a younger stellar population that shines more brightly per unit mass. Because of this, the foreground object is only comparable in brightness to the host over a narrow range of wavelengths longer than the lensing galaxy's 4000 Å break but shorter than the host's. This makes it difficult to see the light from the lens galaxy over the glare from the host galaxy.

The lack of multiple images or signs of time delay from PS1-10afx can also be explained from
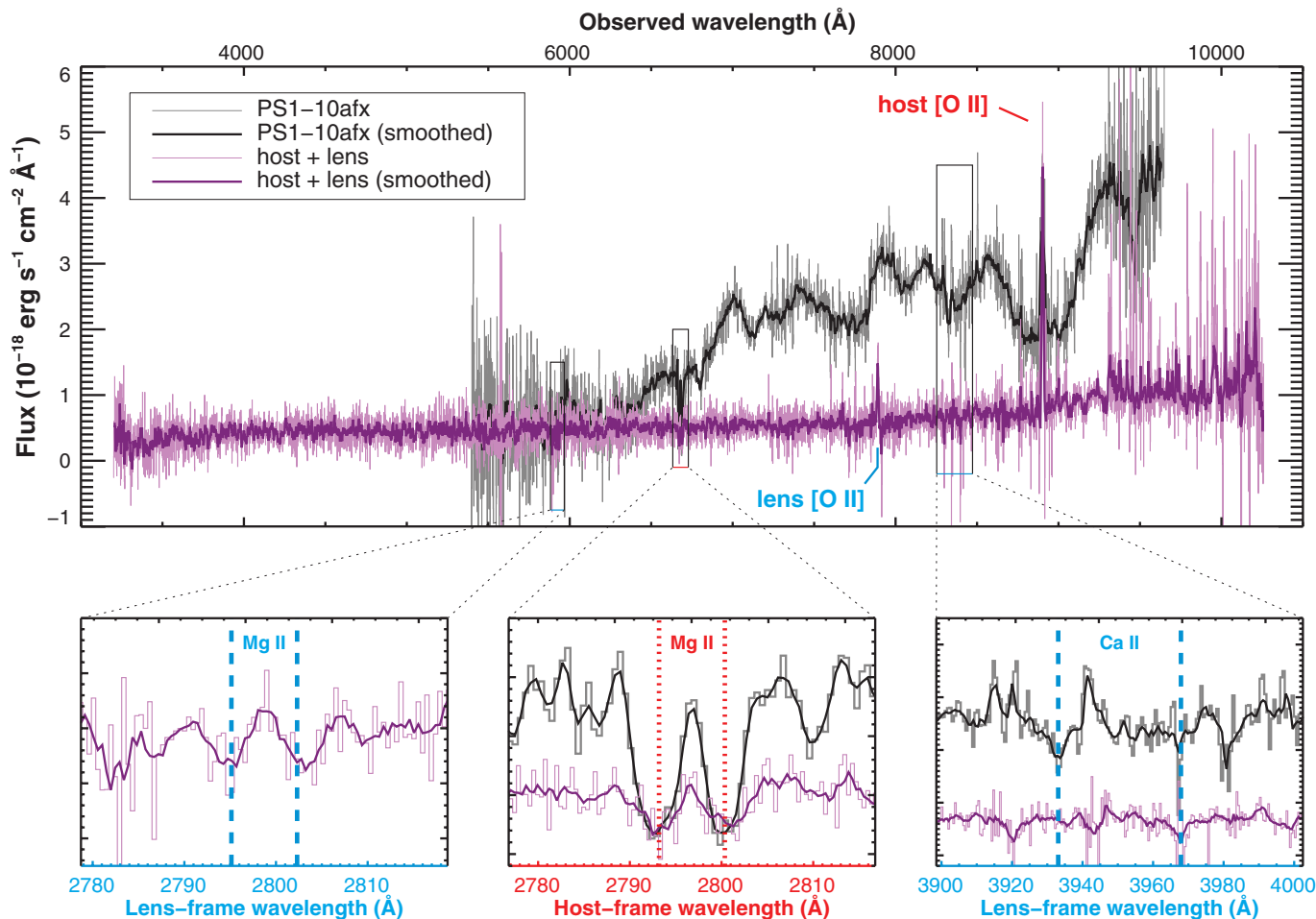
Fig. 1. Spectra of the quiescent light at the location of PS1-10afx. The Keck/LRIS observations (purple), taken ~450 rest-frame days after the supernova reached maximum light, show the presence of two emission features, which we identified as [O II] from galaxies at $z = 1.1168$ and 1.3885. We also detected absorption lines corresponding to the Mg II doublet for both the foreground lens galaxy (blue labels in lower left panel) and the host (red labels in lower middle panel). Vertical lines mark the rest frame wavelengths for the doublets in the lower panels. A spectrum of PS1-10afx taken near maximum light (*1*) is shown in gray for comparison. This supernova spectrum has been shifted slightly to align the Mg II features with the Keck/LRIS data (*16*). The lower right panel shows that the supernova light may be absorbed at wavelengths corresponding to Ca II H and K in the foreground galaxy. Ca II H is coincident with a strong night sky line, but the Ca II K falls in a relatively clean spectral region.
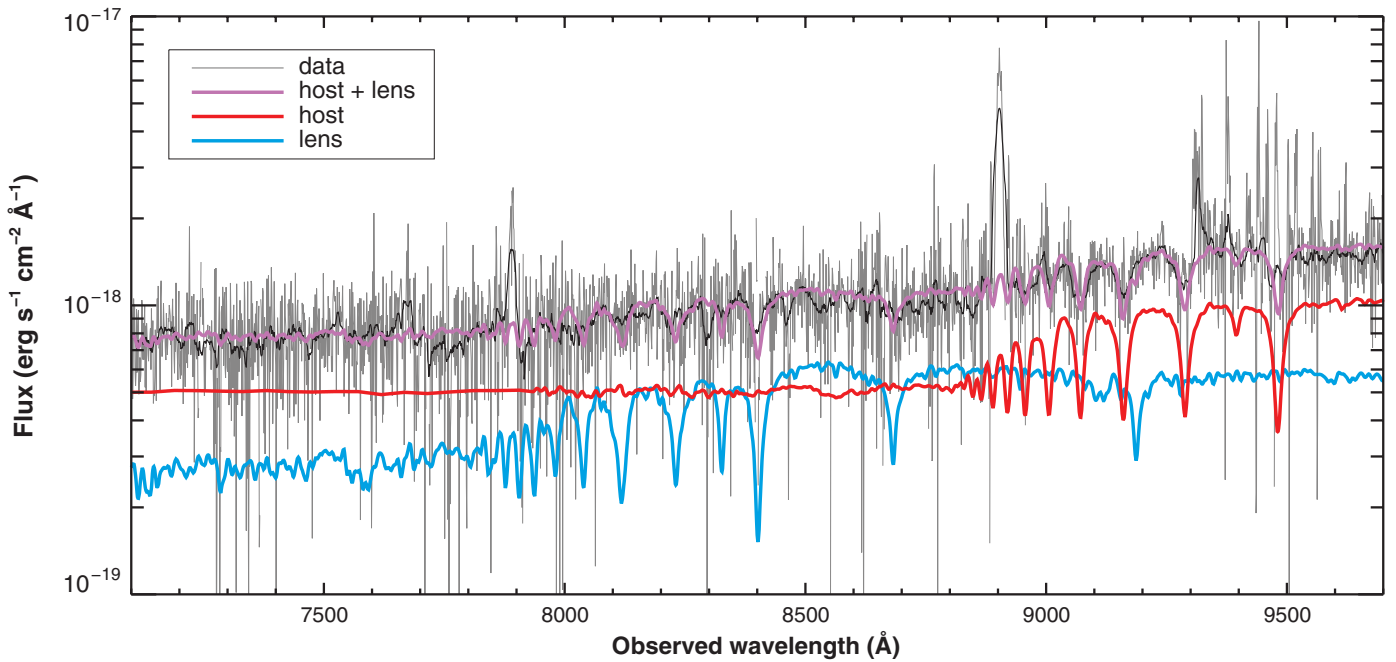
Fig. 2. Decomposition of the observed spectra into lens and host galaxy components. We modeled the lens (blue line) and host (red line) as single stellar populations at $z = 1.1168$ and 1.3885, respectively. We varied the age and total stellar mass of each galaxy to find the sum (purple line) that best matched the observed spectra (gray; smoothed spectra shown in black). The models include only starlight; light emitted by gas, such as the [O II] lines seen at ~8900 and ~7900 Å, is neglected.

our Monte Carlo simulations. The high total magnification of PS1-10afx is best recovered from alignments that produce four images (79% probability of a "quad" system), but the maximum separation between the different multiple images is small ($\Delta\theta < 0.12''$ at 95% confidence), and the maximum phase delay is short ($\Delta t < 1.3$ days at 95% confidence). The available observations of PS1-10afx are thus likely insufficient to resolve any effects from the gravitational lensing other than its magnification.

In the future, high–angular resolution imaging enabled by adaptive optics (AO) or space-based resources like the Hubble Space Telescope (HST) could be used to spatially resolve the multiple images of gravitationally lensed SNIa similar to PS1-10afx. This would not only provide immediate confirmation that gravitational lensing is at play, but it would also provide important constraints on the nature of the lens. In theory, multiple epochs of high-resolution imaging could be used to measure the time delay between each image and the magnification factors for each. Such observations could yield strong constraints on cosmic expansion.

Because the universe is expanding, the path lengths of the more delayed images will be stretched more by cosmic expansion, and the magnitude of this delay is directly tied to the Hubble parameter (22). However, the time delay is also dependent on the mass density profile of the lens, which will be dictated by unobservable dark matter. For objects of known brightness, like SNIa, we can use the readily measurable magnification to break this degeneracy (23). As is probably the case for
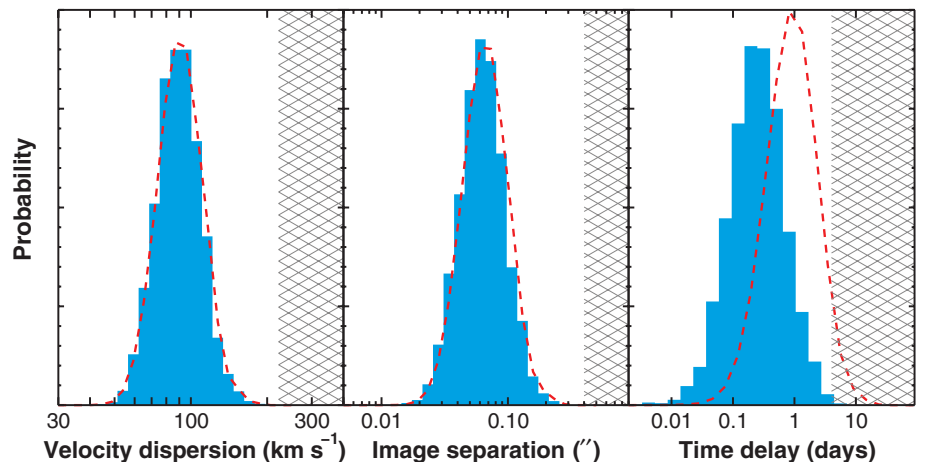
Fig. 3. Probability distributions for the lens parameters. From left to right, the panels show the relative likelihood for the line-of-sight velocity dispersion of the lensing galaxy, the maximum separation between lensed images, and the maximum time delay between lensed images as predicted by our Monte Carlo simulation. The blue histograms account for the total magnification, $\mu = 31 \pm 5$, measured for PS1-10afx (10), and the dashed red curves neglect this prior. The hatched areas are excluded based on the observations of PS1-10afx, specifically the lack of resolved images or evidence for time delays.

PS1-10afx, spectra taken near maximum light can reveal not only the redshift of the supernova but also, with the use of absorption line spectroscopy, the redshift and velocity dispersion of the lens. (Note that at maximum light, the resolving power available from Keck/LRIS may have been sufficient to resolve the Ca II K line from the lens, but the signal-to-noise ratio and resolution of the available observations is too low: $\sigma < 125$ km s^{-1} at 95% confidence.) Thus, future discoveries of

gravitationally lensed SNIa may be used to make a direct and precise measurement of the Hubble constant, but only if the needed follow-up observations commence in a timely manner.

To begin follow-up observations of lensed SNIa candidates while they are still on the rise (needed for accurate delay time measurements) or near maximum light (the optimal phase for absorption line spectroscopy), an efficient vetting process must be employed to eliminate the
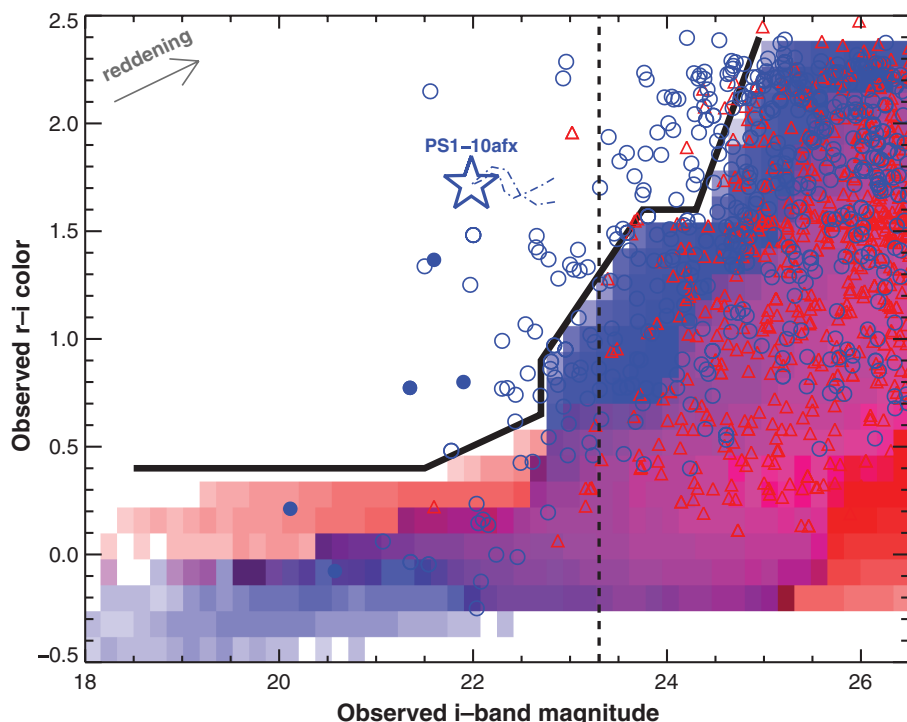
Fig. 4. Color-magnitude diagram showing how lensed SNIa can be distinguished from unlensed events. The blue shaded area shows the expected color-magnitude distribution for unlensed SNIa on a log scale, and the red shaded area corresponds to core-collapse supernovae. The $r − i$ colors for low redshift supernovae are relatively blue. However, at higher redshifts (fainter observed magnitudes), the color becomes red as the peak of the rest-frame spectral energy distribution passes through the observer-frame bands. The red limit for unlensed supernovae at a given i-band magnitude is denoted by the thick black line. Blue circles and red triangles show the distribution of lensed SNIa and core-collapse supernovae, respectively, predicted by Monte Carlo simulations (*16*). Solid symbols indicate objects that could be resolved from ground-based observations, such as those planned by the Large Synoptic Survey Telescope (LSST). Open symbols depict objects that require high–angular resolution follow-up observations to resolve spatially. The open star marks the values corresponding to the peak i-band brightness of PS1-10afx, and the dash-dotted curve shows that the color evolution within one magnitude of this peak is minimal. The vertical dashed line marks the single epoch limit predicted for LSST. The arrow shows the reddening vector, assuming $A_V = 1.0$ magnitude.

olution study of the lens and host galaxies with HST, ground-based AO, and the Atacama Large Millimeter/submillimeter Array could further constrain the lensing model and provide an important reference for future studies of gravitationally lensed SNIa.

References and Notes

1. R. Chornock *et al.*, *Astrophys. J.* **767**, 162 (2013).
2. A. Gal-Yam, *Science* **337**, 927–932 (2012).
3. G. Rakavy, G. Shaviv, Z. Zinamon, *Astrophys. J.* **150**, 131 (1967).
4. Z. Barkat, G. Rakavy, N. Sack, *Phys. Rev. Lett.* **18**, 379–381 (1967).
5. S. E. Woosley, S. Blinnikov, A. Heger, *Nature* **450**, 390–392 (2007).
6. S. E. Woosley, *Astrophys. J.* **719**, L204–L207 (2010).
7. D. Kasen, L. Bildsten, *Astrophys. J.* **717**, 245–249 (2010).
8. R. A. Chevalier, C. M. Irwin, *Astrophys. J.* **729**, L6 (2011).
9. T. J. Moriya *et al.*, *Mon. Not. R. Astron. Soc.* **428**, 1020–1035 (2013).
10. R. M. Quimby *et al.*, *Astrophys. J.* **768**, L20 (2013).
11. M. M. Phillips *et al.*, *Astron. J.* **118**, 1766–1776 (1999).
12. S. Jha, A. G. Riess, R. P. Kirshner, *Astrophys. J.* **659**, 122–148 (2007).
13. M. Hicken *et al.*, *Astrophys. J.* **700**, 1097–1140 (2009).
14. M. Sullivan *et al.*, *Mon. Not. R. Astron. Soc.* **406**, 782–802 (2010).
15. M. Oguri, P. J. Marshall, *Mon. Not. R. Astron. Soc.* **405**, 2579–2593 (2010).
16. Additional information is available in the supplementary materials on *Science* Online.
17. J. B. Oke *et al.*, *Publ. Astron. Soc. Pac.* **107**, 375 (1995).
18. C. Rockosi *et al.*, *Society of Photo-Optical Instrumentation Engineers (SPIE) Conference Series* (SPIE, Bellingham, WA, 2010), vol. 7735.
19. D. K. Erb, A. M. Quider, A. L. Henry, C. L. Martin, *Astrophys. J.* **759**, 26 (2012).
20. G. Kauffmann *et al.*, *Mon. Not. R. Astron. Soc.* **341**, 33–53 (2003).
21. M. R. Blanton *et al.*, *Astron. J.* **129**, 2562–2578 (2005).
22. S. Refsdal, *Mon. Not. R. Astron. Soc.* **128**, 307–310 (1964).
23. M. Oguri, Y. Kawano, *Mon. Not. R. Astron. Soc.* **338**, L25–L29 (2003).

nonlensed supernovae that outnumber lensed SNIa by a few thousand to one. A means to accomplish this feat was demonstrated by the selection of PS1-10afx for follow-up by the Pan-STARRS1 team—they were first motivated to examine PS1-10afx based on its unusually red color (*1*), as seen in Fig. 4 (*16*). PS1-10afx showed a color near maximum light of $r − i \sim 1.7$ (where r and i give the observed fluxes in the SDSS r-band and i-band, respectively, in magnitudes), whereas unlensed supernovae brighter than the Pan-STARRS1 detection limits have $r − i < 0.5$. (Note that quiescent galaxy light is removed from these measurements using presupernova images.) Because the lensing probability increases with redshift and, for a given sky area, the number of supernovae also increases with redshift (because of both rates and increased volume), the majority of lensed SNIa expected from a flux-limited survey will be high-redshift events that will typically appear much redder than the more nearby population of unlensed supernovae.

We thus propose that selecting supernovae with colors redder than a given i-band magnitude (Fig. 4, bold black line) during their rise to peak may be an effective way to identify lensed supernovae. This will bypass the need to detect multiple, resolved images and will thus increase the expected number of lensed SNIa from future surveys by a factor of 5 over traditional selection techniques.

The large magnification and relatively low-mass lens galaxy of PS1-10afx may prove typical of gravitationally lensed SNIa that will be discovered by future, flux-limited surveys given selection bias: Brighter objects are easier to detect, and unresolved images formed by a low-mass lens effectively make a single, brighter object (*16*) (fig. S6). Alternatively, the lens mass and high magnification of PS1-10afx may indicate a problem with our understanding of the starlight–to–dark matter connection in the early universe. Thus, further studies of this system are warranted. A multiwavelength, high–angular res-

The Lunar Apatite Paradox

J. W. Boyce,[1]* S. M. Tomlinson,[1] F. M. McCubbin,[2] J. P. Greenwood,[3] A. H. Treiman[4]

Recent discoveries of water-rich lunar apatite are more consistent with the hydrous magmas of Earth than the otherwise volatile-depleted rocks of the Moon. Paradoxically, this requires H-rich minerals to form in rocks that are otherwise nearly anhydrous. We modeled existing data from the literature, finding that nominally anhydrous minerals do not sufficiently fractionate H from F and Cl to generate H-rich apatite. Hydrous apatites are explained as the products of apatite-induced low magmatic fluorine, which increases the H/F ratio in melt and apatite. Mare basalts may contain hydrogen-rich apatite, but lunar magmas were most likely poor in hydrogen, in agreement with the volatile depletion that is both observed in lunar rocks and required for canonical giant-impact models of the formation of the Moon.

The extreme volatile-element depletion of lunar rocks led to early estimates of less than 1 part per billion (ppb) H in the bulk Moon (1); however, direct measurements of lunar apatite and olivine-hosted melt inclusions indicated terrestrial levels of hydrogen (2–5). H-rich apatites [with abundances exceeding hundreds or even thousands of parts per million (ppm) H_2O in a wide range of lunar rock types (2, 3, 6)] have led to speculations that apatites from Earth and the Moon are produced under similarly hydrous conditions. Apatite also provides a high-fidelity record of H and Cl isotopes in lunar materials, from which arguments for both H-rich and H-poor lunar magmas have been put forth, with water perhaps sourced from cometary materials (2) or chondritic meteorites (6, 7) or perhaps not present at all (8). Given that the prevailing model of Moon formation—the giant-impact hypothesis (9)—is constrained in part by the depletion of volatile elements (including H, but also moderately volatile elements such as K and Rb), recent observations of elevated H [e.g., (10)] have important implications for the conditions of the formation of the Moon as well as our planet (11).

Only a small number of lunar samples contain olivine-hosted melt inclusions that are sufficiently pristine for hydrogen analysis (5), so it is difficult to determine whether they represent melting of a small, particularly volatile-rich fraction of the lunar interior or whether they have more global implications. In contrast, the mineral apatite $Ca_5(PO_4)_3(F,Cl,OH)$ is found in a more diverse (and numerous) suite of lunar samples, one that includes both mare basalts (Fig. 1) and highland rocks. Thus, apatite may provide a record of lunar volatiles that integrates over a wider range of sample ages, localities, and petrogenetic environments. This increased coverage comes at the expense of increased ambiguity: Abundances of volatiles in apatite may be difficult to interpret,

because investigations of apatite as a hygrometer are incomplete (12–15). The explanation initially offered for high hydrogen abundances in lunar apatite was that crystallization of nominally anhydrous minerals (NAMs) from basaltic magmas had concentrated H into the residual melt (2–4). This model treats H as a trace element, with the mineral/melt concentration ratio known as the Nernst-type (or Henrian) partition coefficient [D (16)]. H, F, and Cl are about equally incompatible in NAMs [D << 1 (17–21)], so crystallization of NAMs should enrich both basalts and their apatites in H, F, and Cl (fig. S1) (16). Simultaneous enrichment of H, F, and Cl in apatite is of course impossible because these elements are constrained by apatite stoichiometry to add up very nearly to unity in molar occupancy (22). Under these conditions, apatite is quite insensitive to the increasing H_2O content around it, a troubling conclusion for those who wish to use apatite as an accurate monitor of the abundance of magmatic volatiles from simple Nernst-type D values.

It is more appropriate to treat H, F, and Cl in apatite as major elements, comparable to the way one treats partitioning of Mg and Fe between olivine and melt (23, 24). We implemented this treatment of volatile partitioning between apatite and melt in a numerical model using equilibrium constants for H-F-Cl exchange reactions instead of Henrian partition coefficients. This allows us to predict not only the H, F, and Cl content of melts as a function of mineralogy and degree of crystallization but also of apatite crystalizing from that melt and the feedback between the two, which governs the evolution of volatile abundances in apatite-saturated magmas. When we add apatite to the model of the crystallizing assemblage (Fig. 2 and fig. S2), we now have a mineral into which substantial and variable quantities of both H and F will enter. Our modeling indicates that, during fractional crystallization (where only instantaneous equilibrium exists between the melt and crystals) of a mineral assemblage that includes apatite, F is preferentially removed from the magma because of the preference of apatite for F over Cl and H. This results in melts, and apatite, with elevated H/F and Cl/F ratios. In melts with moderately high P [$P_2O_5 = 0.1$ weight % (wt %)] and F (F = 50 ppm, Cl = H_2O = 1 ppm), the effect of apatite over the range of 90 to 99% crystallization

is to increase the final water concentration of apatite (H_2O_{ap}) by a factor of 25, from 7 to 180 ppm (fig. S3). With initial F ≤ 20 ppm, apatite that grows at ≥94% fractional crystallization contains 1.79 wt % H_2O (100% OH occupancy), an increase of a factor of ~1000, consistent with the highest values reported for mare basalts [~100% molar OH⁻ occupancy, ~1.79 wt % H_2O (25)]. We find that the onset of apatite crystallization changes the H, F, and Cl content of the melt more than the crystallization of all other minerals combined, which in hindsight is not surprising given that these elements are only found in great abundance in apatite.

Our model makes specific testable predictions: First, it depends on fractional crystallization of an assemblage including apatite, so we should observe that populations of apatite crystals grown at different times in the same magma should have different H, F, and Cl abundances (demonstrating
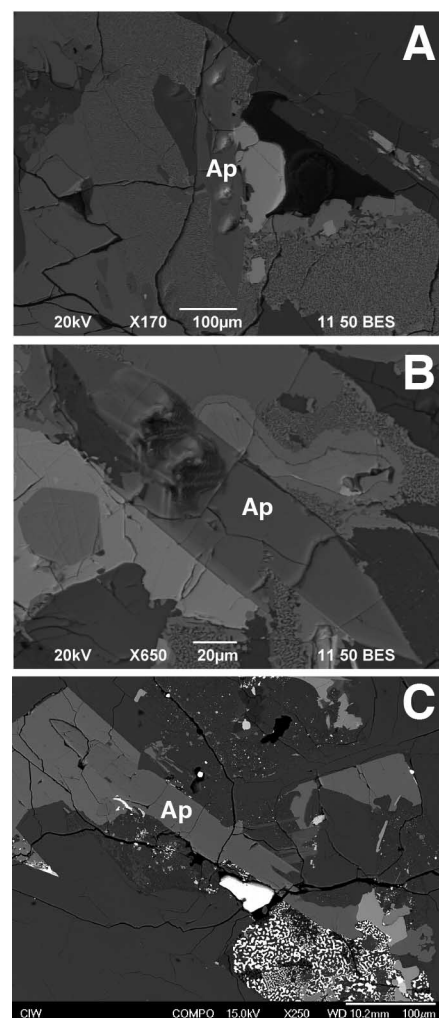
Fig. 1. Back-scattered electron maps of large apatites in mare basalts. (**A**) 12039,42 (2), (**B**) 10044,644 (2), and (**C**) 14053,16 (3). Light gray rim present in the apatite in (B) is likely due to increased REEs, which is consistent with both a fractional crystallization origin and the SiO_2 measurements reported in fig. S2 and (2).

[1]Department of Earth, Planetary, and Space Sciences, University of California, Los Angeles, Los Angeles, CA 90095, USA. [2]Institute for Meteoritics, Department of Earth and Planetary Sciences, University of New Mexico, Albuquerque, NM 87131, USA. [3]Department of Earth and Environmental Sciences, Wesleyan University, 265 Church Street, Middletown, CT 06459, USA. [4]Lunar and Planetary Institute, 3600 Bay Area Boulevard, Houston, TX 77058–1113, USA.

*Corresponding author. E-mail: jwboyce@alum.mit.edu

a lack of equilibrium that accompanies fractional crystallization). Evidence for a lack of equilibrium between apatite crystals and between apatite and their host rocks is ubiquitous among the lunar samples (2, 3, 8). Our modeling demonstrates that, by varying only the degree of crystallization and Cl content of the magma, we can

easily reproduce all the features seen in this diverse suite of lunar apatites (Fig. 2). Chlorine-poor and variably water-rich apatite such as those from LAP-paired samples can be generated during crystallization of less than 20% of the bulk rock after apatite saturation, provided that Cl contents are less than 0.5 ppm (relative to F = 10 ppm and

H_2O = 1 ppm). The shorter, Cl-rich trend of Apollo sample 76535 is observed for the same degree of crystallization in models with ≥5 ppm Cl but the same F and H_2O contents as for the other model curves in Fig. 2. Our model demonstrates that apatite with 0 to 65% molar occupancy H can be generated from magmas with identical H content and reasonable amounts of fractional crystallization.

If diffusion is sufficiently slow or crystallization sufficiently quick, the core of a crystal can become isolated from the evolving melt by the subsequent crystallization of additional material. This process results in crystals with growth zoning and fractional crystallization of elements from the remaining melt. Thus, a second test of our model is the prediction that portions of crystals growing early in the crystallization history (cores) will be F-rich, whereas later-grown portions (rims) will be F-poor, indicative of loss of F resulting from apatite fractionation. We also predict that other, nonvolatile incompatible elements that are enriched by fractional crystallization should be likewise enriched from core to rim. Core-to-rim zoning in volatile and nonvolatile elements consistent with our model is observed in large apatite from Apollo 12 basalt 12039,42 (Figs. 1A and 3) (2), Apollo 11 basalt 10044,644 (Fig. 1B and fig. S4) (2), and Apollo 14 basalt 14053,16 (Fig. 1C and fig. S5) (3). Covariations in both volatile (H, Cl, and F) and nonvolatile [rare earth elements (REEs) and SiO_2] elements suggests that a common process such as fractional crystallization is operating during the period when the apatite is growing. Critically, F is decreasing relative to H
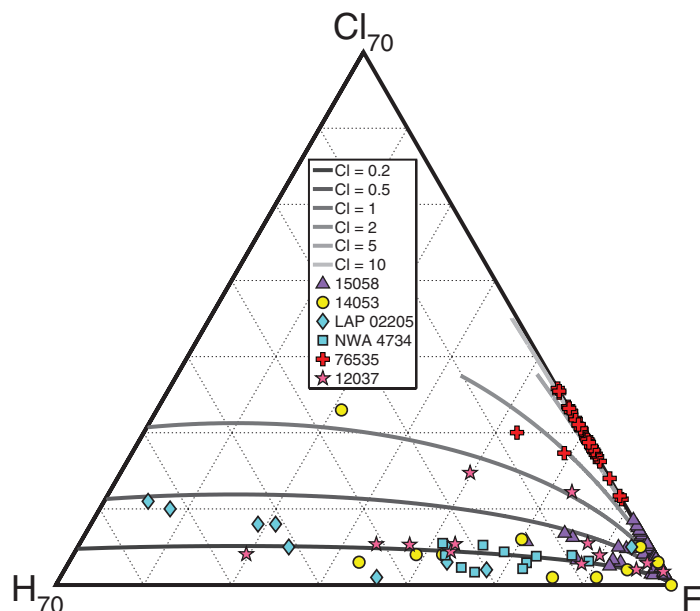
Fig. 2. Truncated ternary diagrams showing grain-to-grain variability of site components (F, Cl, and OH) in apatite within individual lunar samples. Apatite analyses were compiled from literature data (27–31). Curves show apatite composition during fractionation of less than 20% of the bulk rock after apatite saturation for initial conditions of F_{melt} = 10 ppm, H_{melt} = 1 ppm, and varying Cl_{melt} (in ppm).

Fig. 3. Trace elements and volatile profiles in apatite from mare basalt 12039. All analyses are plotted versus relative core-to-termination position (μm from geographic center of crystal in Fig. 1A). Scatter in central values (including consistent outlier datum plotted as a hollow circle) is probably because fine-scale cross-axis heterogeneities as growth take place in all directions, not just along the elongated axis (probably C-parallel) of the crystal. Concave-down core-to-rim decrease in F content is consistent with behavior of F as a compatible element—not just in apatite, but in the bulk assemblage. All other elements are bulk-incompatible and show concave-up core-to-rim trace- and minor-element patterns. Loss of H_2O is insufficient to be explained quantitatively by fractionation and may be affected by degassing. Data are from (2).
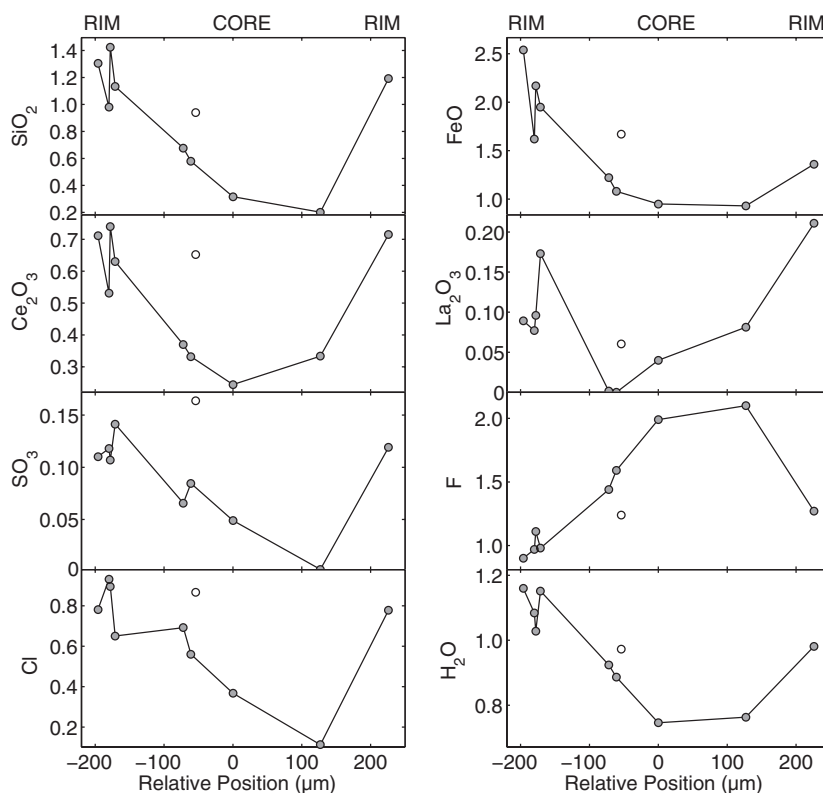
and Cl and other bulk-incompatible elements in all of these sections, which requires apatite in the fractionating assemblage and is not consistent with an assemblage consisting entirely of NAMs.

Our model also predicts that residual melts should be poor in elements such as F and P that are highly compatible in apatite and are thereby depleted during apatite fractionation. An example is the glass in contact with apatite from 10044,644 discussed above (16). This highly evolved glass (>78% SiO_2) has low F, Cl, and P (F < 460 ppm, Cl < 90 ppm, and P < 350 ppm) and yet makes up only $0.1 \pm 0.06\%$ of the total volume of 10044 (26). This is consistent with depletion of the melt in apatite components far below the thousandfold increase that might be expected for a late-stage melt refined by a high degree of fractional crystallization of NAMs. Because fractional crystallization models indicate that order-of-magnitude or greater increases in H_2O_{ap} are possible, it is not trivial to use apatite to estimate minimum water contents in lunar magmas. In cases where fractionation of apatite is a concern, the lowest H values are likely the ones least affected by loss of F and Cl and make for the most robust interpretation of H_2O_{melt}, but only as a maximum value. These H-enriched apatites may be quite abundant: A melt with $H_2O = F = Cl = 1$ ppm bulk (10 ppm at apatite saturation) will produce apatite with initial H_2O abundances of ~200 ppm. This is also the abundance that would be predicted for all apatite crystallizing under conditions approximating equilibrium crystallization. However, given the same starting conditions, fractional crystallization models produce more than 40% by mass apatite with >1000 ppm H_2O and more than 20% apatite with more than 10,000 ppm H_2O.

Apatite has such a strong effect on the volatile content of a magma during fractional crystallization that it is difficult, if not impossible, to learn anything about what conditions were like before apatite saturation unless equilibrium conditions are maintained throughout the life of the apatite. If only H, F, and Cl are considered, the patterns of degassing [decrease in the H/(H + F + Cl) content of apatite with time] and fractionation [increase of the H/(H + F + Cl) content of apatite with time] can be indistinguishable, and other parameters (such as nonvolatile trace elements) should be used to determine the forward-time direction of apatite evolution. Because it is not required that late-stage H_2O_{melt} be elevated in order to explain the elevated abundances of H_2O_{ap}, hydrogen-rich apatite cannot be cited as evidence for elevated H_2O_{melt} a priori. This permits reconciliation of H-rich apatites with the high temperatures and associated volatile depletion required by the giant-impact hypothesis (9) without the need to find those regions of impact-model space that are most permissive to retention of volatiles. Our results are also consistent with the nominally anhydrous ^{37}Cl-enrichment mechanism proposed for lunar materials by (8). Apatite can still serve as a useful target for isotopic studies of H and Cl provided that those studies take into account the possibility that

multiple, initially low-H sources (such as solar wind, surface ice, and spallation products) might be amalgamated and concentrated into apatite. Excluding apatite, the geochemical evidence for large portions of the interior of the Moon being more than nominally anhydrous is greatly reduced.

References and Notes

1. S. R. Taylor, C. M. Pieters, G. J. MacPherson, *Rev. Mineral. Geochem.* **60**, 657–704 (2006).
2. J. P. Greenwood *et al.*, *Nat. Geosci.* **4**, 79–82 (2011).
3. F. M. McCubbin *et al.*, *Proc. Natl. Acad. Sci. U.S.A.* **107**, 11223–11228 (2010).
4. J. W. Boyce *et al.*, *Nature* **466**, 466–469 (2010).
5. E. H. Hauri, T. Weinreich, A. E. Saal, M. C. Rutherford, J. A. Van Orman, *Science* **333**, 213–215 (2011).
6. R. Tartèse, M. Anand, *Earth Planet. Sci. Lett.* **361**, 480–486 (2013).
7. J. J. Barnes *et al.*, *Chem. Geol.* **337-338**, 48–55 (2013).
8. Z. D. Sharp, C. K. Shearer, K. D. McKeegan, J. D. Barnes, Y. Q. Wang, *Science* **329**, 1050–1053 (2010).
9. W. K. Hartmann, D. R. Davis, *Icarus* **24**, 504–515 (1975).
10. H. Hui, A. H. Peslier, H. Zhang, C. R. Neal, *Nat. Geosci.* **6**, 177–180 (2013).
11. K. Pahlevan, D. J. Stevenson, *Earth Planet. Sci. Lett.* **262**, 438–449 (2007).
12. J. D. Webster, C. Tappen, C. Mandeville, *Geochim. Cosmochim. Acta* **73**, 559–581 (2009).
13. E. Mathez, J. Webster, *Geochim. Cosmochim. Acta* **69**, 1275–1286 (2005).
14. M. Huh, J. Boyce, C. Manning, E. Medard, *Am. Geophys. Union Fall Meeting Abst.* **1**, 2534 (2011).
15. K. Vander Kaaden, F. McCubbin, E. Whitson, E. Hauri, J. Wang, *Proc. Lunar Planet. Sci. Conf.* **43**, abstr. 1247 (2012).
16. Methods and materials, figs. S1 to S5, and tables S1 and S2 are found in the supplementary materials.
17. E. H. Hauri, G. A. Gaetani, T. H. Green, *Earth Planet. Sci. Lett.* **248**, 715–734 (2006).
18. J. A. O'Leary, G. A. Gaetani, E. H. Hauri, *Earth Planet. Sci. Lett.* **297**, 111–120 (2010).
19. M. M. Hirschmann, *Annu. Rev. Earth Planet. Sci.* **34**, 629–653 (2006).
20. C. Beyer, S. Klemme, M. Wiedenbeck, A. Stracke, C. Vollmer, *Earth Planet. Sci. Lett.* **337–338**, 1–9 (2012).
21. A. Fabbrizio, R. Stalder, K. Hametner, D. Günther, *Geochim. Cosmochim. Acta* **121**, 684–700 (2013).
22. J. W. Boyce, J. M. Eiler, M. C. Channon, *Am. Mineral.* **97**, 1116–1128 (2012).
23. P. Roeder, R. Emslie, *Contrib. Mineral. Petrol.* **29**, 275–289 (1970).
24. M. J. Toplis, *Contrib. Mineral. Petrol.* **149**, 22–39 (2005).
25. M. Anand, R. Tartese, J. J. Barnes, I. A. Franchi, N. A. Starkey, *Mineral. Mag.* **77**, 589 (2013).
26. D. Beaty, A. Albee, *Proc. Lunar Planet. Sci. Conf.* **9**, 58–60 (1978).
27. M. Anand *et al.*, *Geochim. Cosmochim. Acta* **70**, 246–264 (2006).
28. S. M. Elardo *et al.*, *Meteorit. Planet. Sci.* **49**, 261–291 (2014).
29. F. McCubbin *et al.*, *Am. Mineral.* **95**, 1141–1150 (2010).
30. F. M. McCubbin *et al.*, *Geochim. Cosmochim. Acta* **75**, 5073–5093 (2011).

Preservation of a Preglacial Landscape Under the Center of the Greenland Ice Sheet

Paul R. Bierman,[1]* Lee B. Corbett,[1] Joseph A. Graly,[1]† Thomas A. Neumann,[1]‡ Andrea Lini,[1] Benjamin T. Crosby,[2] Dylan H. Rood[3,4]§

Continental ice sheets typically sculpt landscapes via erosion; under certain conditions, ancient landscapes can be preserved beneath ice and can survive extensive and repeated glaciation. We used concentrations of atmospherically produced cosmogenic beryllium-10, carbon, and nitrogen to show that ancient soil has been preserved in basal ice for millions of years at the center of the ice sheet at Summit, Greenland. This finding suggests ice sheet stability through the Pleistocene (i.e., the past 2.7 million years). The preservation of this soil implies that the ice has been nonerosive and frozen to the bed for much of that time, that there was no substantial exposure of central Greenland once the ice sheet became fully established, and that preglacial landscapes can remain preserved for long periods under continental ice sheets.

A diverse set of geochemical records has been developed from ice recovered in the 3054-m Greenland Ice Sheet Project 2 (GISP2) core. These data provide a detailed history of climate and ice dynamics stretching back over 100,000 years. The lowermost 13 m of the

core, which contain high concentrations of sediment, are less well studied. Here, we used measurements of atmospherically produced (meteoric) [10]Be, carbon, and nitrogen in sediment extracted from this silty ice zone to better understand the source and age of this material and to infer the erosional and thermal history under the center of the Greenland Ice Sheet (GIS) since its inception millions of years ago.

Ice likely was present on Greenland starting ~38 million years ago (Ma), expanding after 14 Ma with glaciations becoming more frequent after ~7 Ma and full coverage of Greenland by ice occurring at ~2.7 Ma (1, 2). Fossils in north Greenland suggest a partially forested tundra landscape some time before the growth of the current ice sheet (3). The more recent history of the GIS (the past 100,000 years) is constrained by ice cores as well as geologic mapping (4), cosmogenic nuclides (5), geochemical proxies (6), sea-level records (7), and ^{14}C dating of sediment (8).

Glacial erosion rates are controlled by thermal conditions at the bed. Ice colder than the pressure melting point is frozen to the bed (cold-based) and non-erosive. Ice warmer than the pressure melting point (warm-based) can erode the bed. Using heat-flux data, one model suggests that >75% of the present GIS is warm-based and thus erosive (9); however, the present-day thermal state of the GIS is known with certainty only where drilling exposes the bed.

The rate at which the GIS erodes its bed and the spatial distribution of sub-ice erosion are uncertain. North Atlantic sediment volume estimates suggest that, on average, ~100 m of rock were removed from glaciated areas of North America and Greenland after sustained glaciation began at 2.7 Ma (10). This corresponds to an average erosion rate of ~40 m per million years—a value that masks variability over space and time.

All GIS cores that have been drilled to or near to the bed contain silty basal ice (11). This ice can contain organic material (12), microorganisms, and high gas concentrations (13) and can display a stable water isotope signature (14) interpreted as indicating warmer conditions when the basal ice formed (11), perhaps in the absence of an ice sheet (15).

At the bottom of the GISP2 ice core (Summit, Greenland; Fig. 1), 13 m of silty ice [average 0.4% solids (16)] overlies 48 cm of diamict con-

taining erratic lithologies and underlain by granitic rock (11, 16, 17). The basal ice has not been dated directly, but the composition of dissolved gases suggests an age of at least 237,000 years (18). Ice at Summit is currently frozen to the bed (–9°C, 6°C below the pressure melting point) (19), and models suggest that it has remained frozen to the bed for at least the last several glacial cycles (20).

To understand the origin and history of the sediment in basal GISP2 ice, we measured the concentration of meteoric [10]Be adhered to sand and silt extracted from 17 samples of GISP2 silty ice. This isotope is continuously produced by cosmic rays in the atmosphere, is delivered to Earth's surface by precipitation and dry fall, and adheres to sediment. It has been used to date soils and infer erosion rates (21). We also measured organic carbon (OC) and total nitrogen (TN) in these same samples. To provide an analog for the GIS data, we measured a meteoric [10]Be profile in a permafrost tundra soil developed on a mid-Pleistocene glacial surface in Alaska (22). Methodological details and data tables are provided in the supplementary materials.

All silty ice sediment samples contained high concentrations of meteoric [10]Be and detectable levels of OC and TN (Fig. 2). Sediment in an 11-cm sample of ice just above the bed had the highest concentration of meteoric [10]Be (3.8×10^8 atoms g[-1]). Other sediment samples contained 0.61×10^8 to 1.02×10^8 atoms meteoric [10]Be g[-1]. In general, we found that [10]Be and OC concentrations decrease with sample distance above the bed. This decrease is consistent with the mixing of two components: (i) locally eroded soil material with both high meteoric [10]Be and OC concentrations, and (ii) eroded rock or sediment containing little meteoric [10]Be or OC. The second component

could be rock flour derived from outcrop abrasion or till sourced from below the depth to which meteoric [10]Be has penetrated soil, regolith, and rock.

The geochemical data suggest that sediment incorporated into the silty ice zone was derived from erosion of a stable cold-region landscape. [10]Be concentrations measured in silty ice sediment are similar to those measured in long-lived soils (21). Compared to 541 [10]Be concentrations measured in soil (21), the maximum [10]Be concentration measured in GISP2 sediment ranks in the 60th percentile (Fig. 3A). Sediment extracted from GISP2 silty ice contains 0.3 to 1.7% OC and 0.03 to 0.14% TN. The OC/TN regression indicates a C/N ratio of ~10, consistent with values reported for mineral-rich subsoils from boreal regions and cryoturbated tundra (23, 24). Both OC and TN concentrations are positively correlated with [10]Be concentration and all decrease above the bed, indicating that [10]Be, C, and N are derived from the same source, most likely a former tundra soil.

We can estimate the inventory of meteoric [10]Be in the soil before burial beneath the GIS. Such a calculation is viable because soil generally retains [10]Be and because [10]Be soil inventories—at least in temperate regions where sufficient data exist to make this comparison—are well correlated on a global scale with the maximum measured concentration of [10]Be in the soil profile (Fig. 3B) (21). Taking the maximum measured meteoric [10]Be concentration (3.8×10^8 atoms g[-1]) at face value suggests an inventory of 6.7×10^{10} atoms meteoric [10]Be cm^{-2} (Fig. 3B). However, if we presume that the soil from which the silty ice was derived predates the GIS and is thus older than 2.7 million years (~2 half-lives of [10]Be), then the concentration when the soil was first buried by ice, after

[1]Department of Geology and Rubenstein School of the Environment and Natural Resources, University of Vermont, Burlington, VT 05405, USA. [2]Department of Geosciences, Idaho State University, Pocatello, ID 83209, USA. [3]Earth Research Institute, University of California, Santa Barbara, CA 93016, USA. [4]Center for Accelerator Mass Spectrometry, Lawrence Livermore National Laboratory, Livermore, CA 94550, USA.

†Present address: Department of Geology and Geophysics, University of Wyoming, Laramie, WY 82071, USA.
‡Present address: Cryospheric Sciences Laboratory, NASA Goddard Space Flight Center, Greenbelt, MD 20771, USA.
§Present address: Scottish Universities Environmental Research Centre, University of Glasgow, East Kilbride G75 0QF, UK.
*Corresponding author. E-mail: pbierman@uvm.edu

Fig. 1. Photograph of GISP2 ice core silty ice zone; the inset shows core stratigraphy (15). Thick gray lines indicate intervals of the ice core that were analyzed for meteoric [10]Be, OC, and TN. Core depth shown in meters by labels. Image from NOAA.

correcting for radioactive decay of ^{10}Be, was higher by a factor of more than 4 (~1.5×10^9 atoms meteoric ^{10}Be g^{-1}). The corresponding soil inventory when the GIS developed was ~3.8×10^{11} atoms meteoric ^{10}Be cm^{-2}. Such concentrations and inventories, while high, are reasonable. The tundra soil from the North Slope of Alaska, developed on a till plain that has been stable for between 150,000 and 750,000 years (22), contains up to 1.1×10^9 atoms meteoric ^{10}Be g^{-1} and has an inventory of 4.0×10^{10} atoms meteoric ^{10}Be cm^{-2}, consistent with the meteoric ^{10}Be concentrations in the silty

ice zone and the inferred meteoric ^{10}Be inventory (Fig. 4).

The duration over which this ancient soil developed in Greenland before expansion of the GIS can be roughly estimated using the delivery rate of meteoric ^{10}Be to the GISP2 site [3.5×10^5 atoms cm^{-2} year^{-1} in the upper, silt-free ice of the GISP 2 core (25)]. With no erosion and assuming the Holocene meteoric ^{10}Be deposition rate, the soil material in the silty ice zone was subaerially exposed for at least 200,000 years (no decay correction) and perhaps more than 1 million years

(decay-corrected). Even using a deposition rate several times higher, assuming a weakened polar vortex and increased precipitation during past warm periods, the soil incorporated in GISP2 basal silty ice requires far longer exposure (on the order of 10^5 years) than can be accounted for by a few millennium-long periods of exposure during extreme interglacials [such as marine isotope stage (MIS) 11]. Therefore, the data are most consistent with soil formation prior to the existence of the present GIS. On the basis of similarly high meteoric ^{10}Be concentrations, ancient

Fig. 2. Geochemical and isotopic data for GISP2 basal silty ice. (**A**) Meteoric ^{10}Be concentration of silt with core depth; horizontal axis has gap and variable scaling to allow plotting of the high-concentration lowermost sample. (**B**) Water oxygen isotopes in ice (14). (**C**) Organic carbon (OC) measured in acidified silt. (**D**) Organic carbon/total nitrogen ratio measured in acidified silt. (**E**) Positive linear relationship between organic carbon and meteoric ^{10}Be in silt samples. Data in table S1.
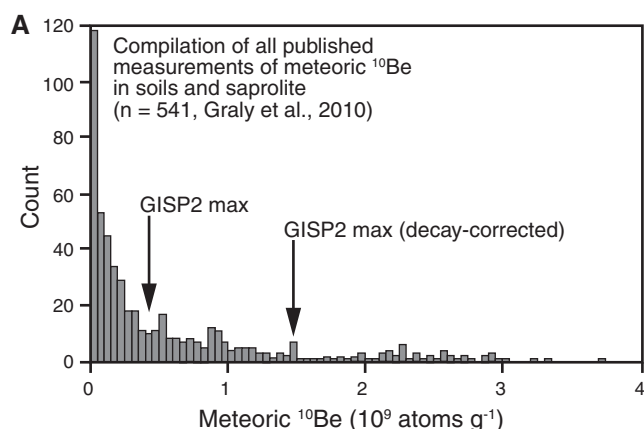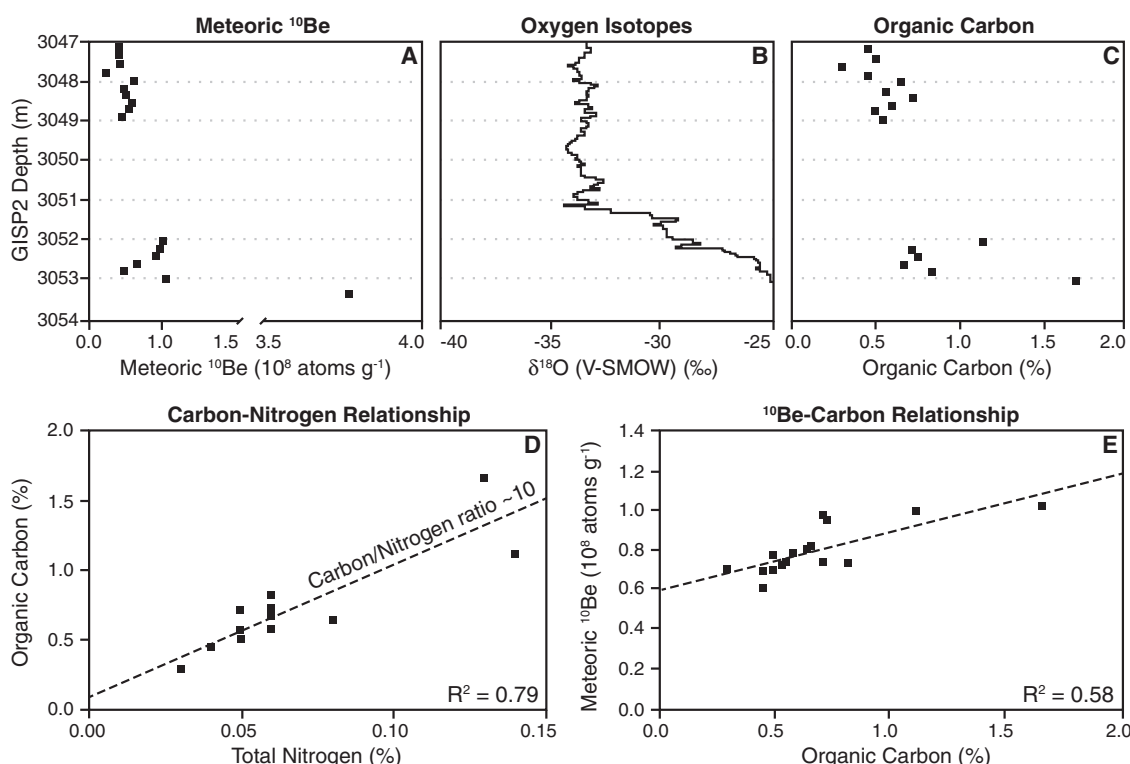
Fig. 3. GISP2 silt contains high concentrations of meteoric ^{10}Be. (**A**) Histogram of 541 measurements of meteoric ^{10}Be made in soils (21) with maximum meteoric ^{10}Be measured in GISP2 silt and decay-corrected concentration assuming burial for two half-lives of ^{10}Be (~2.7 million years). (**B**) Maximum meteoric ^{10}Be concentrations in soil profiles are well correlated to soil meteoric ^{10}Be inventories (21). Using measured and decay-corrected maximum meteoric ^{10}Be concentrations in GISP2 silty ice suggests that meteoric ^{10}Be inventory in pre-GIS soil was at least 6.7×10^{10} atoms cm^{-2} and likely 3.8×10^{11} atoms cm^{-2}.
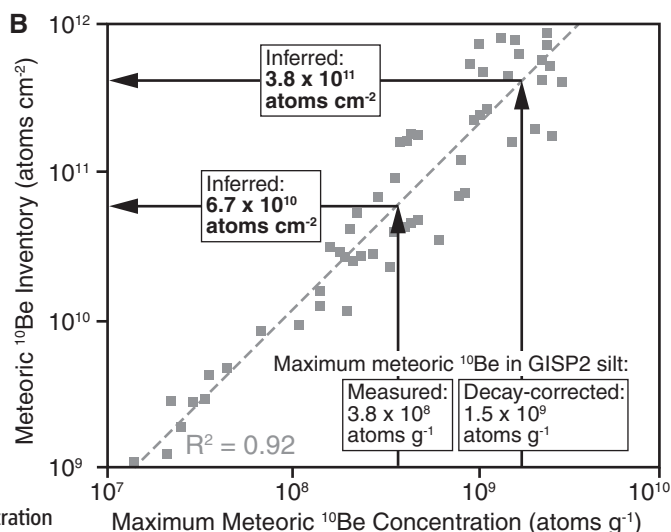
preglacial regolith has been identified on uplands and in glacial sediments preserved on Baffin Island in arctic Canada (26).

Other means of generating high meteoric ^{10}Be concentrations in sediment extracted from the GISP2 silty ice zone do not appear plausible. It is unlikely that the ^{10}Be we measured was concentrated from basal meltwater. Ice in the GISP2 core contains on average 1.4×10^4 atoms meteoric ^{10}Be g^{-1} (25), four orders of magnitude less than measured in the silty ice. Stable water isotope data from basal ice of the nearby Greenland Ice Core Project (GRIP) core (19) fall on the meteoric water line and are inconsistent with large-scale melting that would be needed to concentrate ^{10}Be. The positive, linear correlation between OC and ^{10}Be (Fig. 2) is also inconsistent with delivery of meteoric ^{10}Be from meltwater. Long and/or warm interglacials (MIS 5e, 9, and 11) are unlikely to have melted the entire GIS, and even if they did, the peak of each interglacial is so short (thousands of years) that insufficient meteoric ^{10}Be would be delivered to any exposed soil at Summit to build up even a few percent of the meteoric ^{10}Be inventory we infer. On the basis of the marine isotope record (27), other interglacials were less intense than MIS 5e, 9, and 11 and thus even less likely to melt the entire GIS. In situ production of ^{10}Be by the interaction of cosmic rays (specifically muons) with sediment under the ice sheet, which is several kilometers thick, generates an inventory of only a few atoms ^{10}Be g^{-1} over a period of 2.7 million years (28).

Previous but imprecise measurements of in situ ^{10}Be, ^{26}Al, and ^{36}Cl in rock collected below the silty ice zone of the GISP2 core are consistent with short exposure of that rock (at most a few thousand years) around 0.5 ± 0.2 Ma, possibly during the long MIS 11 interglaciation (29). If there were a short period of exposure during MIS 11, then the pre-Pleistocene soil below GISP2 was not fully eroded during that exposure. Any in situ produced ^{10}Be, ^{26}Al, and ^{36}Cl accumulated in rock during brief exposure at MIS 11 could

have been produced under a cover of uneroded, pre-Pleistocene soil, or the soil we sampled could have been transported from nearby. The ^{10}Be measurements presented here demand a much longer period of subaerial exposure than the data of Nishiizumi et al. (29), many tens to a few hundreds of thousands of years, a duration of exposure only possible at Summit before the expansion of the GIS at ~2.7 Ma.

The continued presence of soil in GISP2 ice for several million years after formation of the GIS indicates extremely low rates of sub-ice erosion and slow rates of horizontal ice advection away from Summit. Such low shear rates are consistent with both long-term stability of the GIS ice divide location and a frozen bed for most, if not all, of the past 2.7 million years. The existence of ancient soil implies low sub-ice erosion rates; however, the 13-m thickness of the silty ice zone suggests erosion, entrainment, and mixing of the preglacial soil. Although persistence of this ancient soil precludes substantial erosion at the bed (16), it is possible that cold-based ice incorporated some basal debris (30). The flux of silty ice past the GISP2 site is likely dominated by deformation within the ice rather than by sliding (11). If warm-based ice was present at Summit for short periods of time in the past, it did little more than mix sediment from the bed into the overlying ice.

Meteoric ^{10}Be data constrain both the preglacial landscape history and the Quaternary history of Summit, Greenland. ^{10}Be and OC data are consistent with inferences, based on the stable oxygen isotopic composition of ice and the concentration and isotopic composition of gases in the silty ice zone, that the GIS overran a local snowfield or ice that itself overlay a soil (13). Since the GIS formed, the soil has been preserved and only slowly eroded, implying that an ancient landscape underlies 3000 m of ice at Summit. These new data are most consistent with continuous cover of Summit by ice for the entire Quaternary, with at most brief exposure and minimal surface erosion during the warmest or longest interglacials.
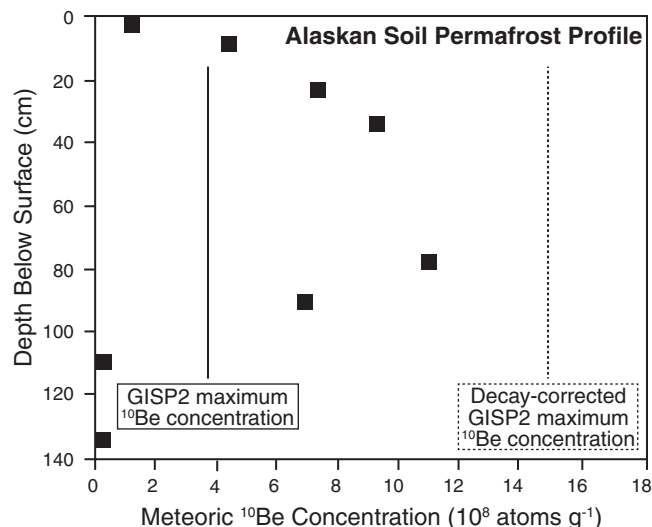
References and Notes

1. J. S. Eldrett, I. C. Harding, P. A. Wilson, E. Butler, A. P. Roberts, Nature 446, 176–179 (2007).
2. H. C. Larsen et al., Science 264, 952–955 (1994).
3. S. Funder, N. Abrahamsen, O. Bennike, R. W. Feyling-Hanssen, Geology 13, 542 (1985).
4. D. Winkelmann, W. Jokat, L. Jensen, H.-W. Schenke, Quat. Sci. Rev. 29, 1069–1077 (2010).
5. L. Håkansson, J. P. Briner, A. Aldahan, G. Possnert, Quat. Res. 76, 452–459 (2011).
6. A. E. Carlson, J. S. Stoner, J. P. Donnelly, C. Hillaire-Marcel, Geology 36, 359 (2008).
7. A. J. Long et al., Earth Planet. Sci. Lett. 272, 8–18 (2008).
8. H. Cremer, O. Bennike, B. Wagner, Quat. Sci. Rev. 27, 312–319 (2008).
9. R. Greve, Ann. Glaciol. 42, 424–432 (2005).
10. E. P. Laine, Quat. Res. 14, 188–198 (1980).
11. M. L. Bender, E. Burgess, R. B. Alley, B. Barnett, G. D. Clow, Earth Planet. Sci. Lett. 299, 466–473 (2010).
12. E. Willerslev et al., Science 317, 111–114 (2007).
13. R. Souchez et al., Geophys. Res. Lett. 33, L24503 (2006).
14. M. Stuiver, P. M. Grootes, Quat. Res. 53, 277–284 (2000).
15. A. J. Gow et al., J. Geophys. Res. 102, 26559 (1997).
16. A. J. Gow, D. A. Meese, Ann. Glaciol. 22, 134 (1996).
17. D. Weis, D. Demaiffe, R. Souchez, A. J. Gow, D. A. Meese, Earth Planet. Sci. Lett. 150, 161–169 (1997).
18. M. Suwa, J. C. von Fischer, M. L. Bender, A. Landais, E. J. Brook, J. Geophys. Res. 111, D02101 (2006).
19. R. Souchez et al., Geophys. Res. Lett. 21, 693–696 (1994).
20. P. Huybrechts, Ann. Glaciol. 23, 226 (1995).
21. J. A. Graly, P. R. Bierman, L. J. Reusser, M. J. Pavich, Geochim. Cosmochim. Acta 74, 6814–6829 (2010).
22. T. D. Hamilton, "Surficial geology of the Dalton Highway (Itkillik-Sagavanirktok rivers) area, southern Arctic foothills, Alaska" (Alaska Division of Geological & Geophysical Surveys Professional Report 121, 2003); www.dggs.alaska.gov/pubs/id/7191.
23. I. Callesen, K. Raulund-Rasmussen, C. J. Westman, L. Tau-Strand, Boreal Environ. Res. 12, 681–692 (2007); http://curis.ku.dk/ws/files/11055152/fulltext.pdf.
24. G. Hugelius, P. Kuhry, C. Tarnocai, T. Virtanen, Permafr. Periglac. Process. 21, 16–29 (2010).
25. R. C. Finkel, K. Nishiizumi, J. Geophys. Res. 102, 26699 (1997).
26. K. A. Refsnider, G. H. Miller, Quat. Sci. Rev. 67, 176–189 (2013).
27. L. Lisiecki, M. Raymo, Paleoceanography 20, PA1003 (2005).
28. B. Heisinger et al., Geochim. Cosmochim. Acta 66, A558 (2002).
29. K. Nishiizumi et al., EOS 77, OS41B (1996).
30. K. M. Cuffey et al., Geology 28, 351 (2000).

Fig. 4. Depth profile of meteoric ^{10}Be measured in a stable soil profile developed on glacial sediment deposited >150,000 years ago, North Slope, Alaska. Prominent subsurface bulge is indicative of a stable soil profile (21). Maximum measured and decay-corrected concentrations of meteoric ^{10}Be measured in GISP2 silt are overlain. Data in table S2.

Organic Matter Stoichiometry, Flux, and Oxygen Control Nitrogen Loss in the Ocean

Andrew R. Babbin,[1]* Richard G. Keil,[2] Allan H. Devol,[2] Bess B. Ward[1]

Biologically available nitrogen limits photosynthesis in much of the world ocean. Organic matter (OM) stoichiometry had been thought to control the balance between the two major nitrogen removal pathways—denitrification and anammox—but the expected proportion of 30% anammox derived from mean oceanic OM is rarely observed in the environment. With incubations designed to directly test the effects of stoichiometry, however, we showed that the ratio of anammox to denitrification depends on the stoichiometry of OM supply, as predicted. Furthermore, observed rates of nitrogen loss increase with the magnitude of OM supply. The variable ratios between denitrification and anammox previously observed in the ocean are thus attributable to localized variations in OM quality and quantity and do not necessitate a revision to the global nitrogen cycle.

The processes that remove nitrogen (N) from the ocean are (i) anaerobic ammonium oxidation (anammox), the autotrophic oxidation of ammonium to N_2 by nitrite, and (ii) denitrification, a stepwise heterotrophic reduction of nitrate (the most abundant species of fixed N in the ocean) to N_2. The existence of anammox was contemplated even before the anammox metabolism was discovered in bacteria (1, 2), based on the observation that ammonium, a by-product from the heterotrophic respiration of N-containing organic matter (OM), does not accumulate within strictly anoxic environments (3), such as the oxygen-deficient zones (ODZs). Because ammonium cannot be removed by oxidation via conventional aerobic nitrification in ODZs, the oxidation of the particulate organic matter (POM)–derived ammonium must occur through anammox. Building on previous work (4), we derived a balance between anammox and denitrification from generic OM stoichiometry rather than from average ocean POM by assuming (i) complete oxidation of POM to CO_2, (ii) no accumulation of ammonium or nitrite, and (iii) that all ammonium liberated by the reduction of nitrate and nitrite must be oxidized via anammox in the absence of molecular O_2. The equation stoichiometry is predicated on previous theoretical (4) and experimental (5) studies that determined the species coefficients, depending on the elemental composition of the POM (see the supplementary materials). From this theoretical balance, the fraction of total N loss via anammox is

$$f_{amx} = \frac{1.02\frac{N}{C}}{0.4 \ + \ 0.1\frac{H}{C} - 0.2\frac{O}{C} \ + \ 0.456\frac{N}{C}} \quad (1)$$

where the variables are the ratios of each of the major elements in the POM substrate with respect to C. From Eq. 1, it becomes apparent that the C/N ratio is the most important parameter in setting the balance, because (i) the N content is modified by the largest coefficient, and (ii) the H and O contents tend to compensate for each other. For the average labile POM stoichiometry in the ocean, $C_{6.6}H_{10.9}O_{2.6}N$ (6), $f_{amx} = 28\%$.

It is somewhat mysterious then that anammox and denitrification often do not appear to be stoichiometrically linked, given the generally conserved average composition (C/N = 6.6) of OM, but rather that one process or the other dominates the total N loss when measured discretely in space and time (7, 8). Spatiotemporal dynamics (7) and failure to include the effect of episodic POM supply in small-volume incubations are likely explanations, although so far unproven. Others have invoked alternative anaerobic mechanisms, such as dissimilatory nitrate reduction to ammonium (8), or benthic ammonium release (9), to provide ammonium for anammox in the absence of measurable denitrification, but these explanations cannot fully satisfy the anammox demand for ammonium. Recently, an extensive data set from the South Pacific showed that on a larger (areal) scale, anammox was 28% of the total N loss (10), as predicted (4) by the average composition of the OM (i.e., C/N = 6.6). However, most sites had low rates of anammox and even lower rates of denitrification, whereas a few discrete locations had very high denitrification rates. The balance between anammox and denitrification is important for understanding N cycling and the energy balance in suboxic zones, and because the two processes have different effects on C mineralization and on the production and consumption pathways of nitrous oxide, a major greenhouse gas and ozone-depleting agent (11), which is a significant intermediate in the denitrification pathway but not of anammox (12).

To investigate the roles of OM stoichiometry and O_2 concentration in controlling N loss in the Eastern Tropical North Pacific ODZ, we performed incubation experiments using isotopically labeled nitrite as a tracer and various OM treatments at the top of the ODZ and the secondary nitrite maximum of two stations, one coastal and one offshore (fig. S1). Anammox and denitrification rates increased by different proportions in response to specific OM additions, with higher proportions of anammox corresponding to greater N relative to C content (i.e., a lower C/N ratio) of the source substrate (Table 1). Experimental treatments included sterilized substrate organic compositions of $C_{9.7}H_{17.8}O_{8.9}NH_3$ for the sucrose and ammonium mixture, $C_{3.6}H_{5.7}ON$ for the casamino acids, and $C_{6.8}H_{11.2}O_{2.7}N$ for the sinking particulate OM (from the average measured POM C/N, with an inferred C/H/O from average POM stoichiometry) (6). Based on experiments at both depths of each of the two stations (Fig. 1), the predicted anammox proportions of N loss of 22, 45, and 27% (Eq. 1), respectively, match the observed values quite closely (Fig. 2). These data confirm that the proportions of the two N loss processes depend on the stoichiometry of the source OM.

The addition of fresh OM-induced changes in observed anammox and denitrification rates, indicating that the total fixed N loss must have been prevailingly limited by OM supply, probably because any ambient dissolved OM before the addition was highly refractory (13). This is confirmed by the measured increase of N loss rates from the addition of OM, regardless of stoichiometry, in 11 of 12 experiments; relative to no OM addition, these rates were stimulated by factors averaging 1.4, 2.4, and 7.0 (Fig. 1) by the addition of sucrose plus ammonium, casamino acids, and sinking POM, respectively. Furthermore, the same anammox rates were observed in the sucrose additions, compared with the no OM–added treatments at the same depths, so ambient OM contributed no ammonium during the incubations. The collected sinking POM induced a much greater increase in the rates as compared with the sucrose and casamino acids treatments, despite there being a lower amount of organic C amended. This indicates that a mixture of diverse organic compound classes in naturally occurring OM is more beneficial to cell growth, perhaps by lowering the energy requirements to build and maintain cells, as compared with a pure carbohydrate or amino acid diet.

The depth distribution of total N loss rates at both stations (Fig. 3), determined from separate experiments with only labeled nitrite tracer added, further supports the link between in situ rates and OM flux. The measured rates decreased as a function of depth, in accordance with a simple power scaling law (14) with an exponent of –1.3. The total areal flux (obtained by integrating the rates with respect to depth) must thus vary as a function of depth with an exponent one unit higher, or –0.3. The value of –0.3 matches that of the sinking POM flux commonly measured in suboxic basins (compared with a global average of –0.8) (14–18). This remarkable correspondence indicates that denitrification is responsible for the organic C remineralization, which in turn drives N loss in the anoxic depths of the water column.

Dissolved O_2 concentrations themselves constrain the domain within the global ocean where N loss can occur, due to the preferential use of O_2 over nitrate as a terminal electron acceptor

[1]Department of Geosciences, Princeton University, Guyot Hall, Princeton, NJ 08544, USA. [2]School of Oceanography, University of Washington, Box 357940, Seattle, WA 98195, USA.

*Corresponding author. E-mail: babbin@princeton.edu

in the remineralization of OM and the regulation by O_2 of the enzymes catalyzing N loss (19). Marine zones where denitrification and anammox can occur have been defined variously as waters with an upper O_2 concentration of 2 to 20 µmol liter^{-1} (20–23). Although this uncertainty in threshold may seem trivial, when integrated over the volume of the ocean, the total volumes of subthreshold water decrease greatly as O_2 concentrations approach zero (24), and therefore the actual threshold for anaerobic processes has important implications for modeling the global N budget.

The effect of O_2 on N loss rates was distinct and apparently immediate: The addition of 3 or 8 µmol liter^{-1} of O_2 with 3 µmol liter^{-1} of NH_4^+ resulted in insignificant N loss rates, suggesting that the O_2 tolerance limit for environmental assemblages is similar to that inferred from cultured organisms (25). Low levels of anammox consistently occurred in the 3 µmol liter^{-1} of O_2 treatment but not at 8 µmol liter^{-1}, whereas denitrification was not consistently detected with either 3 or 8 µmol liter^{-1} of O_2. This O_2 tolerance is consistent with results from (i) the Baltic Sea (26), where an O_2 level of 3 µmol liter^{-1} inhibited anammox and denitrification by 90 and 100%, respectively; (ii) the Black Sea (21), where the anammox O_2 tolerance was estimated to be between 8 and 13 µmol liter^{-1}; and (iii) the Eastern Tropical South Pacific (23), where samples from the core of the ODZ exhibited no anammox when amended with O_2 greater than 3.5 µmol liter^{-1}. The slight variation in the two O_2 tolerances may allow anammox to be coupled to aerobic nitrification in water with low but nonzero O_2. But the magnitude of this difference and the steepness of the observed O_2 gradient overlying the ODZ (4 µmol liter^{-1} of O_2 m^{-1}) are such that the amount of anammox supported independently from denitrification in the ODZs must be negligible.

Rates of anammox and denitrification can be calculated based on the stoichiometry and rates of the OM flux, the exponent of the power law, and the depths bounding the anoxic zone. On the basis of this simple model, the particle fluxes of 24 and 10 mg of C m^{-2} day^{-1} measured in this study (Table S2) at the top of the coastal and off-shore ODZs, respectively, should support local N_2 production rates at the top of the ODZ of 17 and 4 nmol of N liter^{-1} day^{-1}. These rates derived from the measured POM flux are comparable to those measured in the small-vial incubations of 22 and 4 nmol of N liter^{-1} day^{-1} near the depths of sediment trap deployment, and are well within errors associated by bridging two highly disparate types of measurements. The direct agreement between the calculated and measured rates provides evidence that N gas production is causally related to the organic C sedimentation flux and confirms that this simple model may be useful to estimate N loss rates in ODZs. Furthermore, using C flux data from the Mexican margin (27), we can predict the associated N gas production that occurs by differentiating with depth the organic flux driving this oxidation (Fig. 3A). The N_2 production rates implied by these organic C data correspond closely to our measured rates, with rates highest near the surface and decreasing via a power law scaling with depth (Fig. 3B).

In addition to providing an explanation for the relative rates of anammox and denitrification

Table 1. Anammox percent for each OM treatment. Anammox percentages are included for both sampling sites at the base of the oxycline and at the depth of the secondary nitrite maximum (SNM).

Treatment	OM stoichiometry	N/C	C oxidation state	Site				Average ± standard error
				Coastal		Offshore		
				Oxycline 60 m	SNM 100 m	Oxycline 100 m	SNM 150 m	
NH_4^+ only	—	—	—	39.8%	55.8%	33.5%	42.5%	42.9 ± 4.5%
Sucrose + NH_4^+	$C_{9.7}H_{17.8}O_{8.9}NH_3$	0.10	0	25.3%	24.5%	26.5%	21.8%	24.5 ± 1.0%
Sinking POM	$C_{6.8}H_{11.2}O_{2.7}N$	0.15	−0.41	31.2%	29.7%	32.8%	28.3%	30.5 ± 1.0%
Casamino acids	$C_{3.6}H_{5.7}ON$	0.28	−0.19	44.1%	48.3%	40.7%	41.7%	43.7 ± 1.8%
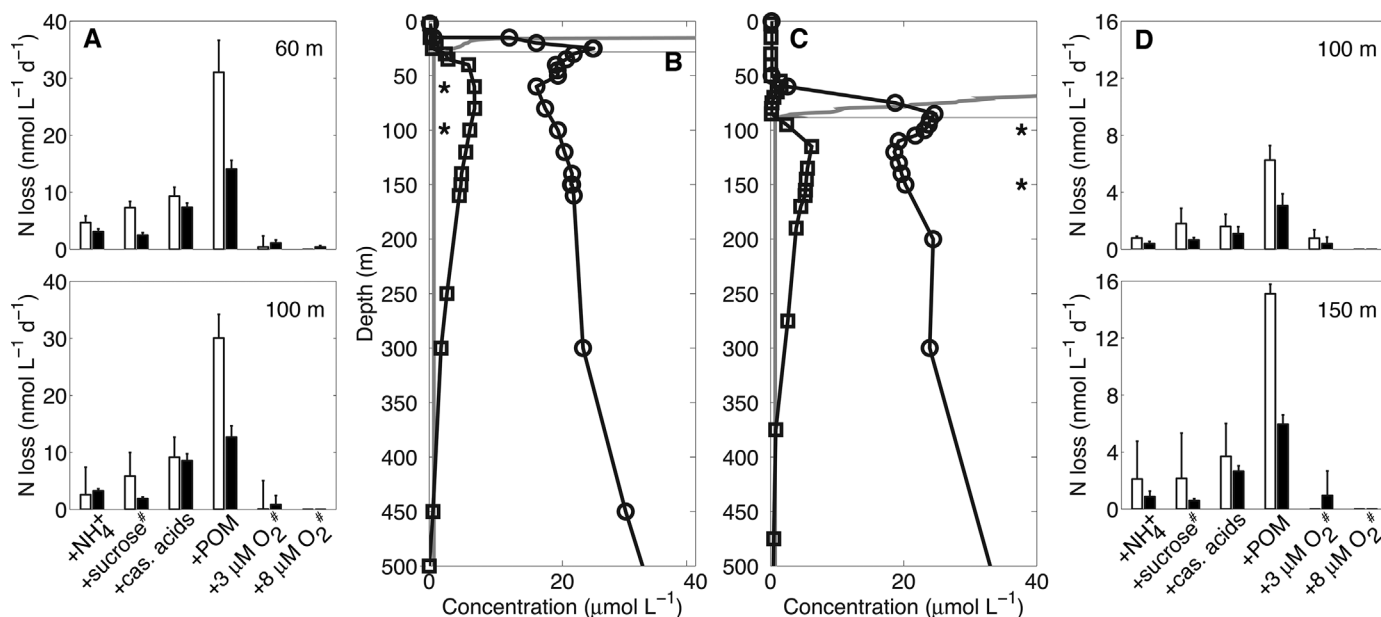
Fig. 1. Measured N loss rates. Biogeochemical parameters (center panels) measured at coastal (**A** and **B**) and offshore (**C** and **D**) sites. Nitrate (circles), nitrite (squares), and O_2 (dark-gray line) concentrations are shown. The horizontal light-gray line indicates the depth of the onset of anoxia. Asterisks indicate depths where experiments were performed, and hash marks in (A) and (D) indicate additions supplemented by $^{14}NH_4^+$. Denitrification (open bars) and anammox (solid bars) rates are shown. Error bars indicate the standard deviation of rates derived from a linear fit to five time points measured in triplicate.

in ODZs and a quantitative relationship between N loss and the flux of OM, the results presented here also have the potential to explain much of the variability in the relative contributions of anammox and denitrification rates observed in the ODZs. Although the average OM C/N in the ocean is 6.6, large variations are observed, based on the phytoplankton community composition or the state of remineralization of the OM (*14*, *28*). For instance, newly formed OM rich in amino acids can stimulate higher relative anammox rates due to the preferential remineralization of N-rich compounds (*16*). Older recalcitrant OM, poor in organic N, however, will result in a smaller proportion of N loss catalyzed by anammox bacteria. Yet, integrated over both space and time, the balance between anammox and denitrification must be constrained by the flux and C/N ratio of the OM in and out of the anoxic zone.

It is also worth noting that the occurrence of nitrite accumulation in the ODZs does not significantly alter the balance between anammox and denitrification, because of the requirement that a large percentage of nitrate reduction proceeds no further than nitrite before a noticeable enrichment in fraction anammox results (fig. S3).

Furthermore, these constraints have applicability to estimating future fixed N loss. The model developed here, predicting water column denitrification rates using POM fluxes and C/N ratios, can be integrated into global biogeochemical models to provide robust constraints on present and past fixed N losses in marine suboxic regions. It is additionally helpful in evaluating the effects of ODZ expansion on future climate (*29*), potential shifts in average C/N ratios with changing atmospheric CO_2 concentrations (*30*), and negative feedbacks to global primary production via N loss.

References and Notes

1. F. A. Richards, in *Chemical Oceanography*, J. P. Riley, G. Skirrow, Eds. (Academic Press, London, 1965), vol. 1, pp. 611–643.
2. M. Bender *et al.*, *Geochim. Cosmochim. Acta* **53**, 685–697 (1989).
3. D. E. Canfield *et al.*, *Science* **330**, 1375–1378 (2010).
4. W. Koeve, P. Kähler, *Biogeosciences* **7**, 2327–2337 (2010).
5. M. Strous, J. J. Heijnen, J. G. Kuenen, M. S. M. Jetten, *Appl. Microbiol. Biotechnol.* **50**, 589–596 (1998).
6. L. A. Anderson, *Deep Sea Res. Part I Oceanogr. Res. Pap.* **42**, 1675–1680 (1995).
7. B. B. Ward *et al.*, *Nature* **461**, 78–81 (2009).
8. P. Lam *et al.*, *Proc. Natl. Acad. Sci. U.S.A.* **106**, 4752–4757 (2009).
9. T. Kalvelage *et al.*, *Nat. Geosci.* **6**, 228–234 (2013).
10. T. Dalsgaard, B. Thamdrup, L. Farías, N. P. Revsbech, *Limnol. Oceanogr.* **57**, 1331–1346 (2012).
11. A. R. Ravishankara, J. S. Daniel, R. W. Portmann, *Science* **326**, 123–125 (2009).
12. B. Kartal *et al.*, *Environ. Microbiol.* **9**, 635–642 (2007).
13. H. Ogawa, Y. Amagai, I. Koike, K. Kaiser, R. Benner, *Science* **292**, 917–920 (2001).
14. J. H. Martin, G. A. Knauer, D. M. Karl, W. W. Broenkow, *Deep Sea Res. Part A* **34**, 267–285 (1987).
15. A. H. Devol, H. E. Hartnett, *Limnol. Oceanogr.* **46**, 1684–1690 (2001).
16. B. A. Van Mooy, R. G. Keil, A. H. Devol, *Geochim. Cosmochim. Acta* **66**, 457–465 (2002).
17. F. Lipschultz *et al.*, *Deep-Sea Res. A Oceanogr. Res. Pap.* **37**, 1513–1541 (1990).
18. W. M. Berelson, *Oceanography (Wash. D.C.)* **14**, 59–67 (2001).
19. W. G. Zumft, *Microbiol. Mol. Biol. Rev.* **61**, 533–616 (1997).
20. L. A. Codispoti, T. Yoshinari, A. H. Devol, in *Respiration in Aquatic Ecosystems*, P. A. DelGiorgio, P. J. le B. Williams, Eds. (Oxford Univ. Press, New York, 2005), pp. 225–247.
21. M. M. Jensen, M. M. M. Kuypers, G. Lavik, B. Thamdrup, *Limnol. Oceanogr.* **53**, 23–36 (2008).
22. A. Paulmier, D. Ruiz-Pino, *Prog. Oceanogr.* **80**, 113–128 (2009).
23. T. Kalvelage *et al.*, *PLOS ONE* **6**, e29299 (2011).
24. D. Bianchi, J. P. Dunne, J. L. Sarmiento, E. D. Galbraith, *Global Biogeochem. Cycles* **26**, 10.1029/2011GB004209 (2012).
25. M. Strous, E. Van Gerven, J. G. Kuenen, M. Jetten, *Appl. Environ. Microbiol.* **63**, 2446–2448 (1997).
26. T. Dalsgaard, *et al.*, paper presented at the Association for the Sciences of Limnology and Oceanography Aquatic Sciences Meeting, New Orleans, 21 February 2013.
27. H. E. Hartnett, A. H. Devol, *Geochim. Cosmochim. Acta* **67**, 247–264 (2003).
28. A. Körtzinger, W. Koeve, P. Kähler, L. Mintrop, *Deep Sea Res. Part I Oceanogr. Res. Pap.* **48**, 661–688 (2001).
29. L. Stramma, G. C. Johnson, J. Sprintall, V. Mohrholz, *Science* **320**, 655–658 (2008).
30. U. Riebesell *et al.*, *Nature* **450**, 545–548 (2007).

Fig. 2. Theoretical f_{amx} from OM stoichiometry. Fractions of N loss attributed to anammox (f_{amx}) are calculated by a modified version of Eq. 1 (supplementary materials text) are shown in color contours. Cas., casamino acids; Suc., sucrose. Predicted (circles) and measured (squares) f_{amx} for each OM treatment are overlaid. The inset shows these values in comparison to the expected 1:1 line.

Fig. 3. Organic C-dependence of N loss. (**A**) Organic C flux previously measured (gray symbols) by benthic lander incubations (*27*) and collected in this study (black symbols) by sediment traps. The derived power law fit (black line) for the benthic lander study is included for reference. (**B**) Total N loss rates for both coastal (solid symbols) and offshore (open symbols) stations from $+^{15}NO_2^-$-only experiments. The power law best fit of these points (dashed gray line) and the theoretical rates (solid black line) driven by and derived from the organic C flux in (A) are also shown. Asterisks denote the rate experiments closest to the sediment trap deployment depths. z, depth; R^2, correlation coefficient.

Conversion of Channelrhodopsin into a Light-Gated Chloride Channel

Jonas Wietek,[1]* J. Simon Wiegert,[2]* Nona Adeishvili,[1] Franziska Schneider,[1]
Hiroshi Watanabe,[3] Satoshi P. Tsunoda,[1] Arend Vogt,[1] Marcus Elstner,[3]
Thomas G. Oertner,[2]† Peter Hegemann[1]†

The field of optogenetics uses channelrhodopsins (ChRs) for light-induced neuronal activation. However, optimized tools for cellular inhibition at moderate light levels are lacking. We found that replacement of E90 in the central gate of ChR with positively charged residues produces chloride-conducting ChRs (ChloCs) with only negligible cation conductance. Molecular dynamics modeling unveiled that a high-affinity Cl⁻-binding site had been generated near the gate. Stabilizing the open state dramatically increased the operational light sensitivity of expressing cells (slow ChloC). In CA1 pyramidal cells, ChloCs completely inhibited action potentials triggered by depolarizing current injections or synaptic stimulation. Thus, by inverting the charge of the selectivity filter, we have created a class of directly light-gated anion channels that can be used to block neuronal output in a fully reversible fashion.

Channelrhodopsins (ChRs), light-gated ion channels that serve as sensory photo-receptors in microalgae (1–3), are now widely used to activate specific neuronal populations in the brain. ChR2 and numerous engineered variants have been demonstrated to induce rapid depolarization, reliably triggering single action potentials (APs) in response to brief light pulses. ChRs with extended open-state lifetimes (step-function rhodopsins), on the other hand, provide sustained depolarization and drive AP trains at high frequencies (4, 5). To study the function of specific classes of neurons within large neuronal networks or in the intact brain, transient inactivation by hyperpolarization can be even more informative than depolarization. For this purpose, light-activated ion pumps have been used as membrane hyperpolarizers (6, 7). Because only a single charge is transported per photocycle, these pumps require constant illumination of high intensities. For in vivo experiments, in which photon capture is typically the rate-limiting step, effective inhibition is restricted to a very small volume, even when light-driven pumps with high cycling rates are used (8).

As an alternative approach, several attempts have been made to convert ChR into a K⁺- or anion-selective channel that might generate outward currents in neurons. However, the preference for K⁺ over Na⁺ could only be improved by a factor of 2.5, which is not sufficient to create a truly inhibitory tool (9, 10). To convey light-induced neuronal inhibition, we sought to engineer an anion-selective ChR. Electrophysiological

data showed that multiple glutamates and lysines are present in transmembrane helix 2 (TM2) of ChR and that these residues line its water-filled pore to transport H⁺ and other cations when the channel is open (11–14). Replacement of these glutamates gradually reduced pore conductance with only small effects on ion selectivity in nearly all cases, with the exception of E90 (15). Because of its direct contact with the retinal Schiff base (9) and its protonation change during the photocycle, E90 plays a critical role in ion conductance and gating (12, 13, 16, 17).

We performed molecular dynamics (MD) simulations (Fig. 1A), taking the x-ray crystal structure of the ChR1/ChR2 hybrid C1C2 as a starting point (9, 18). On the basis of electrical studies on ChR2 wild type and mutants, we assumed that both active side residue E123 and D253 in close proximity to the retinal Schiff base nitrogen are deprotonated (14, 19, 20). In contrast, the nearby E90 is protonated and forms a hydrogen bond with N258, which forms another hydrogen bond

with S63 (fig. S1A). On the basis of MD simulations, we derived structural models for ChR2 and E90 mutants from a most-likely structure (18, 21). For these structural templates, we next computed the water and ion distributions in the protein interior using a reference interaction site model (3D-RISM) (22, 23). The water distribution exhibits a discontinuity around E90 (Fig. 1A), which is in agreement with the water density in the C1C2 x-ray structure (9). This finding in combination with recent electrophysiological and spectroscopic results (9–13, 16, 17) suggests that S63, E90, D253, and N258 together with E123 constitute the central gate. This gate acts as a hydrophobic barrier in darkness and prevents water from entering the inner vestibule between the central gate and an inner gate, the latter composed of Y70, E82, E83, H134, and H265 (9). After chromophore photoactivation, these barriers undergo substantial conformational changes and convert ChR to a pre-active state. We propose that pre-active ChR requires only minor structural alterations or proton transfer reactions to be capable of opening fully for ion conductance (16, 17, 24).

To alter ChR ion selectivity, we replaced the central gate E90 with a lysine that we assumed to be protonated under all physiological conditions. This mutation was combined with the T159C substitution to improve membrane targeting of the protein and retinal binding in the chromophore pocket (25, 26). Photocurrents of ChR2-E90K-T159C (C2-EK-TC) in human embryonic kidney (HEK) 293 cells were weak at high extracellular pH (pH$_e$) (Fig. 2, A and B) but greatly enhanced at low pH$_e$ (Fig. 2C). At low pH$_e$, both inward- and outward-directed currents were enhanced, and the reversal potential (E_{rev}) shifted only marginally to become more positive (Fig. 2, C and D, and fig. S2, A to C). These results suggest that although activated by protons, the channel did not conduct protons even at low pH$_e$. Next, we replaced Na⁺ (140 mM)

[1]Institute for Biology, Experimental Biophysics, Humboldt Universität zu Berlin, D-10115 Berlin, Germany. [2]Institute for Synaptic Physiology, Center for Molecular Neurobiology Hamburg, Falkenried 94, D-20251 Hamburg, Germany. [3]Institute of Physical Chemistry, Karlsruhe Institute of Technology, Karlstrasse 12, D-76131 Karlsruhe, Germany.

*These authors contributed equally to this work.
†Corresponding author. E-mail: hegemann@rz.hu-berlin.de (P.H.); thomas.oertner@zmnh.uni-hamburg.de (T.G.O)

Fig. 1. Structural models obtained from MD simulation. All structures were modeled based on the x-ray crystal structure of the C1C2 chimeric protein (9). Water and Cl⁻ distributions, which are calculated with 3D-RISM, are depicted in light blue and pink, respectively, and the retinal is shown in yellow. (**A**) Model structure of wild-type C2, including the central gate and counterion residues. (**B**) Corresponding model structure of C2-EK. (**C**) Respective C2-ER model structure.

with K^+, N-methyl-glucamine$^+$ (NMG$^+$), Ca^{2+}, or Mg^{2+} (Fig. 2, C and D, and fig. S2, D to F) and measured the photocurrent conducted by C2-EK-TC. High Ca^{2+} increased photocurrents slightly in both directions; however, none of the cation replacements altered E_{rev}. Thus, external binding of H$^+$, and to a lower extent Ca^{2+}, enhanced the conductance without transport of the respective cations. Last, we replaced most of the external Cl$^-$ (150 mM) with aspartate$^-$ to produce an extracellular solution with 10 mM Cl$^-$ and 140 mM Asp$^-$. Under these conditions, currents were inward directed (Fig. 2E), and E_{rev} for both the initial (I_0) and stationary (I_S) currents shifted to +73 mV (Fig. 2, C and D). These data suggested that the observed inward currents were due to an efflux of Cl$^-$ ions.

To investigate subcellular localization, we generated mCherry-tagged ChR-EK derivatives. Partial membrane targeting and considerable cytoplasmic fluorescence (fig. S3) suggested possible folding defects caused by charge repulsion between K90 and K93. To overcome this deficit, we delocalized the charge by replacing E90 with arginine. Photocurrents of ChR2-E90R-T159C (C2-ER-TC) were similar to those of C2-EK-TC, except that improved expression and membrane targeting was observed (fig. S3). In addition, E_{rev} under standard conditions was slightly more negative because of further reduction in H$^+$ conductance ($E_{rev} = -38$ mV) (fig. S4, B to D), making this double mutant promising for inhibition of neuronal activity. From this point forward, C2-ER-TC will be referred to as the chloride-conducting ChR (ChloC).

To further characterize the selectivity of C2-EK-TC and ChloC, we measured the photocurrent under variable Cl$^-$ conditions. High symmetrical Cl$^-$ evoked symmetrical currents, and a gradual reduction in external chloride promoted inward-directed currents, with a concomitant shift of E_{rev} to more positive values (Fig. 3A and fig. S3). The presence of only 10 mM chloride on both sides of the membrane resulted in reduced, symmetrical currents in both directions. Stepwise increases in external chloride promoted Cl$^-$ influx, which was observed as outward currents with a shift in E_{rev} to more negative values (Figs. 2F and 3, A to C, and figs. S4 and S5, A to D). The E_{rev} values for I_S were slightly more positive as compared with I_0 owing to transition from open state O1 to O2 with slightly different selectivity profiles (Fig. 3D and figs. S4 and S5) (27–30).

To fully exploit the potential of ChloC as a neuronal silencer and to optimize it for low-light conditions, we explored step-function mutants after modification of the DC gate (C128 and D156) (fig. S1). ChR2-E90R-D156N-T159C-expressing cells (slow ChloC) showed the largest photocurrent amplitudes, low inactivation in continuous light or upon repetitive flashing, and a mean open-state lifetime of ~10 s (Fig. 3, C to G). E_{rev} of slow ChloC was even more negative (–54 mV) as compared with that of EK-TC (–27 mV), ChloC

(–38 mV) (Fig. 3C and D), and ChR2 wild type (fig. S6). Upon continuous illumination, cells expressing slow ChloC needed almost 10,000 times lower light intensities to produce photocurrents comparable with ChloC at saturation (Fig. 3, H and I).

To better understand the influence of the E90K and E90R mutations, we analyzed extended MD simulations for these mutants, showing that the hydrogen bond to N258 is lost in both cases. In the E90K mutant, the positively charged lysine residue was reoriented toward the active site and formed hydrogen bonds with the counterions (Fig. 1B). In E90R, orientation of the

guanidinium group was more flexible (fig. S7, A to C), pointing to E123 in the active site in the predominantly populated conformation seen in Fig. 1C. Furthermore, hydrogen bonding between N258 and S63 was weaker, especially in E90R, leading to greater flexibility as indicated by larger fluctuations in the hydrogen bonding distances (table S1). Because these residues form hydrogen bonds between helices 1 and 7, weaker bonds led to larger displacement of the two helices. As a result, a larger cavity was created at the expense of protein stability. We computed the ion distribution using 3D-RISM, showing a noncontinuous distribution of Cl$^-$ ions in wild
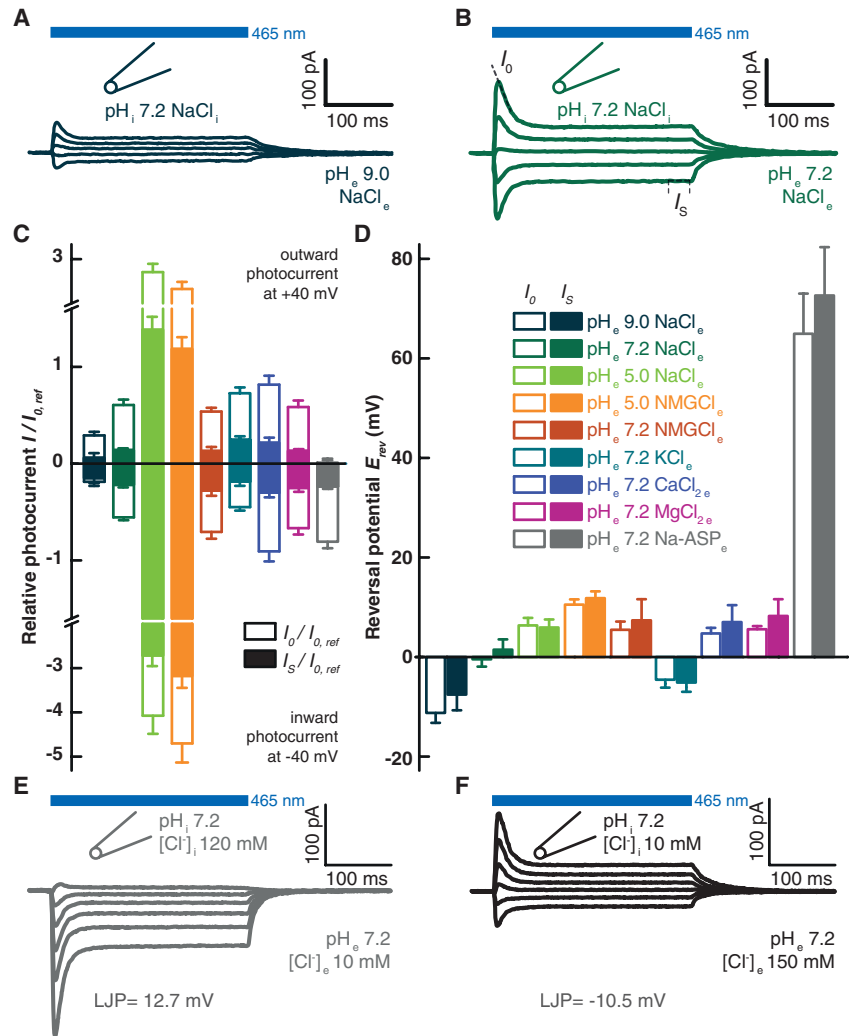
Fig. 2. Ion selectivity of C2-EK-TC. (A and **B)** Representative photocurrent traces of C2-EK-TC recorded in HEK293 cells. The internal solution was maintained at high NaCl, pH$_i$ 7.2, whereas the external solution varied as indicated. Voltage was clamped from –40 mV to +40 mV in 20-mV steps. The initial photocurrent (I_0) is determined by linear extrapolation to $I_{(t=0)}$. (**C)** Comparison of initial current amplitudes at –40 mV and +40 mV for different external cations. Photocurrents were normalized to the initial photocurrent at reference conditions (I_0, ref: high NaCle, pHe 7.2, –60 mV) (**D)** Corresponding reversal voltage (E_{rev}) for all conditions. (D and E) Light-gray bars reflect conditions of reduced external Cl$^-$. (**E** and **F)** Photocurrent traces of C2-EK-TC recorded in HEK293 cells. Voltage was clamped from –60 mV to +40 mV in 20-mV steps in addition to the present liquid junction potential (LJP), as indicated. (E) The internal solution contained high Cl$^-$ (120 mM), and the external solution contained a reduced Cl$^-$ concentration (10 mM). (F) Inverse Cl$^-$ conditions of 10 mM (internal) and 150 mM (external). Mean values ± SEM ($n \geq 6$ HEK293 cells) are illustrated.

type (Fig. 1A), indicating that the protein interior is not accessible for chloride. The Cl^- distribution of the E90K and E90R mutants as shown in Fig. 1, B and C, which denote a region where the free energy is lower than that in bulk phase, is now continuous from the extracellular side to the active site. On the other hand, K^+ free energy decreases by 25% in E90K and 40% in E90R at the maximum point (table S2). The differences in the dark-state Cl^- distributions of E90K and E90R mutants may result from differences in shape and electrostatic interaction in the cavity next to K and R. Taken together, our data demonstrate that increased Cl^- affinity, higher protein flexibility, and a larger cavity induced by disruption of the hydrogen-bonded network may all contribute to the high Cl^- conductance and selectivity of E90K and E90R.

Encouraged by the favorable properties of the engineered chloride channel, we tested its potential application in neuroscience. In the brain, ligand-gated Cl^- channels [such as γ-aminobutyric acid type A ($GABA_A$) receptors] mediate fast inhibition of neural activity by shunting depolarizing currents. Efficient mechanisms for Cl^- removal keep the internal Cl^- concentration low in mature neurons, providing a steep concentration gradient across the plasma membrane (31). On the basis of this, we hypothesized that ChloCs could be used as a tool to provide light-induced inhibition of neuronal spiking. To test this concept, we transfected CA1 pyramidal cells in organotypic hippocampal culture, with a bicistronic

plasmid coding for slow ChloC and a red fluorescent protein (tdimer2). Two-photon imaging of transfected neurons revealed normal spine densities on oblique dendrites (Fig. 4A and fig. S8). Passive and active membrane properties did not differ from neurons expressing the previously characterized and well-tolerated ChR2-E123T-T159C mutant (25) or nontransfected neurons (table S4).

To determine the E_{rev} of slow ChloC, we performed voltage-clamp recordings in CA1 pyramidal cells. Photocurrents were large and outlasted the 2-ms light pulse by many seconds (τ_{off} = 10.5 ± 0.3 s) (Fig. 4B). Current direction reversed at –68.2 ± 0.8 mV (n = 6 neurons)—more negative than ChloC (–61.8 ± 1.0 mV, n = 6 neurons), E90K-T159C (–42.9 ± 1.7 mV, n = 6 neurons), and E123T-T159C (–3.2 ± 2.0 mV, n = 5 neurons), which is consistent with the high Cl^- conductance of E90R mutants observed in HEK293 cells (Fig. 3 and fig. S5). Next, we tested the effects of slow ChloC activation on AP generation. Depolarizing somatic current injections evoked a reproducible train of 5 to 6 APs in transfected neurons. Activation of slow ChloC by a 5-ms light pulse completely blocked AP generation (Fig. 4E), whereas ChloC could be used to block spikes in a more defined time window with millisecond precision (Fig. 4F). Activation of ChloCs was accompanied by a small depolarization, reflecting the difference between the very negative resting voltage of CA1 pyramidal cells (–77 mV) (table S4) and the E_{rev} of ChloC.

Thus, unlike previously published light-driven ion pumps [such as halorhodopsin or archaerhodopsin (Arch)], ChloCs do not provide inhibition by hyperpolarization but shunt excitatory currents very efficiently.

Next, we sought to determine whether ChloC could also prevent APs triggered by strong synaptic input. Stimulating afferent fibers with an extracellular electrode placed in stratum radiatum evoked single APs. Pairing synaptic stimulation with brief pulses of blue light inhibited ~90% of evoked APs in ChloC-expressing neurons, whereas slow ChloC achieved 100% block (fig. S10). How do the light sensitivities of ChloC and slow ChloC compare with the light-driven proton pump Arch (8)? To determine the minimal current necessary to evoke a spike (rheobase), we injected depolarizing current ramps into CA1 pyramidal neurons. In the dark, both transfected and nontransfected neurons had similar rheobases between 150 and 200 pA (table S4). At high light intensities (10 mW/mm²), Arch strongly hyperpolarized neurons and shifted the rheobase by 280 pA. To produce a similar shift in rheobase, cells expressing slow ChloC needed ~10,000 times less light (Fig. 4, G and H). At light intensities of 0.1 mW/mm² and above, slow ChloC-expressing neurons could not be driven to spike anymore. Because fast Na^+ channels tend to inactivate during depolarizing ramps, we also applied voltage step protocols to measure spike output at various light levels, confirming the very high sensitivity of slow ChloC (fig. S11).
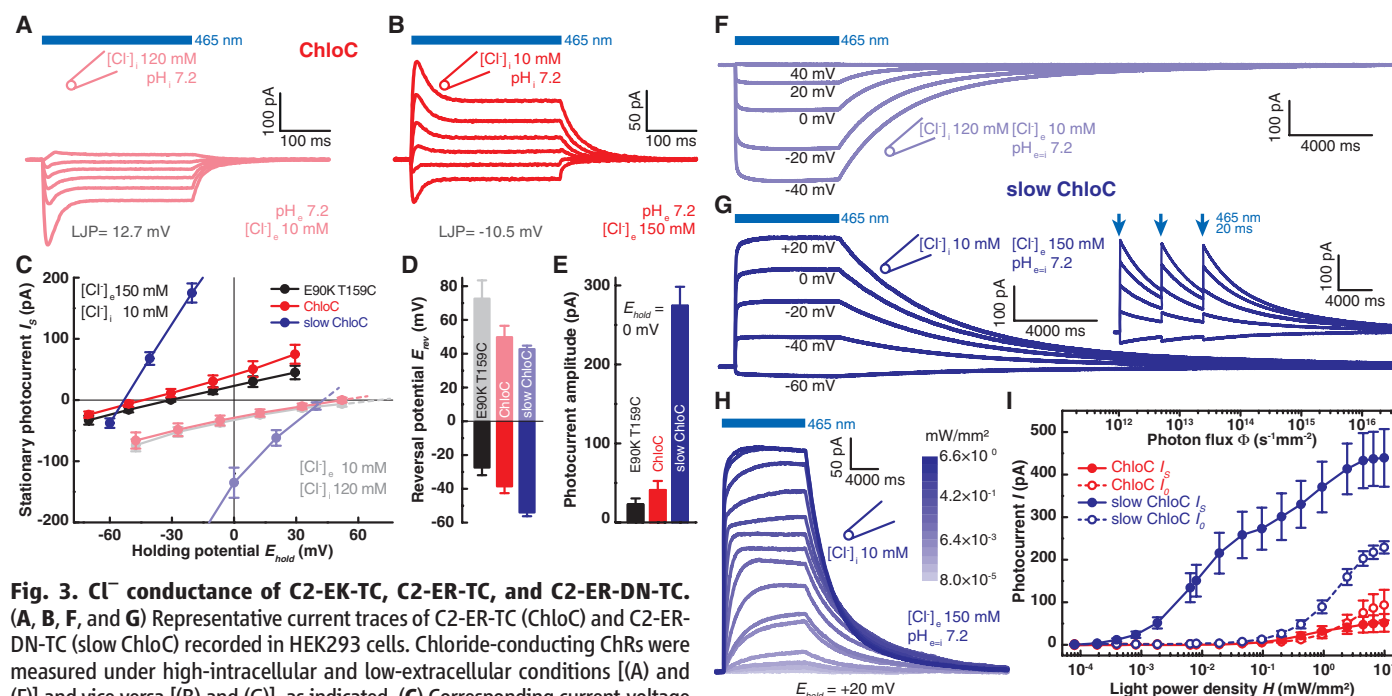
Fig. 3. Cl^- conductance of C2-EK-TC, C2-ER-TC, and C2-ER-DN-TC. (**A**, **B**, **F**, and **G**) Representative current traces of C2-ER-TC (ChloC) and C2-ER-DN-TC (slow ChloC) recorded in HEK293 cells. Chloride-conducting ChRs were measured under high-intracellular and low-extracellular conditions [(A) and (F)] and vice versa [(B) and (G)], as indicated. (**C**) Corresponding current-voltage relationships in comparison with C2-EK-TC. (**D**) Reversal potentials (E_{rev}) for C2-EK-TC, ChloC, and slow ChloC at high-intracellular and low-extracellular conditions (top light bars) and vice versa (bottom dark bars) as same conditions as in (C). (**E**) Comparison of photocurrent amplitudes for different chloride-conducting C2 variants at 0 mV holding potential. (**H**) Photocurrents of slow ChloC at different light intensities. (**I**) Amplitudes of the initial current I_0 (20-ms flash) and stationary current I_S of ChloC (300-ms light pulse) and slow ChloC (12 s illumination) at different light intensities. Mean values ± SEM (n ≥ 6 HEK293 cells) are illustrated.
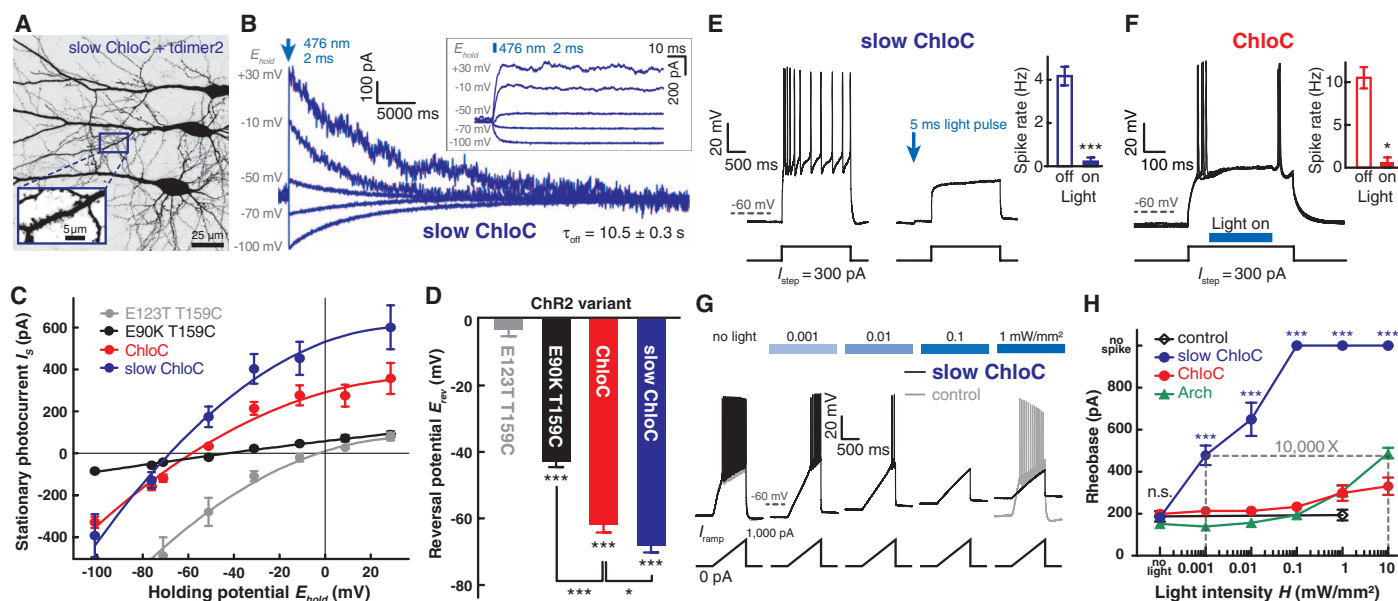
Fig. 4. Characterization of ChloC variants in CA1 pyramidal neurons. (**A**) CA1 pyramidal neurons expressing slow ChloC (C2-ER-DN-TC) and cytosolic tdimer2. Contrast-inverted maximum intensity projection. (**B**) Light-evoked (1 mW/mm^2) photocurrents in a slow ChloC-expressing pyramidal cell at different holding potentials (junction-potential corrected). (Inset) First 100 ms after light pulse. (**C**) I/E relation of stationary photocurrents. (**D**) Reversal potential measurements of photocurrents [one-way analysis of variance (ANOVA), Tukey's test, $P < 0.001$]. (**E**) Somatic current injections (2 s, 300 pA) induced AP firing in slow ChloC-expressing neurons in the dark with typical accomodation. A brief light pulse (5 ms, 476 nm, 1 mW/mm^2) 100 ms before

the current step blocked AP firing (paired t test, $P < 0.001$, $n = 7$ neurons). (**F**) Light activation (300 ms) during somatic current injections (500 ms, 300 pA) blocked AP firing in ChloC-expressing neurons ($P = 0.01$, $n = 4$ neurons). (**G**) In slow ChloC-expressing neurons, blue light at increasing intensities (1 μW/mm^2 to 1 mW/mm^2) gradually raised the rheobase of current-ramp–evoked APs (black traces). There was no effect of blue light in wild-type cells (gray traces). (**H**) Comparison of rheobase at different light intensities between wild-type neurons (control) and neurons expressing ChloC, slow ChloC, or Arch. Rheobase was similar in all cells in the dark ($P = 0.2$). ANOVA, ***$P < 0.001$; n.s., not significant.

Thus, ChloCs mimic the effect of physiological inhibition through GABA$_A$ receptor activation. Photocurrents showed only little inactivation during long light pulses (fig. S9), and optical neuronal inhibition was fully reversible (fig. S12).

Because only one single charge is transported per photocycle, inhibitory ion pumps must be continuously activated with intense light to maintain high turnover and inhibition. In contrast, single-photon absorption of a light-gated chloride channel enables continuous chloride flux until the respective channel closes by means of thermal relaxation. Slow ChloC should be advantageous for in vivo applications because a very large volume of brain tissue could be addressed by a single optical fiber or head-mounted light-emitting diode. For applications requiring temporally precise inhibition in the blue spectrum, ChloC is a viable alternative to Arch or halorhodopsin, and ChloCs with intermediate kinetics could be generated on demand. We hope that blocking the output of identified neurons will enable investigators to assess the contribution of specific neuronal populations to learning, memory, and other brain functions in a fully reversible fashion.

References and Notes

1. G. Nagel et al., *Science* **296**, 2395–2398 (2002).
2. G. Nagel et al., *Proc. Natl. Acad. Sci. U.S.A.* **100**, 13940–13945 (2003).
3. O. A. Sineshchekov, K. H. Jung, J. L. Spudich, *Proc. Natl. Acad. Sci. U.S.A.* **99**, 8689–8694 (2002).
4. O. Yizhar, L. E. Fenno, T. J. Davidson, M. Mogri, K. Deisseroth, *Neuron* **71**, 9–34 (2011).
5. F. Zhang et al., *Cell* **147**, 1446–1457 (2011).
6. X. Han, E. S. Boyden, *PLOS ONE* **2**, e299 (2007).
7. F. Zhang et al., *Nature* **446**, 633–639 (2007).
8. B. Y. Chow et al., *Nature* **463**, 98–102 (2010).
9. H. E. Kato et al., *Nature* **482**, 369–374 (2012).
10. A. P. Plazzo et al., *J. Biol. Chem.* **287**, 4818–4825 (2012).
11. Y. Sugiyama et al., *Photochem. Photobiol. Sci.* **8**, 328–336 (2009).
12. K. Ruffert et al., *Biochem. Biophys. Res. Commun.* **410**, 737–743 (2011).
13. D. Gradmann, A. Berndt, F. Schneider, P. Hegemann, *Biophys. J.* **101**, 1057–1068 (2011).
14. H. C. Watanabe et al., *J. Biol. Chem.* **287**, 7456–7466 (2012).
15. Single-letter abbreviations for the amino acid residues are as follows: A, Ala; C, Cys; D, Asp; E, Glu; F, Phe; G, Gly; H, His; I, Ile; K, Lys; L, Leu; M, Met; N, Asn; P, Pro; Q, Gln; R, Arg; S, Ser; T, Thr; V, Val; W, Trp; and Y, Tyr. In the mutants, other amino acids were substituted at certain locations; for example, E90K indicates that glutamic acid at position 90 was replaced by lysine.
16. K. Eisenhauer et al., *J. Biol. Chem.* **287**, 6904–6911 (2012).
17. V. A. Lórenz-Fonfría et al., *Proc. Natl. Acad. Sci. U.S.A.* **110**, E1273–E1281 (2013).
18. H. C. Watanabe, K. Welke, D. J. Sindhikara, P. Hegemann, M. Elstner, *J. Mol. Biol.* **425**, 1795–1814 (2013).
19. L. A. Gunaydin et al., *Nat. Neurosci.* **13**, 387–392 (2010).
20. S. Ito et al., *J. Am. Chem. Soc.* **136**, 3475–3482 (2014).
21. H. Watanabe, M. Elstner, T. Steinbrecher, *J. Comput. Chem.* **34**, 198–205 (2013).
22. D. Beglov, B. Roux, *J. Phys. Chem. B* **101**, 7821–7826 (1997).
23. A. Kovalenko, F. Hirata, *J. Chem. Phys.* **110**, 10095 (1999).
24. E. Ritter, K. Stehfest, A. Berndt, P. Hegemann, F. J. Bartl, *J. Biol. Chem.* **283**, 35033–35041 (2008).
25. A. Berndt et al., *Proc. Natl. Acad. Sci. U.S.A.* **108**, 7595–7600 (2011).
26. S. Ullrich, R. Gueta, G. Nagel, *Biol. Chem.* **394**, 271–280 (2013).
27. A. Berndt, M. Prigge, D. Gradmann, P. Hegemann, *Biophys. J.* **98**, 753–761 (2010).
28. K. Nikolic et al., *Photochem. Photobiol.* **85**, 400–411 (2009).
29. N. Grossman, K. Nikolic, C. Toumazou, P. Degenaar, *IEEE Trans. Biomed. Eng.* **58**, 1742–1751 (2011).
30. F. Schneider, D. Gradmann, P. Hegemann, *Biophys. J.* **105**, 91–100 (2013).
31. C. Rivera et al., *Nature* **397**, 251–255 (1999).

High-Resolution Genomic Analysis of Human Mitochondrial RNA Sequence Variation

Alan Hodgkinson,[1]* Youssef Idaghdour,[1,2]*† Elias Gbeha,[1] Jean-Christophe Grenier,[1] Elodie Hip-Ki,[1] Vanessa Bruat,[1] Jean-Philippe Goulet,[2] Thibault de Malliard,[1,2] Philip Awadalla[1,2]‡

Mutations in the mitochondrial genome are associated with multiple diseases and biological processes; however, little is known about the extent of sequence variation in the mitochondrial transcriptome. By ultra-deeply sequencing mitochondrial RNA (>6000×) from the whole blood of ~1000 individuals from the CARTaGENE project, we identified remarkable levels of sequence variation within and across individuals, as well as sites that show consistent patterns of posttranscriptional modification. Using a genome-wide association study, we find that posttranscriptional modification of functionally important sites in mitochondrial transfer RNAs (tRNAs) is under strong genetic control, largely driven by a missense mutation in *MRPP3* that explains ~22% of the variance. These results reveal a major nuclear genetic determinant of posttranscriptional modification in mitochondria and suggest that tRNA posttranscriptional modification may affect cellular energy production.

Mitochondria are vitally important for basic cellular function, and mutations in the compact genome of 16,569 base pairs (bp) have been associated with a large number of diseases in humans, as well as fundamental processes such as aging (*1–3*). Although regulation, transcription, and posttranscriptional processing of the human mitochondrial genome are subject to extensive research (*4*), very little is known about the nature, extent, and distribution of sequence variation in the mitochondrial transcriptome (*5*), particularly on a population level. Because it is ultimately translated variation that dictates downstream phenotypes, it is of great interest to investigate the extent and effects of such variation.

To deeply characterize sequence variation in the human mitochondrial transcriptome across a large number of individuals, we sequenced the whole-blood RNA of a random, predominantly French-Canadian population sample of 708 individuals from the CARTaGENE project (*6*) using the Illumina HiSeq platform. We then stringently aligned paired-end sequencing reads, focused on reads mapping to the mitochondria, and called variants using strict filters (*7*). On average, we achieved 6334× coverage (SD = 1139, range = 1456 to 9545) (fig. S1). Within each individual, we observe numerous sites that carry more than one allele (heteroplasmies), representing variation across mitochondrial transcriptomes (mtRNA). Between individuals, we observe high levels of

mtRNA sequence variation, both in terms of the genomic locations of heteroplasmic sites and the proportions of alternative alleles carried at each site (Fig. 1).

On average, each individual carries 14.18 heteroplasmies identified in mtRNA across a total of 650 sites, higher than most previous estimates in human mitochondrial DNA (mtDNA) (*8–12*) (fig. S1, for biallelic site heteroplasmy annotation, see table S1). It is noteworthy that a number of positions are heteroplasmic within a high proportion of the 708 individuals (>25%); three of these sites consistently contain two alleles within each individual who exhibits heteroplasmy (positions C295T, G2129A, and G6691A in cDNA) and are thus potential candidates for RNA editing or modification. However, 13 sites are multiallelic (which here refers to sites containing three or more nucleotides) and often express all four nucleotides systematically within each individual. Sites that mismatch the genome—such that all four bases are observed—are indicative of reverse-transcription errors made at these sites during the process of creating and amplifying cDNA from RNA before sequencing and have been shown to overlap known posttranscriptionally modified sites (*13–16*).

Recently, 2 of the 13 multiallelic sites at positions 2617 (*RNR2*) and 13710 (*ND5*) were described as putative canonical RNA editing events (*5*). However, because we observe all four alleles at these sites across multiple individuals, it is likely that these changes actually represent posttranscriptional modifications. It is intriguing that the remaining 11 multiallelic sites all occur at the ninth position of transfer RNAs (tRNAs) (p9 sites), six of which are known to be posttranscriptionally methylated (*15–17*), which suggests that the presence of multiple alleles in our data represents posttranscriptional methylation at these sites.

We validated our results by sequencing both the whole mtDNA and two regions of mtRNA

containing three p9 sites for five individuals using the IonTorrent platform to an average coverage of 9573× and 9633× for DNA and RNA, respectively, starting from stock DNA and RNA samples. In mtDNA, we find no evidence of alternative alleles above normal sequencing error rates (*7*) at the three p9 sites across all five individuals, whereas all four alleles are present in mtRNA on all occasions (table S2). Most important, the proportions of reads containing alternative alleles at these sites are significantly consistent across sequencing platforms (correlation coefficient $r^2 = 0.731$, $P = 4.89e-5$) (fig. S2). Because sequencing was performed after independent reverse transcription–polymerase chain reactions for each of the two platforms and the proportion of alternative alleles is systematic and repeatable across experiments, we hypothesize that this observed proportion represents the level of posttranscriptional methylation within each individual. Under this assumption, we observe between 0 and 74% methylation at p9 sites across the 708 individuals (fig. S3). We also validate positions 295, 2129, and 6691 as RNA modification events, because no heteroplasmies were found in DNA across the five individuals.

To determine whether methylation is occurring systematically for some mitochondrial organelles and not others, we examined whether alternative alleles at different p9 sites occur on the same read or paired sequencing reads more often than would be expected by chance. For the two positions close enough to be tested, considering the size distribution of our RNA sequencing (RNA-Seq) libraries, we see a significant enrichment of alternative alleles on the same background ($P < 0.001$) (fig. S2), which confirms that, when methylation takes place, it occurs consistently across mtRNA polycistronic molecules. By similar reasoning, we looked for correlations in the proportions of alternative alleles across p9 sites and observed significant correlations between 50 of the 55 pairwise comparisons ($P < 0.05$ after Bonferroni correction) (fig. S2).

Given the systematic, but highly variable, nature of methylation at p9 sites across individuals, we performed a genome-wide association study (GWAS) to test whether nuclear genetic variants are associated with the within-individual proportion of alternative counts at p9 sites. We genotyped all individuals using Illumina Omni2.5M single-nucleotide polymorphism (SNP) arrays and limited the analysis to SNPs with minor allele frequency (MAF) > 5%, in Hardy-Weinberg equilibrium ($P < 0.001$), and not missing in more than 1% of the individuals. We used all 11 p9 sites, calculating the combined alternative allele frequency for each individual, and considered a variety of models (*7*) (QQ plots shown in fig. S4).

The GWAS revealed a region on chromosome 14 that is associated with the within-individual proportion of alternative counts at genome-wide significance (Fig. 2, Table 1, and table S3). The strongest association occurs within the gene *MRPP3* at a missense mutation on the fourth

[1]CHU Sainte-Justine Research Centre, Department of Pediatrics, Faculty of Medicine, Université de Montréal, 3175 Chemin de la Côte-Sainte-Catherine, Montreal, Quebec H3T 1C5, Canada. [2]CARTaGENE, 3333 Queen Mary Road, Office 493, Montreal, Quebec H3V 1A2, Canada.

*These authors contributed equally to this work.
†Present address: Department of Biology, Division of Science and Mathematics, New York University Abu Dhabi, Post Office Box 129188, Abu Dhabi, United Arab Emirates.
‡Corresponding author. E-mail: philip.awadalla@umontreal.ca

exon (*rs11156878*, Asn → Ser, *P* = 6.95e-34). *MRPP3* codes for mitochondrial ribonuclease P protein 3 that forms part of mitochondrial RNase P enzyme complex, along with MRPP1 and MRPP2. This complex is involved in the cleavage and processing of mitochondrial transcripts for translation into proteins of the oxidative phosphorylation system (*18*). MRPP3 has been associated with the processing of the 5′ ends of tRNAs (*16*) and is suggested to contain a metallonuclease domain that would enable RNA hydrolysis (*18*). In vitro experiments have indicated that MRPP1 and MRPP2 may be involved in methylating mitochondrial tRNAs (*16*, *19*); however, MRPP3 has thus far not been implicated in this process. The GWAS did not detect significant associations within *MRPP1* or *MRPP2*, which suggests that genetic variation in *MRPP3* may modulate natural variation in the observed rate of posttranscriptional methylation in humans, either directly or via the processing activity of the mitochondrial RNase P enzyme.

Next, we performed a GWAS for each multiallelic site individually using the same association models as above and obtained the same variant (*rs11156878*) at genome-wide significance across eight p9 sites. We also identified four other genomic regions containing genome-wide significant markers that associate with the putative modification level at multiallelic sites (Table 1). Variation at positions 585 and 1610 show association with a missense variant within the gene *SLC25A26* (*P* values 3.83e-09 and 2.39e-17, respectively), which is a mitochondrial carrier protein, and for position 13710 (a non-p9 multiallelic site in *ND5*) with a missense variant within the gene *MTPAP* (*P* = 2.03e-9), which synthesizes the 3′ poly(A)⁺ tail of mitochondrial transcripts. For position 2617 (a non-p9 multiallelic site in *RNR2*), the peak association falls upstream of *PPP1CB* (*P* = 1.57e-11); however, genome-wide significant associations also occur within *TRMT61B* (peak association has *P* = 3.15e-11), which is a methyltransferase that acts at position 58 of mitochondrial tRNAs and, therefore, may play a role in methylating *RNR2* at a functional position that has been linked to stability in the large ribosomal subunit (*5*).

To replicate the genetic associations in an independent data set, we performed RNA sequencing (average coverage 3029×) and genotyping using Omni 2.5M SNP arrays for an additional 287 individuals, and we find similar levels of variation in the mitochondrial genome (fig. S5). GWAS analyses replicate the peak SNP association in *MRPP3* for all p9 sites combined to a genome-wide significant level (*P* = 2.56e-11) (Table 1), which confirms the strength of this association. We also replicate the same peak SNP in *MRPP3* for three individual p9 sites, as well as an association linked to *SLC25A26*, but failed to replicate the associations with *MTPAP* and *PPP1CB* (Table 1 and table S4).

Variance explained by the missense variant *rs11156878* for all p9 sites combined is high

(r^2 = 22.03%) (Fig. 2), despite the relatively small sample size of our cohort. To fine-map the region most strongly associated with our phenotype, we sequenced the exomes of 96 individuals that were used in the original analysis and repeated the GWAS. We detected the strongest association signal with the same missense variant as before at experiment-wide significance level (*P* = 3.85e-7), which reflects the strength of the association.

It is noteworthy that the frequency distribution of *rs11156878* is not consistent across worldwide populations; specifically, in 1000 Genomes data (*20*), the minor allele frequency shows variation across continents (14% in the Americas, 17% in Europe, 5% in Asian populations, and 4% in African populations). The specific effect of this variant is not known; however, given that the level of methylation at p9 sites has been linked to levels of protein translation and mitochondrial respiration (*16*), variability at this site across worldwide populations may have significant implications on region-specific health and disease.

Finally, given the multiallelic variability across p9 sites, we performed a multiple regression between the putative level of methylation at p9 sites and the basal metabolic rate (BMR) of individuals measured using a body composition analyzer (*7*). BMR represents the total energy expended by the body to maintain normal functions at rest, such as respiration and circulation. For all p9 sites combined, there is no significant association between BMR and the proportion of alternative alleles at p9 sites (*P* = 0.150). However, for two individual p9 sites we find suggestive evidence for a positive association (position 7526, *TRND*, *P* = 0.0034 and position 14734, *TRNE*, *P* = 0.0084), one of which is replicated in our independent data set of 287 individuals (position 7526, *TRND*, *P* = 0.0192). Resolving the significance of any association implicating RNA sequence variation in the basis of organismal phenotypes requires systematic investigations; however, these observations, together with those that highlight the importance of posttranscriptional methylation for the correct folding of tRNA molecules (*21*, *22*), suggest that
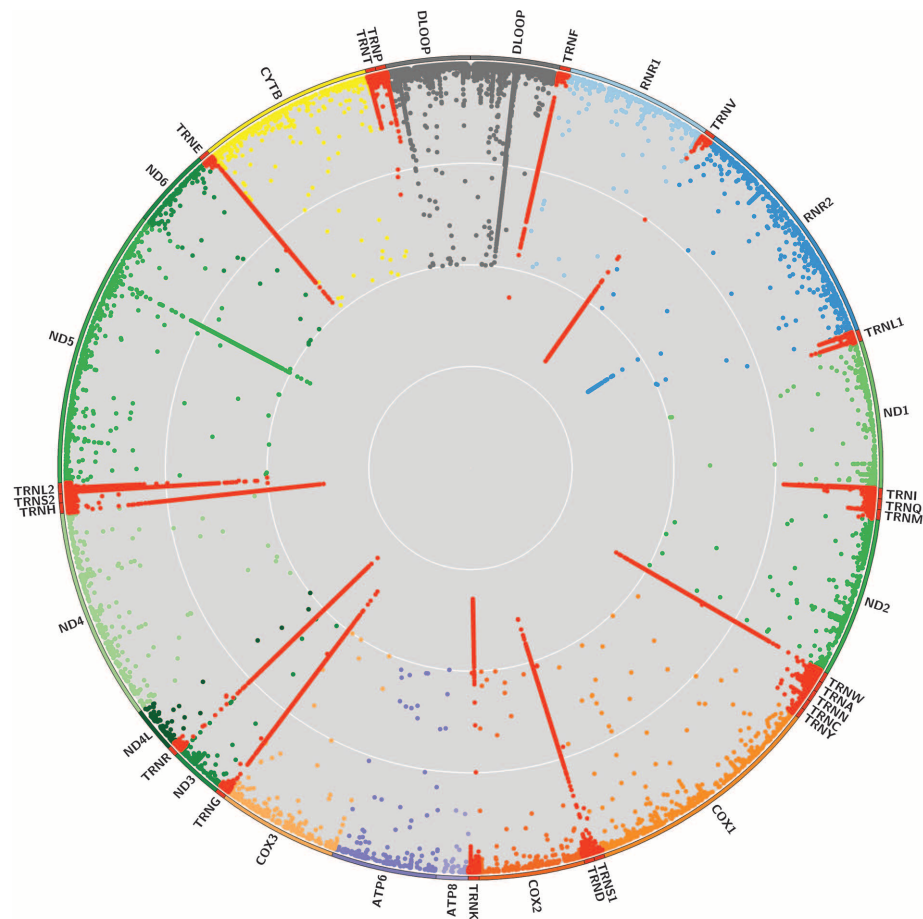
Fig. 1. Polymorphism information content (PIC) for each site in the mitochondrial transcriptome across 708 individuals. PIC is calculated as $1 - \sum_{i=1}^{n} p_i^2$, where p_i is the proportion of sequencing reads containing each nucleotide within an individual and n is the number of different alleles at each site. Each data point therefore represents the PIC value for a single site using allele frequency information from sequencing reads within a single individual. White circular lines represent PIC scores of 0.25, 0.5, and 0.75, from outside to in. Sites with PIC < 0.005 are not shown. For sites containing two alleles, the maximum PIC score is 0.5.

investigating the role posttranscriptional tRNA sequence variation in pathologic contexts is likely to be revealing.

Mitochondrial tRNAs are vitally important to mitochondrial function; to date, ~250 tRNA mutations have been associated with disease (23). Similarly, posttranscriptional events in RNA appear to be common (5, 24) and may be linked to biological function and disease (25). It was pre-viously shown that modification events at p9 sites could be detected in vitro using cells lines (15, 16); however, here we characterize the nature and extent of the between-individual variation in vivo across a large number of individuals at mitochondrial genome-wide scale. Furthermore, we uncovered a previously underappreciated role of *MRPP3*, likely through missense variant *rs11156878*, in modulating the rate of

posttranscriptional modification, either directly or through the processing activities of mitochondrial RNase P. These results warrant further characterization of the mechanism of action of MRPP3 and its potential role in shaping metabolic-related processes in humans. More broadly, our study demonstrates the potential of GWAS to identify genes involved in basic cellular pathways and highlights the use of RNA sequence variation to complement DNA studies to assess variation and its potential consequences at the population level.

References and Notes

1. J. M. Ross *et al.*, *Nature* **501**, 412–415 (2013).
2. R. W. Taylor, D. M. Turnbull, *Nat. Rev. Genet.* **6**, 389–402 (2005).
3. D. C. Wallace, *Science* **283**, 1482–1488 (1999).
4. O. Rackham, T. R. Mercer, A. Filipovska, *RNA* **3**, 675–695 (2012).
5. D. Bar-Yaacov *et al.*, *Genome Res.* **23**, 1789–1796 (2013).
6. P. Awadalla *et al.*, *Int. J. Epidemiol.* **42**, 1285–1299 (2013).
7. Materials and methods are available as supplementary materials on *Science* Online.
8. H. Goto *et al.*, *Genome Biol.* **12**, R59 (2011).
9. Y. He *et al.*, *Nature* **464**, 610–614 (2010).
10. M. Li *et al.*, *Am. J. Hum. Genet.* **87**, 237–249 (2010).
11. B. A. Payne *et al.*, *Hum. Mol. Genet.* **22**, 384–390 (2013).
12. D. C. Samuels *et al.*, *PLOS Genet.* **9**, e1003929 (2013).
13. H. A. Ebhardt *et al.*, *Nucleic Acids Res.* **37**, 2461–2470 (2009).
14. S. Findeiss, D. Langenberger, P. F. Stadler, S. Hoffmann, *Biol. Chem.* **392**, 305–313 (2011).
15. T. R. Mercer *et al.*, *Cell* **146**, 645–658 (2011).
16. M. I. G. Sanchez *et al.*, *Cell Cycle* **10**, 2904–2916 (2011).
17. M. A. Machnicka *et al.*, *Nucleic Acids Res.* **41**, (D1), D262–D267 (2013).
18. J. Holzmann *et al.*, *Cell* **135**, 462–474 (2008).
19. E. Vilardo *et al.*, *Nucleic Acids Res.* **40**, 11583–11593 (2012).
20. G. R. Abecasis *et al.*, *Nature* **491**, 56–65 (2012).
21. M. Helm *et al.*, *Nucleic Acids Res.* **26**, 1636–1643 (1998).
22. M. Helm, R. Giegé, C. Florentz, *Biochemistry* **38**, 13338–13346 (1999).
23. E. Ruiz-Pesini *et al.*, *Nucleic Acids Res.* **35**, (Database), D823–D828 (2007).
24. E. Y. Levanon *et al.*, *Nat. Biotechnol.* **22**, 1001–1005 (2004).
25. N. Paz *et al.*, *Genome Res.* **17**, 1586–1595 (2007).

Fig. 2. GWAS results for all p9 sites combined. The $-\log_{10} P$ values are shown for all sites across the nuclear autosomal genome with each chromosome in a difference color. (**A**) The full model [model 3, see (7)] accounts for age, gender, site of collection, global genetic ethnicity, and complete blood counts. (**B**) The correlation between minor allele count and combined alternative allele frequency is shown for *rs11156878*. (**C**) A magnified section of the full GWAS plot containing the gene *MRPP3*.

Table 1. GWAS results for the full linear model at multiallelic sites. The peak SNP is shown for each region that contains genome-wide significant markers in each test during the discovery phase. The full linear model corrects for age, gender, site of collection, global genetic ethnicity, and complete blood counts. ALL p9 refers to resampled data from all multiallelic p9 sites combined.

Trait	Peak SNP	Position	MAF	Gene	Annotation	Change	P value Discovery	P value Replication
ALL p9	*rs11156878*	14:35735967	0.1939	*MRPP3*	Missense	Asn→Ser	6.95×10^{-34}	2.56×10^{-11}*
1610	*rs11156878*	14:35735967	0.1796	*MRPP3*	Missense	Asn→Ser	7.25×10^{-10}	3.93×10^{-04}
5520	*rs11156878*	14:35735967	0.1807	*MRPP3*	Missense	Asn→Ser	4.89×10^{-16}	5.80×10^{-05}
8303	*rs11156878*	14:35735967	0.1839	*MRPP3*	Missense	Asn→Ser	7.44×10^{-12}	9.14×10^{-03}
9999	*rs11156878*	14:35735967	0.1805	*MRPP3*	Missense	Asn→Ser	2.24×10^{-33}	8.36×10^{-10}*
10413	*rs11156878*	14:35735967	0.1800	*MRPP3*	Missense	Asn→Ser	1.16×10^{-26}	9.19×10^{-06}
12146	*rs11156878*	14:35735967	0.1808	*MRPP3*	Missense	Asn→Ser	1.18×10^{-31}	5.25×10^{-09}*
12274	*rs11156878*	14:35735967	0.1802	*MRPP3*	Missense	Asn→Ser	3.77×10^{-21}	1.08×10^{-06}*
14734	*rs11156878*	14:35735967	0.1796	*MRPP3*	Missense	Asn→Ser	5.73×10^{-11}	1.25×10^{-03}
585	*rs13874*	3:66419956	0.4444	*SLC25A26*	Missense	Thr→Met	3.83×10^{-09}	1.32×10^{-05}
1610	*rs13874*	3:66419956	0.4438	*SLC25A26*	Missense	Thr→Met	2.39×10^{-17}	6.98×10^{-08}*
2617	*rs12714241*	2:28969413	0.3554	*NA*	Intergenic	T→C	1.57×10^{-11}	0.36870
13710	*rs1047991*	10:30629226	0.2512	*MTPAP*	Missense	Arg→Cys	2.03×10^{-09}	0.08675

*The site is also the peak SNP in the replication phase.

Single-Cell Genomics Reveals Hundreds of Coexisting Subpopulations in Wild *Prochlorococcus*

Nadav Kashtan,[1]* Sara E. Roggensack,[1] Sébastien Rodrigue,[1,2] Jessie W. Thompson,[1] Steven J. Biller,[1] Allison Coe,[1] Huiming Ding,[1,3] Pekka Marttinen,[4] Rex R. Malmstrom,[5] Roman Stocker,[1] Michael J. Follows,[6] Ramunas Stepanauskas,[7] Sallie W. Chisholm[1,3]*

Extensive genomic diversity within coexisting members of a microbial species has been revealed through selected cultured isolates and metagenomic assemblies. Yet, the cell-by-cell genomic composition of wild uncultured populations of co-occurring cells is largely unknown. In this work, we applied large-scale single-cell genomics to study populations of the globally abundant marine cyanobacterium *Prochlorococcus*. We show that they are composed of hundreds of subpopulations with distinct "genomic backbones," each backbone consisting of a different set of core gene alleles linked to a small distinctive set of flexible genes. These subpopulations are estimated to have diverged at least a few million years ago, suggesting ancient, stable niche partitioning. Such a large set of coexisting subpopulations may be a general feature of free-living bacterial species with huge populations in highly mixed habitats.

The cyanobacterium *Prochlorococcus* is the smallest and most abundant photosynthetic cell in the oligotrophic oceans, contributing substantially to global photosynthesis (*1*). A single species by traditional measures, *Prochlorococcus* can be divided into several major clades, or ecotypes, defined by the intergenic transcribed spacer (ITS) region of their ribosomal RNA (rRNA) genes. These ecotypes are physiologically distinct (*2*–*4*); display distinctive seasonal, depth, and geographic patterns (*3*); and, like other microorganisms (*5*–*10*), embody tremendous genotypic and phenotypic diversity (*4*). To begin to understand the scope and limits of ecologically meaningful diversity within the canonical *Prochlorococcus* ecotypes, we examined cell-by-cell genomic diversity within a small sample of seawater and explored how it shifts in a dynamic environment.

We applied single-cell genome sequencing (*11*–*14*) to wild *Prochlorococcus* cells from samples collected at the Bermuda-Atlantic Time-series Study (BATS) site at three separate times of year (November 2008, February 2009, and April 2009) (Fig. 1A) (*15*). Because light, temperature, nutrients, and co-occurring communities change with winter deep mixing (*15*, *16*) (Fig. 1A), cells experience substantial environmental changes over tens of generations, enough to cause shifts in abundance of ITS-defined ecotypes (*2*, *15*, *17*).

[1]Department of Civil and Environmental Engineering, Massachusetts Institute of Technology (MIT), 77 Massachusetts Avenue, Cambridge, MA 02139, USA. [2]Département de Biologie, Université de Sherbrooke, 2500 Boulevard de l'Université, Sherbrooke, Québec J1K 2R1, Canada. [3]Department of Biology, MIT, 77 Massachusetts Ave, Cambridge, MA 02139, USA. [4]Helsinki Institute for Information Technology, Department of Information and Computer Science, Aalto University, Post Office Box 15400, FI-00076 Aalto, Finland. [5]Department of Energy Joint Genome Institute, 2800 Mitchell Drive, Walnut Creek, CA 94598, USA. [6]Department of Earth, Atmospheric and Planetary Sciences, MIT, 77 Massachusetts Avenue, Cambridge, MA 02139, USA. [7]Bigelow Laboratory for Ocean Sciences, East Boothbay, ME 04544, USA.

*Corresponding author. E-mail: chisholm@mit.edu (S.W.C.); nadav.kashtan@gmail.com (N.K.)

Fig. 1. Cell-by-cell *Prochlorococcus* population composition in samples from three separate times of year at the BATS site. Cells were collected within the mixed layer at 60 m depth in November 2008, February 2009, and April 2009 [see (*15*)]. (**A**) Schematic of seasonal dynamics at BATS and sampling design. (Top) A typical mixed-layer depth profile and context of our three samples. (Bottom) Typical average dynamics of light [smoothed mean surface photosynthetically active radiation (PAR) from 2004 to 2009], temperature, and nitrogen (within the mixed layer, averaged from 1999 to 2009) experienced by cells (*15*). Winter deep mixing brings cold nutrient-rich water to the surface. (**B**) Phylogenetic trees from pairwise genetic distances of ITS-rRNA sequences of individual cells from each sample [based on multiple alignment (*15*)]. The relevant sub-tree range of the known ecotypes (*2*) is marked above each tree if cells belonging to that ecotype are found, as is the division into low-light–adapted (LL) and high-light–adapted (HL) groups (*2*). (**C**) Heat maps describing the pairwise distance matrix between ITS-rRNA sequences of individual cells from each sample. Rows and columns are arranged according to the order of leaves of the trees shown in (B). The color map represents genetic distances as a percentage of base substitutions per site (log scale), such that the blue blocks identify very closely related ITS ribotypes. ITS sequences from cultured isolates with completely sequenced genomes are denoted by asterisks centered on the relevant line. Names of the largest clusters are marked in bold (e.g., cN2).
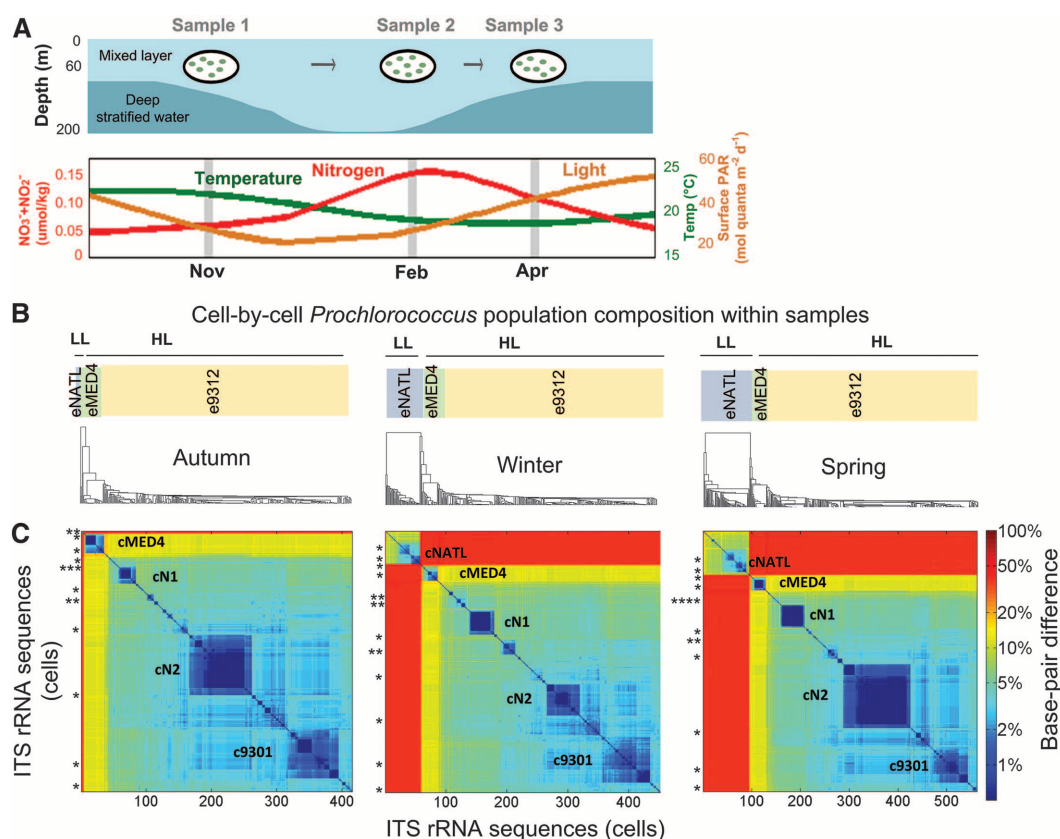
Flow sorting and DNA amplification (*11–14*) of more than 1000 co-occurring *Prochlorococcus* cells allowed us to explore the cell-by-cell genomic composition of these wild populations. We were able to identify coherent subpopulations at the whole-genome level and their relationship to those defined by the ITS region, explore finely resolved diversity patterns within and between subpopulations, and examine shifting abundances with seasonal changes in the habitat.

We first examined the population composition by sequencing the ITS regions of hundreds of *Prochlorococcus* cells in each sample, revealing the presence of finely resolved clusters within the broadly defined ecotypes (Fig. 1B). The populations were composed of tens to hundreds of nearly identical ITS clusters (>98% similar) within the coarse-grained ecotypes (Fig. 1, B and C). The relative abundance of cells belonging to the different clusters changed with season (Fig. 1, A to C) (*15*), suggesting shifts in their relative fitness in response to environmental changes.

To study the fine-scale genomic variation and compare it with the ITS-defined clusters, we sequenced the partial genomes (representing, on average, 70% of the total genome) of 90 individual cells (30 per sample) from the largest nearly identical ITS cluster, cN2 (Figs. 1C and 2), as well as 6 cells from two other clusters, cN1 and c9301. For each time of year, cells were randomly selected for genome sequencing from within the major ITS ribotypes (>99% similar) within cluster cN2 (C1 to C5) (30 cells), as well as from c9301-C8 and cN1-C9 (one cell each), as detailed in (*15*). We used a modified mediator genome reference assembly approach (*15, 18*) to analyze between-cell variation in the partial genomes recovered. The topologies of the ITS and genomic trees were highly congruent (Fig. 2), indicating that ITS sequences can serve as a proxy for genome sequences in *Prochlorococcus* at a much finer level of resolution than previously demonstrated (*4, 19*). The genomic data further revealed that the largest cluster cN2 is divided into five major clades [C1 to C5 (Fig. 2)] and a few additional minor clades represented by only one cell each. The delineation of clades C1 to C5 was highly robust and also observed in trees constructed from genomic position subsets (figs. S1 and S2).

To explore the evolutionary forces that shaped the cN2 C1 to C5 clades, we examined differences in nucleotide sequences within and between clades. For example, the C1 and C3 subpopulations (Fig. 2B) differ in 52,885 dimorphic single-nucleotide polymorphisms (SNPs), which represent 3.2% of their genomes (Fig. 3A, blue). The dimorphic SNPs between C1 and C3 are scattered across the genomes, occurring in 1519 out of 1974 genes (most of them core genes); 8% of these SNPs are found in intergenic regions (9% of the genome is noncoding). Of the intragenic SNPs, 37% are nonsynonymous, thus affecting the amino acid sequences of the proteins they encode. In contrast to the scattered nature of the sequence variation between the C1 and C3 clades, the polymorphism within them is confined to a few regions of the genome (Fig. 3A, black), indicating that most regions along the genome are conserved within clades and are different between them (*15*), which is true for all pairwise comparisons within C1 to C5 (figs. S3 and S4).

This emerging pattern was further supported by a standard measure of genetic differentiation between populations, the fixation index (F_{ST}) (*20*), applied at gene-by-gene resolution to the five cN2 clades, C1 to C5 (Fig. 3, B and C). Seventy-five percent of the core genes had high F_{ST} values (>0.8), (Fig. 3, B and C) (*15*), meaning different clades contained significantly different alleles. Some of the differentiated core genes have functions involved in the interaction between the cell and environmental stimuli [e.g., transporters, genes that affect oxidative stress responses, and cell surface biosynthesis and modification (Data S1)]; that is, they are not all simply "housekeeping genes" that control central metabolism. For example, alleles of phosphoglucosamine mutase, which is involved in the biosynthesis of outer membrane lipopolysaccharides (*21*), differ by an average of 10% of their amino acid sequences (Fig. 3C), with substitutions in the hydrophilic center of the enzyme (*21*), possibly affecting its specificity and kinetics.

We next asked whether different clade subpopulations carry distinct sets of flexible genes. Using de novo assemblies to capture regions unmapped by the reference assemblies (*15*), we found that each subpopulation carries a small set of distinct genes, typically in the form of cassettes within genomic islands (Table 1). Cassettes containing genes in the glycosyltransferase family account for much of the gene content variation between these clade subpopulations (Table 1 and table S1). The gene content in these cassettes suggests involvement in outer membrane modifications, possibly affecting phage attachment (*22*), recognition by grazers (*23*), cell-to-cell communication, or interactions with other bacteria (*24*).

We conclude that these clade subpopulations have distinct "genomic backbones" (and are
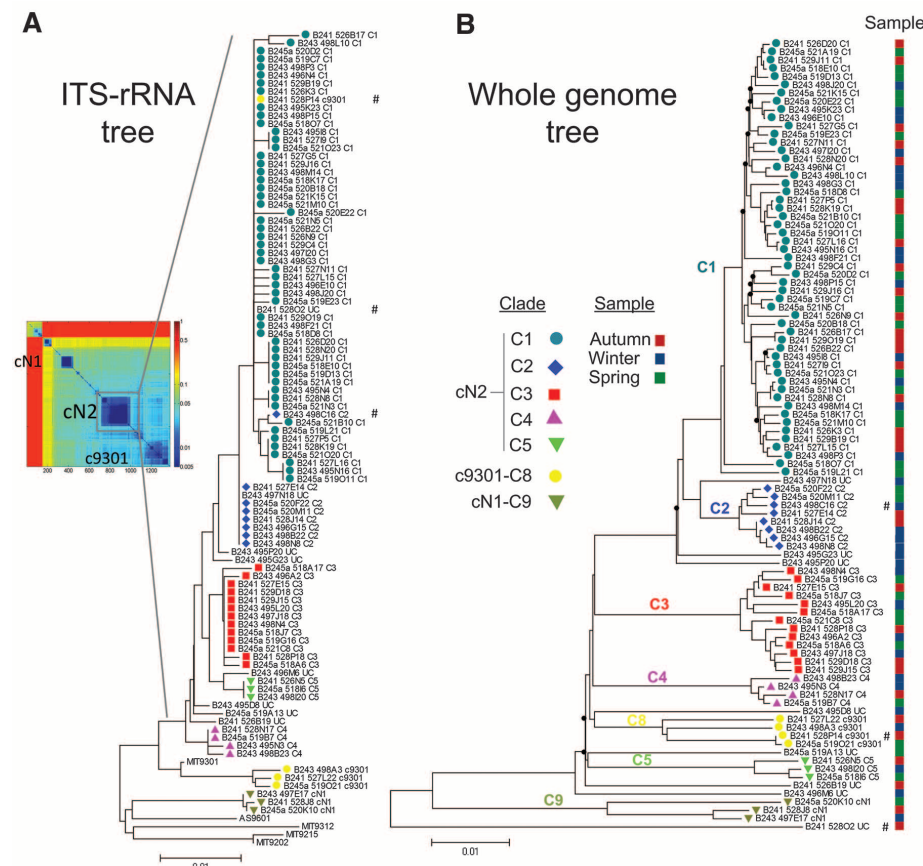
Fig. 2. ITS-rRNA sequence and whole-genome neighbor-joining phylogenetic trees at a fine resolution of diversity. (**A**) Phylogenetic tree based on ITS-rRNA sequences of 96 single cells (90 cN2 ribotypes, three cN1 ribotypes, and three c9301 ribotypes), as well as additional five high-light–adapted cultured strains. (**B**) Phylogenetic tree of the 96 single cells based on whole-genome sequences. The colored symbols to the left of the leaf labels in (A) and (B) represent the different clades depicted from the deep branches observed in the whole-genome tree. The sample origin of each cell is marked with red, blue, and green squares (representing autumn, winter, and spring, respectively) on the right. Distance units are base substitutions per site (see scale bar) (*15*). Bootstrap values <80 are marked as black dots on the internal nodes in (B) (fig. S1). Cells marked with # fall into an ITS clade that differs from the genome-defined clade. Neighbor-joining trees in (A) and (B) were constructed using p-distance.
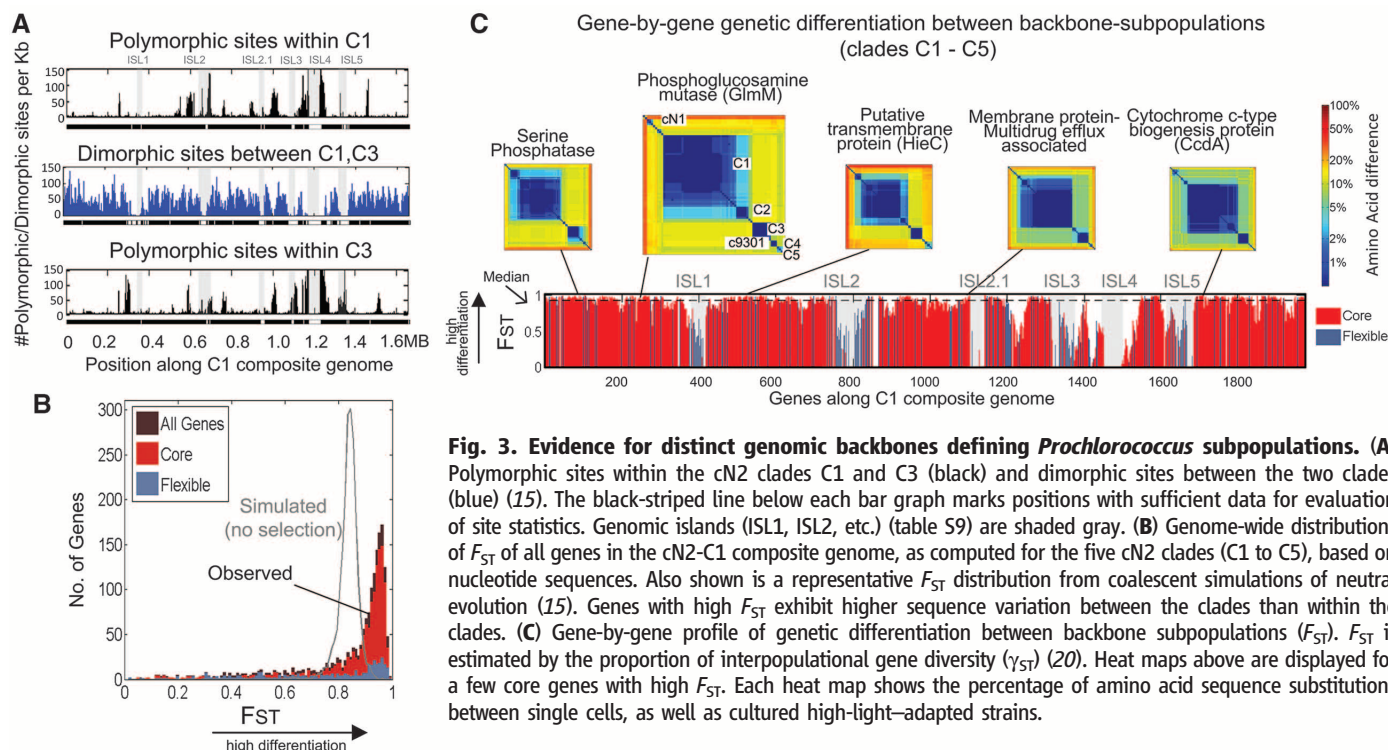
Fig. 3. Evidence for distinct genomic backbones defining *Prochlorococcus* subpopulations. (A) Polymorphic sites within the cN2 clades C1 and C3 (black) and dimorphic sites between the two clades (blue) (*15*). The black-striped line below each bar graph marks positions with sufficient data for evaluation of site statistics. Genomic islands (ISL1, ISL2, etc.) (table S9) are shaded gray. **(B)** Genome-wide distributions of F_{ST} of all genes in the cN2-C1 composite genome, as computed for the five cN2 clades (C1 to C5), based on nucleotide sequences. Also shown is a representative F_{ST} distribution from coalescent simulations of neutral evolution (*15*). Genes with high F_{ST} exhibit higher sequence variation between the clades than within the clades. **(C)** Gene-by-gene profile of genetic differentiation between backbone subpopulations (F_{ST}). F_{ST} is estimated by the proportion of interpopulational gene diversity (γ_{ST}) (*20*). Heat maps above are displayed for a few core genes with high F_{ST}. Each heat map shows the percentage of amino acid sequence substitutions between single cells, as well as cultured high-light–adapted strains.
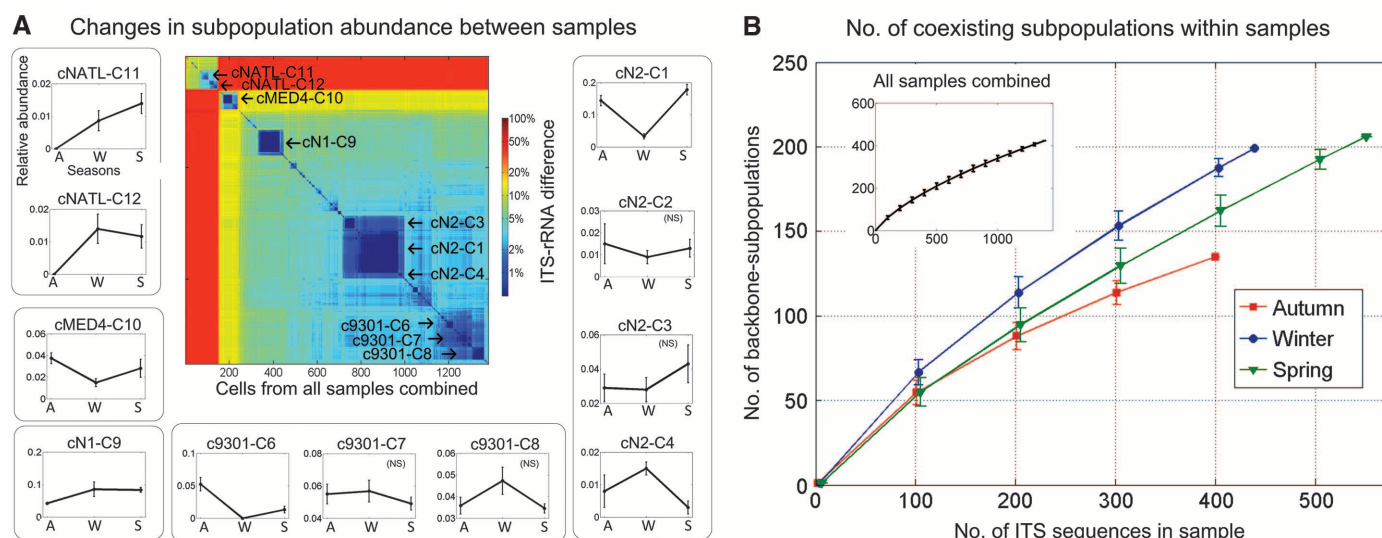
Fig. 4. Abundance profiles of backbone subpopulations and the estimated number of coexisting subpopulations within samples. (A) Relative abundance profiles of the 11 largest backbone subpopulations in our samples within the ITS clusters cNATL, cMED4, cN1, cN2, and c9301. A, autumn; W, winter; S, spring. Backbone names are marked near the relevant cluster on the ITS heat map. Backbone subpopulations were

henceforth referred to as "backbone subpopulations" consisting of highly conserved (within subpopulation) alleles of the majority of core genes and a small distinct set of flexible genes that is linked with a particular backbone. This covariation between the core alleles and flexible gene content, and its fine scale resolution, represents a new dimension of microdiversity within wild *Prochlorococcus* populations. It is noteworthy that similar patterns have been identified in cultured isolates and metagenomic assemblies within coexisting members of a few other microbial species with very different ecologies (*5–10, 25*), suggesting that differentiated genomic backbones may be a feature of diverse types of microbial populations.

At a finer resolution of diversity, we observed that cells within the five cN2 backbone sub-

predicted by 99% ITS similarity for the full set of 1381 ITS sequences. Error bars represent SEM. NS, no significant changes between seasons (false discovery rate, $\alpha = 0.05$) (*15*). **(B)** Rarefaction curves estimating the number of coexisting backbone subpopulations within samples (*15*). Backbones predicted as in (A). Error bars represent 95% confidence intervals. (Inset) Rarefaction curve of all samples combined.

populations differ by 19,000 nucleotide positions on average, in comparison to 77,000 positions between backbone subpopulations (equivalent to 1.2 and 4.7% of the genome, respectively) (Fig. 2B). The most similar pairs of individual cell genomes in our samples differ in a few hundred base pairs [close to the detection limit when one considers single-cell processing and sequencing error (*15*)]; some of these pairs likely have identical

Table 1. Flexible gene cassettes associated with different cN2 backbone subpopulations highlighting gene content that may contribute to ecological differentiation. GT, glycosyltransferase; ABC-T, adenosine triphosphate–binding cassette (ABC) transporter; HLIP, high-light–inducible protein; CO, Cytochrome oxidase c subunit VIb; HlpA, histone-like protein; CpsL, polysaccharide biosynthesis protein. In the "Selected gene annotations" column, numbers before gene annotation refer to number of that type of gene. A complete list of the genes in each cassette is described in table S1 (*15*).

Clade	Cassette ID	Position	No. of genes in cassette	Selected gene annotations	Cassette function
cN2-C1	CST_I	Island 2.1	4	HLIP, CO	Redox stress response
	CST_II	Island 4	7	3GT, ABC-T	Outer membrane modification
cN2-C2	CST_II	Island 4	7	3GT, ABC-T	Outer membrane modification
cN2-C3	CST_III	Island 1	2	2GT	Outer membrane modification
cN2-C4	CST_I	Island 2.1	4	HLIP, CO	Redox stress response
	CST_IV	Island 4	14	3GT, HlpA, CpsL	Outer membrane modification
cN2-C5	CST_V	Island 4	5	2GT	Outer membrane modification

gene content (*15*). Except for these few pairs, each cell carries at least one gene cassette not found in any other. In some cases, a few closely related cells (a subclade) within backbones share a distinct gene cassette. Among these genes are, again, glycosyltransferase genes, as well as transporters and genes involved in nucleotide binding and processing. In a few cases, cells from different backbone subpopulations carry similar flexible gene cassettes [e.g., high-light–related genes (Table 1) and phosphonate related genes], demonstrating the combinatorial nature of backbones and flexible genes.

If backbone subpopulations have differential fitness, we would expect their relative abundance to change with changing environmental conditions (Fig. 1). Accordingly, the majority of the largest subpopulations exhibited significant seasonal abundance variation (Fig. 4A), higher than expected by chance (*15*), consistent with the hypothesis that this reflects selection, but more data are needed to draw that conclusion. Backbone subpopulations maintain their genomic composition between seasons (tested for C1) (*15*), which we would expect, as the establishment of new mutations and the acquisition and loss of genes are not likely to be in play on these time scales (*15*).

The congruency of genomic and ITS phylogenies in *Prochlorococcus* at both coarse (*4*, *19*) and fine resolution (Fig. 2) suggests that ITS-ribotype clusters coincide, in most cases, with distinct genomic backbones (*15*). This allowed us to estimate the number of coexisting backbone subpopulations in our samples through rarefaction analysis, revealing at least hundreds of coexisting subpopulations with distinct backbones (Fig. 4B) in each sample. These backbone subpopulations are estimated to have diverged at least a few million years ago (*15*), suggesting ancient, stable niche partitioning. That they have different alleles of genes associated with environmental interactions, carry a distinct set of flexible genes, and differ in relative abundance profiles as the environment changes suggests strongly that they are ecologically distinct.

Enormous population sizes and immense physical mixing probably played a role in the evolution of diverse genomic backbones in *Prochlorococcus*. A simple fluid mechanics model bridging the micrometer and kilometer scales for a typical ocean suggests that just-divided cells will be centimeters apart within minutes, tens of meters apart within an hour, and a few kilometers apart within a week (*15*). Thus, *Prochlorococcus* populations are expected to be well mixed over large water parcels (~10 km^2 area by 3 m depth) on ecologically relevant time scales (~1 week) (*15*). This mixing and a stable collective *Prochlorococcus* population density of 10^7 to 10^8 cells liter^{-1} (*17*) make the size of each backbone subpopulation in such parcels enormous (>10^{13} cells) (*15*). The effective population size is arguably close to this census population size (*15*), implying that *Prochlorococcus* evolution is governed by selection, not genetic drift [based on population genetics theory (*26*)]. Consistent with this argument, the difference in the observed F_{ST} distribution from that estimated for no selection (Fig. 3B) provides further evidence that the differentiation of genomic backbones in *Prochlorococcus* is a product of selection (*15*).

The correlation between phylogeny and flexible gene content (Table 1, tables S1 and S13, and fig. S5) leads us to propose that the emergence of a genomic backbone is initiated by the acquisition of a beneficial flexible gene cassette, followed by slow fine-adjustment of the core gene alleles to the new niche dimension afforded by the acquired cassette. Given the huge effective population size, even extremely weak fitness differentials among alleles (*27*) can facilitate fine-adjustment of core genes (*15*) over the millions of years of evolution after divergence.

The diverse set of hundreds of subpopulations with distinct genomic backbones probably plays an important role in the dynamic stability of the *Prochlorococcus* "collective" in the global oceans (fig. S6). Small fitness differentials, niche differentiation, and selective phage and grazer predation, in the context of temporal and spatial environmental variation, help to explain their coexistence (*28*, *29*). On seasonal time scales, the *Prochlorococcus* collective maintains a relatively stable population size through temporal and local adjustments in the relative abundance of backbone subpopulations (Figs. 1C and 4A and fig. S6D). On longer time scales (decades to millions of years), the collective may respond to shifting selective pressures through the exchange of gene cassettes between and within backbone subpopulations, and through the evolution of the backbones themselves. The coherence of the collective population holds as long as subpopulations do not diverge to the point where they are no longer able to exchange flexible genes and backbone extinction and emergence rates are relatively balanced. If *Prochlorococcus* backbone subpopulations were designated as distinct species (*30*), it would imply that the global collective is an assortment of thousands of species. It is likely that such a large set of coexisting subpopulations with distinct genomic backbones is a characteristic feature of free-living bacterial species with very large population sizes living in highly mixed habitats.

References and Notes

1. F. Partensky, W. R. Hess, D. Vaulot, *Microbiol. Mol. Biol. Rev.* **63**, 106–127 (1999).
2. L. R. Moore, G. Rocap, S. W. Chisholm, *Nature* **393**, 464–467 (1998).
3. Z. I. Johnson *et al.*, *Science* **311**, 1737–1740 (2006).
4. G. C. Kettler *et al.*, *PLOS Genet.* **3**, e231 (2007).
5. J. Grote *et al.*, *MBio.* **3**, e00252-12 (2012).
6. D. E. Hunt *et al.*, *Science* **320**, 1081–1085 (2008).
7. S. L. Simmons *et al.*, *PLOS Biol.* **6**, e177 (2008).
8. H. Cadillo-Quiroz *et al.*, *PLOS Biol.* **10**, e1001265 (2012).
9. A. Gonzaga *et al.*, *Genome Biol. Evol.* **4**, 1360–1374 (2012).
10. R. T. Papke *et al.*, *Proc. Natl. Acad. Sci. U.S.A.* **104**, 14092–14097 (2007).
11. S. Rodrigue *et al.*, *PLOS ONE* **4**, e6864 (2009).
12. T. Kalisky, P. Blainey, S. R. Quake, *Annu. Rev. Genet.* **45**, 431–445 (2011).
13. R. Stepanauskas, *Curr. Opin. Microbiol.* **15**, 613–620 (2012).
14. R. S. Lasken, *Nat. Rev. Microbiol.* **10**, 631–640 (2012).
15. Materials and methods are available as supplementary materials on *Science* Online.
16. A. F. Michaels *et al.*, *Deep Sea Res. Part I* **41**, 1013–1038 (1994).
17. R. R. Malmstrom *et al.*, *ISME J.* **4**, 1252–1264 (2010).
18. O. Wurtzel, M. Dori-Bachash, S. Pietrokovski, E. Jurkevitch, R. Sorek, *PLOS ONE* **5**, e15628 (2010).
19. M. Mühling, *Environ. Microbiol.* **14**, 567–579 (2012).
20. M. Nei, in *Human Genetics, Part A: The Unfolding Genome*, B. Bonné-Tamir, T. Cohen, R. M. Goodman, Eds. (Alan R. Liss, New York, 1982), p. 167.
21. R. Mehra-Chaudhary, J. Mick, L. J. Beamer, *J. Bacteriol.* **193**, 4081–4087 (2011).
22. S. Avrani, O. Wurtzel, I. Sharon, R. Sorek, D. Lindell, *Nature* **474**, 604–608 (2011).
23. J. Pernthaler, *Nat. Rev. Microbiol.* **3**, 537–546 (2005).
24. F. Malfatti, F. Azam, *Aquat. Microb. Ecol.* **58**, 1–14 (2009).
25. U. Dobrindt, B. Hochhut, U. Hentschel, J. Hacker, *Nat. Rev. Microbiol.* **2**, 414–424 (2004).
26. J. F. Crow, M. Kimura, *An Introduction to Population Genetics Theory* (Harper & Row, New York, 1970).

27. R. D. Barrett, D. Schluter, *Trends Ecol. Evol.* **23**, 38–44 (2008).
28. A. D. Barton, S. Dutkiewicz, G. Flierl, J. Bragg, M. J. Follows, *Science* **327**, 1509–1511 (2010).
29. F. Rodriguez-Valera *et al.*, *Nat. Rev. Microbiol.* **7**, 828–836 (2009).
30. C. C. Thompson *et al.*, *Microb. Ecol.* **66**, 752–762 (2013).

Structure-Guided Transformation of Channelrhodopsin into a Light-Activated Chloride Channel

Andre Berndt,[1]* Soo Yeun Lee,[1]* Charu Ramakrishnan,[1] Karl Deisseroth[1,2,3]†

Using light to silence electrical activity in targeted cells is a major goal of optogenetics. Available optogenetic proteins that directly move ions to achieve silencing are inefficient, pumping only a single ion per photon across the cell membrane rather than allowing many ions per photon to flow through a channel pore. Building on high-resolution crystal-structure analysis, pore vestibule modeling, and structure-guided protein engineering, we designed and characterized a class of channelrhodopsins (originally cation-conducting) converted into chloride-conducting anion channels. These tools enable fast optical inhibition of action potentials and can be engineered to display step-function kinetics for stable inhibition, outlasting light pulses and for orders-of-magnitude-greater light sensitivity of inhibited cells. The resulting family of proteins defines an approach to more physiological, efficient, and sensitive optogenetic inhibition.

The microbial opsins (*1–3*) used for optical control of genetically targeted cellular activity (*4–7*) include light-activated proton and Cl⁻ pumps and the cation channels called channelrhodopsins (ChRs). ChRs are derived from algae (*3, 8–10*) and, when expressed in neurons, can elicit precise action potential (AP) firing (*11–15*). ChRs conduct K^+, Na^+, protons, and Ca^{2+} (*3, 10, 16, 17*); because of this non-selective cation-conductance, ChRs display reversal potentials (V_{rev}) near 0 mV under physiological conditions and therefore depolarize neurons, leading to AP generation (*18*).

Direct light-triggered inhibition of neuronal activity is possible with inward-pumping Cl⁻-transporting opsins and outward-pumping proton-transporting opsins (*10*); hyperpolarization to –150 mV or beyond can be achieved (*18–20*). However, pumps are inefficient in neural systems because only one ion is moved per photon and no input resistance decrease is elicited (failing to recruit the most potent mechanism of spiking inhibition). Moreover, because the pumps use energy to transport ions against electrochemical gradients, the creation of abnormal gradients is more likely (*18*). Last, pumps cannot take advantage of certain molecular engineering opportunities to achieve light sensitivity and long-term photocurrent stability enhanced by many orders of magnitude (but which depend on formation of a transmembrane pore) (*21–23*). Therefore, the creation of inhibitory channels has long been a central goal of optogenetics.

Given typical ion balance in neural systems, identification or creation of light-activated K^+ or Cl⁻ channels could give rise to inhibitory optogenetic tools. ChRs can be engineered to alter kinetics, spectrum, and selectivity among cations (*10, 24, 25*). However, V_{rev} has not been shifted sufficiently for nondepolarizing spike inhibition in neurons. We have designed a family of ChRs for Cl⁻ permeability and capability to inhibit APs without depolarizing neurons to or beyond the AP-generation threshold.

Building on the high-resolution crystal structure of the ChR chimera C1C2 (*24*), we noted that the ion-selectivity pore of ChR is less ordered as compared with the well-defined symmetry of tetrameric K^+-selective channels such as KcsA and NaK2K (*26–31*). Therefore, we speculated that the specific cation selectivity of ChR is rather a result of negative electrostatic potential surrounding the pore and vestibule; for instance, the C1C2 structure shows seven glutamates framing the conduction pathway (*24*). We hypothesized that systematic replacement of such residues within or close to the pore according to structure-guided electrostatic modeling could reverse this polarity and create an inhibitory ChR, if it were possible to maintain proper protein folding, membrane expression, optical activation, and pore gating.

We initiated a broad structure-guided screen by introducing single site-directed mutations into C1C2 (Fig. 1A). We expressed all variants in cultured rat hippocampal neurons and tested photocurrents using whole-cell patch-clamp so as to ensure proper function in neurons (external/internal [Cl⁻], 147 mM/4 mM). We quantified stationary photocurrent amplitudes across a range of holding potentials (Fig. 1B), with particular attention to V_{rev}, in order to identify permeability variants (Fig. 1C). C1C2 exhibits V_{rev} of –7 mV under these conditions, which is typical for nonspecific cation channels (*16, 26, 32, 33*). Certain mutations with powerful effects on V_{rev} displayed concomitant adverse effects on photocurrent sizes (such as E136R and E140K) (Fig. 1B), and were not studied further (*34*). More promising mutations, such as N297Q and H173R, exhibited both potent currents and altered V_{rev} (Fig. 1C) and were combined in a series of increasingly integrated mutations. The fivefold mutation T98S/E129S/E140S/E162S/T285N and fourfold mutation V156K/H173R/V281K/N297Q both displayed prominently-shifted V_{rev} (in the range of –40 mV) while maintaining functionality (Fig. 1, D and E).

We next combined these constructs to generate a ninefold mutated variant with contiguous shifts in expected electrostatic potential distribution (Fig. 2A and fig. S1) (*24*). We expressed the ninefold variant in human embryonic kidney (HEK) 293 cells to test both V_{rev} and permeability under controlled ion composition and optimized voltage clamp settings (Fig. 2B). We mapped photocurrents over a broad range of membrane potentials (Fig. 2C) (from –75 mV to +55 mV) (*35*). Under these conditions (external/internal [Cl⁻], 147mM/4mM), the combined ninefold mutation exhibited V_{rev} of –61 mV, which is far more negatively shifted than was the C1C2 backbone or either parental 4× or 5× construct (Fig. 2D). Despite this major change in functionality, both peak and stationary photocurrents remained fast and robust (predicting suitability for optogenetics, especially because this channel could also recruit a reduced-membrane resistance mechanism for spiking inhibition), and the original blue light–activation spectrum of C1C2

[1]Department of Bioengineering, Stanford University, Stanford, CA 94305, USA. [2]Department of Psychiatry and Behavioral Sciences, Stanford University, Stanford, CA 94305, USA. [3]Howard Hughes Medical Institute, Stanford University, Stanford, CA 94305, USA.

*These authors contributed equally to this work.
†Corresponding author. E-mail: deissero@stanford.edu

was maintained, compared with the red-activation capability of the Cl⁻ pump eNpHR3.0 (thus maintaining a separable channel for inhibitory control in optogenetic applications) (Fig. 2E). We termed this ninefold variant "iC1C2."

Because the shifted V_{rev} could be attributable to increased K⁺ selectivity or a new Cl⁻ conductance, we measured V_{rev} under varying ion compositions (corrected for the calculated junction potential arising from each condition) (35) in order to determine the specific ion selectivity of iC1C2. ChRs are highly permeable for protons and typically show no selectivity between K⁺ and Na⁺ (16). Therefore, with a pipette solution composition of 120 mM KCl at pH 7.3 and a bath solution of 120 mM NaCl also at pH 7.3, virtually no chemical gradient for permeant ions would be expected, and indeed, under these conditions V_{rev} for both C1C2 and iC1C2 was ~0 mV (Fig. 2F). Replacement of external KCl by CsCl would create a strong outward-directed gradient for K⁺ ions, and as expected under this condition, V_{rev} of C1C2 dropped to –17.4 mV, which is consistent with K⁺ as a major charge carrier. However, there was no such V_{rev} shift for iC1C2 ($V_{rev} = $–1mV). These data do not support a hypothesis that iC1C2 achieves shifted V_{rev} through increased K⁺ conductance,

and in fact, iC1C2 does not appreciably conduct K⁺ under these conditions (Fig. 2F). To test the other possibility of new Cl⁻ conductivity, we replaced external Cl⁻ with gluconate (for a chemical Cl⁻ gradient of 8 mM$_{ext}$/128 mM$_{int}$ and shifting its Nernst potential to +71 mV). Despite this strong outward-directed Cl⁻ gradient, C1C2 showed no shift in V_{rev} (0 mV), which was as expected because the native C1C2 does not conduct Cl⁻. In contrast, iC1C2 exhibited a positively shifted V_{rev} of +48 mV, revealing a strong contribution of Cl⁻ to the photocurrent (Fig. 2F). Last, we replaced internal Cl⁻ with gluconate to create a strong inward-directed Cl⁻ gradient (128 mM [Cl⁻]$_{ext}$/8 mM [Cl⁻]$_{in}$; $V_{Nernst-Cl} = $–71mV). The resulting V_{rev} was –6 mV for C1C2 but –57 mV for iC1C2, confirming a potent contribution from conducted Cl⁻ ions to iC1C2 photocurrents (Fig. 2G).

Because the V_{rev} for iC1C2 was not identical to the calculated $V_{Nernst-Cl}$, other ions such as protons (16) could be conducted as well. To explore this possibility in physiological Cl⁻ gradients, we altered the proton concentrations of internal and external solutions while maintaining the inward-directed Cl⁻ chemical gradient (128 mM$_{ext}$/8 mM$_{in}$; $V_{Nernst-Cl} = $–71 mV) (Fig. 2H). We varied pH of external and internal solutions together (no proton

chemical gradient; $V_{Nernst-H+} = 0$ mV) and measured iC1C2 responses at physiological (7.3) and low (6.0) pH, with matched internal/external proton concentrations. We expected that at lower pH and more negative membrane potential, protons would contribute more to the iC1C2 photocurrent and thus positively shift V_{rev} toward the 0 mV Nernst potential for protons. Surprisingly, we found that the iC1C2 V_{rev} was more negatively shifted at pH 6 as compared with pH 7.3 (Fig. 2H), suggesting that iC1C2 conducts Cl⁻ even more robustly and maintains a prominently negative V_{rev} at lower pH values. Total iC1C2 photocurrents were greater at lower pH values (Fig. 2, I and J), which is consistent with a proton-enhanced Cl⁻ permeability. We calculated the ratio of Cl⁻ to proton permeability at the different pH values ($\alpha = P_{Cl}/P_H$) (35). Indeed, at pH 6 the contribution of Cl⁻ to the overall current was 35 times higher than at pH 7.3, suggesting that even excursions to lower pH—as can happen during extreme neural activity—will not impair the important Cl⁻ conductance.

We next expressed C1C2 and iC1C2, each fused to enhanced yellow fluorescent protein (eYFP), in cultured hippocampal neurons (fig. S2). Mean resting potentials were not different (C1C2, –65 mV; iC1C2, –69 mV), and input resistances were in the expected range (above 200 megohms) for both constructs. We determined V_{rev} (Fig. 3A), which for iC1C2 ($V_{rev} = $–64 mV) was negatively shifted by 56 mV compared with C1C2 ($V_{rev} = $–7 mV) (Fig. 3B). This V_{rev} of iC1C2 lies more negative than the measured threshold for AP generation ($V_{AP} = $–55 mV) (Fig. 3C). Consequently, at V_{AP}, in a voltage clamp C1C2 generated an inward-directed photocurrent of –475 pA, whereas iC1C2 produced an outward-directed photocurrent of +42 pA; in a current clamp, C1C2 depolarized neurons by +20 mV, whereas iC1C2 hyperpolarized neurons by –3 mV (Fig. 3D). In addition, input resistance dropped by ~50% during light in cells expressing iC1C2, indicating increased ion flux through membrane pores, and after light-off input resistance recovered to original levels (Fig. 3E).

The iC1C2 input-resistance effects and iC1C2 membrane polarization effects, that together would tend to maintain membrane potential below spike-firing threshold (Fig. 3F), suggested utility in optogenetic control of spiking. Indeed, optical activation of iC1C2 sufficed to inhibit electrically evoked spikes without exerting a depolarizing effect (Fig. 4, A to C). To further explore the properties of iC1C2, we mutated cysteine-167 to mimic step-function mutations of channelrhodopsin (21), which decelerate channel closure and extend lifetime of the ion-conducting state; as a result, brief light stimulation induces prolonged depolarization, and light sensitivity of cells expressing these variants is greatly increased (21–23). The inhibitory versions here define the SwiChR variants (for Step-waveform inhibitory ChR), including C167T (SwiChR$_{CT}$) and C167A (SwiChR$_{CA}$). We first expressed SwiChR$_{CT}$ in HEK cells to determine channel kinetics and sensitivity. Both inward- and outward-directed photocurrents were

Fig. 1. Rational design and screen: V_{rev}-shifted ChRs. (**A**) C1C2 crystal structure [Protein Data Bank (PDB) 3UG9] (24), with residues used for screening in blue (retinal chromophore in magenta). (**B**) C1C2 mutations screened in neurons for photocurrent size at –80 mV (n = 6 to 8 cells). Arrows indicate nine mutations selected for C1C2_5x (T98S/E129S/E140S/E162S/T285N) and C1C2_4x (V156K/H173R/V281K/N297Q) constructs. (**C**) V_{rev} of C1C2 single-mutation constructs (n = 6 to 8 cells). (**D**) Comparison of photocurrent sizes for C1C2, C1C2_4x, and C1C2_5x. (**E**) Comparison of V_{rev} for C1C2, C1C2_4x, and C1C2_5x (n = 8 to 10 cells). Error bars indicate SEM.
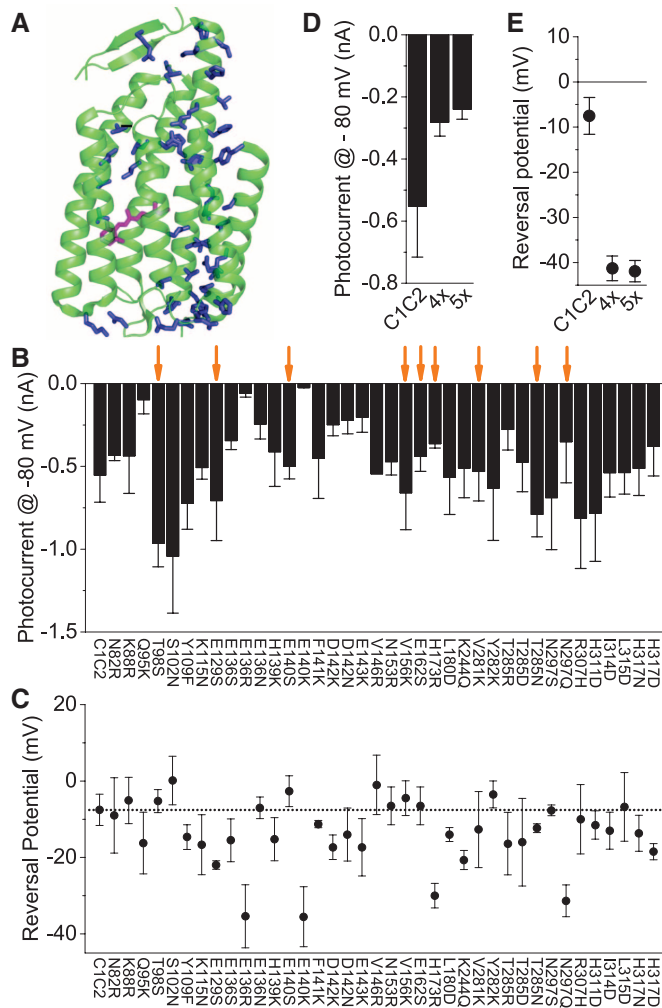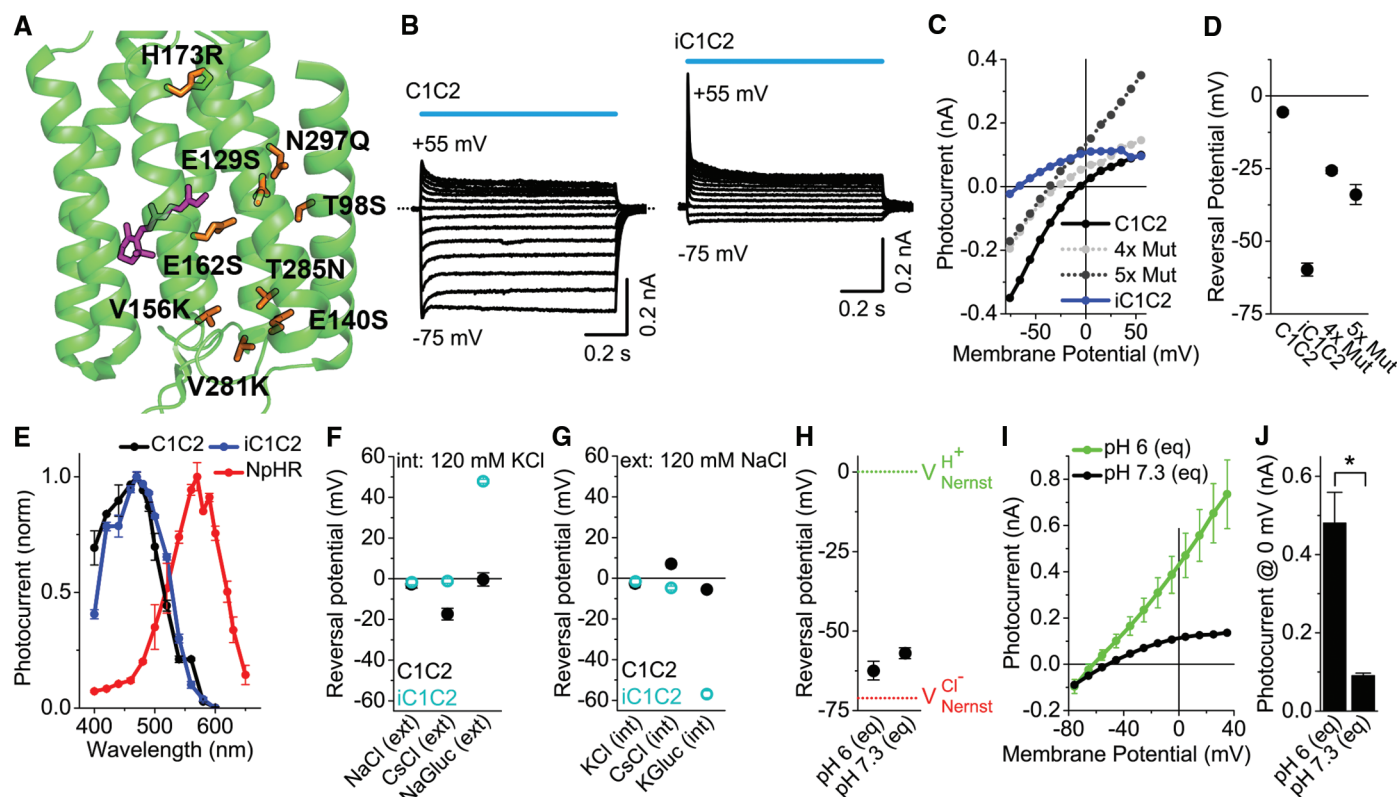
Fig. 2. iC1C2: biophysical properties. (**A**) C1C2 structure, with the nine residues mutated in C1C2_4x and C1C2_5x in orange. (**B**) Representative photocurrents and (**C**) corresponding current-voltage relationships recorded at membrane potentials from −75 mV to +55 mV upon 475 nm light activation (power density, 5 mW/mm²). (**D**) V_{rev} of C1C2, iC1C2, C1C2_4x, and C1C2_5x [neuronal recording solutions are available in (35)]. (**E**) Activation spectra of NpHR, C1C2, and iC1C2 measured at power density 0.65 mW/mm² for each wavelength and normalized to the maximum amplitude ($n = 6$ cells). (**F**) V_{rev} of C1C2, iC1C2, C1C2_4x, and C1C2_5x, with internal (int) 120 mM KCl and external (ext) 120 mM NaCl, CsCl, or NaGluconate, pH 7.3, char-

acterized in HEK cells. (**G**) As in (A), with ext 120 mM NaCl and int 120 mM KCl, CsCl, or KGluconate, pH 7.3 ($n = 6$ to 17 cells). (**H**) V_{rev} of iC1C2 under equal (eq) external and internal pH, generating a Nernst potential for protons of 0 mV (dotted green line) at pH 6 and 7.3. $[Cl^-]_i$ concentration was 8 mM, and $[Cl^-]_o$ was 128 mM, generating a Nernst potential for Cl⁻ of −71 mV (dotted red line) ($n = 6$ to 9 cells). (**I**) Current-voltage relationship recorded with equal external and internal pH values at pH 6 and 7.3; internal and external $[Cl^-]$ of 8 mM and 128 mM, respectively ($n = 3$ to 8 cells). (**J**) Photocurrent of iC1C2 at 0 mV from the current-voltage relationship in (I). Error bars indicate SEM.

Fig. 3. Characterization of iC1C2 in mammalian neurons. (**A**) Representative photocurrents of C1C2 (left) and iC1C2 (right) recorded at membrane potentials ranging from −80 to 0 mV. 475 nm light (blue bar) was applied at 5 mW/mm². (**B**) Corresponding current-voltage relationship for photocurrents. (**C**) V_{rev} of C1C2 and iC1C2 relative to threshold for spike generation (V_{AP}) and to neuron resting potential (V_{rest}) ($n = 8$ to 22 cells). (**D**) Photocurrent amplitudes (left) and membrane polarization at V_{AP} (right) ($n = 9$ to 14 cells). (**E**) Mean changes in input resistances were normalized to pre-light value ($n = 9$ to 20 cells). (**F**) Sample voltage traces of iC1C2-expressing neuron stimulated with varying current injections for 1.5 s, and additional 0.5 s, 475 nm, 5 mW/mm² pulses showing effective clamping toward V_{rev}: shown are hyperpolarizing responses below V_{AP}. Error bars indicate SEM.
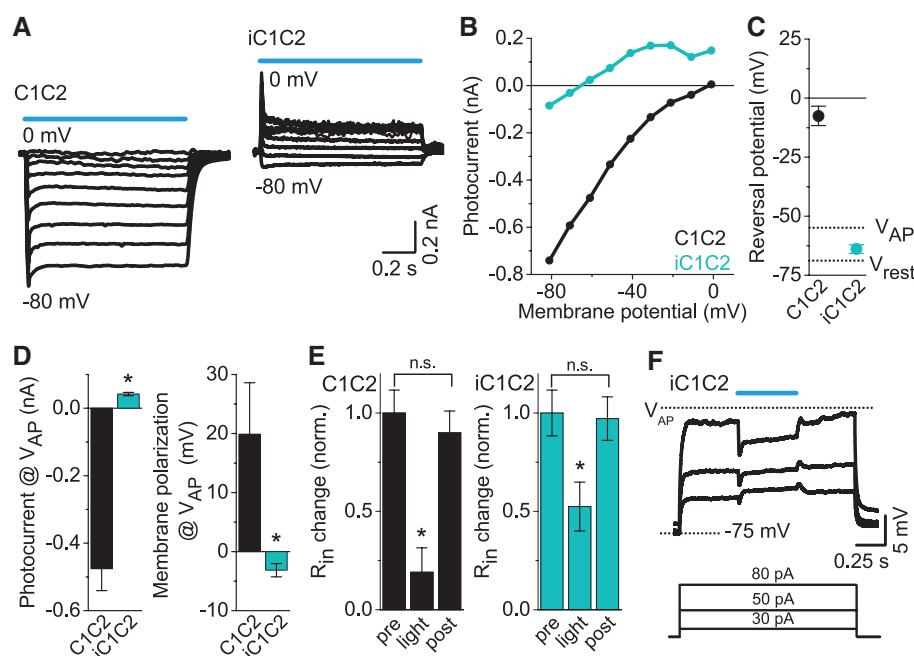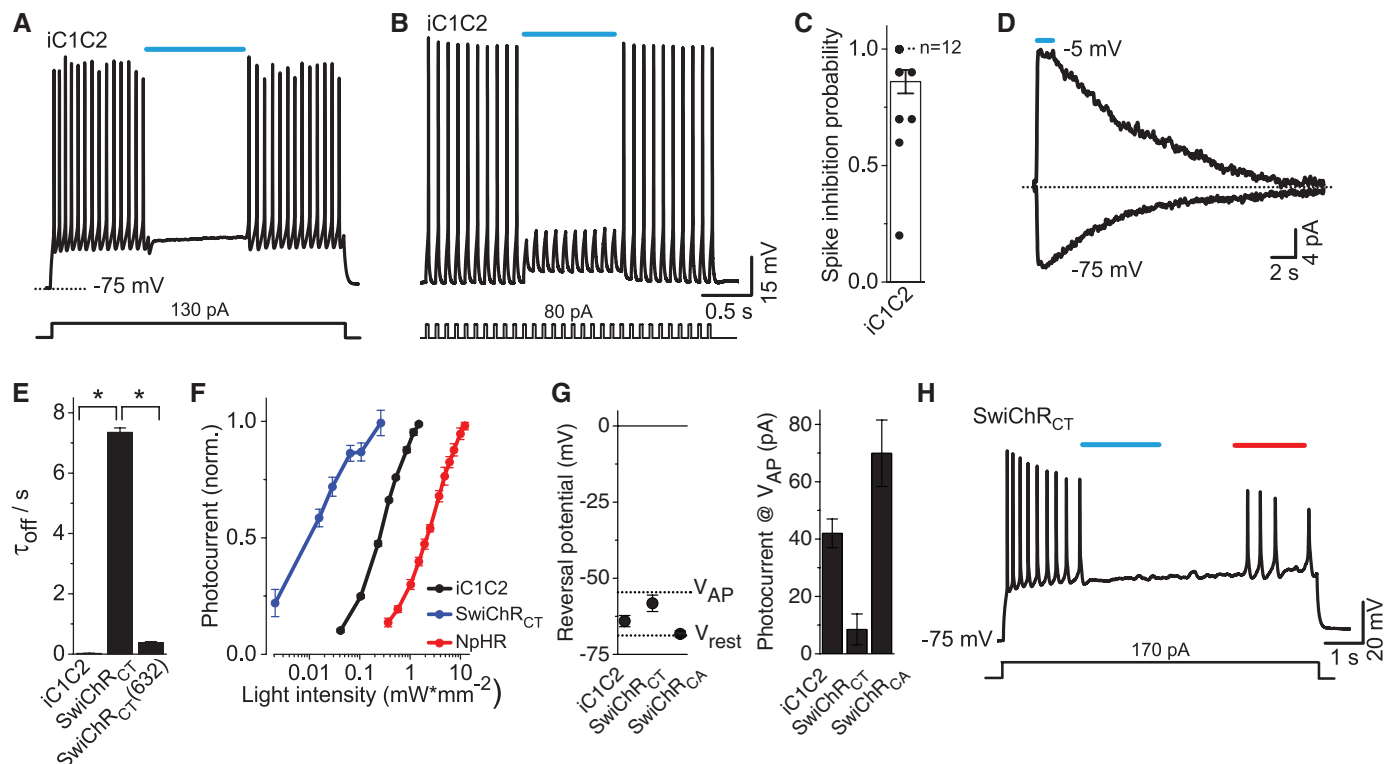
Fig. 4. Fast and bistable inhibition of neuronal spiking with iC1C2 and SwiChR. (**A** and **B**) Representative voltage traces of iC1C2-expressing neurons stimulated with either (A) a continuous electrical pulse (3s) or (B) pulsed current injections (10Hz/3s). Electrically evoked spikes were inhibited by 475 nm of light (blue bar) at 5 mW/mm². (**C**) Distribution of spike-inhibition probability for iC1C2-expressing cells ($n = 18$ neurons; fraction of spikes blocked shown). (**D**) Inward and outward photocurrents of SwiChR$_{CT}$ in HEK cell upon 475 nm of light (blue bar). (**E**) Channel off-kinetics (τ) for iC1C2, SwiChR$_{CT}$, and SwiChR$_{CT}$ exposed to red light during channel closure. (**F**) Light sensitivity of SwiChR$_{CT}$ compared with that of iC1C2 and NpHR. iC1C2 and SwiChR$_{CT}$ were activated with 470 nm, and NpHR was activated with 560 nm. Photocurrents were measured at light intensities between 0.0036 and 5 mW/mm², and holding potential was −80 mV. Amplitudes were normalized to the maximum value for each construct ($n = 6$ to 8 cells). (**G**) Reversal potential of iC1C2, SwiChR$_{CT}$, and SwiChR$_{CA}$ relative to V_{AP} and V_{rest} ($n = 10$ to 22) (left). Photocurrent amplitudes at V_{AP} are shown at right ($n = 9$ to 15 cells). (**H**) Bistable spiking modulation by SwiChR$_{CT}$. Spiking was induced with a continuous electrical pulse (3 s) and stably inhibited with 475 nm light (blue bar). Spiking resumed after 632 nm of light application (red bar). Light power density was 5 mW/mm². Error bars indicate SEM.

stabilized by orders of magnitude after light-off (Fig. 4D). The time-constant of channel closure (τ_{off}) for SwiChR$_{CT}$ was 7.3 s, compared with 24 ms for the parent iC1C2 (Fig. 4E). Beyond stability, another feature of step-function variants is the ability to quickly convert to the closed state upon redshifted light application (*21*), and indeed, SwiChR$_{CT}$ channel closure was accelerated by application of 632 nm of light (SwiChR$_{CT}$ $\tau_{off-632}$ = 375 ms) (Fig. 4E). Another feature of step-function variants is increased light sensitivity of expressing cells, which effectively become photon integrators for long light pulses (*23*). Indeed, SwiChR$_{CT}$-expressing cells showed a 25-fold increase in light sensitivity as compared with that of iC1C2, and a 200-fold increase compared with that of the pump-based inhibitor NpHR (Fig. 4F). Similar results were observed in neurons; SwiChR$_{CT}$ generated outward current at AP threshold in neurons with reversal potential of –61 mV and −68 mV for SwiChR$_{CA}$ (Fig. 4G and fig. S3). This sufficed to stably and reversibly inhibit spiking (Fig. 4H and fig. S3) with minimal directly driven current (Fig. 4G and fig. S3) or membrane potential change (Fig. 4H and fig. S3), presenting desirable properties for optogenetic investigation.

We have demonstrated structure-guided conversion of a cation-selective ChR into a light-activated Cl⁻ channel. The iC1C2 mechanism provides more physiological inhibition that does not require a major membrane potential change, and variants enable improvement of stability and light sensitivity by orders of magnitude over existing inhibitory tools. Depolarization-block strategies with excitatory tools (*18, 36, 37*), although useful in some settings, may not reliably inhibit all targeted cells because light intensities are highly variable in scattering tissue (*18, 36–38*); in contrast, iC1C2-based tools can only depolarize membranes to V_{rev} of ∼–64 mV (well below V_{AP}) and hyperpolarize when membrane potential is above V_{rev} (Fig. 3F).

Although aspects of final functionality arose by design (for example, removal of acidic residues and introduction of basic residues) (Fig. 2A), other properties remain to be fully explored. For example, iC1C2 showed dependence on external pH; we hypothesize that one or more basic residues within the ion-conducting pathway are protonated and positively charged at physiological and lower external pH, which in turn facilitates association and permeation of anions. Subsequent

improvements in iC1C2 and SwiChR variants by using structure-guided engineering strategies may further enhance photocurrent properties and may be easily ported to complementary and closely related ChR backbones, such as the potent chimeric red (*23, 39*) and two-photon/infrared (*40*) light-activated ChRs. The new Cl⁻ permeability of iC1C2 not only provides an unexpectedly effective illustration of cation-channel to anion-channel conversion (*41–43*) but also demonstrates structure-guided design of ChRs for new classes of functionality.

References and Notes
1. D. Oesterhelt, W. Stoeckenius, *Nat. New Biol.* **233**, 149–152 (1971).
2. A. Matsuno-Yagi, Y. Mukohata, *Biochem. Biophys. Res. Commun.* **78**, 237–243 (1977).
3. G. Nagel et al., *Science* **296**, 2395–2398 (2002).
4. K. Deisseroth, *Nature* **505**, 309–317 (2014).
5. K. Deisseroth, *Nat. Methods* **8**, 26–29 (2011).
6. L. Fenno, O. Yizhar, K. Deisseroth, *Annu. Rev. Neurosci.* **34**, 389–412 (2011).
7. A. M. Packer, B. Roska, M. Häusser, *Nat. Neurosci.* **16**, 805–815 (2013).
8. C. Nonnengässer, E. M. Holland, H. Harz, P. Hegemann, *Biophys. J.* **70**, 932–938 (1996).
9. O. A. Sineshchekov, K. H. Jung, J. L. Spudich, *Proc. Natl. Acad. Sci. U.S.A.* **99**, 8689–8694 (2002).
10. F. Zhang et al., *Cell* **147**, 1446–1457 (2011).

11. E. S. Boyden, F. Zhang, E. Bamberg, G. Nagel, K. Deisseroth, *Nat. Neurosci.* **8**, 1263–1268 (2005).
12. T. Ishizuka, M. Kakuda, R. Araki, H. Yawo, *Neurosci. Res.* **54**, 85–94 (2006).
13. X. Li *et al.*, *Proc. Natl. Acad. Sci. U.S.A.* **102**, 17816–17821 (2005).
14. A. R. Adamantidis, F. Zhang, A. M. Aravanis, K. Deisseroth, L. de Lecea, *Nature* **450**, 420–424 (2007).
15. A. M. Aravanis *et al.*, *J. Neural Eng.* **4**, S143–S156 (2007).
16. A. Berndt, M. Prigge, D. Gradmann, P. Hegemann, *Biophys. J.* **98**, 753–761 (2010).
17. G. Nagel *et al.*, *Proc. Natl. Acad. Sci. U.S.A.* **100**, 13940–13945 (2003).
18. J. Mattis *et al.*, *Nat. Methods* **9**, 159–172 (2012).
19. S. Geibel *et al.*, *Biophys. J.* **81**, 2059–2068 (2001).
20. A. Seki *et al.*, *Biophys. J.* **92**, 2559–2569 (2007).
21. A. Berndt, O. Yizhar, L. A. Gunaydin, P. Hegemann, K. Deisseroth, *Nat. Neurosci.* **12**, 229–234 (2009).
22. C. Bamann, R. Gueta, S. Kleinlogel, G. Nagel, E. Bamberg, *Biochemistry* **49**, 267–278 (2010).
23. O. Yizhar *et al.*, *Nature* **477**, 171–178 (2011).
24. H. E. Kato *et al.*, *Nature* **482**, 369–374 (2012).
25. S. Kleinlogel *et al.*, *Nat. Neurosci.* **14**, 513–518 (2011).
26. D. B. Sauer, W. Zeng, S. Raghunathan, Y. Jiang, *Proc. Natl. Acad. Sci. U.S.A.* **108**, 16634–16639 (2011).
27. B. Roux, R. MacKinnon, *Science* **285**, 100–102 (1999).
28. G. Yellen, *Nature* **419**, 35–42 (2002).
29. M. Köhler *et al.*, *Science* **273**, 1709–1714 (1996).
30. C. M. Nimigean, J. S. Chappie, C. Miller, *Biochemistry* **42**, 9263–9268 (2003).
31. D. Bichet, M. Grabe, Y. N. Jan, L. Y. Jan, *Proc. Natl. Acad. Sci. U.S.A.* **103**, 14355–14360 (2006).
32. A. Berndt *et al.*, *Proc. Natl. Acad. Sci. U.S.A.* **108**, 7595–7600 (2011).
33. D. E. Clapham, C. Montell, G. Schultz, D. Julius; International Union of Pharmacology, *Pharmacol. Rev.* **55**, 591–596 (2003).
34. Single-letter abbreviations for the amino acid residues are as follows: A, Ala; C, Cys; D, Asp; E, Glu; F, Phe; G, Gly; H, His; I, Ile; K, Lys; L, Leu; M, Met; N, Asn; P, Pro; Q, Gln; R, Arg; S, Ser; T, Thr; V, Val; W, Trp; and Y, Tyr. In the mutants, other amino acids were substituted at certain locations; for example, E136R indicates that glutamic acid at position 136 was replaced by arginine.
35. Materials and methods are available as supplementary materials on *Science* Online.
36. H. Liske, X. Qian, P. Anikeeva, K. Deisseroth, S. Delp, *Sci. Rep.* **3**, 3110 (2013).
37. A. M. Herman, L. Huang, D. K. Murphey, I. Garcia, B. R. Arenkiel, *eLife* **3**, e01481 (2014).
38. Y. Andrews-Zwilling *et al.*, *PLOS ONE* **7**, e40555 (2012).
39. J. Y. Lin, P. M. Knutsen, A. Muller, D. Kleinfeld, R. Y. Tsien, *Nat. Neurosci.* **16**, 1499–1508 (2013).
40. R. Prakash *et al.*, *Nat. Methods* **9**, 1171–1179 (2012).
41. J. L. Galzi *et al.*, *Nature* **359**, 500–505 (1992).
42. M. J. Gunthorpe, S. C. Lummis, *J. Biol. Chem.* **276**, 10977–10983 (2001).
43. H. Yang *et al.*, *Cell* **151**, 111–122 (2012).

Neural Mechanisms of Object-Based Attention

Daniel Baldauf* and Robert Desimone

How we attend to objects and their features that cannot be separated by location is not understood. We presented two temporally and spatially overlapping streams of objects, faces versus houses, and used magnetoencephalography and functional magnetic resonance imaging to separate neuronal responses to attended and unattended objects. Attention to faces versus houses enhanced the sensory responses in the fusiform face area (FFA) and parahippocampal place area (PPA), respectively. The increases in sensory responses were accompanied by induced gamma synchrony between the inferior frontal junction, IFJ, and either FFA or PPA, depending on which object was attended. The IFJ appeared to be the driver of the synchrony, as gamma phases were advanced by 20 ms in IFJ compared to FFA or PPA. Thus, the IFJ may direct the flow of visual processing during object-based attention, at least in part through coupled oscillations with specialized areas such as FFA and PPA.

When covertly attending to a location in the periphery, visual processing is biased toward the attended location, and the sources of top-down signals include the frontal eye fields (FEF) (*1*, *2*) and parietal cortex (PC). FEF may modulate visual processing through a combination of firing rates and gamma frequency synchrony with visual cortex (*2*). For nonspatial attention, the mechanisms of top-down attention are much less clear. When people attend to a feature, such as a particular color (*3–5*), or to one of several objects at the same location (*6–8*), activity in the extrastriate areas representing properties of the attended object is enhanced. But where do the attentional biases (*9*) come from, and how do they enhance object processing when the distractors are not spatially separate?

We combined magnetoencephalography (MEG), supplemented by functional magnetic resonance imaging (fMRI) and diffusion tensor

imaging to optimize both spatial and temporal resolution. In the MEG experiment, two spatially overlapping streams of objects (faces and houses) were tagged at different presentation frequencies (1.5 and 2.0 Hz) (Fig. 1, A and B) (*5*, *10–12*). The stimuli went in and out of "phase coherence," so that they were modulated in visibility over time but did not change in luminance or flash on and off. When subjects were cued to attend to one of the streams and to detect occasional targets within the cued stream, frequency analyses allowed identifying brain regions that followed the stimulus oscillations.

Using MEG data only (*13*), the strongest activity evoked by the face tag was in the right fusiform gyrus, whereas the activity evoked by the house tag was more medially in the inferior-temporal cortex (IT) (Fig. 1C; figs. S1 and 2 for individual subjects and alternative source reconstruction approaches). These areas were roughly consistent with the locations of fusiform face area (FFA) and parahippocampal place area (PPA) determined previously in fMRI (*14–16*). To increase the accuracy of localization in each sub-

ject, we added high-resolution fMRI localizers for FFA and PPA (Fig. 2, B and D, and fig. S3A), which were focused at the expected spots (Fig. 2F).

To identify other areas important for non-spatial attention, we contrasted the brain state when attending to one of the two superimposed object classes with a similarly demanding state that did not require attending to either object class. The attention-related fMRI localizers revealed consistent activation in the inferior frontal junction (IFJ) at the intersection of the inferior-frontal and precentral sulcus (*17–19*) (Fig. 2, A, C, and E), with weaker and less-consistent signals in posterior-parietal and in inferior-temporal cortex (fig. S3C). A control experiment confirmed that IFJ's activation was indeed related to non-spatial attention, rather than simply memory (fig. S4).

Each subject's individual fMRI localizers were then used as regions of interest (ROIs) to guide the analysis of the MEG signals (see supplementary material for a description of the co-registration of fMRI and MEG). The modulation of sensory responses by attention in the tagging-frequency range is shown in Fig. 2G (fig. S5B for individual subjects). FFA and PPA had the strongest responses, with FFA more responsive to the attended face tag (*t* test, $P < 0.001$) and PPA more responsive to the attended house tag (*t* test, $P < 0.01$). Thus, object-specific attention modulates the sensory responses in FFA and PPA. Weaker sensory responses were found in region V1.

Although weaker in amplitude, sensory responses were also found in IFJ, and the attention effects were much stronger—there was a tagging frequency response only to the attended object (both *t* test, $P < 0.001$). Control regions in the FEF (localized in separate fMRI runs, fig. S3D), PC (localized in the attention-related fMRI experiment in some participants) and the frontal pole (anatomically defined) showed only minor and less consistent responses. The general pattern of

McGovern Institute for Brain Research, Massachusetts Institute of Technology, Cambridge, 02139 MA, USA.

*Corresponding author. E-mail: baldauf@mit.edu

results did not depend on the specific tagging frequency assignment to faces or houses (fig. S5).

In temporal cortex, both MEG and fMRI results showed a moderate tendency of lateralization: FFA to the right and PPA to the left hemisphere (Fig. 2H).

The attentional effects in IFJ were slightly lateralized to the right.

We used Fourier transformations to extract the phase relation between the frequency-tag response and the stimulus on the screen, i.e., the latency of the sensory responses (Fig. 2I). The phase lag of IFJ (corresponding to 208 ms) was shifted by about 25 ms in comparison to FFA and PPA (188 and 171 ms) (Fig. 2J and fig. S5) (20), which likely accounts for transmission time and synaptic delays between areas.
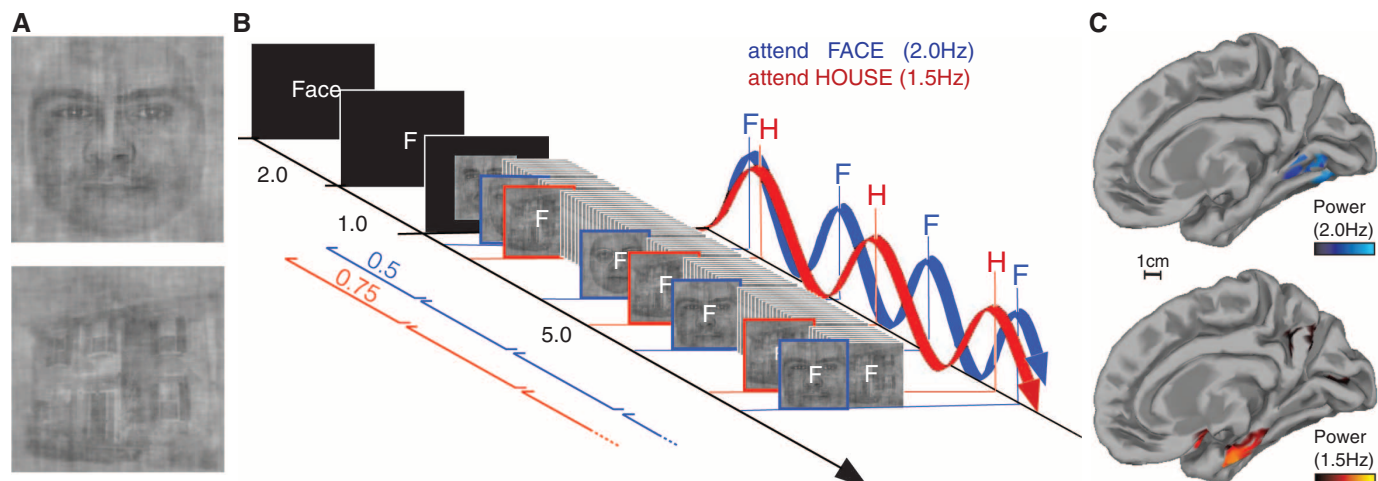
Fig. 1. Stimuli and attention. (**A**) Stimuli used in the MEG experiment (see online methods). (**B**) Sequence of stimuli consisting of an overlay of two streams of objects (faces and houses), fading in and out of a phase-scrambled noise mask at different frequencies (1.5 and 2.0 Hz). Subjects had to attend the cued stream and report occasional 1-back repeats. (**C**) Fourier-transform of the minimum norm estimate when attending to faces (2.0 Hz) or houses (1.5 Hz, $P < 0.05$, FDR-corrected).
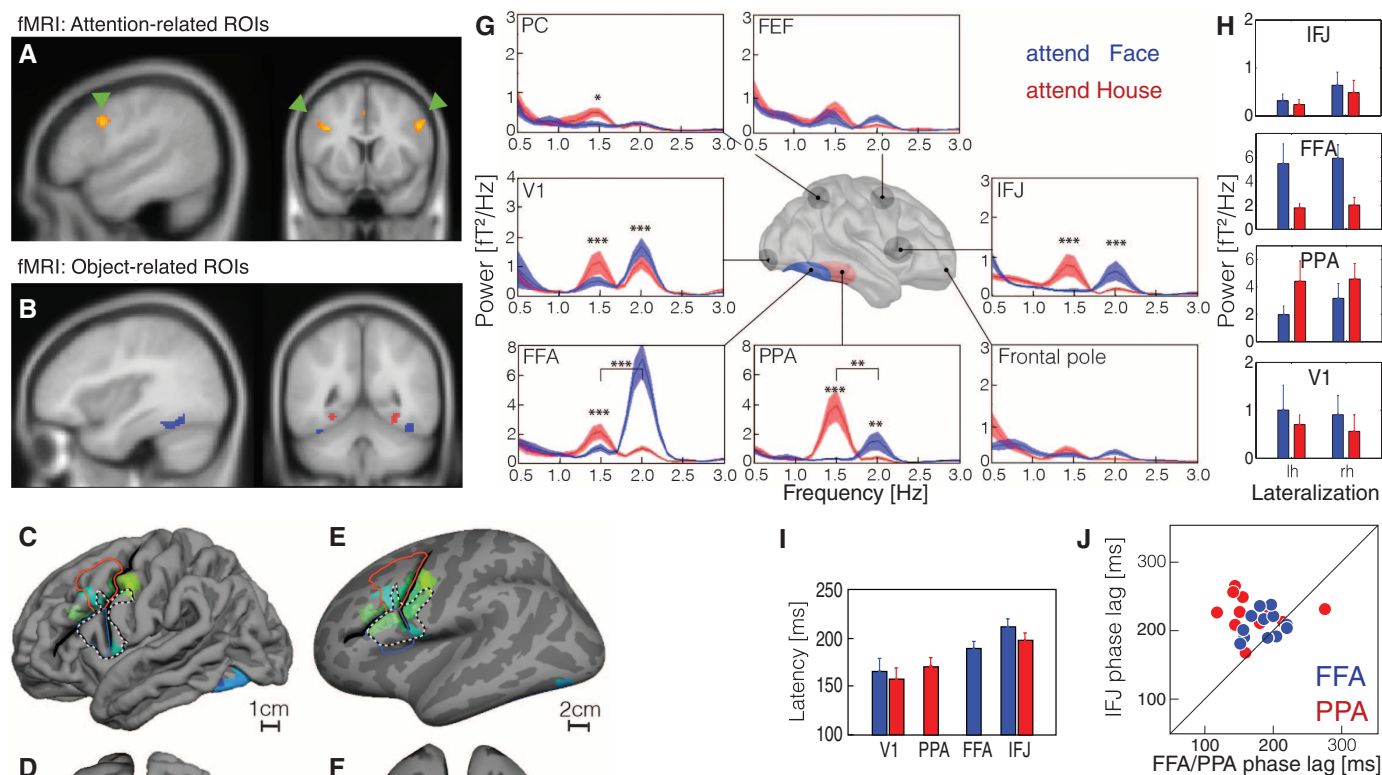
Fig. 2. Measures of attention localization. (**A**) Average of the fMRI localizers for attention-related and (**B**) object-related ROIs (blue: FFA, red: PPA, $P < 0.001$, FW error-corrected). (**C** and **D**) All subjects' individual ROIs superimposed on a standardized brain surface (red: middle frontal gyrus; blue: inferior frontal gyrus; dashed line: BA44) and (**E**) on an inflated brain. (**F**) Comparison of the average MEG-based (filled) and fMRI-based (outlines) localization of face- (blue) and house-related (red) activity. (**G**) Spectral power in the participants' individual ROIs when attending houses (1.5 Hz, red) or faces (2.0 Hz, blue). (**H**) Lateralization of the attentional effects. (**I**) Phase lags of the neural activity to the physical stimuli on screen. (**J**) Systematic phase advancement from FFA/PPA to IFJ.

To test for functional interactions among the areas, we analyzed coherence between the frontal and temporal ROIs (Fig. 3C) across a wide frequency spectrum, including frequency bands that were not time-locked to the stimuli (see time-frequency power spectra and an analysis of frequency nesting in fig. S6). The baseline-corrected coherence between IFJ-FFA (top) and IFJ-PPA (bottom) in the tagging-frequency range is shown in Fig. 3A. When attending into an area's preferred stimulus domain, that area became functionally connected with IFJ at the respective tagging frequency (both t test, $P < 0.001$), as responses in both areas were phase-locked to the attended stimulus but with different phase lags.

Coherence at frequencies higher than the tagging frequency was dominated by shared background coherence, as typical in MEG. To reduce the influence of background coherence, we analyzed patterns of domain-specific coherence by computing an attention index, the

AIC = (attend preferred – attend unpreferred)/
(attend preferred + attend unpreferred)

which directly contrasts both attentional conditions and, therefore, is more sensitive to subtle attentional effects on coherence (Fig. 3B). When attending to faces (top, blue) coherence between IFJ and FFA increased not only at the tagging frequency (2.0 Hz) but also in a high-frequency band (70 to 100 Hz, both t test, $P < 0.05$). Similarly, when attending to the house stimuli (red), IFJ and PPA exhibited increased coherence, both at the tagging frequency (1.5 Hz) and in a high-frequency band (60 to 90 Hz, both t test,

$P < 0.01$). In this high-frequency gamma range, the individual subjects varied considerably in their respective peak modulation frequency. As a check for whether the coherence in the gamma range resulted from common stimulus-locked onsets, we reran the analysis in a control data set, with shuffled trial order within each ROI (fig. S7C), which completely eliminated gamma coherence. Attentional modulations of coherence between IT and PC were weaker and nonsignificant (fig. S7D).

To test the directionality of the gamma-band coherence between IFJ and FFA/PPA, we analyzed the instantaneous phase lags between the two areas. Because portions of the signal in both sites are shared background coherence (due to electromagnetic field spread) or random noise, we first baseline-corrected the phase lag distributions to dissociate shared background coherence (which is simultaneous) and noise (which is uniformly distributed) from phase coherence that results from axonally transmitted synchronization (see supplementary methods and figs. S8 and S9). We then compared the residual phase lag distribution across a range of frequency bands around the subject's frequency of maximal coherence (peak ±10 Hz). In most subjects (9 out of 12), the baseline-corrected phase lags systematically increased as a function of frequency, consistent with IFJ leading FFA/PPA with a constant time lag of about 20 ms (SE = 6 ms) (Fig. 3D and figs. S10 and S11). The three other subjects seemed to have stronger bottom-up or balanced coherence (see supplementary materials).

To determine whether IFJ is anatomically connected with FFA or PPA, we computed maps of probabilistic connectivities (21) to the seed regions

in FFA and PPA. When normalizing to the site of maximal activity within frontal cortex, both FFA- and PPA-connectomes revealed areas around IFJ to have the highest connection probabilities (see Fig. 3E and fig. S12).

The neural mechanism that enables attention to an object or feature seems intuitively more complex than spatial attention, which may only require a spatial-biasing signal that targets a relevant location. Yet the present study reveals some striking parallels in neural mechanisms: Prefrontal cortex seems to be a common source of top-down biasing signals, with FEF supplying signals for spatial attention and IFJ supplying signals for object or feature attention. With spatial attention, cells in FEF and visual cortex begin to oscillate together in the gamma frequency range, with FEF the "driver" in these oscillations (2). Here, we find that IJF—although it has delayed sensory responses—is also the "driver" in coupled gamma oscillations with FFA/PPA. In primates, coherent gamma oscillations in FEF are phase-shifted by about 10 ms compared with oscillations in area V4, which has been argued to account for the axonal conductance time and synaptic delays between the two areas (2). With the phase shift, spikes of FEF cells presumably affect cells in V4 at a time of maximum depolarization, which increases their impact. Here, a phase shift of 25 ms may allow for longer transmission times from IFJ to FFA and PPA in humans. Thus, spikes originating from IFJ may arrive in FFA and PPA respectively, and vice versa, at a time of maximum depolarization in the receiving area, magnifying their impact. The directing of IFJ signals to the FFA versus PPA may not be inherently more
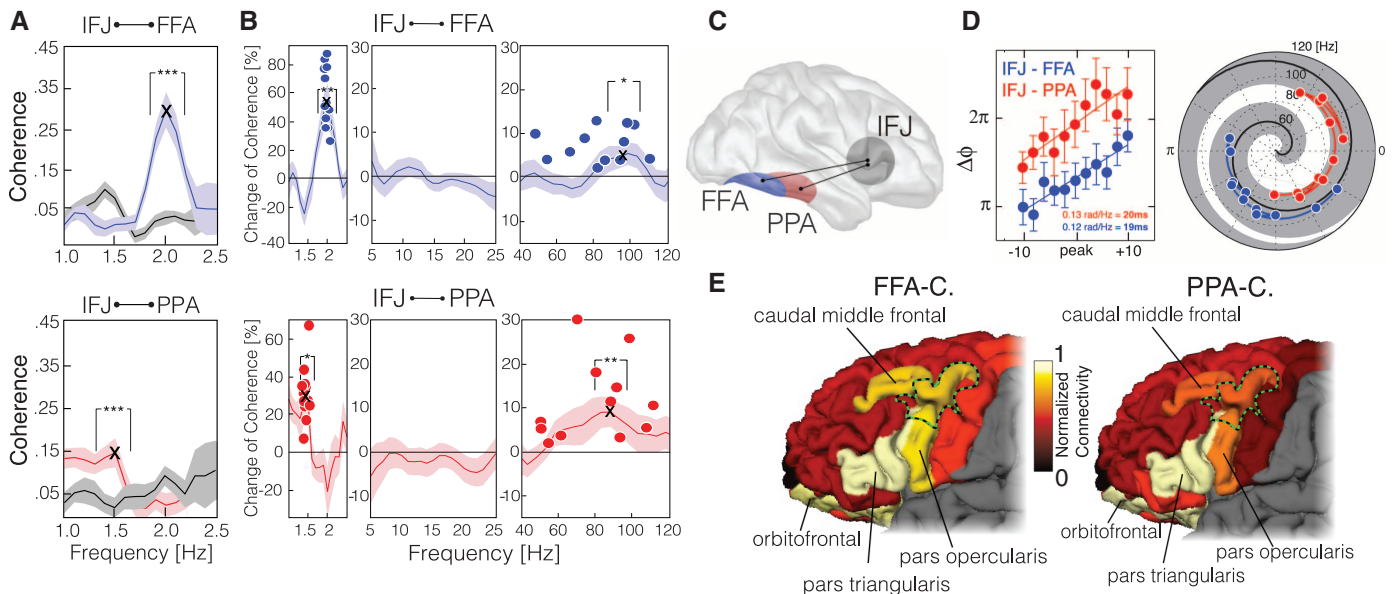
Fig. 3. Coherence measures of attention. (**A**) Cross-area coherence spectra. (**B**) Attention indices, converted into changes of coherence. When attending to the preferred stimulus (faces for FFA, houses for PPA), coherence between IFJ and the respective temporal area increased at the respective tagging frequency and in a high-frequency band (70 to 100 Hz). Dots represent subjects' peaks of attentional modulations. (**C**) Schematic of the fronto-temporal connectivity.

(**D**) Directionality measure of gamma phase-lags between IFJ and FFA/PPA in polar (right) and Cartesian (left) coordinates. In 9 of 12 subjects the phase-lag of FFA/PPA to IFJ increased linearly with increasing frequencies around the subject's peak of gamma coherence, consistent with IFJ cycles leading over FFA/PPA cycles. (**E**) Parcellation-based probability maps of frontal connectivity to FFA/PPA.

complex than shifting FEF signals between different locations in the visual field.

IFJ may include areas that function as general executive modules (22, 23). Also, IFJ is close to areas Ba45 and Ba46, homologs of which have been described in nonhuman primate recordings to encode information about object-categories in delayed match-to-sample tasks (23, 24). Indeed, the "attentional template" that specifies the relevant location or object in spatial or feature attention is hardly distinguishable from working memory for these qualities (9), which is known to involve prefrontal cortex (24). Coupled interactions between prefrontal areas and visual areas (25–31) could underlie many cognitive phenomena in vision, with shared neural mechanisms but variations in the site of origin and the site of termination.

References and Notes

1. T. Moore, K. M. Armstrong, *Nature* **421**, 370–373 (2003).
2. G. G. Gregoriou, S. J. Gotts, H. Zhou, R. Desimone, *Science* **324**, 1207–1210 (2009).
3. S. Treue, J. C. Martínez Trujillo, *Nature* **399**, 575–579 (1999).
4. J. T. Serences, G. M. Boynton, *Neuron* **55**, 301–312 (2007).
5. M. A. Schoenfeld, J.-M. Hopf, C. Merkel, H.-J. Heinze, S. A. Hillyard, *Nat. Neurosci.* **17**, 619–624 (2014).
6. K. M. O'Craven, P. E. Downing, N. Kanwisher, *Nature* **401**, 584–587 (1999).
7. J. Duncan, *J. Exp. Psychol. Gen.* **113**, 501–517 (1984).
8. V. M. Ciaramitaro, J. F. Mitchell, G. R. Stoner, J. H. Reynolds, G. M. Boynton, *J. Neurophysiol.* **105**, 1258–1265 (2011).
9. R. Desimone, J. Duncan, *Annu. Rev. Neurosci.* **18**, 193–222 (1995).
10. R. Hari, M. Hämäläinen, S.-L. Joutsiniemi, *J. Acoust. Soc. Am.* **86**, 1033–1039 (1989).
11. P. Lakatos, G. Karmos, A. D. Mehta, I. Ulbert, C. E. Schroeder, *Science* **320**, 110–113 (2008).
12. L. Parkkonen, J. Andersson, M. Hämäläinen, R. Hari, *Proc. Natl. Acad. Sci. U.S.A.* **105**, 20500–20504 (2008).
13. M. S. Hämäläinen, R. J. Ilmoniemi, *Med. Biol. Eng. Comput.* **32**, 35–42 (1994).
14. N. Kanwisher, J. McDermott, M. M. Chun, *J. Neurosci.* **17**, 4302–4311 (1997).
15. D. Y. Tsao, S. Moeller, W. A. Freiwald, *Proc. Natl. Acad. Sci. U.S.A.* **105**, 19514–19519 (2008).
16. R. Epstein, N. Kanwisher, *Nature* **392**, 598–601 (1998).
17. M. Brass, J. Derrfuss, B. Forstmann, D. Y. von Cramon, *Trends Cogn. Sci.* **9**, 314–316 (2005).
18. T. P. Zanto, M. T. Rubens, A. Thangavel, A. Gazzaley, *Nat. Neurosci.* **14**, 656–661 (2011).
19. A. Gazzaley, A. C. Nobre, *Trends Cogn. Sci.* **16**, 129–135 (2012).
20. J. Liu, A. Harris, N. Kanwisher, *Nat. Neurosci.* **5**, 910–916 (2002).
21. Z. M. Saygin et al., *Nat. Neurosci.* **15**, 321–327 (2011).
22. J. Duncan, *Trends Cogn. Sci.* **14**, 172–179 (2010).
23. E. Fedorenko, J. Duncan, N. Kanwisher, *Curr. Biol.* **22**, 2059–2062 (2012).
24. G. Rainer, W. F. Asaad, E. K. Miller, *Nature* **393**, 577–579 (1998).
25. F. Barceló, S. Suwazono, R. T. Knight, *Nat. Neurosci.* **3**, 399–403 (2000).
26. P. Fries, *Trends Cogn. Sci.* **9**, 474–480 (2005).
27. O. Jensen, J. Kaiser, J.-P. Lachaux, *Trends Neurosci.* **30**, 317–324 (2007).
28. A. K. Engel, P. Fries, W. Singer, *Nat. Rev. Neurosci.* **2**, 704–716 (2001).
29. T. Womelsdorf et al., *Science* **316**, 1609–1612 (2007).
30. M. Siegel, T. H. Donner, R. Oostenveld, P. Fries, A. K. Engel, *Neuron* **60**, 709–719 (2008).
31. R. T. Canolty et al., *Science* **313**, 1626–1628 (2006).

A Chloroplast Retrograde Signal Regulates Nuclear Alternative Splicing

Ezequiel Petrillo,[1]* Micaela A. Godoy Herz,[1] Armin Fuchs,[2] Dominik Reifer,[2] John Fuller,[3] Marcelo J. Yanovsky,[4] Craig Simpson,[3] John W. S. Brown,[3,5] Andrea Barta,[2] Maria Kalyna,[2]† Alberto R. Kornblihtt[1]‡

Light is a source of energy and also a regulator of plant physiological adaptations. We show here that light/dark conditions affect alternative splicing of a subset of *Arabidopsis* genes preferentially encoding proteins involved in RNA processing. The effect requires functional chloroplasts and is also observed in roots when the communication with the photosynthetic tissues is not interrupted, suggesting that a signaling molecule travels through the plant. Using photosynthetic electron transfer inhibitors with different mechanisms of action, we deduce that the reduced pool of plastoquinones initiates a chloroplast retrograde signaling that regulates nuclear alternative splicing and is necessary for proper plant responses to varying light conditions.

Light regulates about 20% of the transcriptome in *Arabidopsis thaliana* and rice (1, 2). Alternative splicing has been shown to modulate gene expression during plant development and in response to environmental cues (3). We observed that the alternative splicing of *At-RS31* (Fig. 1A), encoding a Ser-Arg–rich splicing factor (4), changed in different light regimes, which led us to investigate how light regulates alternative splicing in plants.

Seedlings were grown for a week in constant white light to minimize interference from the circadian clock and then transferred to light or dark conditions for different times (see the supplementary materials). We observed a two- and fourfold increase in the splicing index (SI)—defined as the abundance of the longest splicing isoform relative to the levels of all possible isoforms—of *At-RS31* [mRNA3/(mRNA1 + mRNA2 + mRNA3)] after 24 and 48 hours in the dark, respectively (Fig. 1B). This effect was rapidly reversed when seedlings were placed back in light, with total recovery of the original SI in about 3 hours (Fig.

1C), indicating that the kinetics of the splicing response is slower from light to dark than from dark to light.

The light effect is gene specific (fig. S1) and is also observed in diurnal cycles under short-day conditions (Fig. 1D and fig. S2). Furthermore, three circadian clock mutants behaved like the wild type (WT) in the response of *At-RS31* alternative splicing to light/dark (fig. S3). Changes in *At-RS31* splicing are proportional to light intensity both under constant light and in short-day–grown seedlings (fig. S4).

Both red (660 nm) and blue (470 nm) lights produced similar results as white light (Fig. 1E). Moreover, *At-RS31* alternative splicing responses to light/dark are not affected in phytochrome and cryptochrome signaling mutants (5, 6), ruling out photosensory pathways in this light regulation (Fig. 1F and figs. S5 and S6).

Light-triggered changes in *At-RS31* mRNA patterns are not due to differential mRNA degradation. First, the light effect is not observed in the presence of the transcription inhibitor actinomycin D (Fig. 1G). Second, the effects are still observed in *upf* mutants, defective in the nonsense-mediated mRNA decay (NMD) pathway (7) (Fig. 1H and fig. S7). Third, overexpression of the constitutive splicing factor U2AF[65] (8) in *Arabidopsis* protoplasts mimics the effects of light on *At-RS31* alternative splicing (Fig. 1I).

mRNA1 is the only isoform encoding a full-length At-RS31 protein (9). *mRNA3* and *mRNA2* are almost fully retained in the nucleus (fig. S8). *mRNA1* levels decrease considerably in dark without significant changes in the total amount of *At-RS31* transcripts (Fig. 2A and fig. S9), which suggests that alternative splicing is instrumental

[1]Laboratorio de Fisiología y Biología Molecular, Departamento de Fisiología, Biología Molecular y Celular, IFIBYNE-CONICET, Facultad de Ciencias Exactas y Naturales, Universidad de Buenos Aires, Ciudad Universitaria, Pabellón 2, C1428EHA Buenos Aires, Argentina. [2]Max F. Perutz Laboratories, Medical University of Vienna, A-1030 Vienna, Austria. [3]Cell and Molecular Sciences, The James Hutton Institute, Invergowrie, Dundee, Scotland. [4]Fundación Instituto Leloir, IIBBA-CONICET, C1405BWE Buenos Aires, Argentina. [5]Division of Plant Sciences, University of Dundee at The James Hutton Institute, Invergowrie, Dundee, Scotland.

*Present address: Max F. Perutz Laboratories, Medical University of Vienna, A-1030 Vienna, Austria.
†Present address: Department of Applied Genetics and Cell Biology, BOKU, University of Natural Resources and Life Sciences, Muthgasse 18, A-1190 Vienna, Austria.
‡Corresponding author. E-mail: ark@fbmc.fcen.uba.ar

in the control of *mRNA1* cellular levels and, consequently, At-RS31 protein abundance. To assess how interference with *At-RS31* alternative splicing regulation could affect *Arabidopsis* phenotype, we obtained transgenic plants overexpressing either a cDNA (mRNA1ox) or a genomic version (31 genOX) of *At-RS31* and a knock-out (31 mut) line (fig. S10). *At-RS31* total mRNA is more abundant in the mRNA1ox and 31 genOX lines compared with the WT (fig. S10). Whereas the mRNA1ox line expresses almost exclusively the *mRNA1* isoform and at higher levels than the other lines, the 31 genOX line is mostly enriched in *mRNA3* and *mRNA2* isoforms, and *mRNA1* levels are not much higher than those in WT seedlings (Fig. 2, B and C, and fig. S10). Under photoperiodic conditions (16 and 8 hours of light and dark, respectively) no major phenotypes are observed for these lines (Fig. 2D, "L" in Fig. 2E, and fig. S11). However, when plants are either exposed to long darkness (3 days) (Fig. 2E), or grown under

constant low light intensity (50 µmol m^{-2} s^{-1}) (Fig. 2F), the mRNA1ox line shows a dramatic phenotype, characterized by small and yellowish seedlings concomitantly with faster degradation of chlorophylls a and b (fig. S12). This suggests that down-regulation of *mRNA1* in the dark through alternative splicing is important for proper growth of the plant in response to changing environmental light conditions.

As sensory photoreceptors do not participate, we investigated whether retrograde signals from the chloroplast were involved (1). Increasing concentrations of DCMU [3-(3,4-dichlophenyl)1,1-dimethylurea] (10), a drug that blocks the electron transfer from photosystem II (PSII) to the plastoquinone (PQ) pool, inhibited the effect of light on *At-RS31* alternative splicing (Fig. 3A), confirming chloroplast involvement. Roots have no chloroplasts, so the light effect should only be observed in the green tissue in dissected seedlings (Fig. 3B). However, the effect was observed

both in dissected leaves and roots, with roots showing a time delay in the response (Fig. 3, D and F). When shoots were separated from roots before the light/dark treatment (Fig. 3C), dissected shoots retained the response (Fig. 3E), but light had no effect on *At-RS31* splicing in detached roots (Fig. 3G). Similar results were obtained by covering the different parts of the seedlings (fig. S13). No chlorophyll was detected in the roots of pre- or post-dissected plants (fig. S14), strengthening the hypothesis that a mobile signal generated in the leaves triggers root alternative splicing responses to light.

About 39% of the 93 alternative splicing events (table S1) tested using a high-resolution reverse transcriptase polymerase chain reaction (RT-PCR) panel (11) changed significantly in response to light (tables S2 to S4 and fig. S15). The effects of light were not due to sugar starvation during darkness (fig. S15), indicating that the chloroplast role in this light signaling pathway is not primarily

Fig. 1. Effects of light/dark transitions on *At-RS31* alternative splicing. (**A**) *At-RS31* splicing event. *PTC, premature termination codon; triangles, primers for splicing evaluation (see also fig. S10a). (**B**) *Arabidopsis thaliana* seedlings were incubated in light/dark for different times (see the supplementary materials). (**C**) After 48 hours of darkness, transferring the seedlings to light causes a rapid change in the SI of *At-RS31* to "light values" (see the supplementary materials). Light+Light, 48 hours + 3 hours light; Dark+Dark, 48 hours + 3 hours dark; Dark+Light, 48 hours dark + 3 hours light. (**D**) Seedlings were grown for 2 weeks under short-day conditions (~100 µmol m^{-2} s^{-1}). Samples were collected 2 hours before lights off [6 hours Zeitgeber time (zt)] and 2 hours before lights on (22 hours zt). (**E**) Plants were grown in constant light, transferred to dark for 48 hours, and then treated in light/dark for 6 hours with light-emitting diodes to provide specific wavelengths (see the supplementary materials). (**F**) *hyh* and *hy5* mutants for integrators of photoreceptor-signaling pathways show the same *At-RS31* alternative splicing regulation by light as WT plants. WS, *Wassilewskija* ecotype. (**G**) Actinomycin D (ActD) causes the loss of the light/dark transition effect. ActD (+) was added 2 hours before light/dark treatments. Dimethyl sulfoxide, control (–). (**H**) SI change induced by the light/dark transition is preserved in the NMD-impaired mutants *upf1-5* and *upf3-1*. (**I**) Effect of U2AF^{65} overexpression in *A. thaliana* protoplasts. In all experiments: white bars, light; black bars, darkness. Data represent means ± SD ($n \geq 3$); significant *P* values (Student's *t* test) are shown.
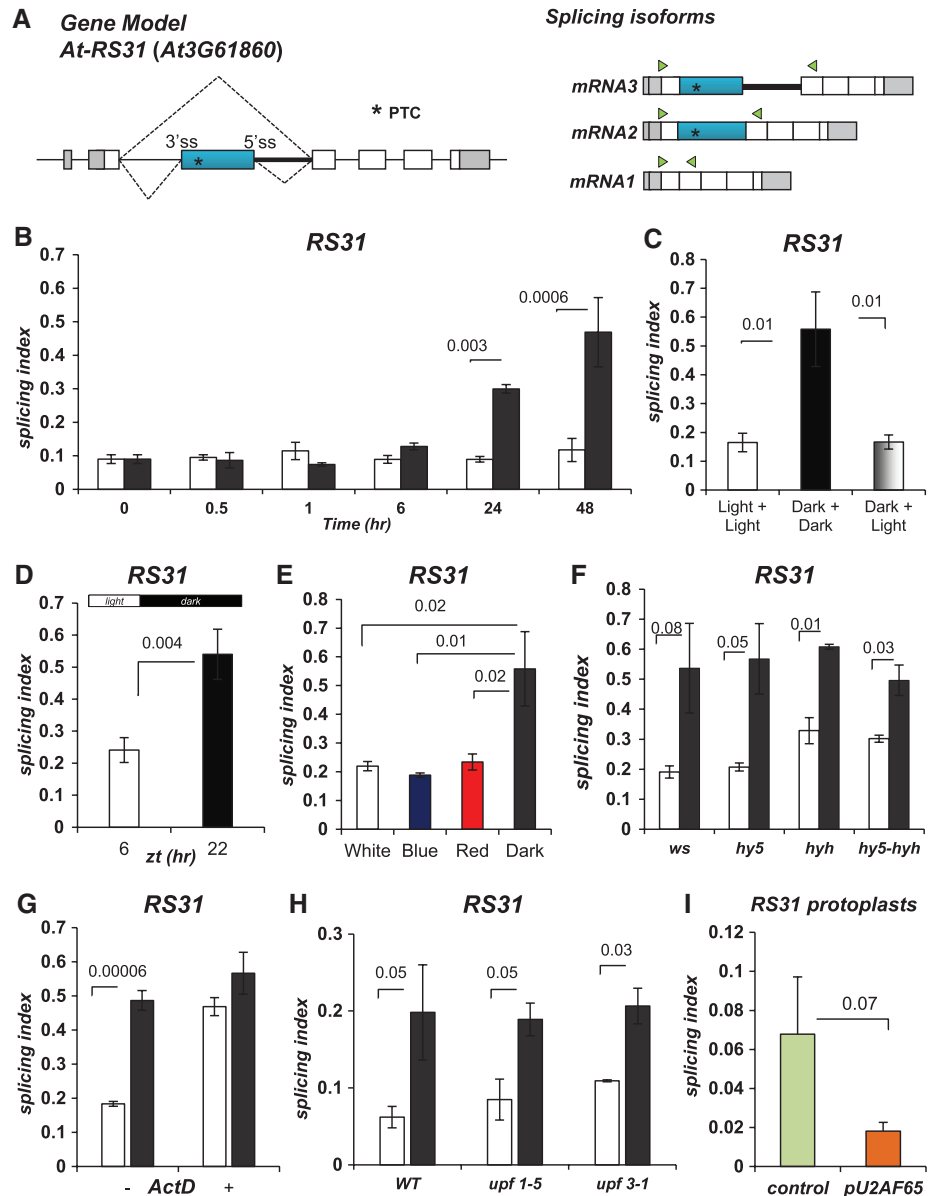
Fig. 2. *At-RS31* alternative splicing regulation is important for proper adjustment to light changes. (**A**) Quantitative RT-PCR analysis of *At-RS31 mRNA1* levels relative to *Actin*. The graph shows the relative expression of *mRNA1* in two different time points of light/dark treatment (2 and 4 hours). (**B**) Quantitative RT-PCR analysis of *At-RS31 mRNA1* isoform expression in the different genotypes and treatments. (**C**) (Top) *At-RS31* SI in the different genotypes in response to light/dark (see the supplementary materials). (Bottom) Representative gel images for the alternative splicing pattern of *At-RS31* in the different genotypes in response to light/dark transitions. *Actin*, as control. L, light; D, dark. (**D**) All lines were grown on Murashige and Skoog medium (MS) agar plates with 1% sucrose for 1 week in light/dark cycles (16/8 hours), 120 µmol m^{-2}s^{-1} white light. Similar size sections of plates are shown. (**E**) Seedlings of the different genotypes were grown under a 16/8 hours light/dark regime for 2 weeks and then transferred to dark for 3 days (D) or kept in photoperiod as controls (L). (**F**) Seedlings for each genotype were grown on MS plates in constant light conditions (~50 µmol m^{-2}s^{-1}). Similar size sections of plates are shown. Bar color code and statistics as in Fig. 1.
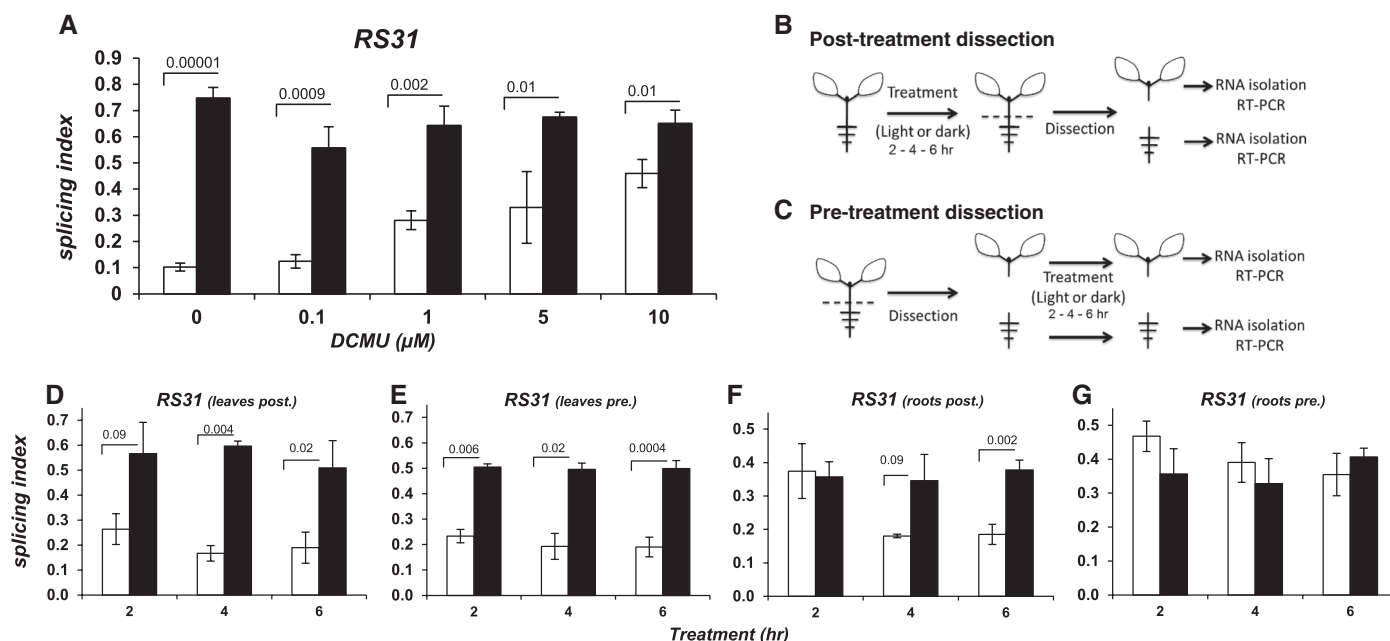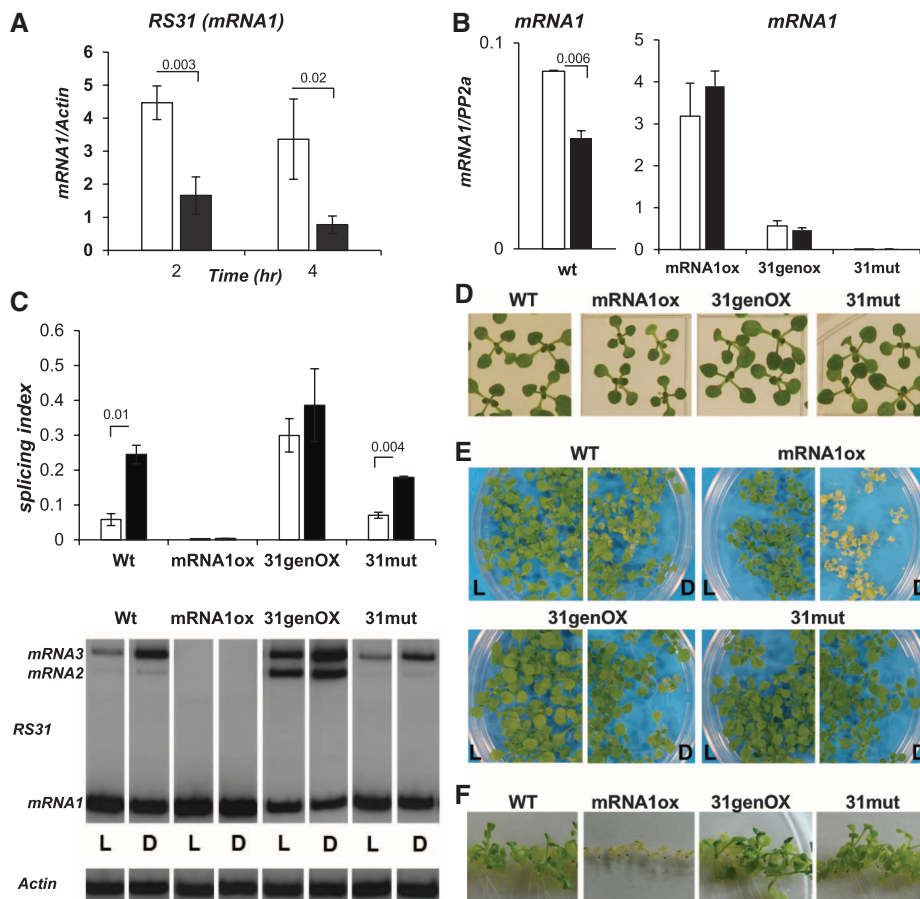
Fig. 3. The light signal is generated in the photosynthetic tissue and travels through the plant. (**A**) Seedlings were grown in constant light, transferred to darkness for 48 hours, and then treated with DCMU during a 6-hour light/dark further incubation. (**B** to **G**) Light regulation of *At-RS31* alternative splicing in green tissues and roots after a 2-, 4-, or 6-hour light/dark exposure of whole seedlings [(B), (D), and (F)] or in the isolated parts exposed separately to light or dark [(C), (E), and (G)]. [(B) and (C)] Schemes for post- and pre-exposure dissections (see the supplementary materials). [(D) and (F)] *At-RS31* alternative splicing assessment in green tissue (D) or in the roots (F) of light/dark treatments performed using intact seedlings (dissection performed after light/dark treatment). [(E) and (G)] *At-RS31* alternative splicing assessment in response to light/dark treatments using predissected (E) green tissue or (G) roots (dissection performed before light/dark treatment). Bar color code and statistics as in Fig. 1.
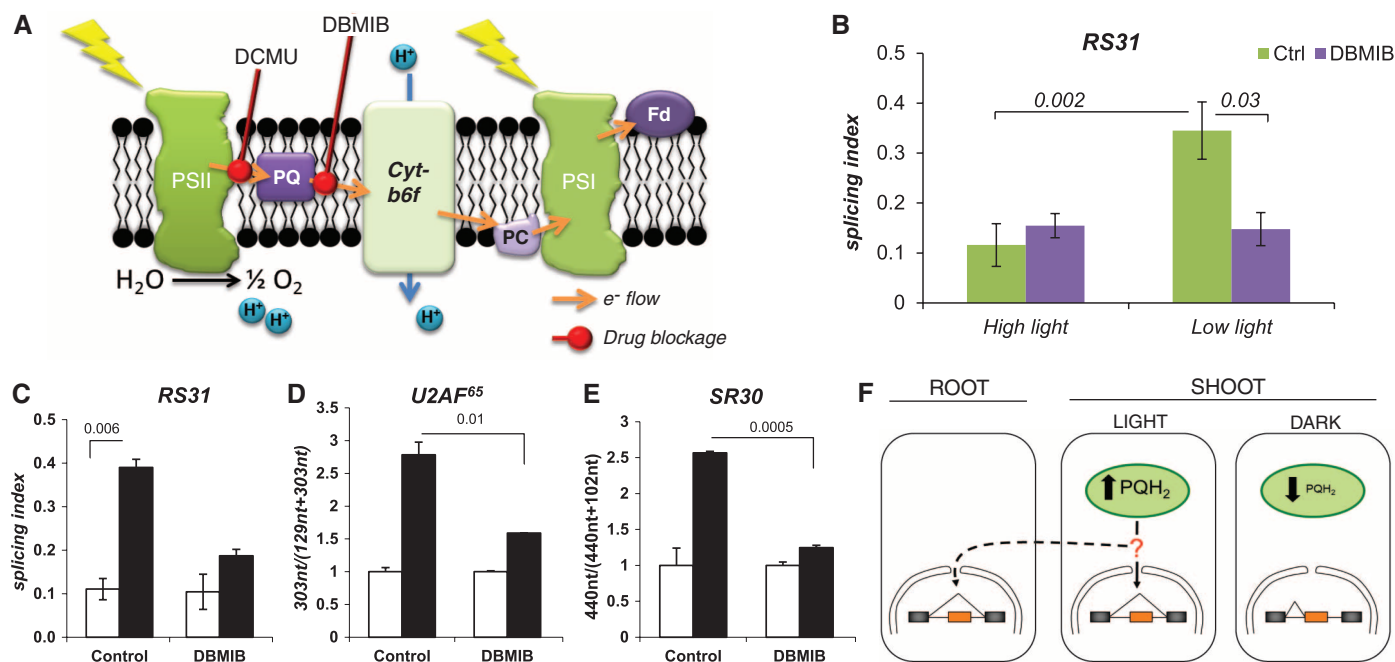
Fig. 4. The plastoquinone redox state mediates alternative splicing regulation by light. (**A**) Diagram showing the action of DBMIB and DCMU in the photosynthetic electron transport chain. (**B**) Effects of the addition of 30 μM DBMIB to seedlings under medium (80 μmol m^{-2} s^{-1}) and low (15 μmol m^{-2} s^{-1}) light on *At-RS31* alternative splicing. (**C** to **E**) Addition of 30 μM DBMIB reduces the effects of light/dark transitions on *At-RS31* (C), *At-U2AF^{65}* (D), and *At-SR30* (E) alternative splicing patterns. (**F**) Model for the light regulation of alternative splicing. Light-induced reduction of plastoquinone to plastoquinol (PQH$_2$) generates a signal that modulates alternative splicing in the nucleus. This signal, or a derived one, travels to the roots and provokes similar effects. Bar color code and statistics as in Fig. 1.

associated with the energy state of the cells (fig. S16a). In addition, we ruled out the participation of sugar-sensing pathways (fig. S16, b and c) reported to control nuclear gene expression (*12*, *13*).

Analysis of light-responsive splicing events revealed an enrichment in those of RNA-binding and processing protein coding genes (fig. S17 and table S3). The SR protein genes *At-SR30* and *At-U2AF^{65}* showed the biggest changes (fig. S18 and table S2), and DCMU treatment also confirmed a role for chloroplast involvement in their responses (fig. S19).

Experiments shown in figs. S20 and S21 revealed that plastid gene expression, the tetrapyrrole pathway, and reactive oxygen species (*14*) are not involved in *At-RS31* alternative splicing regulation. Because methyl viologen takes electrons from PSI (*15*) with no effect on *At-RS31* alternative splicing (fig. S21a), we inferred that the signal must be generated between PSII and PSI. To prove this, we used DBMIB (2,5-dibromo-3-methyl-6-isopropyl-p-benzoquinone). Both DCMU and DBMIB inhibit the overall electron transport chain, but whereas DCMU increases the oxidized PQ pool by blocking the electron transfer from PSII to PQ (*10*), DBMIB keeps the PQ pool reduced by preventing the electron transfer to cytochrome b6/f (*15*) (Fig. 4A). Addition of DBMIB potentiates the decrease in *At-RS31* SI when seedlings are exposed to low light in comparison to the lack of effect under high light (Fig. 4B). It was shown that when externally added in the dark, DBMIB can act as a reduced quinone ana-

log (*16*, *17*). Consistently, DBMIB decreases *At-RS31* SI in the dark, mimicking the effects of light (Fig. 4C). Similar results were obtained for *At-U2AF^{65}* and *At-SR30* (Figs. 4, D and E).

Our results reveal a retrograde pathway linking the photosynthetic redox state to the regulation of nuclear alternative splicing, mediated by the PQ pool, together with a signaling molecule, of yet unknown nature, that is able to travel through the plant to affect alternative splicing (Fig. 4F).

References and Notes

1. M. E. Ruckle, L. D. Burgoon, L. A. Lawrence, C. A. Sinkler, R. M. Larkin, *Plant Physiol.* **159**, 366–390 (2012).
2. P. Gyula, E. Schäfer, F. Nagy, *Curr. Opin. Plant Biol.* **6**, 446–452 (2003).
3. N. H. Syed, M. Kalyna, Y. Marquez, A. Barta, J. W. Brown, *Trends Plant Sci.* **17**, 616–623 (2012).
4. S. Lopato, E. Waigmann, A. Barta, *Plant Cell* **8**, 2255–2264 (1996).
5. J. J. Casal, M. J. Yanovsky, *Int. J. Dev. Biol.* **49**, 501–511 (2005).
6. R. Sellaro, U. Hoecker, M. Yanovsky, J. Chory, J. J. Casal, *Curr. Biol.* **19**, 1216–1220 (2009).
7. S. H. Kim *et al.*, *Plant Cell* **21**, 2045–2057 (2009).
8. C. Domon, Z. J. Lorković, J. Valcárcel, W. Filipowicz, *J. Biol. Chem.* **273**, 34603–34610 (1998).
9. M. Kalyna, S. Lopato, V. Voronin, A. Barta, *Nucleic Acids Res.* **34**, 4395–4405 (2006).
10. A. Khandwal, T. Elvitigala, B. Ghosh, R. S. Quatrano, *Plant Physiol.* **148**, 2050–2058 (2008).
11. C. G. Simpson *et al.*, *Plant J.* **53**, 1035–1048 (2008).
12. P. P. Dijkwel, C. Huijser, P. J. Weisbeek, N. H. Chua, S. C. Smeekens, *Plant Cell* **9**, 583–595 (1997).
13. J. Hanson, S. Smeekens, *Curr. Opin. Plant Biol.* **12**, 562–567 (2009).
14. S. Koussevitzky *et al.*, *Science* **316**, 715–719 (2007).
15. G. Schansker, S. Z. Tóth, R. J. Strasser, *Biochim. Biophys. Acta* **1706**, 250–261 (2005).
16. G. Finazzi, F. Zito, R. P. Barbagallo, F. A. Wollman, *J. Biol. Chem.* **276**, 9770–9774 (2001).
17. T. D. Elich, M. Edelman, A. K. Mattoo, *EMBO J.* **12**, 4857–4862 (1993).

Supplementary Materials

Always had a global view?

MAKE GREAT THINGS HAPPEN

Opportunities for research scientists and professionals: Are you interested in exploring, researching, developing new ideas? Welcome to EMD. When it comes to innovations we are way out front. The spectrum of our pioneering research extends from specialist therapeutic areas, to analysis of microorganisms, all the way to liquid crystals for LCDs. We offer excellent development perspectives and challenging research projects in a team-oriented environment for committed and highly qualified experts. Join us and take part in shaping our diversified global business. Ready to tread new paths?

Merck KGaA, Darmstadt, Germany – with more than 300 years of progress and about 38,000 employees in over 60 countries, we are leading in chemicals and pharma.
Our subsidiaries in Canada and the United States operate under the umbrella brand EMD. With passion, dedication and innovative ideas, we pursue one global goal: to improve people's quality of life.
Like to join in? Welcome to the team!

come2emd.com

EMD

A Comprehensive Evaluation System for the Application and Promotion of Chinese Medical Devices

Jing Wang, Xiaodong Wu, Yuguo Tang*, Yile Wang, and Xiaoman Xing
Chinese Academy of Sciences Suzhou Institute of Biomedical Engineering and Technology, Suzhou, China
*Corresponding author: tangyg@sibet.ac.cn

ABSTRACT

Medical equipment not only plays a key role in a robust national health care system, but also forms one of the two industrial pillars in modern medicine, the other being therapeutics. In today's world, the development of medical devices has become an important measure of national scientific/technological progress and economic modernization.

China's medical device industry started small, but has grown rapidly. Yet neither its production capacity nor its research and development ability can match the market demand. The Chinese government believes that the development of the medical device industry has an important role to play in promoting social development. In an effort to improve the policy environment and support this industry, in 2011 the "Domestic Medical Device Product Application Demonstration and Evaluation Project" was created. Suzhou City, due to its unique geographical and industrial characteristics, was chosen as the site to launch this project.

This article focuses on the establishment of a scientific information management and evaluation system as part of the abovementioned project, which will provide a mechanism to ensure the long-term quality and stability of the medical device industry in China. A total of 180 companies have been enrolled to date, making over 1,000 different devices. Also in the system are 17 large medical institutions in Suzhou City that act as evaluation sites. Thus far, the medical products that have been through the evaluation process represent a total value of 60.6 million yuan (US$9.7 million), while the applications described herein promise to benefit over 400 million people.

INTRODUCTION

Reviewing data collected since the 1980s, developed countries show a 1:1 ratio when comparing output from the pharmaceutical industry with the medical equipment sector (*1*). The United States is the industry leader in medical devices, with sales accounting for over 36% of the global market, followed by Western Europe (30%) and Japan (11%) (*2*). The total sales from the global medical device market have risen from US$187 billion in 2001 to US$355.3 billion in 2009, representing a compound annual growth rate over this period of 8.35%. In 2013, global sales totaled US$400 billion (*3*). The Chinese medical device industry has developed rapidly, particularly in the last two decades, with the industrial output rising from 59.2 billion yuan (US$9.5 billion) in 2007 to 140 billion yuan (US$22.5 billion) in 2011, representing an average annual growth of 24%. Output in 2013 exceeded 200 billion yuan (US$32.1 billion). But the delayed inception of the medical device industry in China resulted in the uneven development of this sector. This has created inflated health care costs and insufficient access to state-of-the-art medical equipment and the latest treatments, especially in rural locations. According to statistics from the Chinese Medical Association, 35% of patients nationwide go directly to large hospitals, while only 7% choose urban community medical rehabilitation centers. Citizens distrust older, cheaper technologies, while new equipment resources in the few larger hospitals that can afford them are very limited. China is therefore faced with the challenge of improving the quality and availability of medical devices in underserved areas in order to create a balanced and equitable health care system. To this end, the government is improving the policy environment for the health care industry, guiding a more objective allocation of health care resources, and supporting industrial development in the medical device sector. In late 2011, through two ministries (the Ministry of Health and the Ministry of Science and Technology) a demand-oriented, innovation-driven, and collaboration-based project was initiated called the "Domestic Medical Device Product Application Demonstration and Evaluation Project." Jiangsu province, one of the 10 evaluation sites, was first to launch this project in the city of Suzhou.

RESEARCH METHODOLOGY AND FINDINGS

Studies to test and validate medical devices require the involvement of scientific research institutes, medical institutions, government administration bureaus, and medical device companies as well as patients. The purpose of such testing is to enhance the quality of domestic medical devices and further their industrialization, to eventually improve health care overall. Below, we discuss the establishment of long-term supply and service mechanisms in parallel with the industrial development of medical devices in China as well as a scientific information management and evaluation system to support device testing.

Project Implementation

To ensure that the desired objectives are achieved, various teams have been put in place to aid the implementation of the Domestic Medical Device Product Application Demonstration and Evaluation Project. A project leadership team—composed of representatives from research institutes, local governments, and health care institutes—is responsible for the supervision, guidance, and direction of the testing as well as addressing any problems that might arise. The leadership team oversees the project execution team (composed mainly of staff from those institutions participating in the project), which is responsible for selection of medical institutions and representatives from participating companies, as well as overall organization and coordination. Finally, the expert evaluation team, also working under the leadership team, provides independent evaluation and feedback based on the information collected from the companies and medical institutions involved, from the actual testing of the devices, and also from patient feedback.

The main steps in the evaluation process are as follows (also see Fig. 1):

1. *Products and institution participation.* The project execution group reviews medical institutions and companies, and selects those products deemed most needed by the medical institutions; companies/institutions are then invited to join the project

2. *Evaluation process.* Selected companies provide specific medical devices to corresponding hospitals for evaluation. The evaluation team collects feedback from doctors, patients, and scientific experts following the evaluation period, which is then provided to the medical device companies in order to improve and upgrade their devices. The research institutes provide scientific and technological support for the companies during the upgrade process, while the enhanced research platforms and market information generated through this process aid the research institutes in exploring new ideas and applications. Concurrently, the medical institutions provide clinical information and testing facilities for the companies and offer essential practical information to enhance the product improvement process. By making domestic medical devices available to medical institutions, particularly those lacking up-to-date facilities, health care costs can be reduced and consensus can be built regarding standards of technical support and personnel training needed for proper application of the devices. Through this process, the research and medical institutions as well as the medical device companies can generate a strong cooperative

relationship, supporting each other and generating a positive outcome for all.

3. *Evaluation results.* Through the process of constant evaluation and iterative improvement, it is hoped that domestically produced medical devices will reach a level of quality that is recognized and accepted by the global device market. Concomitantly, the research and development ability of research institutes as well as the overall vitality of domestic medical device industry will improve, resulting in a strengthening of the treatment programs at medical institutions and the training of larger numbers of medical personnel needed to run, support, and maintain the medical devices in use. This will create a virtuous cycle of medical device research and development, application, and promotion.

Information Management System

In order to improved efficiency and ease of management for the evaluation of medical devices in China, an information management system was established. The names and details of all companies, medical institutions, and experts have been entered into a database system for easy access and searching.

As part of the evaluation workflow, the project execution team uploads information on those medical devices selected for evaluation into the system database; medical institutions and enterprises already in the system can then be paired with device companies and a cooperative relationship established through the signing of a contract (outside of this system). Following the evaluation period, product feedback is uploaded and the final report submitted to the relevant enterprises in a secure, easy-to-use, and closed-loop management system (Fig. 2).

Presently, 52 devices have been allocated to large, national hospitals for evaluation, while 108 are being used in smaller, regional hospitals, and 91 are being tested in community health centers. Over 250 more devices are ready and waiting to enter the evaluation process. One example of a product currently under evaluation is a remote, real-time heart monitoring and health management system from the Jiangsu Yocaly Health Management Company. More than 500 heart patients are currently using this device, and to date it has been used by over 30 million people. An example of success on the institute side is the Suzhou New District People's Hospital, which has upgraded eight major pieces of equipment through evaluation projects, including an ultrasound device and digital X-ray machine from Mindray Medical and other well-known Chinese companies. A positive outcome was also achieved at the Liu Garden Community Health Center, which received a digital X-ray machine from Yuwell Medical, making it the first community center to use such a high-end device. It also established a remote diagnostics network together with larger municipal hospitals and thoroughly upgraded its medical equipment, including diagnostic systems, ultrasound equipment, and biochemical analyzer, amongst others, enabling it to provide robust primary health services to the surrounding community.

SUMMARY AND OUTLOOK

We have to date completed a preliminary assessment of the information management system and long-term supply and service process for the industrial development of medical devices in China using an evaluation system paradigm. The real advantage of this setup is that a large number of new and novel medical devices can be provided to hospitals, not only improving the level of service in Chinese medical institutions, but also providing a means to promote the improvement of medical devices and at the same time reduce health
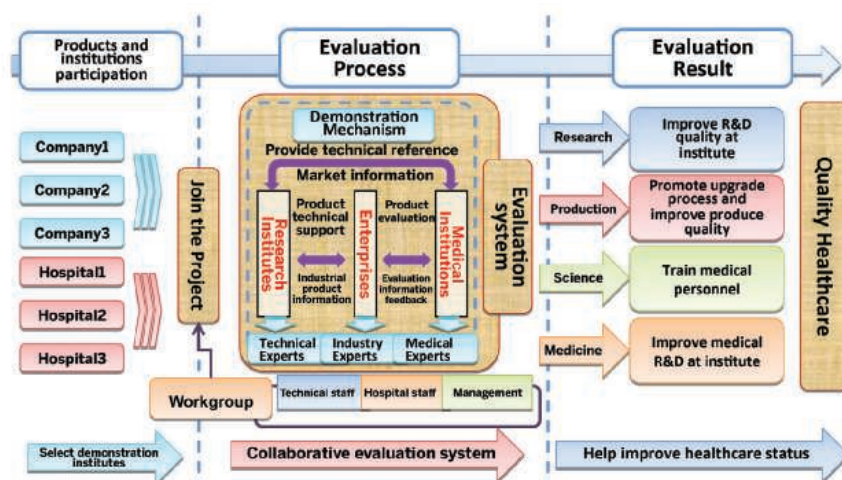
Figure 1. The long-term supply and service process.
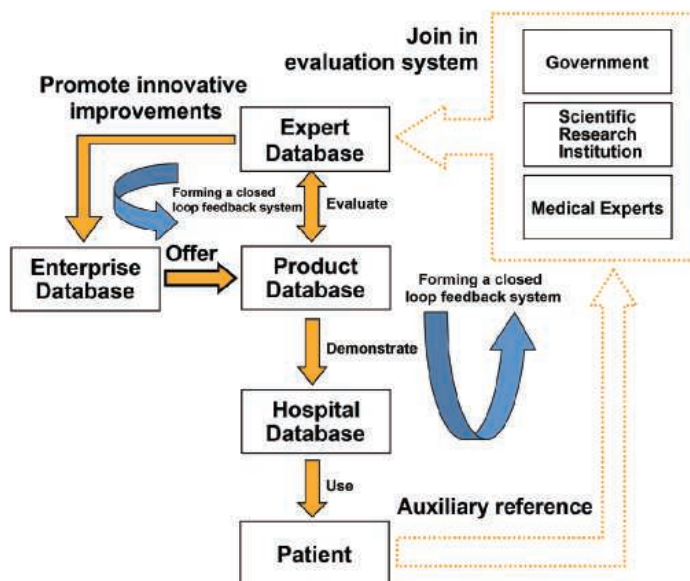
Figure 2. Information management system.

care costs. The targeted allocation of suitable products to primary health care institutions in particular has been very positively received.

With this in mind, we believe that the use and expansion of the evaluation system should be continued in order to promote innovation in the medical device space, create better products, and bring them to market more quickly. This will both benefit public health in general and accelerate development of a strategic emerging medical device industry.

REFERENCES

1. http://www.ptl-group.com/blogs/medical-equipment-in-china.
2. Fact sheet: medical device sector commission staff working document-impact assessment on the revision of the regulatory framework for medical devices, Appendix 4, Brussels, 26 September, 2012, http://ec.europa.eu/health/medical-devices/files/revision_docs/revision_ia_part3_appendices_en.pdf.
3. http://electronics-info.org/electronics/can-medical-devices-save-japanese-electronics-industry/.

aCGH DATA ANALYSIS

Complimentary with all CytoSure array purchases, the latest version (4.5.3) of CytoSure Interpret Software is a powerful and easy-to-use package for the analysis of aCGH data, the gold-standard for copy number variation (CNV) detection. Offering an impressive combination of advanced features, including Automatic Aberration Classification, the software allows the choice of standardized or customized user-defined data analysis. With this latest version, OGT has introduced several innovative new features that further facilitate and standardize the data analysis workflow in order to deliver rapid access to meaningful results. By using information available in online databases such as DECIPHER and settings defined by the user, the Automatic Aberration Classification enables users to configure the software to automatically perform an initial classification of any detected CNV, accelerating analysis and standardizing the interpretation process. CytoSure Interpret Software allows simultaneous access to sample and experiment information across a network, providing the potential for labs on multiple sites to access a central database.

Oxford Gene Technology

For info: +44-(0)-1865-856826 | www.ogt.com/interpret

MLPA ANALYSIS

The latest version of the GeneMarker Software includes automated quality control evaluation in the widely used MLPA analysis module. Multiplex Ligation-dependent Probe Amplification (MLPA) is a powerful technique to detect deletions and insertions and is used in clinical research on a variety of genetic diseases and cancers. MLPA reactions are composed of several steps; quality control fragments in MLPA reactions indicate success or failure of polymerase chain reaction, denaturation, ligation, hybridization, and adequate DNA concentration for the reaction. Before the inclusion of this automated quality control evaluation feature, the analyst would review the raw data prior to analysis and identify any problematic samples. The automated evaluation of quality control fragments detects and flags any sample that does not meet the criteria of the MLPA kit, increasing efficiency of data analysis and improving workflow. The software processes and normalizes raw data files, allowing the user to load their raw data, process the data, and proceed directly to MLPA analysis.

SoftGenetics

For info: 814-237-9340 | www.softgenetics.com

NEXT GENERATION SEQUENCING LIMS

The Exemplar Next Generation Sequencing (NGS) Laboratory Information Management System (LIMS) will track multiple NGS platform workflows from request through processing and analysis. Exemplar's NGS LIMS features all of the following: prebuilt CLIA standard workflows for leading NGS platforms, instrument integrations with NGS platforms and leading QC instruments, support for automation via integration with leading robotic sample preparation platforms, a highly graphical and intuitive interface, graphical executive dashboard for viewing lab activity in any timeframe, and complete consumables management for reagents and other consumables with reorder alerts. It is a 100% web-based solution with no extra software required from the client and is usable on iPads and other tablets. The system is scalable for small labs to large multinational, multi-lab deployments. Exemplar NGS LIMS is targeted at NGS labs, but retains the full capability of the Exemplar ecosystem to address any lab's needs, such as genotyping and proteomics.

Sapio Sciences

For info: 410-800-4620 | www.sapiosciences.com

DNA COPY NUMBER ANALYSIS

Version 7.5 of Nexus Copy Number software introduces a new next generation sequencing (NGS) module for analysis of sequence variants from array or NGS platforms and detection of copy number from sequencing data. The software expands support for the Affymetrix platform with support for the OncoScan FFPE Assay Kit and Affymetrix Axiom Human Genotyping array. Notable features for the case review workflow include new filters that quickly cut variations down to potential pathogenic ones, including a trio analysis filter to remove parental calls from the proband, and the ability to display previous samples containing a variant under review. For cancer applications, improvements include ASCAT 2.1—which does not require a matched normal—and the ability to detect copy number variations from whole-genome and whole-exome sequencing. Nexus version 7.5 features integrated analysis allowing identification of sequence variants overlapping copy number aberrations or homozygous regions, along with the added ability to store and query sequence variants in the Nexus DB genomic data repository.

BioDiscovery

For info: 310-414-8100 | www.biodiscovery.com

ICP-MS SOFTWARE

Syngistix software is a workflow-based software designed to improve efficiencies in the laboratory. It features an easy-to-use, intuitive interface, along with new automated method setup tools for faster implementation. The software's user-defined and customizable reporting capabilities facilitate support for a variety of peripherals, including online auto-dilution systems, laser ablation, flow injection, and field-flow fractionalization. The software's optional dedicated Nano Application Module can be combined with the NexION 350 ICP-MS for nanomaterial detection and characterization.

Perkin Elmer

For info: 877-754-6373 | www.perkinelmer.com

Electronically submit your new product description or product literature information! Go to www.sciencemag.org/products/newproducts.dtl for more information.

Newly offered instrumentation, apparatus, and laboratory materials of interest to researchers in all disciplines in academic, industrial, and governmental organizations are featured in this space. Emphasis is given to purpose, chief characteristics, and availability of products and materials. Endorsement by Science or AAAS of any products or materials mentioned is not implied. Additional information may be obtained from the manufacturer or supplier.

immunogenomics 2014

September 29 - October 1, 2014

HudsonAlpha Biotechnology Campus

Huntsville, Alabama, USA

Bringing together preeminent leaders and thinkers at the intersection of genomics and immunology

Our Keynote Speakers:

Christophe Benoiste
Professor, Department of Microbiology and Immunobiology, *Harvard Medical School*

Mary Ellen Conley
Federal Express Chair of Excellence and Professor, Department of Pediatrics, *University of Tennessee, College of Medicine, Memphis*

Mark Davis
Investigator, Howard Hughes Medical Institute; Professor, Department of Microbiology and Immunology; Director, Institute for Immunity, Transplantation, and Infections, *Stanford University School of Medicine*

Register today at
haig.aaas.org

presented by

HUDSONALPHA
INSTITUTE FOR BIOTECHNOLOGY

Science
AAAS

Sponsored by

Platinum Sponsors

iRepertoire, Inc.

Gold Sponsors

UAB
COMPREHENSIVE ARTHRITIS, MUSCULOSKELETAL, AND AUTOIMMUNITY CENTER

Silver Sponsors

GenapSys

illumina®

Interested in sponsoring Immunogenomics 2014?
Visit our website for more information.

follow
@immunogenomics
on
twitter

Antibodies for Intracellular Flow Cytometry

from Cell Signaling Technology

WB · **F** · **IHC** · **ChIP** · **IF** · **IP**

In vertebrates, the Wnt/β-Catenin signaling pathway is important in early embryonic development and tumorigenesis. CST offers flow cytometry validated antibodies to multiple intracellular components in the Wnt/β-Catenin pathway.

:: **Validated for intracellular proteins**

:: **Highly specific and sensitive antibodies**

:: **Lot-to-lot consistency**

:: **Technical support from the CST scientists who produced and validated your antibody**

Request a Flow Cytometry Reference Wheel:
www.cellsignal.com/flowscience

Wnt/β-Catenin Signaling

OFF-State

ON-State

Target Genes: Myc, Cyclin D1, TCF-1, PPAR-δ, MMP-7, Axin-2, CD44, etc.

Migration ↑
Adhesion ↓
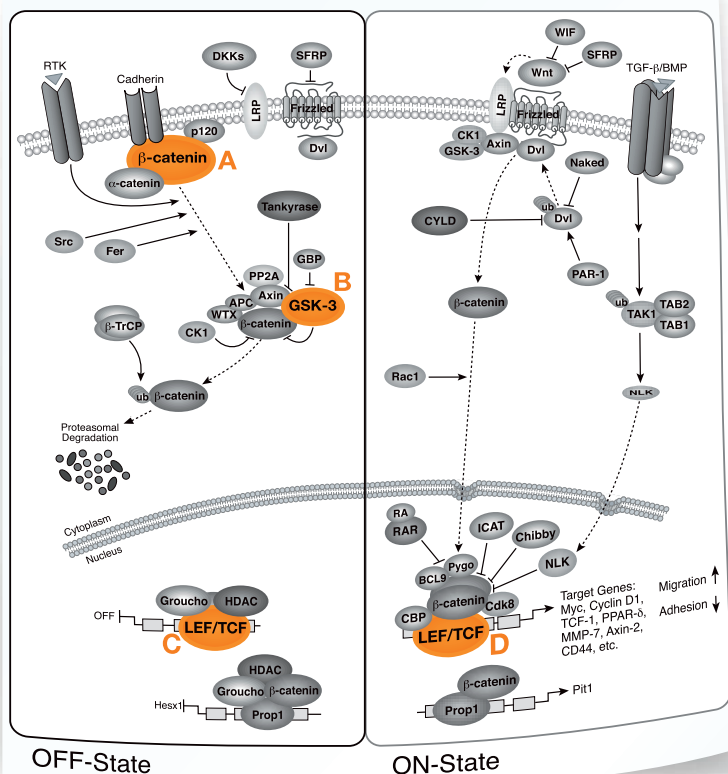
#4627 detects β-Catenin in HeLa (positive), but not NCI-H28 (negative) cells.

A

β-Catenin (Alexa Fluor® 647 Conjugate)

β-Catenin (L54E2) Mouse mAb (Alexa Fluor® 647 Conjugate) #4627: Analysis of NCI-H28 cells (blue) and HeLa cells (green).

#8466 detects Ser9 phosphorylated GSK-3β in stimulated cells.

B

Phospho-GSK-3β (Ser9) (PE Conjugate)
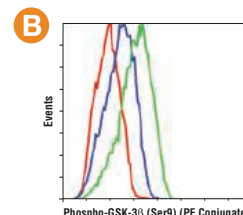
Phospho-GSK-3β (Ser9) (D85E12) XP® Rabbit mAb (PE Conjugate) #8466: Analysis of NIH/3T3 cells treated with hPDGF-BB #8912 and λ phosphatase (red), untreated (blue), or treated with hPDGF-BB #8912 only (green).

C

IgG Control   LEF1

LEF1 (Alexa Fluor® 488 Conjugate)
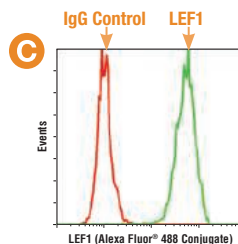
LEF1 (C12A5) Rabbit mAb (Alexa Fluor® 488 Conjugate) #8490: Analysis of Jurkat cells using LEF1 (C12A5) Rabbit mAb (Alexa Fluor® 488 Conjugate) (green) compared to Rabbit (DA1E) mAb IgG XP® Isotype Control (Alexa Fluor® 488 Conjugate) #2975 (red).

D

IgG Control   TCF-1

TCF1 (Pacific Blue™ Conjugate)
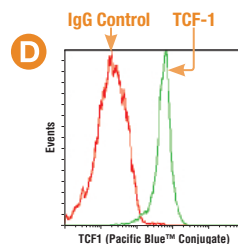
TCF1 (C63D9) Rabbit mAb (Pacific Blue™ Conjugate) #9066: Analysis of Jurkat cells using TCF1 (C63D9) Rabbit mAb (Pacific Blue™ Conjugate) (green) compared to Rabbit (DA1E) mAb IgG XP® Isotype Control (Pacific Blue™ Conjugate) #9078 (red).

Cell Signaling
TECHNOLOGY®

Recruitments of talents abroad by Nanjing University of Science and Technology

NANJING UNIVERSITY OF SCIENCE & TECHNOLOGY

南京理工大学

http://rczp.njust.edu.cn/urp-portal/portal/group/Recruit

Nanjing University of Science and Technology (NUST) is one of the first national "211 Project" universities affiliated with the Ministry of Industry and Information Technology. It has become a multi-disciplinary and coordinated developing engineering-based university along with science, liberal arts, economics, management, law, education, etc. It is an ideal place for research work for its strong scientific research ability, prominent advantages, perfect construction of infrastructural facilities and it's also a pleasant place to live in since the beautiful scenery of Dr. Sun Yat-sen's Mausoleum which is only less than one mile away.

Please refer to the following application guidelines and we welcome your applications.

Majors for recruitment:

Related disciplines of Ordnance Science and Technology, Mechanical Engineering, Instrumentation Science and Technology, Chemical Engineering and Technology, Chemical, Electronic Science and Technology, Information and Communication Engineering, Optics, Optical Engineering, Computer Science and Technology, Control Science and Technology, Electrical Engineering, Transportation Engineering, Aerospace Science and Technology, Power Engineering and Thermal Physics, New Energy, Mechanics, Mathematics, Physics, Civil Engineering, Materials Science and Engineering, Environmental Science and Engineering, Biomedical Engineering, Law, Intellectual Property, Public Administration, Sociology, Economics, Management Science, (Applied) Linguistics and Literature, Art and Design.

Position and requirements:

Recruiting position: "Zijin scholars" distinguished professor, "Young Talents Professors", Professor, Associate Professor, Assistant Professor.

Basic qualities: Overseas talents with a doctorate degree, passion for education, high academic achievement and strong research capability and, good professionalism, academic character and team spirit as well. Among them, the candidates for "Young Talent Professor" staff position should be under 35 years old.

Related treatment:

The full-time employed teachers will be directly categorized into national institution, enjoying free medical care, pensions and other state welfare, and the family issues such as children's nursery and schooling will be addressed. We provide the high-level personnel and young talents with transitional housing, financial relief, research funding and other supports with generous salaries, comfortable working and living conditions. For high-level talents, we help settle down in terms of team building, work, housing, etc. Specific treatment will be determined by personal discussion.

1. For the full-time "Thousands of Plans" and other leading talents, NUST will provide 600 thousand to 1 million RMB annual salary and no less than 8 million RMB research start-up funds.

2. For the "Thousands Youth Talents" and other related talents, we provide no less than 300 thousand RMB annual salary, 1 million RMB financial relief and 2-4 million RMB research start-up funds.

3. For the "Zijin scholars" distinguished professor, we provide 500 thousand to 2 million RMB financial relief, 1 to 5 million RMB research funds and stipulated wages and other benefits along with certain amount of professor allowances per year.

4. For the "Young Talented Professors", we provide 300 thousand RMB annual salary, with certain financial relief and start-up funds.

5. For the professor, associate professor, assistant professor, we will provide salary and financial relief which is competitive in the same region, as well as starter home, and provide appropriate amount of research funds.

Way for recruitment:

The recruitments of talents abroad by NUST is under way regularly, please log in NUST Recruitment Network http://rczp.njust.edu.cn/urp-portal/portal/group/Recruit to have a registration, or contact us directly.

Contact us:

JI Wenchao   Meng Yang

Tel: 86-25-84316943

Mail: rcb@njust.edu.cn

NUST website: www.njust.edu.cn

Sun Yat-sen University, Professor or Associate Professor in Marine Sciences

South China Sea Resource Exploitation and Protection Collaborative Innovation Center (SCS-REPIC) has been recently established in Sun Yat-sen University, Guangzhou, China. SCS-REPIC invites applications for several faculty positions at Associate Professor and Full Professor levels.

All applicants must have a Ph.D. or equivalent degree, and a strong record of research accomplishments. Successful applicants are expected to establish and maintain an extramurally funded research program with emphasis in the areas of (marine geology, physical oceanography, marine ecology, marine chemistry, marine natural products, data mining with big data, marine biology).These positions include a 12-month salary, fringe benefits, competitive start-up package, and modern laboratory facilities or by negotiations.

To apply for these positions, please send your CV and a brief statement of research interests to hanmox@mail.sysu.edu.cn.

Review of applicants will begin as soon as the applications are submitted and will continue until the positions are filled. Anticipated start-date is the spring or summer of 2014.The SYSU is an equal opportunity employer and encourages persons of any races, ethnicity, ages and genders to apply.

2015 Vetlesen Prize

Call for Nominations

The Vetlesen Prize, established in 1959 by the G. Unger Vetlesen Foundation, is awarded for scientific achievement that has resulted in a clearer understanding of the Earth, its history, or its relations to the universe. The prize consists of a medal and a cash award of $250,000. Nominations are now open for the next prize, which will be awarded in 2015.

As of 2015, the prize will be awarded to a single individual, who can reside and work anywhere in the world. The prize is administered by Columbia University's Lamont-Doherty Earth Observatory.

Nomination packages should include at least two letters that describe the nominee's contributions to a fuller understanding of the workings of our planet, along with a one-paragraph biographical sketch and the full curriculum vitae of the candidate.

For more information about the Vetlesen Prize:
http://www.ldeo.columbia.edu/vetlesen-prize

Past Vetlesen Laureates

2012	Susan Solomon, Jean Jouzel
2008	Walter Alvarez
2004	W. Richard Peltier, Sir Nicholas J. Shackleton
2000	W. Jason Morgan, Walter C. Pitman III, Lynn R. Sykes
1996	Robert E. Dickinson, John Imbrie
1993	Walter H. Munk
1987	Wallace S. Broecker, Harmon Craig
1981	M. King Hubbert
1978	J. Tuzo Wilson
1974	Chaim L. Pekeris
1973	William A. Fowler
1970	Allan V. Cox, Richard R. Doell, S. Keith Runcorn
1968	Francis Birch, Sir Edward Bullard
1966	Jan Hendrik Oort
1964	Pentti E. Eskola, Arthur Holmes
1962	Sir Harold Jeffreys, Felix Andries Vening Meinesz
1960	W. Maurice Ewing

Women in Science Booklet

Science and the L'Oréal Foundation present

Read inspiring profiles of women making a difference in biology.

**Free download at
ScienceCareers.org/LOrealWIS**

∞ IRENA
International Renewable Energy Agency

Director Knowledge, Policy and Finance Centre D-1

Location: Abu Dhabi (United Arab Emirates), IRENA Headquarters
Duration: Two years Fixed Term Appointment, with possible extension
Closing Date: 18 May 2014

The International Renewable Energy Agency (IRENA) seeks to recruit a Director for the Knowledge, Policy and Finance Centre (KPFC) in the IRENA Secretariat.

IRENA is an inter-governmental organisation, mandated by governments to promote the widespread adoption and sustainable use of all forms of renewable energy. It facilitates and catalyses sharing of best practices and lessons learned regarding policy frameworks, capacity-building, finance mechanisms and other relevant measures for accelerating and expanding the demonstration and deployment of renewable energy technologies.

KPFC is IRENA's central knowledge repository and a centre of excellence for renewables policy and finance issues. KPFC's information collection and analysis supports the work of other divisions, as well as providing critical knowledge products to IRENA's Members and the public. The division is also a platform for engagement with the private sector and civil society.

Under the direct supervision of the Director-General and within delegated authority, the Director, KPFC, undertakes a range of analytical and advisory activities aimed at providing accurate information, sound advice and a broader knowledge base to assist countries in making informed renewable energy policy decisions.

Further details of the vacancy announcement and information on how to apply can be obtained at **www.irena.org/Jobs** .